UNIVERSITY OF CALIFORNIA SAN DIEGO

Nucleation, Fabrication, and Competition in Antiferromagnetic Textures Studied with Coherent Resonant Soft X-ray Scattering

A dissertation submitted in partial satisfaction of the
requirements for the degree
Doctor of Philosophy

in

Physics

by

Rourav Basak

Committee in charge:

Professor Alex Frano, Chair
Professor Daniel Arovas
Professor Eric Fullerton
Professor Tenio Popmintchev
Professor Oleg Shpyrko

2024

The dissertation of Rourav Basak is approved, and it is acceptable in quality and form for publication on microfilm and electronically.

University of California San Diego

2024

DEDICATION

To Ma, Baba, and Esha.

TABLE OF CONTENTS

LIST OF FIGURES

LIST OF TABLES

ACKNOWLEDGEMENTS

I would like to thank my advisor, Prof. Alex Frano, for his unwavering support and guidance. He inspired me to explore a vast variety of problems which gave me the opportunity to diversify my horizon. I am deeply indebted to him. I would also like to thank my committee members Prof. Daniel Arovas, Prof. Eric Fullerton, Prof. Tenio Popmintchev, and Prof. Oleg Shpyrko for their guidance, teaching and support during my PhD at UCSD.

I am grateful to the postdoctoral researchers who helped me understand the nuances of the fields. Martin Blushcke and Ivan Zaluzhnyy taught me coherent scattering patiently. I learned about strongly correlated systems from Alejandro Ruiz and Sarmistha Das. Shan Wu taught me a lot of things including strongly correlated magnetic systems. Their mentoring, support, and encouragement were very precious along my journey.

Beamtimes were a significant portion of the research and beamtimes are always a great time to develop friendships. Boyan, Erik, Brandon, Nelson, Elliot, Biswajit, Mayia, Dong, Francis, Robin, Nicolo, Josh, Holden, Andy, Nathan, Shan, Youzhe, Sarmistha, Alejandro, Ivan, Kirsty, and Wenxin: thank you all for the fun, for the shared journey towards success and failure, and the stimulating discussions along the way. The hardship of the beamtimes became a cakewalk with them. I am also extremely grateful to share the 3rd floor of Mayer hall with them and Reno, Kate, Amy, Ash, Ashley, Adolfo, and Quinn.

I loved the physics classes in UCSD and somehow I learned every course in Physics from a condensed matter physics professor. Thanks to Dan Arovas, Nigel Goldenfeld, Yi-Zhuang You, John McGreevy, Michael Fogler, and Tarun Grover for the classes. I learned a lot and enjoyed them thoroughly. My professors in New York University: L. Andrew Wray, Lorcan Forlan, Vladimir Tsifrinovich, Edward Wolf and David Grier - I am thankful for the classes, research opportunities and guidance. Apart from classes, I learned significantly from the beamline scientists who are like libraries themselves. Fanny Rodolakis, Andi Barbour, Yi-de Chuang, and Eugene Weshcke were instrumental in my research. Among other beamline scientists, I was

fortunate enough to work with Claudio Mazzoli, Xiao Chen, Andrei Fluerasu, Christie Nelson, Raul Acevedo-Esteves, Rahul Jungid, Jonathan Pelliciari, John Freeland, Jessica McChesney, Philip Ryan, Jong-Woo Kim, Eric Dufresne, Suresh Narayan, Christoph Klewe, Alpha N'Diye, Padraic Shafer, Sujoy Roy, Sophie Morley, Andreas Scholl, Anoitne Wojdyla, Vivek Thampy. I want to thank them all for their dedication, shared enthusiasm, and support during the beamtime.

I am also thankful to Uday , Frances, Nirjhar, and Robert Dynes for the samples related to the focused helium implantation. Tianxing, Nareg, Junjie, Ben, Henry, and Ali were also significantly helpful in characterizing the thin film using transport. I am also thankful for the support system of UCSD which manifested through Sharmila Poddar, Catherine McConney, Brad Hanson, Feifei Yu, Tina Silva, Robin Knoxx, Maio Rojas, and Lester Brooks.

My friends in San Diego: Ieva and Boyan, Rinki and Abhra, Varun, Sridip, Ahanjit, Shouvik, Nirjhar, Evgueni, Sourjya and Soumi, my friends in New York: Shayantani, Amitabha, Mainak, Erica, Igor, Paul, Alex - thank you for being the support system. Arkarup, Sanchari, Sanghita, Shyamal, and Joydip Ghosh thank you for guiding me during the early days of Physics and graduate applications. Thank you Prof. Raj Gandhi for meeting me and giving me directions on how to find my path. I am also forever indebted to my friend Pratim. Thank you.

Since my father taught me the first lesson in geometry, I was hooked to Physics. Thank you for teaching me so nicely during my childhood. My mother taught me how to question and my father taught me how to be curious. My parents provided the essential environment and taught me everything that I needed to learn. Thank you for being the amazing people you are. I found a similar set of amazing people as my parents-in-laws. Thank you for the confidence and support you provide everyday. Finally, Esha, my wife - I don't even know where to begin. I am just thankful everyday that you are in my life.

Chapter 2, in part, has been published in Science Advances, 8, 29, 2022, Martin Bluschke*, Rourav Basak*, Andi Barbour, Ashley N. Warner, Katrin Fursich, Stuart Wilkins, Sujoy Roy, James Lee, Georg Christiani, Gennady Logvenov, Matteo Minola, Bernhard Keimer, Claudio

Mazzoli, Eva Benckiser, Alex Frano (* indicates equal contribution), ”Imaging mesoscopic antiferromagnetic spin textures in the dilute limit from single-geometry resonant coherent x-ray diffraction”. The dissertation author was the primary investigator and author of this paper.

Chapter 4, in part, has been published in Physics Review Letters, 131, 186701, 2023, Shan Wu*, Rourav Basak*, Wenxin Li, Jong-Woo Kim, Philip J. Ryan, Donghui Lu, Makoto Hashimoto, Christie Nelson, Raul Acevedo-Esteves, Shannon C. Haley, James G. Analytis, Yu He, Alex Frano, and Robert J. Birgeneau (* indicates equal contribution), ”Discovery of Charge Order in the Transition Metal Dichalcogenide FexNbS2”. The dissertation author was the primary investigator and author of this paper.

VITA

2012	B. Tech. in Electrical Engineering, National Institute of Technology Durgapur india
2018	M. S. in Applied Physics, New York University
2024	Ph. D. in Physics, University of California San Diego

PUBLICATIONS

X. Chen, A. Ruiz, A. J. Bishop, B. Gunn, R. Basak, T. Zhu, Y. He, M. Vranas, E. Weschke, R. K. Kawakami, R. J. Birgeneau, A. Frañó, "Antiferromagnetic order in a layered magnetic topological insulator $MnBi_2Se_4$ probed by resonant soft x-ray scattering", Physical Review B, 2024.

Y. H. Wu, C. Hu, Y. Xie, B. G. Jang, J. Huang, Y. Guo, S. Wu, C. Hu, Z. Yue, Y. Shi, R. Basak, Z. Ren, T. Yilmaz, E. Vescovo, C. Jozwiak, A. Bostwick, E. Rotenberg, A. Fedorov, J. Denlinger, C. Klewe, P. Shafer, D. Lu, M. Hashimoto, J. Kono, A. Frañó, R. J. Birgeneau, X. Xu, J. X. Zhu, P. Dai, J. H. Chu, M. Yi, "Spectral Evidence for Local-Moment Ferromagnetism in van der Waals Metals Fe_3GaTe_2 and Fe_3GeTe_2, Physics Review B, 2024.

Y. Wang, Y. Zhou, Q. Yang, R. Basak, Y. Xie, D. Le, W. Shipley, A. Frañó, G. Arya, A. R. Tao, "A Multiphysics Approach for Self-Assembly of Nanocrystal Checkerboards via Non-Specific Interactions", Nature Communications, 2024.

H. Navarro, S. Das, F. Torres, R. Basak, E. Qiu, N. M. Vargas, P. N. Lapa, I. K. Schuller, A. Frañó, "Disentangling transport mechanisms in a correlated oxide by photoinduced charge injection", Physical Review Materials, 2023.

S. Wu*, R. Basak*, W. Li, J. W. Kim, P. J. Ryan, D. Lu, M. Hashimoto, C. Nelson, R. Acevedo-Esteves, S. C. Haley, J. G. Analytis, Y. He, A. Frañó, R. J. Birgeneau, "Discovery of Charge Order in the Transition Metal Dichalcogenide Fe_xNbS_2", Physics Review Letters, 2023.

K. Scott, E. Kisiel, T. J. Boyle, R. Basak, G. Jargot, S. Das, S. Agrestini, M. Garcia-Fernandez, J. Choi, J. Pelliciari, J. Li, Y. D. Chuang, R. Zhong, J. A. Schneeloch, G. Gu, F. Légaré, A. F. Kemper, K. J. Zhou, V. Bisogni, S. Blanco-Canosa, A. Frañó, F. Boschini, E. H. da Silva Neto, "Low-energy quasi-circular electron correlations with charge order wavelength in $Bi_2Sr_2CaCu_2O_{8+\delta}$", Science Advances, 2023.

V. Sunko, Y. Sun, M. Vranas, C. C. Homes, C. Lee, E. Donoway, Z.-C. Wang, S. Balguri, M. B. Mahendru, A. Ruiz, B. Gunn, R. Basak, S. Blanco-Canosa, E. Schierle, E. Weschke, F. Tafti, A. Frañó, and J. Orenstein, "Spin-carrier coupling induced ferromagnetism and giant resistivity peak in $EuCd_2P_2$", Physics Review B, 2023.

A. Ruiz, B. Gunn, Y. Lu, K. Sasmal, C. M. Moir, R. Basak, H. Huang, J. S. Lee, F. Rodolakis, T. J. Boyle, M. Walker, Y. He, S. Blanco-Canosa, E. H. da Silva Neto, M. Brian Maple & Alex Frañó, "Stabilization of three-dimensional charge order through interplanar orbital hybridization in $Pr_xY_{1-x}Ba_2Cu_3O_{6+\delta}$", Nature Communications, 2022.

M. Bluschke*, R. Basak*, A. Barbour, A. N. Warner, K. Fürsich, S. Wilkins, S. Roy, J. Lee, G. Christiani, G. Logvenov, M. Minola, B. Keimer, C. Mazzoli, E. Benckiser, A. Frañó, "Imaging mesoscopic antiferromagnetic spin textures in the dilute limit from single-geometry resonant coherent x-ray diffraction", Science Advances, 2022.

L. Miao, C. H. Min, Y. Xu, Z. Huang, E. C. Kotta, R. Basak, M. S. Song, B. Y. Kang, B. K. Cho, K. Kißner, F. Reinert, T. Yilmaz, E. Vescovo, Y. D. Chuang, W. Wu, J. D. Denlinger, L. A. Wray, "Robust Surface States and Coherence Phenomena in Magnetically Alloyed SmB_6", Physics Review Letters, 2021.

L. Miao, R. Basak, S. Ran, Y. Xu, E. Kotta, H. He, J. D. Denlinger, Y.D. Chuang, Y. Zhao, Z. Xu, J. W. Lynn, J. R. Jeffries, S. R. Saha, I. Giannakis, P. Aynajian, C. J. Kang, Y. Wang, G. Kotliar, N. P. Butch, L. A. Wray, "High temperature singlet-based magnetism from Hund's rule correlations", Nature Communications, 2019.

R. Basak, V. I. Tsifrinovich, Electron capture beta decay of partially polarized nuclei, Modern Physics Letters A, 2019.

S. Pal, U. Panda, R. Basak, "Process control for parallel run of two Helium Liquefiers at VEC Centre, Kolkata", Proceedings of the ninth international workshop on personal computers and particle accelerator controls, 2012.

R. Basak "Novel Experimental Setup to Study the Magneto-Resistance of Semiconductors and Its Industrial Application", International Journal of Applied Physics and Mathematics, 2012.

*contributed equally

ABSTRACT OF THE DISSERTATION

Nucleation, Fabrication, and Competition in Antiferromagnetic Textures Studied with Coherent Resonant Soft X-ray Scattering

by

Rourav Basak

Doctor of Philosophy in Physics

University of California San Diego, 2024

Professor Alex Frano, Chair

Strongly correlated electron physics host complex phenomena. Often such complex phenomenon are found close to Anti-ferromagnetic phase by tuning one parameter with which the spin degrees of freedom couple to. Examples of such complex phenomena include pseudo-gap phase, spin density wave, charge density wave, superconductivity and many more. Furthermore, phase competition and phase coexistence is ubiquitous in these materials. Here we focus on such strongly coupled antiferromagnets and utilize coherent resonant scattering to study their real space structures. We will see that the real space evolution of meso scale structure encodes many crucial information about the physics of the complex system. Finally we end our discussion with

proposing modification to existing coherent scattering experiments to study dynamic equilibrium states of metastable matter.

Chapter 1

Pattern formation in antiferromagnets

A homogeneous universe would have been a boring universe. Our captivating universe showcases intricate structures at different length scales. A simple short ranged interaction between nearest neighbors can manifest long range orders of thermodynamically large number of constituents and break the symmetry. The system is considered to have gone a 'phase transition'. The collective behavior of the constituents in a long range order can behave significantly different from the fundamental property of the constituents [1]. One striking example is superconductivity where individual electrons instead of repelling each other forms 'cooper pair' to conduct energy without dissipation. That knowing the physics of constituent particles does not automatically allow us to predict the properties of the system at a larger length scale where collective behavior becomes important, is the central theme of condensed matter physics, one of the many things that makes our lives significantly interesting.

The length scale of our problem begins at $\mathring{A}$ where the ions are organized in a precise manner to form a crystal structure. The typically discussed interactions in condensed matter physics ranges from nearest neighbor interaction to a few nanometers. However we consider thermodynamically large number of ions and equivalent number of electrons as the constituents. Thus, statistical properties of this ensemble dictates the likely state the system. Furthermore,

at this length scales quantum effects become important also. Different degrees of freedom of electrons follow symmetry and topology of the space they span. In strongly correlated electron systems, such as high temperature superconductors different degrees of freedom couple on top of the many body interaction they exhibit. Thus, such strongly interacting many body quantum systems become quite complex to understand.

Understanding strongly correlated electron physics opened up doors to new technologies. One such example is Giant Magneto-Resistance (GMR) which revolutionized the field of data storage[2]. The phenomena strongly correlated electrons harbor are also extremely important for technological perspective. For example, nickelates host highly tunable metal-insulator transition which can be used to create next generation energy efficient computer architechture known as neuromorphic computing[3]. High temperature superconductors host the key to the future in terms of realizing practical quantum computation, faster transportation and many more[4]. Colossal magnetoresistance in manganates [5], metal-insulator transition in vanadates shows incredible promise for next generation quantum devices[6]. Thus, understanding phenomena in strongly correlated electron systems will not only benefit the scientific motivation but also facilitate technological aspirations as well.

1.1 Common themes of strongly correlated electrons

Explaining phenomena in strongly correlated electron systems is probably one of the fundamental pursuit of present condensed matter physics research efforts. As a result phenomena in transition metal oxides such as cuprates, nickelates, vanadates, manganates, ruthenates etc. are studied typically. It is usual to study the response of the system as a thermodynamic parameter, say γ is varied. Typically for a given value of the theromodynamic parameter the system is cooled down to lower temperatures where the collective phase of the constituents change to indicate a phase transition. For strongly correlated materials it is often found that the phase space is textured,

such that a little change in the external tuning parameter results in a large change of the ground state phase as shown in the Figure 1.3. To understand strongly correlated electron systems and explain complex phenomena we must find common traits among seemingly different systems.

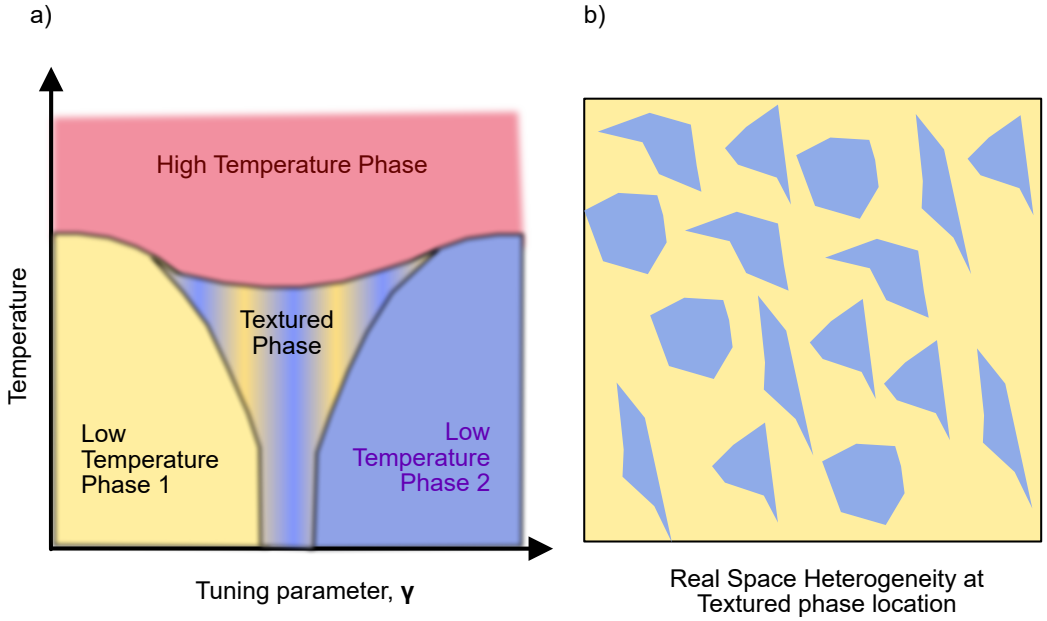

Figure 1.1: **Phase competition and phase coexistence in strongly correlated electron systems** (a) As a function of the tuning parameter a metastable textured phase emerges for in-between values where neither phase is preferred for a low temperature ground state phase. (b) Schematical representation of a textured phase

Phase texture: In such strongly correlated electron systems one of the main themes is complexity and organization of structures[7]. A common characteristic of the phase diagrams of various complex oxides is that different low temperature ground states emerge from a general high temperature state upon the judicious varying of a tuning parameter, represented schematically in Figure 1.3. This leads to the competition and/or coexistence between phases where neither of the two low temperature phases is strongly favored and are nearly degenerate. Furthermore, often at these border regions of parameter space where both phases are degenerate there is a local tendency toward either of the phases but globally neither of the phases dominate. Thus,

a metastable, laterally textured pattern emerges across the sample with lengths on the order of nanoscale to mesoscale . Also, at these border regions between phases one usually finds exotic quantum ground states (e.g., charge density waves [8]) and unusually large responses to small external perturbation (e.g., colossal magneto resistance [7]. A typical example of a metastable state is found during first order phase transition where the system exhibits hysteresis. For such metastable states it is important to characterize the heterogeneity locally.

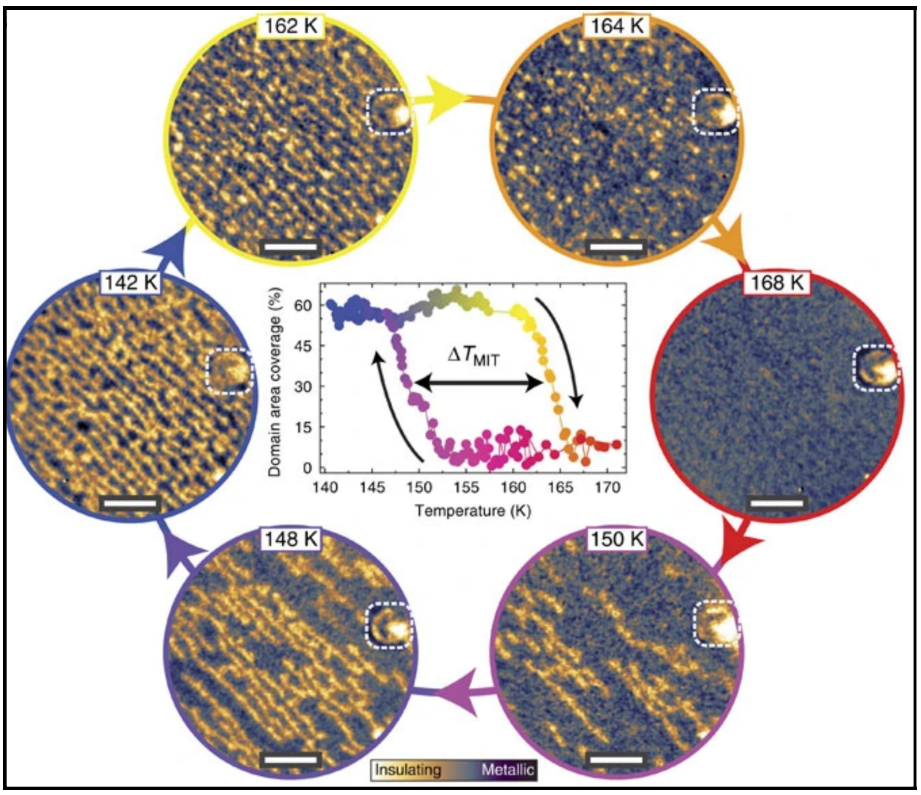

Figure 1.2: **Real space texture evolution during a first order phase transition** Here we have reproduced the result of Mattoni *et.al*. where the authors have shown the heterogeneity of electronic state in $NdNiO_3$ films. Measurements were done using X-ray photoelectron emission microscopy (X-PEEM)[9]. Throughout the thesis for simulation purposes we have used their measurements as masks to create hypothetical real space structure

For example, in the nickelates, various recent reports using x-ray photoelectron emission microscopy (X-PEEM) have observed a preferential nucleation and growth of insulating domains

in a background of metallic regions along surface morphology indicating the active role of the structure on the phase separation [9]. New imaging techniques deployed on an NdNiO3 film to visualize textured metal-insulator state found the coexistence of a first- and second-order phase transition phenomena at the domain boundaries which was attributed to coupling of charge and spin order parameters [10]. Another astounding report using a nano-focused x-ray beam tuned to the Ni L3 edge to detect the Bragg peak associated with the antiferromagnetic order noticed fractal geometric arrangement of antiferromagnetic domains hinting towards a proximity to a critical point [11]. In the manganates, disorder driven heterogeneous texture of two competing phases of ferromagnetic metal and antiferromagnetic insulator is observed when colossal magneto resistance emerges and argued to be related to each other both experimentally and theoretically [12]. The vanadates also feature remarkably inhomogeneous Mott insulating phases. At the onset the first-order transition, the rutile metallic phase coexists with an insulating monoclinic phase, forming non-trivial domain textures. These domains have recently been observed to form filaments upon the application of electric field pulses, which leads to resistive switching[13] . Near these exotic quantum phases and meta-stability dominated phase space whether the emergence of lateral heterogeneity is a cause or an effect of exotic quantum states remains unanswered.

Antiferromagnetism: Furthermore, a typical strongly correlated electron system is realized in Mott insulating paradigm which is defined as a strong nearest neighbor Coulomb interaction regime which prohobits even a half filled electron band to be itinerant. In such Mott insulators the electrons have to pay a high price in energy if they want to hop to the nearest neighbor site to doubly occupy a site. However, the desire of electrons to hop and lower its kinetic energy gives rise to an interesting phenomena of antiferromagnetism[14]. In some insulating materials electrons from the half filled shells of cations find intermediate coupled state with the non-magnetic anion. Though the anion the electrons hop from cation to cation to lower its energy. This mechanism is known as the super-exchange. The high energy interaction between cation and anion can be integrated out in favor of a low energy description of the spin in terms of Heisenberg

spin model where the nearest neighbor spin Hamiltonian is described as

$$H_{AFM} = J \sum_{\langle ij \rangle} \mathbf{S_i} \cdot \mathbf{S_j} \tag{1.1}$$

Such super exchange interaction usually results in a J>0 effective description of the spin Hamiltonian if the half filled cations overlap with the same anion orbital. Pauli's exclusion principle protects the super-exchange interaction and enforce J>0. In such scenario, the energy is further lowered by the nearest neighbor cation spins anti-aligning with each other. Thus, often Mott insulating strongly interacting electron systems are observed to be Antiferromagnetic. A slight de-tuning of the electronic environment from the typical Mott insulating state results in these novel quantum phases in the vicinity of decreasing spin correlation. This is shown in the figure below with different phase diagrams of oxides showing interesting exotic phases emerge near the antiferromagnetic phase.

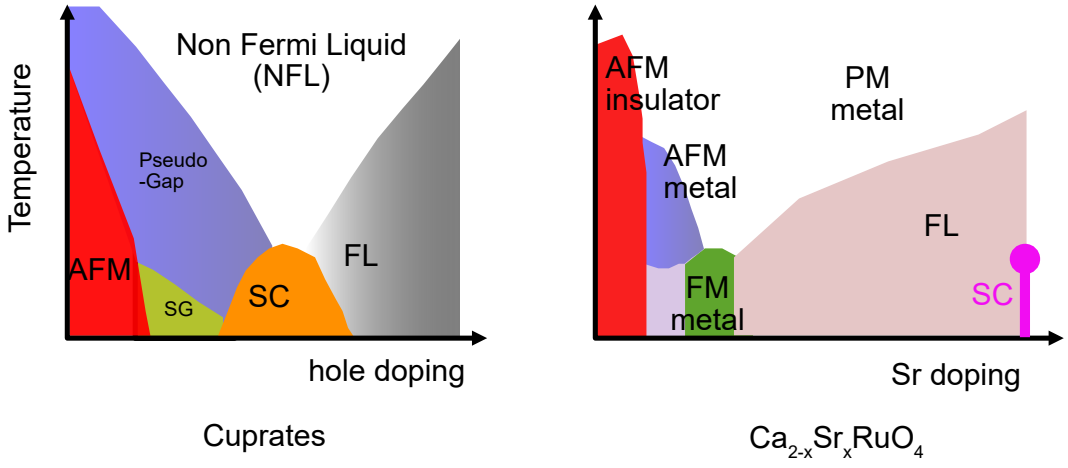

Figure 1.3: **Representative phase diagrams** Out of many correlated oxides here we show two phase diagrams highlighting the proximity of the Antiferromagnetic(AFM) phase to complex electronic phases such as pseudo-gap phase, splin glass (SG), antiferromagnetic metal etc.

Thus, we see incredibly rich physics exist near the vicinity of Mott insulating antiferro-

magnetic phase where one phase is not energetically favored over the other but a heterogeneous meta-stable textured phase of the material prevail. Locally exceptional events such as defects can favor one phase over the other for such strongly coupled electronic systems. Furthermore, due to strong coupling different degrees of freedom and by extension different phases of the material compete and co-exist with other phases. Thus, the phase organization in real space at the meso scale gets significantly influenced by the physics of the lower length scale in strongly correlated electron system. Even though meso-scale phase heterogeneity and evolution is such an important feature in the these systems [15] little advancement has been made understanding them majorly due to the lack of proper experimental tool to tackle the problem at different length scales simultaneously.

1.2 Antiferromagnetic textures relevant for technology

Antiferromagnetic materials are extremely important for next generation emerging technology of spintronics, which specializes in low energy and high speed information processing. Instead of charge in electronics, spintronics utilizes the spin degrees of freedom for storing and transporting information. Antiferromagnets are advantageous for such application due to the following characteristics it posses:

- they are robust against external magnetic field perturbation
- they do not produce stray fields
- they display ultrafast dynamics, orders of magnitude faster than its ferromagnetic counterpart
- they generate large magneto-transport effects for efficient read out of the information

Antiferromagnetic materials further exhibit vanishingly small dipolar interaction making the nearest neighbors free to gain a phase. That phase term evolves slowly over long distance

resulting in interesting textures such as domain walls, vortices, and skyrmions, interpreted as the topological defects of the order parameter field. Since the topological defects in antiferomagnets are further protected from fluctuations they offer robust memory solutions. The wider variety of spin textures for a given ordering vector allows richer realization of different domain wall configurations. Furthemore, light-like motion of the textures limited by the magnon group velocity enables high speed transport of robust memory extremely important for next generation computation technology. We briefly discuss here a few of the antiferromagnetic textures to

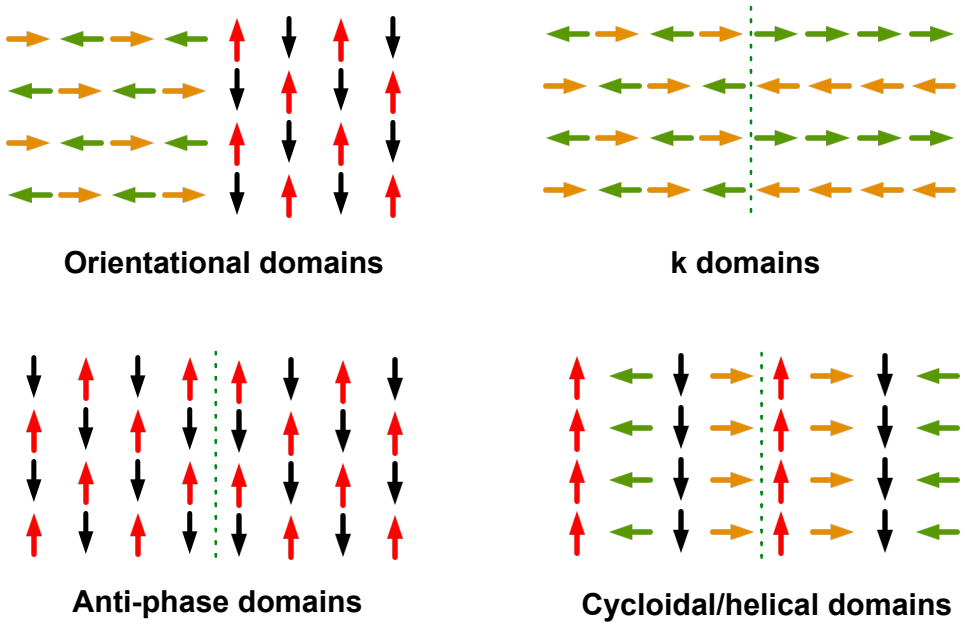

Figure 1.4: **Different antiferromagnetic domains and domain walls** Many different ways of classifying the order parameter to distinguish two domain state for antiferromagnets exist resulting into a zoo of domain structures. We show here the domains we discuss in the text after [16]

provide a broader over view of the richness this field offers. In an antiferromagnetic crystal a

domain is the spatial expanse over which the amplitude and the phase of the order paramteter corresponds to a given domain state. For a given crystal lattice symmetry the anti-ferromagnetic superlattice can be realized having different momentum vector orientation relative to the crystal lattice reciprocal space vectors. These are called k-domains. Furthermore, the relative orientation between magnetic moment directions between two domains can be different even though they follow antiferromagnetic coupling resulting into orientational-domains. Translational domains have same moment orientation and same wave vector of spin modulation but differ in phase. Thus we see that due to zero magnetization the choice of phase can be arbitrary resulting into complex spin textures. For instance, the phase of the spin moments can turn in a cycloidal or helical fashion. They can be colinear and non-colinear. So far we had been discussing domains which differed in one dimensions and allowed a domain wall in between. However, the structures separating two domains can become more complex. For such complex spin orientations the idea of a domain wall can be generalized in higher dimensions using the definition of topological defects of a field defined as

$$\oint_C \nabla \mathbf{M} \cdot d\mathbf{r} \tag{1.2}$$

This is known as winding number of the field and is non-zero for a loop around a topological defect. If the antiferromagnetic moment is confined to two dimensions it results into the structures called vortex and anti-vortex. For a three dimensional spin moment we realize skyrmion. Both vortices and skyrmion themselves are two dimensional structures.

1.4 shows a Z_4 type vortex on a two dimensional lattice. In thin films of α-Fe_2O_3, $Fe_{1/3}TaS_2$, and $Ca_2SrTi_2O_7$ observation of Z_6 AFM vortex/anti-vortex have been reported [16]. The skyrmions in antiferromagnets can be manipulated using spin polarized currents [17]. This further opens up possibilities of studying driven-disipative systems in the context of antiferromagnetic textures. Ideas similar to magnetic race-track memory but in the context of antiferromagnets can leverage higher frequency of operation along with low error in encoding information due to stray fields.

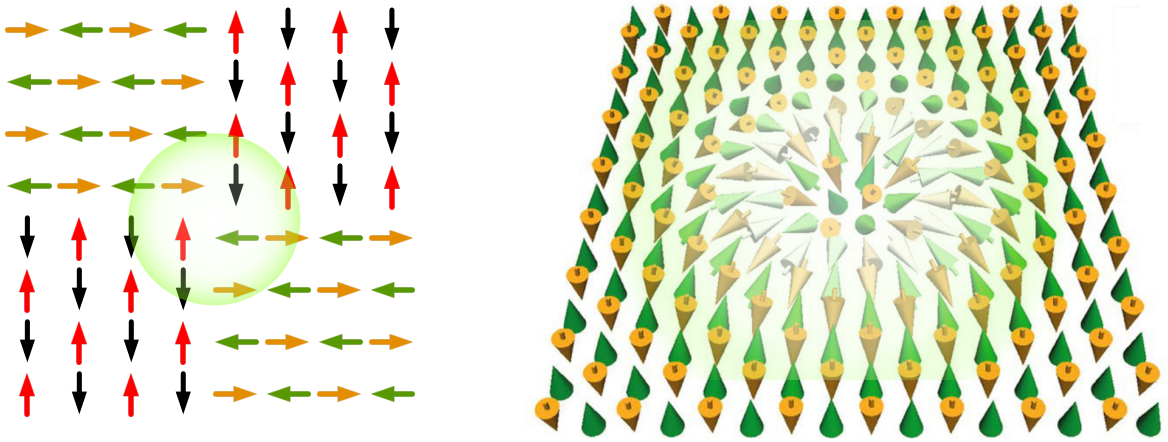

Figure 1.5: **Vortices and Skyrmion** (left)Schematic representation of a Z_4 vortex defect, (right) skyrmion phase. The shaded region represent a loop that encompasses the singularity in the antiferrmagnetic field. Thus winding number evaluated over these paths will result into a non-zero value

1.3 Experimental methods for studying AFM Textures

Spatial inhomogeneity can be studied fundamentally in two ways:

- Scanning mode
- Single shot mode

Scanning mode: A typical scanning mode experiment involves rastering an atomically fine tip sensitive to electronic states over a large region of the sample to study the heterogeneity. Fig shows one such example where the magnetic phase heterogeneity of the material could be studied. Scanning tunneling microscopy sensitive to the gapped states had been extremely impor-

tant in the study of cuprates and twisted bilayer graphene finding out longer length scale phase organizations emerging from smaller scale interactions. Scanning techniques for studying antiferromagnetism are prevalent and utilized for both direct and indirect probes. These techniques include resonant and nonresonant scanning magnetic diffraction, spin-polarized scanning tunneling microscopy, magneto-optical Kerr effect microscopy, magnetic force microscopy, spatially resolved second harmonic generation, and magnetic linear dichroic scanning transmission x-ray microscopy (STXM), among others. However, the method suffers from two major difficulties

1. Since it is a scanning mode experiment at the atomic resolution it is difficult to gain statistical information about a phase organization phenomena. Thus the measurement is confined to a limited region of observation.

2. Since the atomic scale sensitivity requires high stability the measurement process is inherently slow limiting the use of it to study the evolution of the textures under perturbations. Thus the measurement can not be extended to study kinetics or dynamics of the phases.

The tool to study the electronic phase heterogeneity in complex quantum materials should be sensitive to the $\mathring{A}$-nanometer scale correlations while being able to map the heterogeneous phase of a specific correlation at tens of micrometer length scale. Furthermore, to study the evolution of the phase texture we need them to be faster. Thus there is a requirement to have single-shot experiment to characterize the heterogeneity of electronic phases. **Single shot mode:** Single shot experiments usually utilize electromagnetic radiation over a large field of view and the sensitivity of light-matter interaction at the lowest length scale to capture the heterogeneity of phase in a system. A single-shot experiment to discern heterogeneity relies on a contrast mechanism. The fundamental idea about contrast is that if the sensitive region responds to one mode of incoming radiation (infrared, optical, or X-rays) and the rest of the material does not, then one can image a certain state of electronic configuration using a single shot of exposure over a large field of view. Magneto-Optic-Kerr-Effect microscopes are based on creating the contrast

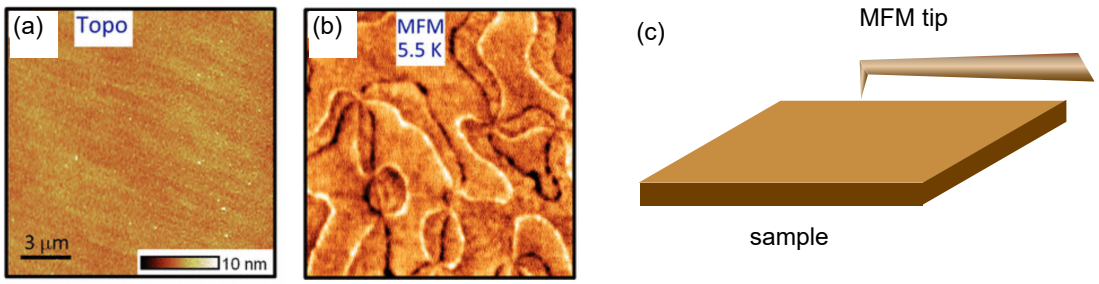

Figure 1.6: **Antiferromagnetic texture from Magnetic Force Microscopy (MFM) measurement** (a) topography of the sample, (b) vortex phase adapted from [18]

mechanism in optical reflection based on the polarization sensitivity of the magnetic moment. Other single-shot experiments involve X-ray photoelectron emission microscopy which develops the contrast mechanism based on the occupied electronic levels of the system. Thus, for a given energy the photo-electron emission will create a spatial filter for the states responding to it by ejecting photo-electrons. Those electrons are captured by a high electric field objective lens and focused to form an image. The advantage of this method relies on the direct observation of the contrast. However, the experimental method requires putting the sample under a strong electric field and high X-ray flux. Both of which can potentially damage the sample. The high flux is necessary to generate a statistically significant signal from a small field of view as big as 15 μm with a resolution of 30 nm. X-ray magnetic linear dichroism can be used in conjunction with X-PEEM to make the experiment sensitive to image heterogeneous antiferromagnetic phase.

Another mode of single shot experiment relies on interference patterns generated by the scattered intensity to sense the heterogeneity of phase. We discuss this methodology in great detail throughout the thesis. Interference patterns are a way to generate contrast by taking the Fourier transform of sensitive regions using a coherent incoming beam. The structures of the heterogeneity leave their mark on the Fourier transform amplitude which we detect. Throughout the dissertation, we will discuss how to interpret such a scattering outcome. Coherent scattering

is inherently a large field of view operation. We can make it sensitive to the electronic correlation by making it resonant with the electronic degrees of freedom. This requires incredible upgrading in terms of high brilliance requirements for X-ray light sources around the world. Recently more and more light sources are moving towards a fully coherent mode of X-ray generation tunable to a specific energy and polarization. Thus, in a timely study, we dive into developing experiments and understanding resonant coherent scattering data collected from strongly correlated electron systems.

1.4 Overview: Antiferromagnetic Textures in the context of this thesis

Through the investigation of antiferromagnetic materials, we analyze the textured real space caused from a strong coupling of charge and spin. We demonstrate that this strong coupling results in a textured real space in antiferromagnetic materials. Parallely, to visualize the phenomena, we develop and apply soft X-ray coherent scattering to explore these real-space textures[16]. The dissertation is organized as follows:

In Chapter 2 , we introduce the method of resonant coherent soft X-ray scattering. We explain its principles and its application in imaging antiferromagnetic textures. This technique leverages the resonant enhancement of X-rays at specific absorption edges enabling high contrast and high spatial resolution in magnetic imaging. We further illustrate the methodology, stemming from the technique, to observe nucleation and growth. Our observations and conclusions provide insights that underscore the utility of coherent X-ray scattering in studying magnetic phenomena at the nano-scale, especially in the dilute limit.

Chapter 3 extends the use of resonant coherent soft X-ray scattering. In conjunction with other spectro-microscopy techniques, we create and analyze artificial lateral hetero-structures. Our novel approach of using helium nano-focused ion beam implantation to locally modify the

properties of nickelate thin films effectively engineers these artificial antiferromagnetic textures; thus modifying the local physics in the material. As we observe and control the formation of these antiferromagnetic domains, we discuss the possibility of using this methodology in tailoring a material towards targeted magnetic properties.

In Chapter 4, we explore the melting phenomena in antiferromagnets using coherent resonant soft X-ray scattering using Fe-intercalated transition metal dichalcogenides. The material exhibits a highly tunable magnetic phase diagram providing an opportunity to study the melting process under thermal fluctuations and phase competition. Our simultaneous sensitivity to a specific antiferromagnetic order through resonance Bragg condition and the real space distribution of the ordered regions through the coherent aspect of the scattering is shown to be extremely helpful in understanding phase competition in strongly correlated magnetic systems.

Finally, in Chapter 5, we introduce a new approach to resonant coherent soft X-ray scattering by splitting a coherent beam spot into multiple beam spots. We show that our methodology offers improved data acquisition efficiency and enhanced flexibility in experimental design as compared to traditional single-beam experiments. We discuss the technical implementation of this dual-beam approach and its potential applications in studying complex magnetic textures. The thesis concludes by proposing further advancements in coherent scattering techniques, demonstrating the potential for these methods to provide deeper understanding into the properties of strongly correlated electrons at the mesoscale [15].

Bibliography

[1] P. W. Anderson. More is different. *Science*, 177(4047):393–396, 1972.

[2] The discovery of giant magnetoresistance, Oct 2007.

[3] Hai-Tian Zhang, Tae Joon Park, Ivan A. Zaluzhnyy, Qi Wang, Shakti Nagnath Wadekar, Sukriti Manna, Robert Andrawis, Peter O. Sprau, Yifei Sun, Zhen Zhang, Chengzi Huang, Hua Zhou, Zhan Zhang, Badri Narayanan, Gopalakrishnan Srinivasan, Nelson Hua, Evgeny Nazaretski, Xiaojing Huang, Hanfei Yan, Mingyuan Ge, Yong S. Chu, Mathew J. Cherukara, Martin V. Holt, Muthu Krishnamurthy, Oleg G. Shpyrko, Subramanian K.R.S. Sankaranarayanan, Alex Frano, Kaushik Roy, and Shriram Ramanathan. Perovskite neural trees. *Nature Communications*, 11(1):2245, May 2020.

[4] J George Bednorz and K Alex Müller. Possible high t c superconductivity in the ba- la- cu- o system. *Zeitschrift für Physik B Condensed Matter*, 64(2):189–193, 1986.

[5] Arthur P. Ramirez. Review article: Colossal magnetoresistance. *Journal of Physics: Condensed Matter*, 1997.

[6] L Hu, XB Zhu, and YP Sun. Strongly correlated antiferromagnetic vanadates. *APL Materials*, 11(9), 2023.

[7] Elbio Dagotto. Complexity in Strongly Correlated Electronic Systems. *Science*, 309(5732):257–262, July 2005.

[8] Alex Frano, Santiago Blanco-Canosa, Bernhard Keimer, and Robert J Birgeneau. Charge ordering in superconducting copper oxides. *Journal of Physics: Condensed Matter*, 32(37):374005, 2020.

[9] Giordano Mattoni, Pavlo Zubko, Francesco Maccherozzi, Alexander JH van der Torren, Daan B Boltje, Marios Hadjimichael, Nicola Manca, Sara Catalano, Marta Gibert, Yanwei Liu, et al. Striped nanoscale phase separation at the metal–insulator transition of heteroepitaxial nickelates. *Nature communications*, 7(1):13141, 2016.

[10] K. W. Post, A. S. McLeod, M. Hepting, M. Bluschke, Yifan Wang, G. Cristiani, G. Logvenov, A. Charnukha, G. X. Ni, Padma Radhakrishnan, M. Minola, A. Pasupathy, A. V. Boris,

E. Benckiser, K. A. Dahmen, E. W. Carlson, B. Keimer, and D. N. Basov. Coexisting first- and second-order electronic phase transitions in a correlated oxide. *Nature Physics*, 14(10):1056–1061, October 2018. Publisher: Nature Publishing Group.

[11] Jiarui Li, Jonathan Pelliciari, Claudio Mazzoli, Sara Catalano, Forrest Simmons, Jerzy T Sadowski, Abraham Levitan, Marta Gibert, Erica Carlson, Jean-Marc Triscone, et al. Scale-invariant magnetic textures in the strongly correlated oxide ndnio3. *Nature communications*, 10(1):4568, 2019.

[12] Tian Miao, Lina Deng, Wenting Yang, Jinyang Ni, Changlin Zheng, Joanne Etheridge, Shasha Wang, Hao Liu, Hanxuan Lin, Yang Yu, et al. Direct experimental evidence of physical origin of electronic phase separation in manganites. *Proceedings of the National Academy of Sciences*, 117(13):7090–7094, 2020.

[13] Javier del Valle, Yoav Kalcheim, Juan Trastoy, Aliaksei Charnukha, Dimitri N Basov, and Ivan K Schuller. Electrically induced multiple metal-insulator transitions in oxide nanodevices. *Physical Review Applied*, 8(5):054041, 2017.

[14] John B Goodenough. Theory of the role of covalence in the perovskite-type manganites [la, m (ii)] mn o 3. *Physical Review*, 100(2):564, 1955.

[15] R. B. Laughlin, David Pines, Joerg Schmalian, Branko P. Stojkovic, and Peter Wolynes. The middle way. *Proceedings of the National Academy of Sciences*, 97(1):32–37, 2000.

[16] Sang-Wook Cheong, Manfred Fiebig, Weida Wu, Laurent Chapon, and Valery Kiryukhin. Seeing is believing: visualization of antiferromagnetic domains. *npj Quantum Materials*, 5(1):1–10, January 2020. Publisher: Nature Publishing Group.

[17] O Gomonay, V Baltz, A Brataas, and Y Tserkovnyak. Antiferromagnetic spin textures and dynamics. *Nature Physics*, 14(3):213–216, 2018.

[18] Yanan Geng, Nara Lee, YJ Choi, S-W Cheong, and Weida Wu. Collective magnetism at multiferroic vortex domain walls. *Nano letters*, 12(12):6055–6059, 2012.

Chapter 2

Coherent Scattering of Resonant X-rays

A scattering produced by phase-coherent electromagnetic radiation is what we define as coherent scattering. A phase coherence among different parts of the wavefront both in a spatial and temporal sense is achieved to make the incoming X-rays coherent. A fully coherent beam, like a laser, has a well-defined phase relationship between two sections of the beam separated in space-time. When such phase-structured light scatters from an assembly of scatterers the information about spatial distribution of the scatterers gets embedded into the phase of the scattered beam. Now, in the far field limit different parts of the beam interfere with each other to give rise to an interference pattern on the detector. So in a coherent scattering experiment, the outcome is an interference pattern which is a fingerprint of the spatial distribution of the scatterers.

Every coherent scattering is essentially an interference experiment where spatial coherence of the incoming beam is exploited like Young's double slit experiment 2.1. Before going any further into the discussion we would like to contrast this with Michelson's interference experiment where the temporal coherence of the incoming beam is utilized. In a Michelson interferometer, a coherent beam is split in 'time' where one part travels a reference distance the other part goes into investigating the physics in question, and in the end, both of them are made to interfere. In such an interference experiment, the field is measured over time to extract the interference pattern.

On the other hand, here a coherent portion of the beam is split in 'space' and the two sections encode their phase environments into their phase information. Finally, they are made to interfere with each other on a detector where we observe an interference pattern in space. Unlike the Michelson experiment where field variation over time is measured here we record spatial intensity distribution in reciprocal space. Similar to Young's double-slit experiment where observed fringe

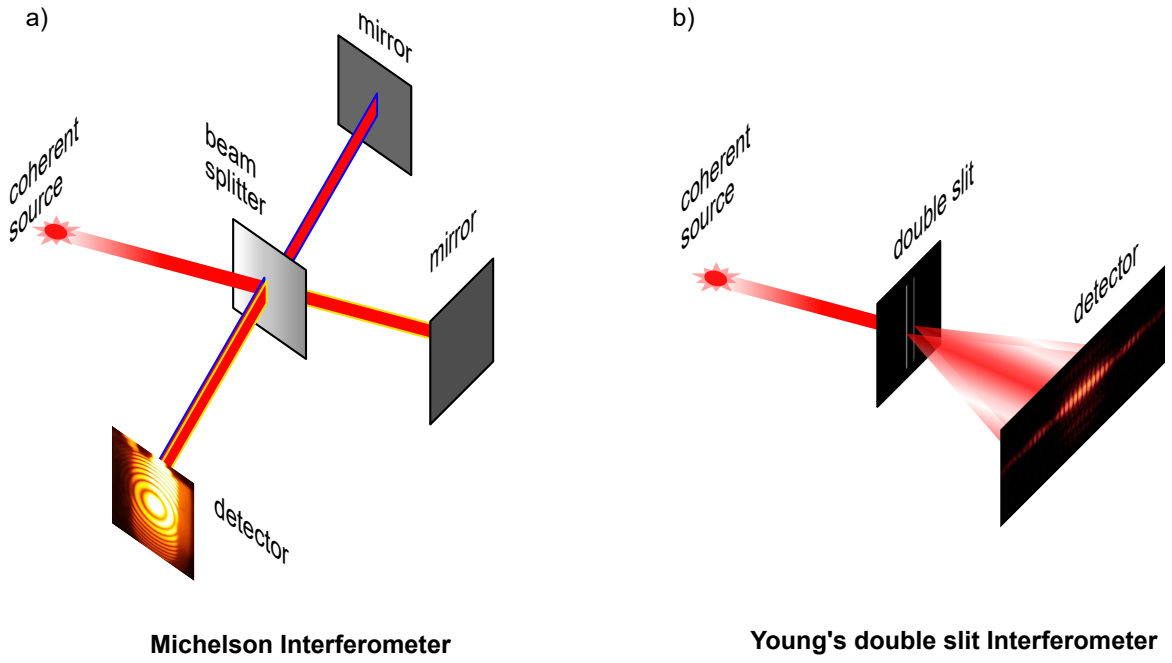

Figure 2.1: Schematic of two basic interference experiment: (a)Michelson interferometer, where the incoming coherent beam is split in time (here represented with two different colors of the edges of the beam) and (b)Young's double slit interferometer, where the incoming coherent beam is split in space. The representative detector images are taken from Wikimedia Commons. The beam split in time undergoes different path length differences before coming back together to interfere with each other. The detector images are enlarged for clarity

separation in the interference pattern is used to evaluate the structure of the slit arrangement, i.e. their separation, we can extract structural information about the distribution of scatters. However, as we will see in the later parts of the thesis often the arrangement of the scatterers is complex and thus leads to a complex interference pattern. The complexity arises both from the number of

scatterers and their relative random arrangement. The interference pattern we observe in coherent scattering experiments is known as the 'speckle pattern' from its origin in astronomy.

2.1 Young's Double Slit Interference

In this section, we revisit Young's double-slit interference to introduce the ideas related to coherent scattering. First, we will describe the intensity observed as a statistical quantity and introduce ideas such as 'contrast' and 'mutual coherence function'. We will use this result to introduce the ideas such as transverse and longitudinal coherence. A schematic of the experiment is shown in the figure below.

From the two pinholes separated by d, coherent light passes to reach the detector at a distance D on the propagation axis. Following the superposition principle, the waves are added on their amplitude basis and then squared to find the resultant intensity distribution on the intensity-sensitive detector. Since the detector time response is usually low for photon counting operations, the quantity is time-averaged to find the intensity distribution. The spatial distribution of the time-averaged intensity is a sinusoidal function - the fringe pattern. We can express the intensity at a position $\mathbf{q}$ as, -

$$I(\mathbf{q}) = \langle \psi^*(\mathbf{q},t)\psi(\mathbf{q},t)\rangle, \tag{2.1}$$

where the $\psi(\mathbf{q},t)$ is the superpositioned resultant of the two individual amplitudes and $\langle..\rangle$ represent averaging over time. Since we are interested in expressing this intensity in terms of the two pinholes we redefine the amplitude as a weighted superposition of the individual amplitudes at those pinholes, subscripted by 1 and 2

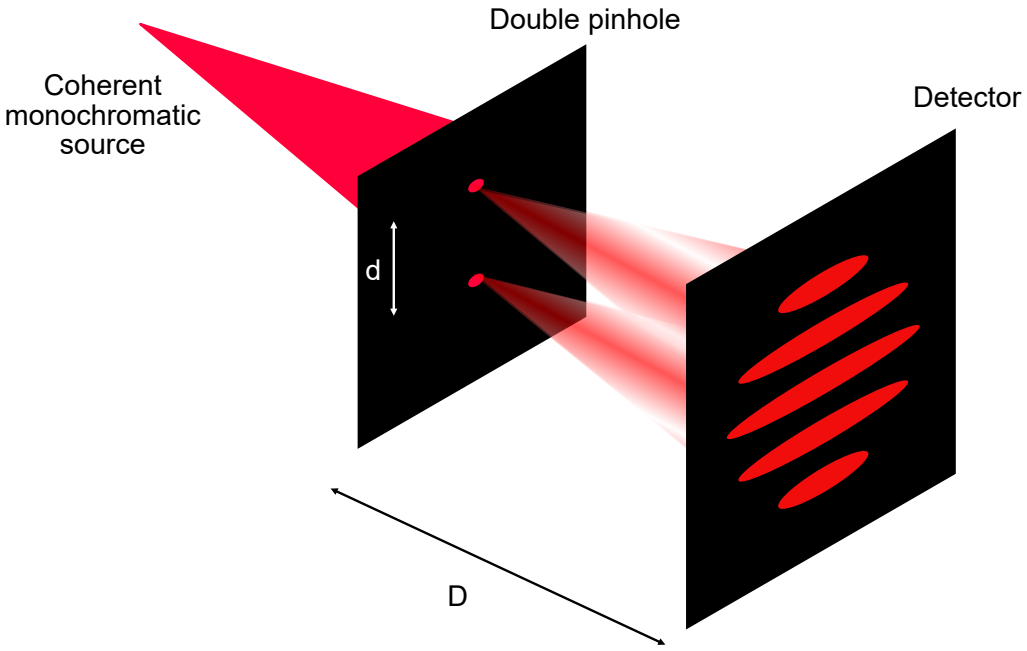

Figure 2.2: Interference through two pinholes observed as a sinusoidal intensity variation on the detector. The intensity distribution in detector is measured in $I(\mathbf{q})$. The position of the two pinholes More details in the text

$$\psi(\mathbf{q},t) = A_1\psi(\mathbf{p_1},t-\frac{\mathbf{r_1}}{c}) + A_2\psi(\mathbf{p_2},t-\frac{\mathbf{r_2}}{c})$$

The locations of the pinholes 1 and 2 are denoted by $\mathbf{p_1}$ and $\mathbf{p_2}$. We further note that, $\mathbf{r_i} = \mathbf{q} - \mathbf{p_i}$, where $i \in 1,2$. Here we retarded the wavefronts in time and considered a general scenario where the two signals are added with a ratio of $A_1 : A_2$ both of which are complex constants. Putting this back into equation 2.1 -

$$I(\mathbf{q}) = I_1(\mathbf{q}) + I_2(\mathbf{q}) + A_1A_2^*\langle\psi(\mathbf{p_1},t-\frac{\mathbf{r_1}}{c})\psi^*(\mathbf{p_2},t-\frac{\mathbf{r_2}}{c})\rangle + c.c. \tag{2.2}$$

Now, $I_1(\mathbf{q})$ and $I_2(\mathbf{q})$ are the incoherent contribution from respective pinholes and equates to $I_i(\mathbf{q}) = |A_i|^2\langle|\psi(\mathbf{p_1}, t - \frac{\mathbf{r_i}}{c})|^2\rangle$, for $i \in 1,2$. The cross-terms become relevant only in coherent scattering. They are called *mutual coherence function* and defined as -

$$\Gamma_{12}(\tau) = \langle\psi(\mathbf{p_1}, t+\tau)\psi^*(\mathbf{p_2}, t)\rangle \tag{2.3}$$

This is the first order in amplitude cross-correlation between the two sources. Since we propagate the wave function by a phase to evaluate the intensity at the detector, it is evident that the cross-correlation also propagates preserved and shows up in the intensity distribution at the detector. Redefining time as $t \to t + \frac{\mathbf{r_2}}{c}$ we have,

$$I(\mathbf{q}) = I_1(\mathbf{q}) + I_2(\mathbf{q}) + A_1A_2^*\Gamma_{12}(\frac{\mathbf{r_2} - \mathbf{r_1}}{c}) + A_1^*A_2\Gamma_{21}(\frac{\mathbf{r_1} - \mathbf{r_2}}{c}) \tag{2.4}$$

From 2.2 we see that the mutual coherence function has the property such that $\Gamma_{12}(-\tau) = \Gamma_{21}^*(\tau)$. Incorporating this we can simplify the the expression of $I(\mathbf{q})$ further into:

$$I(\mathbf{q}) = I_1(\mathbf{q}) + I_2(\mathbf{q}) + 2A_1A_2Re[\Gamma_{12}(\frac{\mathbf{r_2} - \mathbf{r_1}}{c})], \tag{2.5}$$

where we have also considered A_i to be purely imaginary constants. This is the central equation describing the coherent scattering. Since Γ_{12} is a function of $\mathbf{r_2} - \mathbf{r_1}$ whose magnitude is d, we have successfully shown to capture the structural information of the sample plane in the intensity distribution of the interference pattern on the detector plane. For a purely monochromatic illumination illuminating ideal pinholes, the mutual coherence function is just a simple phase, and thus the real part of it is just a sinusoidal function. This is observed as a fringe pattern on the intensity distribution at the detector.

From this exercise, we can directly see that the inclusion of complexity comes from just increasing the number of pinholes, which in turn increases the number of fields to account for during superposition at $\mathbf{q}$. The resultant intensity will thus depend on all possible cross terms that can come from considering the superposition of multiple sources resulting in a very complex intensity distribution. Even then, the intensity distribution will only depend on the structural distribution relations of the pinholes in the sample plane. This is the primary reason for the great interest in coherent X-ray scattering. Later we will look at ways to understand this intensity distribution and how that reveals information about the spatial distribution of scatterers. For the derivation, we considered a fully coherent beam illuminating the pinholes. In the following sub-section, we will explore how the fringe visibility depends on the coherent property of the beam.

2.1.1 Measure of Coherence:

Turning the argument upside down, fringe visibility from a double slit interference can be used as a measure to quantify the coherence property of the illuminating beam. The coherence property of the illuminating beam is defined in terms of coherence lengths: longitudinal coherence length, and transverse coherence length, defined with respect to the beam propagation direction, $\mathbf{k}_{in}$.

Transverse Coherence: To discuss transverse coherence we relax the condition of a point source illuminating the two pinholes, for an extended source. Different elementary areas of the extended source independently radiate wavefronts. We are interested in finding the upper bound of such an extended source which can still produce interference fringes. Here, each will produce the interference fringes independent of The other. Fringe Visibility ($\mathbb{V}$) is defined by Michelson for a modulated intensity varying between I_{max} and I_{min} as -

$$\mathbb{V} = \frac{I_{max} - I_{min}}{I_{max} + I_{min}} \tag{2.6}$$

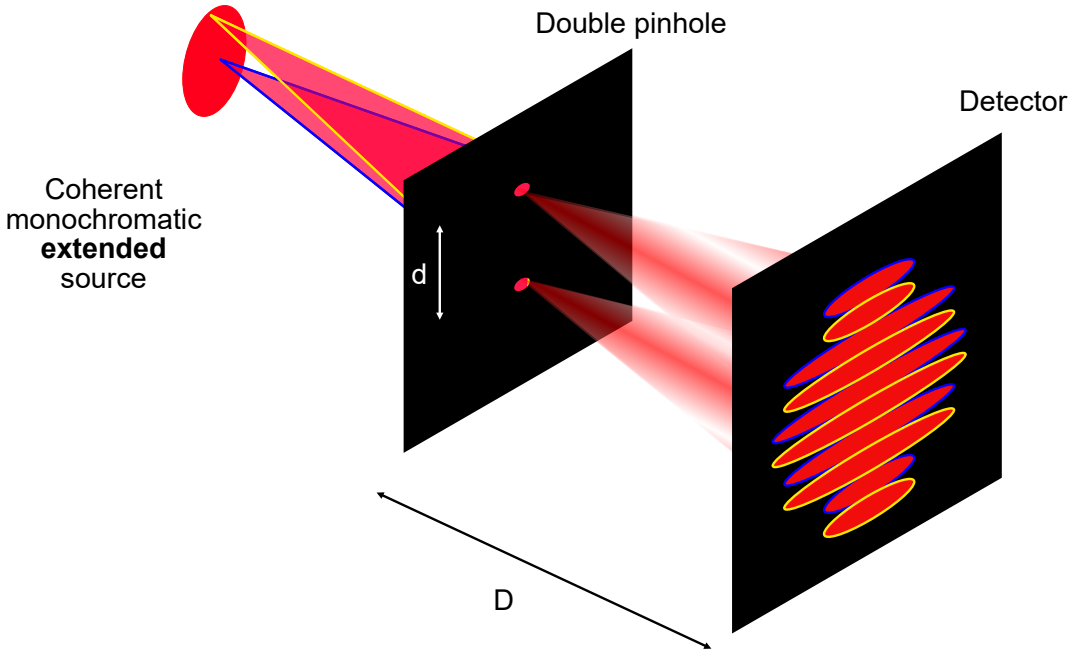

Figure 2.3: Effect of extended source: The extension of source decreases transverse coherence. This is schematically explained in this figure where the source point away from the propagation axis can be understood as a source experiencing tilt. Then the interference pattern will be tilted in the other direction. For a tilt that shifts the central maxima of the boundary source point of the extended source by one fringe width we will lose the fringe contrast and the detector will appear uniformly illuminated. This argument is a simple way to evaluate the relation between transverse coherence and source size. However, in reality, every source points superposition together before interfering to get the overall fringe pattern. This exercise was a first order approximation for the complex process.

Clearly, the fringe visibility will wash out if the fringe pattern produced by the central emitter and the boundary emitter overlap out of phase. It is easy to evaluate for a forward scattering in a small angle approximation where the angles subtended by the source at the sample plane add up to the angles of diffraction where the central maxima will show up. In other words, a shift away from the central axis translates the fringe pattern by an angle subtended by the

source on the pinhole plane. The higher order of maxima will be separated by $\frac{\lambda D}{d}$, where λ is the wavelength of illumination, d is the slit separation, and D is the sample plate to detector distance. Thus for such an extended emitter, the condition for total loss of contrast is found

$$\frac{w_{max}L}{2R} = \frac{\lambda L}{2d} \tag{2.7}$$

where R is the distance between the source and the pinholes. Thus for a source with transverse dimensions below w_{max}, we will see interference fringes. The separation on the pinhole for a given dimension w is called the coherence length in the transverse direction (ξ_T). Thus for a given source of w dimension, the coherence length is

$$\xi_T = \frac{\lambda R}{w}.$$

Longitudinal Coherence: The discussion about longitudinal coherence is where we relax the condition of monochromaticity. $\mathbb{V}$ will reduce to zero if two wavelengths appear out-of-phase with each other. Then similar to the above situation where the maxima of one wavelength appears a minima of the other will overlap. Let us consider the spread in the wavelength as $\Delta\lambda$. Similarly, we compare the fundamental frequency (λ) and the extreme outlier ($\lambda + \Delta\lambda$ to find the coherence length. The longitudinal coherence length is defined as the length (ξ_L) such that, When the primary component oscillates N times within that length the other one must oscillate N-$\frac{1}{2}$. Thus solving for N from $N\lambda = (N - \frac{1}{2})(\lambda + \Delta\lambda)$ and substituting into the definition we find,

$$\xi_L = N\lambda = \frac{\lambda^2}{2\Delta\lambda}.$$

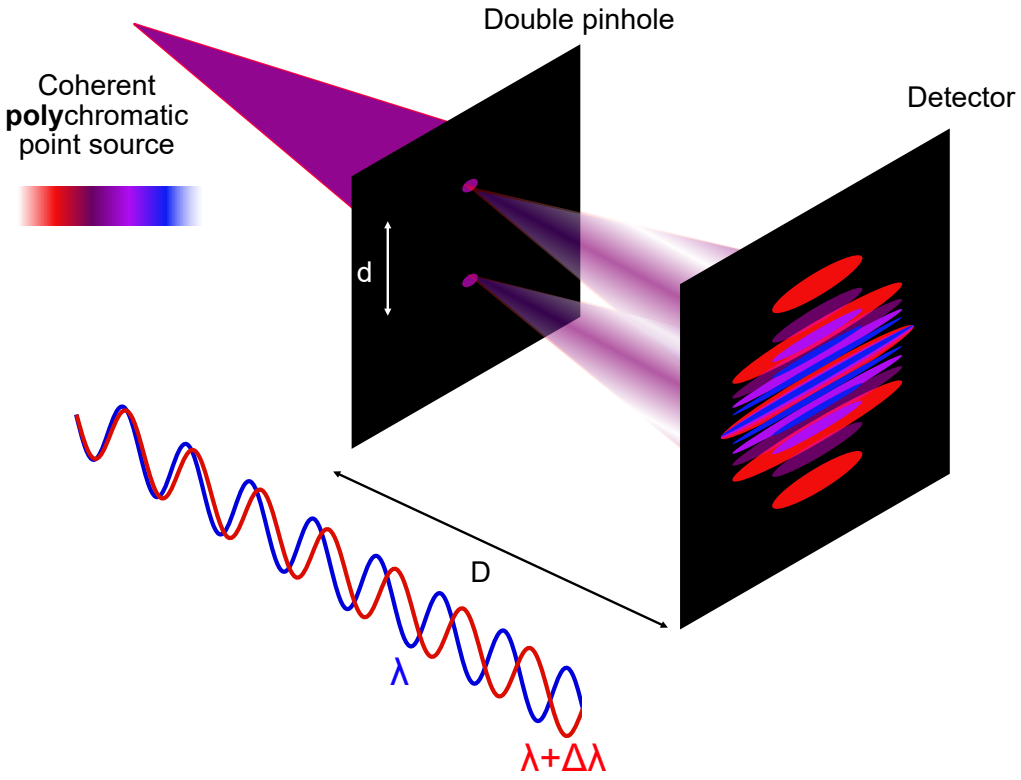

Figure 2.4: Effect of polychromatic source: the polychromatic source decreases longitudinal coherence. The loss of fringe contrast is achieved but in a different path than the case of an extended source. We have shown for the case of a polychromatic source of 4 different wavelengths. Two extreme wavelengths are compared to assist the derivation of longitudinal coherence length (ξ_L). It can be seen that for 8 wavelengths of the blue wave, the red wave completes only 7.5.

2.1.2 Coherence in Synchrotron Radiation sources:

There are two main types of X-ray photon sources: (1), Gaussian or chaotic light sources, such as X-ray tubes, Synchrotron radiation storage rings, and (2) single mode emission in self-amplified spontaneous emission (SASE) in X-ray free electron lasers. Here we focus on the

experiments in Synchrotron radiation sources. The ideas we discussed before apply directly to Synchrotron radiation sources where multiple modes are present. However, we will see that a coherent portion can be extracted following the ideas developed so far. However, no coherent source at a Synchrotron is fully coherent for this reason. Here we always deal with partially

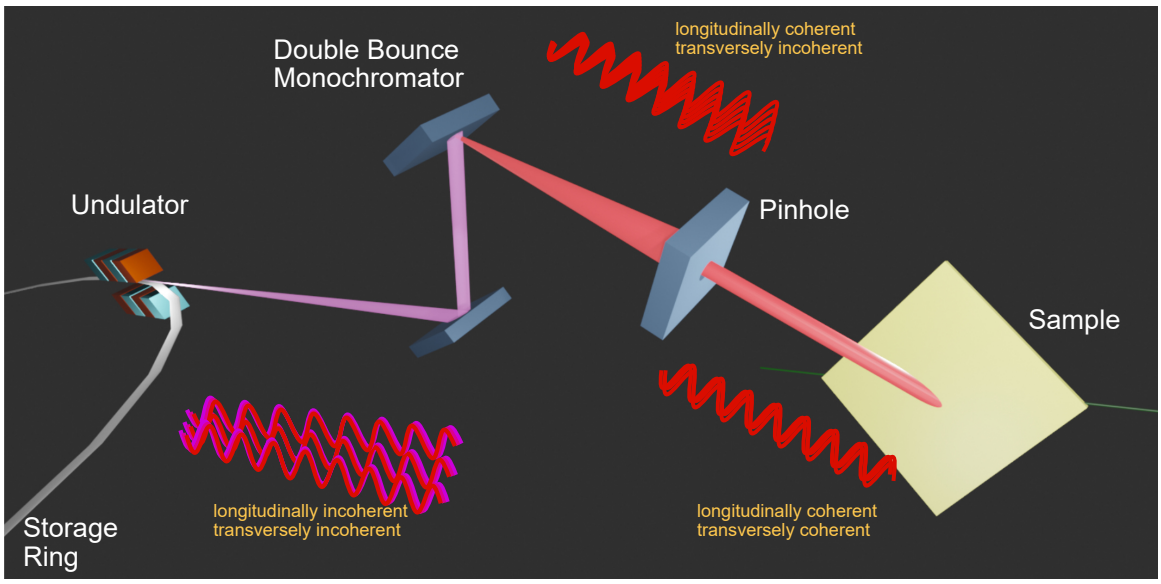

Figure 2.5: Coherent beam formation in Synchrotron sources: Double bounce monochromators make the beam longitudinally coherent then pinhole is employed to filter out the divergent section of the beam. We schematically represent the wave fronts as the beam propagates through the instruments and gets processed to become fully coherent. While the phase relationship between different parts of the incoherent beam evolves longitudinally or transversely, for the coherent beam it remains fixed. Coherence does not require the phase to be the same for every section of the beam but to be well-defined. This is schematically represented in this figure.

coherent Synchrotron radiation. We saw that limiting the spatial extension perpendicular to the propagation axis helps us improve the coherent percentage of the incoming beam. This is achieved using pinholes or slits along the beam path. On the other hand temporal filtering is done by using a monochromator to extract a small $\Delta\lambda$. A double bounce monochromator as shown in the figure 2.5 is a typical choice to do the job that achieves a $E/\Delta E \sim 10^4$. However, the price we pay is a huge loss of intensity. But if the source has enough photon flux to begin with, such as third-generation Synchrotron sources the coherent flux achieved after filtering has enough photon

to get speckle patterns after scattering. Undulators, compared to bending magnets and wigglers offer considerably more Brilliance, $\mathbb{B}$, defined as the number of photons per unit time, generated per unit source area, per unit solid angle, and 0.1% fractional bandwidth.

Measure of Coherent Flux: Synchrotron radiation sources have a Gaussian intensity distribution. If we consider the source has a size of $\sigma_h \times \sigma_v$ in horizontal and vertical direction respectively. The corresponding coherence lengths are given by

$$\xi_T^a = \frac{\lambda R}{2\pi\sigma_a},$$

for $a \in h, v$. For a typical source size of $\sigma_v \approx 10 - 50\mu m$ and $\sigma_h \approx 100 - 500\mu m$, at a wavelength of 1 Å, and a typical distance of 40m away from the source, the transverse coherence area is 3-10 $\mu m \times$ 25-100 μm.

Now, let us estimate the photon flux through such a single coherence area spanned by $\xi_h \times \xi_v$. If the source has a brilliance of $\mathbb{B}$ the photon flux, F, transmitted by the coherence area is

$$F = \mathbb{B} \times 4\pi^2\sigma_h\sigma_v \times \frac{\xi_T^h \xi_T^v}{R^2} \times \frac{\Delta\lambda}{\lambda}$$

which reduces to

$$F = \mathbb{B}\lambda\Delta\lambda \tag{2.8}$$

Thus we find that the key quantities of the source longitudinal coherence length, transverse coherence area, and flux through the coherence area depend primarily on the brilliance $\mathbb{B}$, the wavelength of choice λ, and the bandwidth of the monchromator$\Delta\lambda$. A typical Si(111) monochromator has a bandwidth on the order of 10^{-4} which gets us a longitudinal coherence length of 400nm and a flux on the order of 10^{11} photons.s^{-1}, sufficient for investigations in condensed matter systems, provided we have a Bragg peak to scatter off from.

2.2 Coherent X-ray Scattering

2.2.1 Principles of Coherent Scattering:

Coherent illumination of an aperture function results in an intensity distribution on the detector plane that is related to the aperture function through the Fourier transform. In this section, we will go through the basic result of the Rayleigh-Sommerfeld diffraction solution in scalar diffraction theory. The result we obtain will be used in interpreting the detector speckle pattern.

Here the field distribution in the source plane is given by $\psi_s(\xi,\eta)$. Following the Huygens-Fresnel principle of wave propagation, each point on the aperture plane will act as a secondary source emitting a spherical wave with wave vector **k**, where $|k| = \frac{2\pi}{\lambda}$ and λ is the monochromatic coherent beam illuminating the aperture plane. Let us consider that both the detector plane and the aperture plane are normal to **k** and their separation is R. Then the instantaneous intensity at the (q_x, q_y) in the detector plane can be found from the superposition of all spherical waves -

$$\Psi(q_x,q_y) = \frac{\iota}{\lambda}\int_A \psi_s(\xi,\eta)\frac{e^{\iota \mathbf{k}\cdot\mathbf{r}}}{r}d\xi d\eta \tag{2.9}$$

From the figure we can write $r = \sqrt{r_0^2 + (q_x-\xi)^2 + (q_y-\eta)^2}$ where r_0 is considerably larger than other terms. Thus, we can utilize binomial expansion to express them as

$$r = r_0 + \frac{\xi^2+\eta^2}{2r_0} - \frac{q_x\xi + q_y\eta}{r_0} \tag{2.10}$$

As R increases so does r_0. since ξ and η are finite the contribution from the curvature term decreases with increasing R. Let us consider that $\xi,\eta < a$, then for a separation beyond $r_0 \sim R > \frac{a^2}{\lambda}$ this term contributes unity. Such a separation separates the Fresnel diffraction regime from the Fraunhofer diffraction regime. The curvature of the spherical wavefronts remains important in the superposition in the Fresnel diffraction regime where $R < \frac{a^2}{\lambda}$. In chapter 6, we will utilize the expression including the curvature and the nuances it brings into the observed

intensity distribution. However, here we focus on the Fraunhofer regime. Furthermore, in this far-field regime, $\mathbf{k}$ and $\mathbf{r}$ are approximately parallel yielding $\mathbf{k}\cdot\mathbf{r} = kr$.Thus, with these considerations, the equation appears as follows:

$$\Psi(q_x, q_y) = \frac{\imath}{\lambda} e^{\imath k r_0} \int_A \psi_s(\xi,\eta) e^{-\imath \frac{k}{r_0} q_x \xi} e^{-\imath \frac{k}{r_0} q_y \eta} d\xi d\eta \tag{2.11}$$

This is just the Fourier transform of $\psi_s(\xi,\eta)$. Thus, in the far field limit the intensity distribution ($I(q_x, q_y)$)can be found

$$I(q_x, q_y) = \Psi^* \Psi = |\mathcal{F}(\psi_s)|^2 \tag{2.12}$$

This is the result we set out to show. The immediate consequence observed is that the phase information of the complex field ψ_s is lost. This is known as the phase problem in coherent scattering. However, a considerable amount of research has shown that under certain circumstances iterative algorithms can retrieve the phase. However, this falls outside the scope of this thesis. Interested readers may consult these papers for reference.

2.2.2 Coherent Scattering in practice:

So far we have shown that coherent scattering measures the mutual coherence function at the detector plane and the resultant intensity distribution is given by the Fourier transform of the scatterers in the aperture plane. However, to produce a coherent outcome on the detector we need to scatter from within the coherence volume of the X-rays generated in a high brilliance Synchrotron source. In this section, we will consider further experimental considerations for a scattering experiment.

First, we will note the trivial consequence of transverse coherence length. This limits the largest size of the object (a) studied under a single shot of exposure. Next, we consider the consequence of longitudinal coherence for an experiment where momentum transfer $\mathbf{q}$ happens

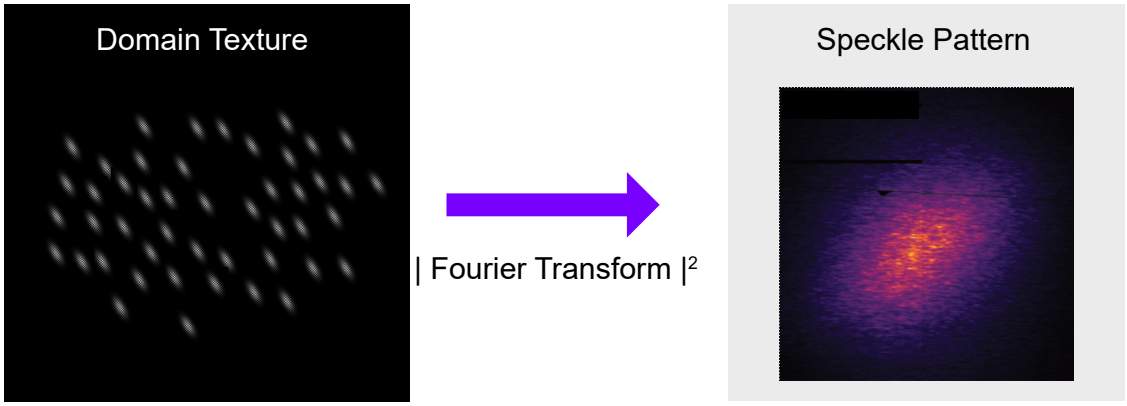

Figure 2.6: The real space texture of an electronic order is related to the speckle pattern by an amplitude Fourier transform. Since the detector is insensitive to phase information we only retrieve amplitude information.

with $\mathbf{q} = \mathbf{k}_{out} - \mathbf{k}_{in}$, where $\mathbf{k}_{out}$ and $\mathbf{k}_{in}$ are the wave vectors of the scattered and incoming beam. This is often the case we will explore. In such a situation the path length difference between the waves from the center of the sample and the edge of the sample should be below the longitudinal scattering length, or

$$\frac{\lambda^2}{\Delta\lambda} > asin(2\theta) \tag{2.13}$$

Relating $q = 2ksin(\theta)$ we can rewrite the equation as

$$\frac{\lambda^2}{\Delta\lambda} > a\frac{q}{k}\sqrt{1 - q^2/4k^2}, \tag{2.14}$$

and follow by neglecting higher order terms in $\frac{q}{k}$ as

$$\frac{\lambda^2}{\Delta\lambda} > a\frac{q}{k}. \tag{2.15}$$

Thus if $q = \frac{2\pi}{d}$ where d denotes the d-spacing of the lattice planes in question then we find

$$\frac{\Delta\lambda}{\lambda} > \frac{d}{a} \tag{2.16}$$

Thus for a given coherent diffraction experiment investigating a coherent intensity pattern on the Bragg peak with a defined d-spacing the maximum object size investigated under a single shot is limited by the above equation.

2.2.3 Coherent Resonant Scattering:

In what we discuss further in this thesis it will involve doing a resonant scattering experiment in coherent mode. Incorporating resonance scattering with a coherent source opens up interesting possibilities and challenges. Furthermore, the experiments we perform are mostly done in the soft X-ray regime. Firstly, in resonance conditions scattered intensity is enhanced tremendously which compensates for the relatively low coherent flux for larger wavelengths in soft X-rays following the equation of F.

Secondly, the experiment benefits from a longer coherence length. However, the penetration depth of the beam remains sufficiently small at the resonance condition. Since the top few hundred nm of the sample absorb the incoming photon with a high cross-section, the coherent volume remains very small yielding high contrast compared to non-resonant scattering experiments. Furthermore, if we are exploring an order with a correlation length larger than the penetration depth of the coherent beam the scatter distribution can be considered effectively two dimensional. That we can neglect the thickness of the sample for a small thickness of scattering volume, is called the projection approximation.

Furthermore, short scattering length due to resonance significantly decreases the chances of multiple scattering. On top of this when we are investigating the electronic order the light-matter interaction is already very weak. We enhance the cross-section significantly by using

resonance conditions. However, it is still a very low-intensity peak compared to any structural Bragg peak. Thus resonant coherent scattering is inherently photon-hungry. In a nutshell, the weak scattering, projection approximation, and hence the lack of multiple scattering makes the coherent scattering in resonance conditions a high contrast coherent investigation. Due to such added advantages experiments of coherent imaging are possible in coherent scattering in the soft X-ray limit.

To carry out imaging experiments the soft X-ray beam needs to be focused down to a tight spot. However, the focusing optics such as zone plates are difficult to work with in the soft X-ray regime. At soft X-ray wavelength, the focal length is extremely low sometimes within 1-2mm from the sample surface, where an order sorting aperture needs to be fit. This challenge is however avoided if the experiment can be performed using a pinhole. Most of the experiments in this thesis utilize pinholes of diameter 10 μm.

The main incentive to conduct coherent resonant scattering lies in the physics investigated. Through resonance conditions, the incoming beam is sensitive to electronic domains and textures. In strongly correlated electron physics multiple degrees of freedom couple to each other. Order formation in one degree of freedom such as say spin, affects the energy landscape of the other degrees of freedom for example the charge, and as a result, co-existence and competition of orders emerge. The study of coherent resonant scattering is fundamentally the study of the emergence, growth, coexistence, competition, and melting of electronic orders. We will explore them time and again within the context of the thesis.

2.3 Correlation Analysis

In the previous section we have shown that mutual coherence function is the cross correlation between two amplitudes and shows up as intensity modulation on the detector. In this section we investigate the correlations that survive if instead, we correlate two intensity patterns.

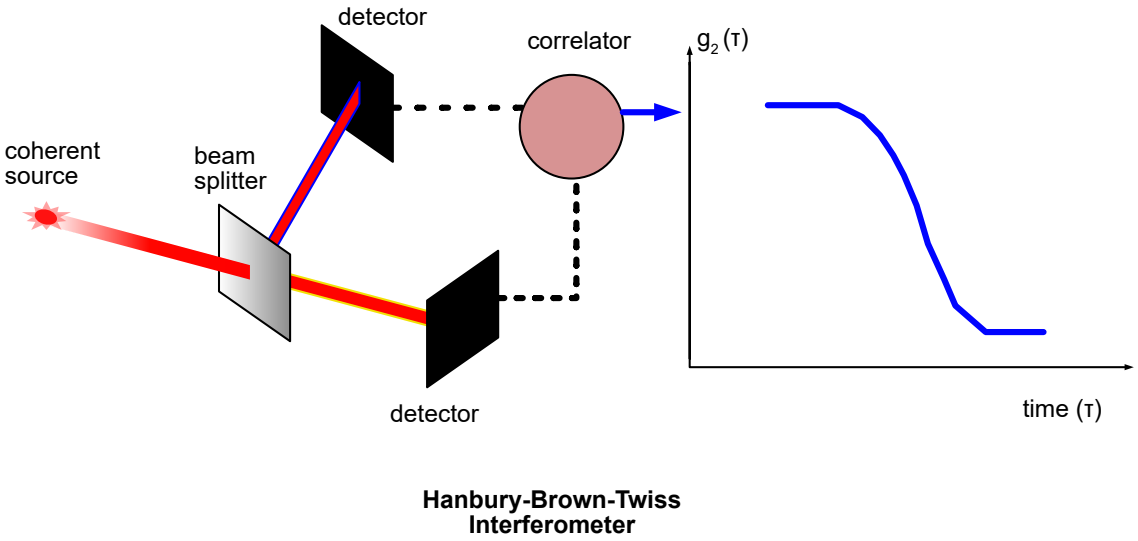

Figure 2.7: The correlation analysis is based on the Hanbury-Brown and Twiss interferrometer where the intensities observed in two detectors are correlated to evaluate the cross correlation

This is modeled after Hanbury-Brown-Twiss interferometry, where intensity measured on two separate detectors is cross-correlated. Here we will not use two different detectors however, we will correlate two instances of the same detector.

Hanbury-Brown and Twiss's experiment measured temporal coherence of the second order. A quasi-monochromatic light from scatterers was incident upon a 1:1 beam-splitter where half intensity was directed towards one detector and the other half to the second detector. The two detectors are photon counters and measure the intensity on the detector surface. The two measured intensities are then time delayed by τ before being correlated. This is called two-time auto-correlation.

$$g^{(2)}(\tau) = \frac{\langle I(t)T(t+\tau)\rangle_t}{\langle I(t)\rangle_t^2} \tag{2.17}$$

In contrast to first-order correlations where scattered field amplitudes from the sample are correlated, here we find the second-order correlations correlating the intensities. As we found previously the mutual coherence function is a two-point correlation finding correlation between

points at $\mathbf{r}_2$ and $\mathbf{r}_1$. Following the same argument, the intensity correlation in its full generality is a four-point correlation. Writing it at its most generality we find,

$$g^{(2)}(\mathbf{q}_1,\mathbf{q}_2,\tau) = \frac{\langle \Psi(\mathbf{q}_1,t)^* \Psi(\mathbf{q}_1,t) \Psi(\mathbf{q}_2,t+\tau)^* \Psi(\mathbf{q}_2,t+\tau) \rangle_t}{\langle I(\mathbf{q}_1,t) \rangle_t^2} \tag{2.18}$$

where τ is the time separation between two measurements and $\mathbf{q}_1$ and $\mathbf{q}_2$ are two points on the detector. In this general definition of two-point two-time cross-correlation, we have set up a relationship among the scattered fields observed on the detector. In condensed matter systems, we study $g^{(2)}$ between two measured intensities taken at two instances of a parameter varied. Often that parameter is the time, temperature, or magnitude of an external field which changes the domain distribution and hence the speckle pattern on the detector. Experimentally the correlation function is evaluated by the convolution of two speckle patterns observed at two different parameter values. Furthermore, often in practice, we evaluate the speckle pattern evolution at a given $|\mathbf{q}|$, or a region of interest (ROI) in the detector space with $(\Delta q_x, \Delta q_y)$ width at a position (q_x, q_y). Schematically such a measurement is shown for a parameter t in the figure. Many instances of the detector intensity distribution are measured and recorded. Then the intensity at (q_x, q_y) can be cross-correlated for each frame. Equation 2.18 becomes simpler for the present situation where

$$\mathbf{q}_1 = \mathbf{q}_2 = \mathbf{q} = (q_x, q_y)$$

and the $g^{(2)}$ function then can be written for the parameter t as

$$g^{(2)}(\mathbf{q},\tau) = \frac{\langle \Psi(\mathbf{q},t)^* \Psi(\mathbf{q},t) \Psi(\mathbf{q},t+\tau)^* \Psi(\mathbf{q},t+\tau) \rangle_t}{\langle I(\mathbf{q},t) \rangle_t^2} \tag{2.19}$$

Such cross-correlation functions are measured during the experiments and used to find

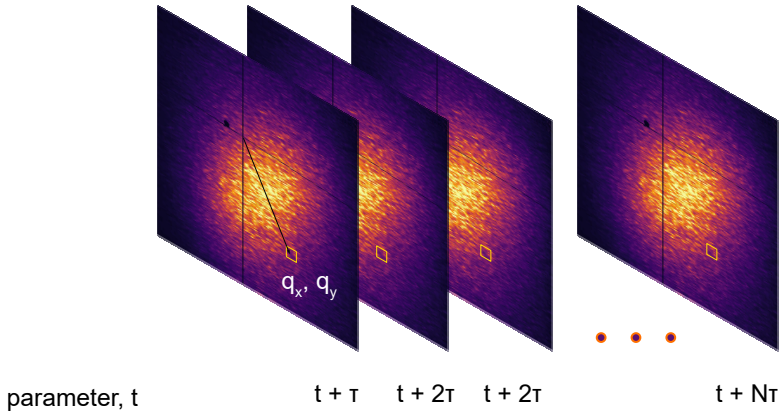

Figure 2.8: Measurement of intensity speckle pattern as a function of a parameter (can be time, temperature, external field)

the evolution of heterogeneity as a function of the parameter. $g^{(2)}$ as defined above evaluates the average change observed by the correlation function as a function of the parameter difference τ. The cross-correlation between any two different images can be plotted for all intensity patterns recorded as well. Such a measure of correlation is not averaged over the parameter variable but is usually averaged over sample positions for a better signal-to-noise ratio and is defined formally as, -

$$g^{(2)}(\mathbf{q},t_1,t_2) = \frac{\langle \Psi(\mathbf{q},t_1)^* \Psi(\mathbf{q},t_1) \Psi(\mathbf{q},t_2)^* \Psi(\mathbf{q},t_2) \rangle}{\langle I(\mathbf{q},t) \rangle^2} \tag{2.20}$$

The $\langle \ldots \rangle$ is taken over sample positions which is equivalent to the parameter space average for an ergodic system but different for a non-ergodic system. The measure of the two-time correlation function $g^{(2)}(\mathbf{q},t_1,t_2)$ can measure the equilibrium and non-equilibrium fluctuation. While the correlation function $g^{(2)}(\mathbf{q},\tau)$ measures the equilibrium fluctuation of a system. Such

equilibrium fluctuation can happen between two or more equivalent energy states the system can traverse in its configuration space. Thus the $g^{(2)}(\mathbf{q},\tau)$ function can be related to the dynamical structure factor of a system, $S(\mathbf{q},\omega)$ which captures the essence of the statics (distribution of constituents to form equilibrium structure) and dynamics (fluctuation of the structure around equilibrium position) of a structure in the reciprocal space. The dynamic structure factor can also be measured in an inelastic scattering experiment. However, the range of energy scales to be accessed is different for the two methods [1]. The inverse Fourier transform in frequency (ω) of the dynamic structure factor is related to the time evolution of the structure and is known as the intermediate scattering function.

$$S(\mathbf{q},\omega) = \frac{1}{2\pi}\int_{-\infty}^{\infty} e^{-\imath\omega t}\langle\rho(\mathbf{q},0),\rho(-\mathbf{q},t)\rangle,$$

where ρ denotes the spatial Fourier transform of the charge density scattering the X-rays at a given time.

X-ray photon correlation spectroscopy measures the photon fluctuation at a given $\mathbf{q}$, following the four-point correlation function. Usually, dynamic signatures of scatterers are probed in this experiment probing energy scales of fluctuations and correlated motions. In the context of the condensed matter systems we can probe domain fluctuations at slow time scales using X-ray photon correlation spectroscopy. Van-Cittert-Zernicke theorem relates the four-point correlation function to the two-point correlation function $g^1(\mathbf{q},\tau)$, which is defined as follows:

$$g^{(1)}(\mathbf{q},\tau) = \frac{\mathbf{1}}{\mathbf{N}}\langle\rho(\mathbf{q},\mathbf{0}),\rho(-\mathbf{q},\mathbf{t})\rangle$$

Under the ergodic approximations and short ranged fluctuations the four-point correlation relates to the two point correlation as

$$g^{(2)}(\mathbf{q},\tau) = 1+\beta g^{(1)}(\mathbf{q},\tau), \tag{2.21}$$

where β is the contrast of the speckle pattern measured from equation 2.6. The decay of the two point correlation can be modeled via $(\mathbf{q},\tau) = e^{-\frac{\tau}{\tau_f}}$, where τ_f is the time-constant of the fluctuation as well as the decay of the correlation. Time correlation experiments are done in hard and soft X-ray scattering and called X-ray Photon Correlation Spectroscopy [2, 1]. Plethora of experiments have been able to study the change of time scales in equilibrium fluctuations of domains of the electronic orders and been able to connect it to the fluctuation of electronic phases and phase transitions [3, 4, 5, 6, 7].

Similar to the correlation function between any two time of the evolution, we can define correlation function which can be used to find correlation btween speckle pattern measured at two different temperatures T_1 and T_2. In that case it will be called two-temperature correlation function $g^{(2)}(\mathbf{q}, T_1, T_2)$. We will use this correlation between two different temperatures to find similarity index between two speckle patterns of a melting antiferromagnetic phase. Such experimental characterization is also used by the authors to study the texture evolution of charge density wave order as a function of temperature [8]. Similarly suppose a system is textured with ordered domains that couple to a thermodynamic force, such as strain, temperature, or field. We can evaluate two instances of speckle pattern as we vary the external thermodynamic force and found the correlation among the patterns. This finds the response of the texture to the external thermodynamic perturbation and many interesting physics can be investigated utilizing this method. A comprehensive reference can be found in the work of Chesnel *et al.* where the authors studied ferromagnetic domain evolution under external field and temperature [9].

Since the detector we measure is an area detector we can define regions of interest around $\mathbf{q}_1$ and $\mathbf{q}_2$ for no time delay, i.e. $\tau = 0$. This is utilized in finding angular cross-correlation from the scattered intensity. This is essentially symmetry in the auto-correlation function, which can be used to investigate angular symmetries for short-range correlations. If the system had long-range correlation these structures would have given a Bragg peak. However, due to short-range correlation, they are found as a ring in the q-space. Evaluating the correlation in this ring

helps us find the hidden order in the apparent disorder of the material [10, 11, 12, 13]. The intensity-intensity angular correlation term relating to the angular symmetry of the real texture is defined following equation 2.20 as -

$$C(q,\Delta) = \frac{\langle I(q,\phi)I(q,\phi+\Delta)\rangle_\phi}{\langle I(q,\phi)\rangle_\phi^2} - 1 \tag{2.22}$$

In practice we subtract the incoherent background from the raw speckle pattern to extract the purely coherent signal. We find the correlation between two coherent speckle pattern through convolution. The correlation measured in this way can be related to the two point correlation and hence structural properties of the material. We discuss extracting correlation function and similarity of speckle pattern in details later in Chapter 4.

2.4 Results:

Nucleation of Antiferromagnetic Domains

The correlated antiferromagnetic ground state observed in rare-earth nickelates is of interest both fundamentally as well as for technological application. In the past years, the non-collinear antiferromagnetism observed in $LaNiO_3$, $PrNiO_3$, and $NdNiO_3$ has been studied extensively both in thin films [14, 15, 16, 17, 18] as well as in multilayer heterostructures [19, 20, 21, 22]. Here we investigate the antiferromagnetic transition in a 40 nm $PrNiO_3$ thin film using coherent x-rays tuned to the $2p \rightarrow 3d$ electronic transition of the Ni ions. This electronic resonance is referred to as the Ni L_3 resonance, and it can be exploited to embed valuable information in the x-ray scattering cross section about the valence $3d$ electronic states and, for example, the antiferromagnetism which they host. Transverse and longitudinal x-ray beam coherence lengths on the order of micrometers enable sensitivity to mesoscopic real space structures with comparable length scales.

Figure 2.9(a) shows a schematic of the resonant coherent x-ray diffraction (RCXD) experimental setup. The orientation of the sample and position of the detector are chosen with respect to the incidence beam such that the antiferromagnetic Bragg peak at momentum transfer $\mathbf{q}_{\mathrm{AFM}} = (\mathbf{\frac{1}{4}}\ \mathbf{\frac{1}{4}}\ \mathbf{\frac{1}{4}})_{\mathrm{pc}}$ is recorded on the detector.

A 40 nm thin film of $PrNiO_3$ was grown by pulsed laser deposition from a stoichiometric target using a KrF excimer laser with 2 Hz pulse rate and 1.6 Jcm^{-2} energy density. The film was deposited on a (001)-oriented $[\mathrm{LaAlO3}]_{0.3}[\mathrm{Sr_2AlTaO_6}]_{0.7}$ (LSAT) substrate in a 0.5 mbar oxygen atmosphere at 730 °C. The film was then annealed post-growth in a 1 bar oxygen atmosphere at 690 °C for 30 min. We note that although the LSAT substrate is known to undergo a structural transition near 150 K [23], this transition does not lead to a diffraction peak at the Q-vector corresponding to $(\frac{1}{4}\ \frac{1}{4}\ \frac{1}{4})$ in pseudocubic reciprocal lattice units of the $PrNiO_3$ film.

DC electrical resistivity measurements were performed in the 4-point van der Pauw geometry using a Quantum Design Physical Properties Measurement System. Growth and characterization of the film were performed at the Max-Planck-Institute for Solid State Research in Stuttgart. The temperature dependence of the diffraction intensity is plotted in figure 2.9(b) and compared with the DC electrical resistance of the film. As expected in this system, both signals are hysteretic, indicative of the first-order nature of this phase transition. The resonant coherent x-ray diffraction experiments were performed at the coherent x-ray scattering (CXS) beamline of the NSLS-II synchrotron light source at Brookhaven National Laboratory, which provides the coherent high photon flux necessary to observe antiferromagnetic domains with sub-micrometer length scales. Immediately before reaching the sample, a 10 μm laser ablate pinhole aperature selects the most coherent portion of the beam and defines the probe size. The longitudinal coherence length was approximately 1.25 μm, that is about one order of magnitude longer than the soft x-ray pathlength through our thin film. The measurements were performed using π-polarized incident photons, with an energy bandwidth of $\sim$0.5 eV centered at the Ni L_3 resonance ($\sim$853.4 eV). In order to access the first order antiferromagnetic Bragg peak of the

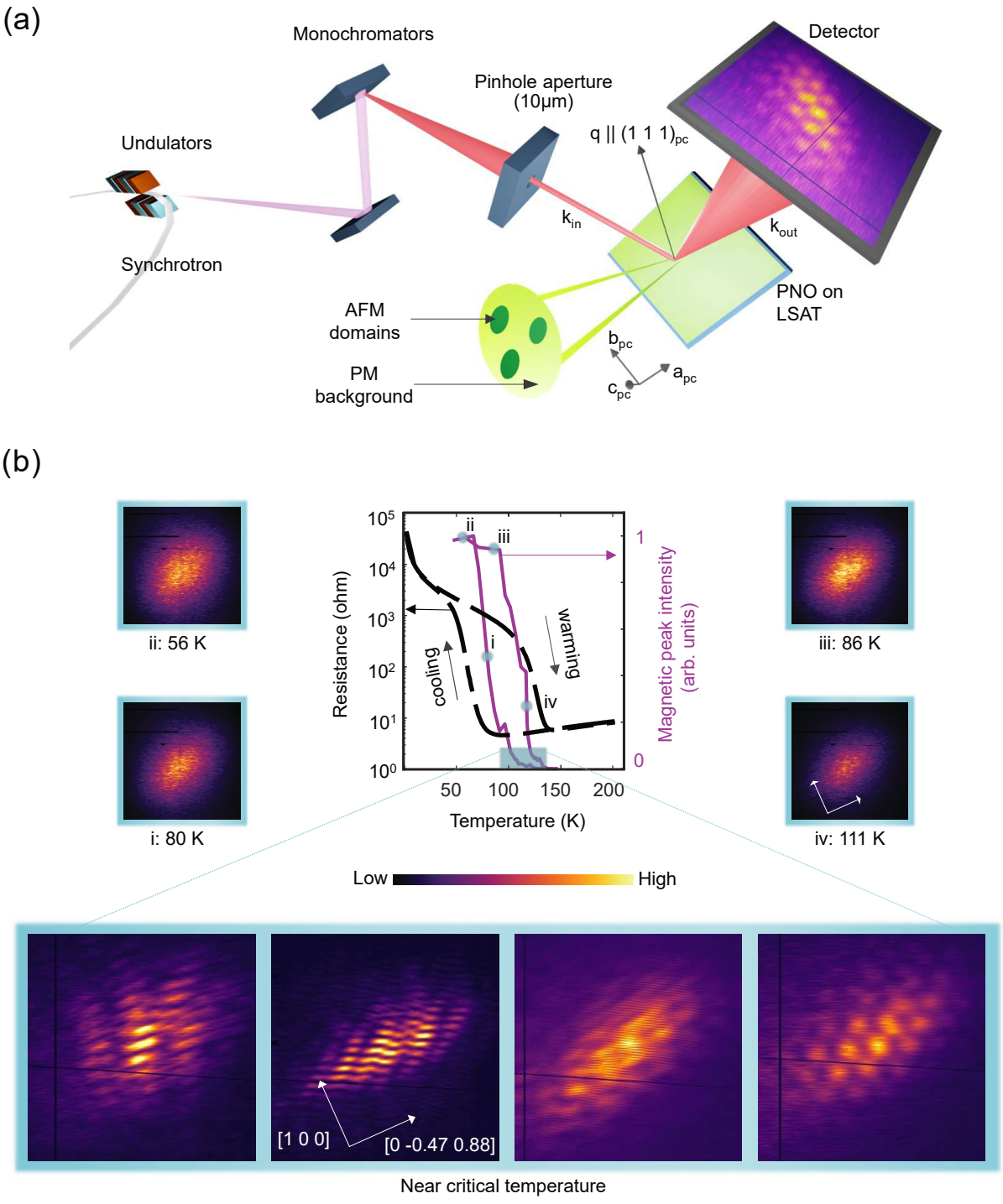

Figure 2.9: Observation of small-q modulation on the anti-ferromagnetic Bragg peak

Ni spin spiral, the sample was mounted on a $\chi = 55^\circ$ wedge so as to bring the pseudocubic (pc) [111] direction into the vertical scattering plane. The $\mathbf{q}_{\mathrm{AFM}} = (\frac{\mathbf{1}}{\mathbf{4}}\ \frac{\mathbf{1}}{\mathbf{4}}\ \frac{\mathbf{1}}{\mathbf{4}})_{\mathrm{pc}}$ momentum transfer was then reached by going to the approximate scattering angles $\theta = 55^\circ$ and $2\theta = 110^\circ$. The scattered photons were detected using a fast charge coupled device (CCD) camera, which descriminates neither the polarization nor the energy of the scattered photons. The reported intensities thus correspond to an integration over both the π and σ outgoing polarization channels, as well as over both elastic and inelastic scattering processes.

The data shows a complex speckle pattern well below the transition temperature of T_{Neel}. However, the surprising feature of our data is observed for temperatures near the critical temperature of the antiferromagnet [highlighted in figure 2.9(b)]. In this temperature regime the antiferromagnetic diffraction peak is modulated by a small-**q** superstructure. This is in contrast to the typical speckle pattern [24] which is observed at lower temperatures, where the insulating antiferromagnetic phase is well established. In figure 2.9(b), examples of the magnetic Bragg peak at various temperatures are used to demonstrate the evolution of the diffraction pattern through one full cooling and warming cycle.

Due to the coherence of the x-ray beam, interference between x-rays scattered at mesoscopic distances from one another (up to micrometers) is capable of producing a modulation of the Bragg peak intensity in reciprocal space. These modulations encode information about the relative sizes, positions, shapes and phases of the domains from which the x-rays are scattered. In the limit of many domains distributed across the entire beamspot, the resulting modulations are complex and the speckle size is inversely related to the size of the beam [25]. Such a typical speckle pattern is observed on the low temperature antiferromagnetic Bragg Peak in figure 2.9(b). However, in the limit of very few scatterers occupying only a portion of the beamspot, well defined oscillations of the Bragg peak intensity are observed in reciprocal space, and can be directly interpreted in terms of the real space distances between domains or domain boundaries. Hence, our study represents the first observation of a small-**q** modulation of an antiferromagnetic

Bragg peak associated with the mesoscopic domain arrangement of the antiferromagnetic order. In our experiment, the small-**q** superstructure observed near the critical temperature is interpreted in terms of interference between the very first few domains to undergo the antiferromagnetic transition. The appearance of bubbles of antiferromagnetically ordered spins on the background of a disordered spin lattice is consistent with the bulk bimodal nature of the metal-insulator transition observed in the closely related material $NdNiO_3$ [17].

In a RCXD experiment, although the phase of the incident light is well defined, the phases of the scattered x-rays are lost at the detector, where the collected intensities correspond to the absolute value squared of the spatial Fourier transform of the electronic states selected in the resonant process. This is known as the so-called phase problem, which implies that the real-space arrangement of the scatterers cannot be directly retrieved by applying an inverse Fourier transform to the recorded diffraction pattern without some additional information about the phase of the scattered x-rays (or preexisting information about the real space arrangement of the scatterers). The phase problem can be overcome either using holography approaches, which make use of a reference beam with known phase to determine the phase of the scattered light [26], or ptychographic [27] and coherent diffractive imaging methods [28], which are based on iterative reconstruction algorithms [29, 30]. For the purpose of our proof-of-principle, we focus explicitly on the limit of very few scatterers, which we will refer to as the "dilute" coherent scattering regime. Working in the dilute regime, the small-**q** modulations of the antiferromagnetic Bragg peak can be interpreted by eye and modelled by trial and error based on knowledge of the system. Due to the heightened likelihood of a unique solution to the phase problem in 2 dimensions[31, 32], one can be reasonably confident that the model which reproduces the observed diffraction pattern is correct, thereby circumventing the need for a complex phase-retrieval algorithm.

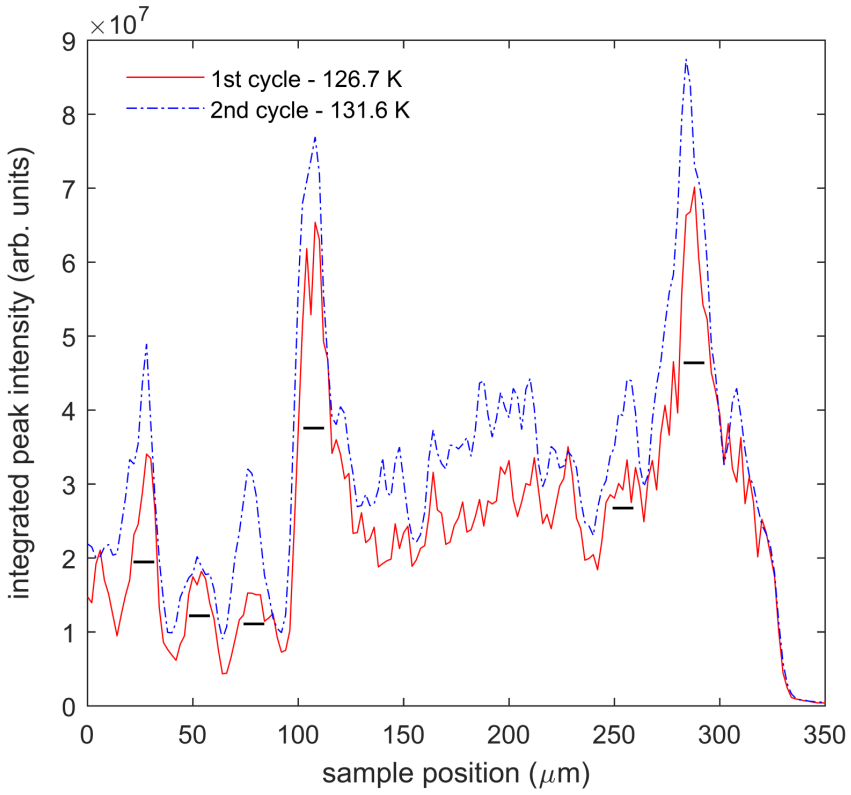

Figure 2.10: **Magnetic peak intensity as a function of beam position.** The integrated antiferromagnetic Bragg peak intensity recorded on the CCD is plotted as a function of the relative beam-sample position. The two curves were taken upon warming during separate cycles through the antiferromagnetic-paramagnetic transition. The black bars indicate the width of the beam (10 μm), and highlight features whose width corresponds approximately to one beam width. The sample position scale has been given an arbitrary starting point.

2.4.1 Modeling the small-q modulation:

To model the small-**q** modulations of the antiferromagnetic Bragg peak, we take the absolute value squared of the Fourier transform of small numbers of staggered antiferromagnetic domains, whose spatial arrangement is chosen to reflect the symmetries of the modulation patterns. By translating the beam across the sample we were able to identify the observed coherent diffaction patterns as location specific, disappearing when the beam is translated by approximately one beam width. Based on this observation, we exclude repeating structures with the same symmetry as the determined domain arrangements. In fact, a domain configuration with the minimum number of domains needed to reproduce the observed modulation pattern is consistent with the approximate space filling of the ordered phase, which is small at the onset of the transition. We first show the measurement of the integrated intensity of the peak when we scanned the beam on the sample. Diluteness of the domain is visible from the sparse high-intensity points with a spread equivalent to the beam spot size indicating a smaller spread of domain arrangement.

Guiding the modeling process in this way quickly produces a simple real space image of the relative positions and sizes of the first-ordered domains formed in the illuminated region of the film. Note that this level of analysis does not capture the detailed shape of the domains, which are given an ellipsoidal profile in order to reproduce the observed peak elongation. In general, any first-order phase transition with some degree of spatial inhomogeneity is expected to exhibit a dilute set of nucleation sites in some temperature regime near the ordering temperature. In the current system, cycling of the temperature through the phase transition reveals that the first antiferromagnetic domains formed in the nucleation regime reappear at the same locations, thereby indicating that the seeding centers are likely pinned to structural features that are immobile for temperatures up to the maximum cycling temperature 300 K. Indeed, the substrate may play an important role in determining this spatial inhomogeneity, for example via inhomogeneous strain fields, structural domain patterns, or step edges of the substrate's terraced surface, all of which

may locally suppress or seed the metal-insulator transition and accompanying antiferromagnetism. This interpretation is further supported by the observation that the same location-specific patterns are recurrent after warming to temperatures well into the paramagnetic phase. The experimentally observed RCXD pattern for 3 beam positions on the sample are shown in figure 2.11. The first column shows the diffraction patterns as observed upon warming during a first cycle through the transition. The remaining columns show diffraction patterns observed upon warming during the second cycle (approximately 24 hours later and after warming to 300 K) and for a series of temperatures in the vicinity of the antiferromagnetic transition. Looking carefully at these diffraction patterns, it is clear that the same basic features of the small-**q** modulations are retrieved when returning to the same sample position and approximately the same temperature, even after fully cycling through the entire transition. At the lowest temperatures shown, the diffraction patterns begin to change due to the sudden appearance of additional ordered domains within the beamspot.

The results of our modelling process are demonstrated for two diffraction patterns in figure 2.12. The Fourier transforms of the model domain configurations agree well with the measured diffraction patterns, even without the application of a numerical fitting algorithm to optimize the fits. The additional background intensity and reduced speckle contrast observed in the experimental data may arise in part from short range antiferromagnetic fluctuations which are not captured in our model. We emphasize that although the solution to the real space domain arrangement remains ambiguous with respect to the trivial operations translation, phase-shift, and inversion-conjugation, the 2-dimensional nature of the probed domain arrangement allows us to exclude more complex alternate solutions [31, 32]. While inversion of our coherent scattering data using an iterative phase retrieval algorithm was beyond the scope of this study, our results imply that the numerical inversion of such resonant coherent antiferromagnetic diffraction data is possible in the dilute limit, and will likely be capable of both resolving finer domain morphology features, as well as extracting information from the complex speckle diffraction patterns observed

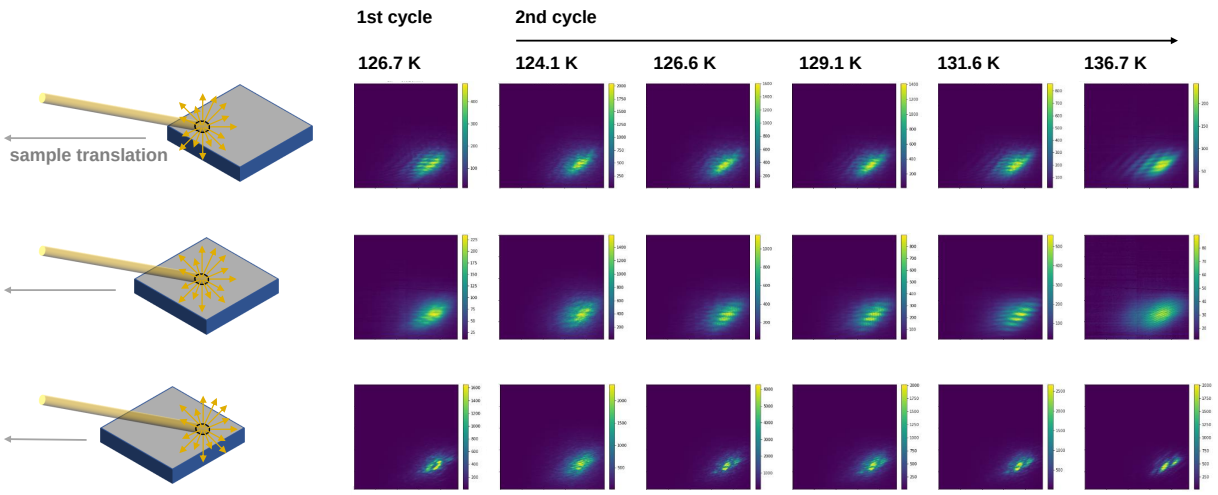

Figure 2.11: **Position and temperature dependence of the small-q superstructure.** Antiferromagnetic RCXD patterns are recorded in the near-critical regime of the antiferromagnetic transition in $PrNiO_3$. Data is presented for 3 non-overlapping sample positions. Each row corresponds to a unique sample position, whereas each column corresponds to a fixed temperature value from either the first or second cycle, as labelled. The second cycle through the transition was performed approx. 24 hours after the first cycle, and after warming to 300 K and cooling to 30 K in between.

at low temperatures, provided that the necessary sampling conditions are observed[33].

2.4.2 Detector orientation in reciprocal space

The $\chi = 55^\circ$ scattering geometry used to align the momentum transfer along the pseudocubic body diagonal results in a non-trivial projection of the detector plane onto the H, K, and L reciprocal space directions. This orientation of the detector in reciprocal space is depicted in figure 2.13(a, b). In order to interpret the small-**q** modulations in terms of interfering diffraction from domains separated laterally in the plane of the film ($a-b$ plane), the diffraction pattern is projected onto the $H-K$ plane. This has been done in figure 2. After projecting out the L component, the detector direction having had most L component is effectively stretched. In figure 2.13 (d-g) we demonstrate the effect of unstretching the real and reciprocal space images after projecting onto the $a-b$ and $H-K$ planes. In the main manuscript we have chosen to present the

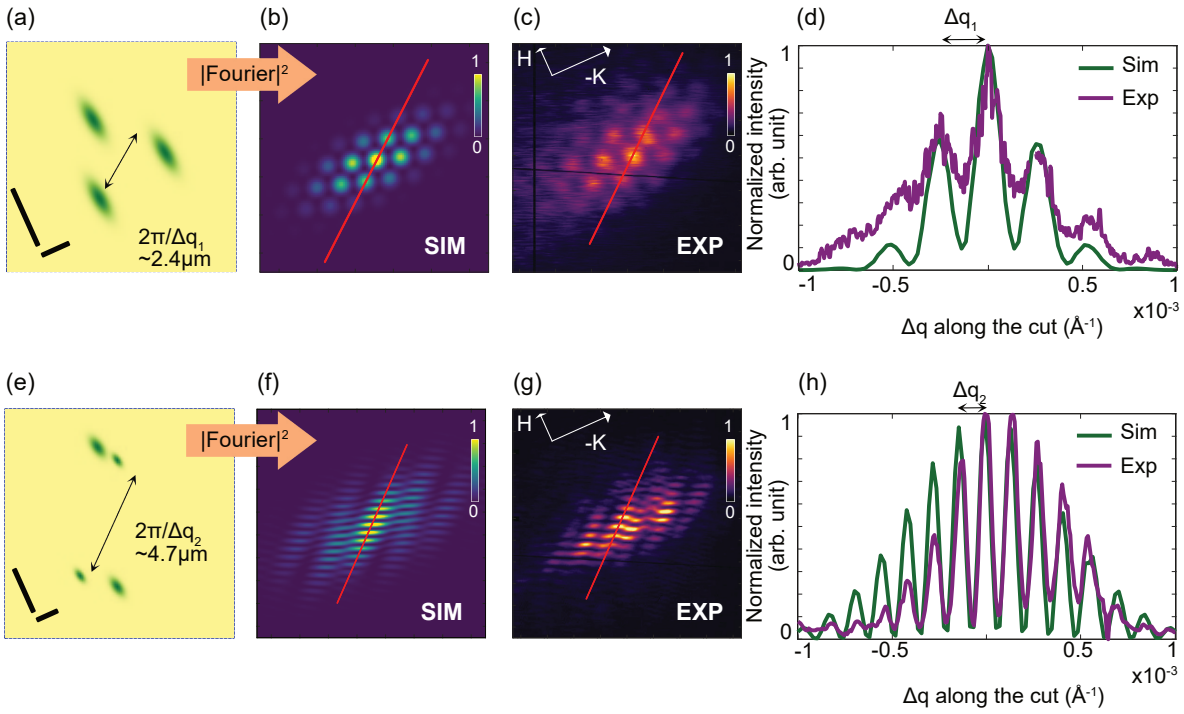

Figure 2.12: **Modelling of experimental RCXD patterns.** (a) Model configuration in real space of three antiferromagnetic domains within the beamspot. The scale bars correspond to 2 μm along the [100] direction (long bar) and along the [010] direction (short bar). (b) Absolute value squared of the Fourier transform of the model shown in (a). Scale bars are the same as in (c). (c) Experimentally observed reciprocal space map of the antiferromagnetic Bragg peak at momentum transfer $\mathbf{q}_{\mathrm{AFM}} = (\frac{1}{4}\ \frac{1}{4}\ \frac{1}{4})_{\mathrm{pc}}$ in the pseudocubic setting of $PrNiO_3$. After projecting the detector image onto the $H-K$ plane, the lengths of the arrows labelled H and K correspond to 0.001 $\mathrm{Å}^{-1}$ respectively along the (100) and (010) directions. (d) Comparison of cuts taken from (b) and (c) along the indicated red line. A constant has been subtracted from the experimental curves such that the intensity at the detector edge is zero. (e)-(h) same as (a)-(d) but for a different experimentally observed diffraction pattern (g) and the corresponding model and simulation in (e) and (f).

reciprocal space patterns and associated real-space domain configurations in their stretched form, thereby emphasizing how the stretching of the $H-K$ plane diffraction pattern onto the skew detector translates into a stretched real-space image following the inverse Fourier transform. The reader should note that it is only possible to project out the L component and directly interpret the modulation patterns on the detector in terms of $H-K$ plane diffraction due to our pre-existing knowledge that the scattering is constrained to the quasi-2D thin film geometry. In our case, the

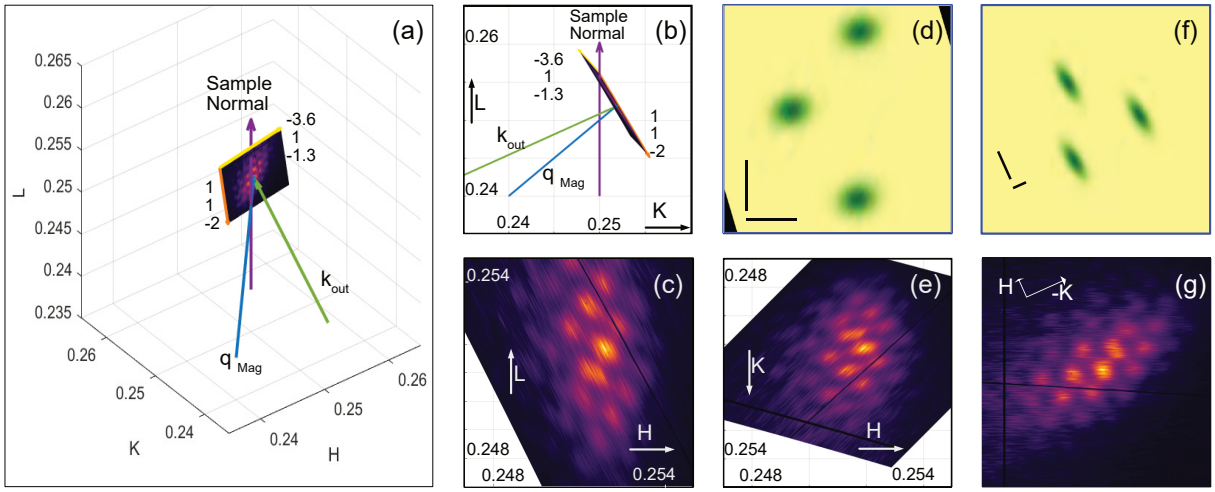

Figure 2.13: **Detector orientation and alternate visualizations of the real and reciprocal space patterns.** (a) Depiction of the detector oriented in 3-dimensional reciprocal space. (b) Detector in reciprocal space viewed along the H direction. This perspective captures the strong coupling of K and L components along the detector direction perpendicular to (1 0 0). (g) Experimental diffraction pattern captured by the detector with scale bars in the projected $H-K$ plane (0.001 Å^{-1}) given by the lengths of the white arrows. (c) Same pattern projected onto the $H-L$ plane and (e) projected onto the $H-K$ plane. The peak elongation appears primarily in the L direction. (f) Domain arrangement in the stretched real space depiction whose squared Fourier transform corresponds to the experimentally observed diffraction pattern in (g). The scale bars in (f) both correspond to 1 μm along the [1 0 0] (long bar) and [0 1 0] (short bar) directions. The stretching of the real and reciprocal space images in (f) and (g) results from projecting out the significant L component along one direction of the detector and then interpreting the pattern in terms of $H-K$ plane diffraction. The unstretched real and reciprocal space patterns (equal 1 μm scale bars in both directions) are shown in panels (d) and (e). In addition to unstretching, the patterns in (d) and (e) have been rotated to align the a/b and H/K directions with the page horizontal and vertical.

antiferromagnetic domains being probed are pancake-like objects with hundreds of nm correlation lengths in the $a-b$ plane, but constrained in the growth direction by the 40 nm film thickness.

2.5 Outlook

In the following outlook section, we consider hypothetical dynamically driven magnetic textures and argue that time-resolved RCXD, in the dilute scattering limit, presents a powerful opportunity to study the motion of antiferromagnetic domains or topological defects in an

antiferromagnetic spin texture. Figures 2.14(a)-(e) depict a series of hypothetical dilute antiferromagnetic domain configurations in real space. Figure 2.14(a) corresponds to a single circular domain, whereas figures 2.14(b)-(d) depict snapshots of one domain passing in between two other domains of equal size, and then disappearing in Fig. 2.14(e). The diffraction patterns in the vicinity of the first order antiferromagnetic Bragg peak originating from each of the real-space domain arrangements shown in figures 2.14(a)-(e) are simulated in figures. 2.14(f)-(j) respectively. The number and relative positions of the probed domains are clearly reflected in the symmetries of the small-**q** modulations of the antiferromagnetic Bragg peak intensity.

Next we extend the concept of dilute magnetic textures to encompass the notion of a dilute set of topological defects on an antiferromagnetic lattice, such as antiferromagnetic knife edge dislocations observed in the skyrmion nucleation regime of helical antiferromagnets [34], or theoretically predicted antiferromagnetic vortices and skyrmions [35, 36]. Figures 2.14(p)-(t) demonstrate the sensitivity of the simulated RCXD cross section around a first-order antiferromagnetic Bragg peak, to the presence and relative arrangements of a dilute set of antiferromagnetic vortices depicted in real space in figures 2.14(k)-(o). The diffraction patterns in figures 2.14(p)-(t) correspond to a resonant magnetic scattering polarization channel which selects the spin x-component. In figures 2.14(k) and (p) the trivial case of a homogeneously ordered antiferromagnetic lattice is considered, whereas figures 2.14(l)-(m) and (q)-(r) illustrate the motion of one antiferromagnetic vortex past two stationary vortices. Removing vortices from the beamspot, panels (n) and (s) correspond to just a pair of antiferromagnetic vortices, and panels (o) and (t) to a single vortex. For the purposes of this demonstration we considered equal antiferromagnetic vortices, each corresponding to a topological defect of winding number $w = 1$, with the spins winding in the plane of the lattice. Similar scattering signatures are expected to arise in the presence of antiferromagnetic skyrmions [35, 36], where the antiferromagnetic spin orientations wind in three-dimensions. Note that in our results, the number of angular nodes in the simulated antiferromagnetic Bragg intensity corresponds to twice the number of $w = 1$ vortices present in

the beamspot, or more generally, the net topological charge of the spin texture contained within the beamspot. This indicates an important quantitative sensitivity of the RCXD cross section to the mesoscopic winding of the antiferromagnetic order parameter, reminiscent of the results of Zhang, van der Laan and Hesjedal in the skyrmion material Cu_2OSeO_3 [37], or the resonant x-ray scattering method for determining the topological invariant of nondegenerate band crossings in Weyl semimetals proposed by Kourtis [38].

To model the antiferromagnetic vortices depicted in Fig. 2.14(k-o), we assign each lattice site with a complex number, whose real and imaginary parts represent the x- and y-components of its spin orientation

$$m_x = \Re\left(\Pi_n e^{\imath\omega_n \arctan\frac{y-y_n}{x-x_n}}\right) \tag{2.23}$$

$$m_y = \Im\left(\Pi_n e^{\imath\omega_n \arctan\frac{y-y_n}{x-x_n}}\right), \tag{2.24}$$

where (x_n, y_n) and ω_n are the position and winding number of the n^{th} vortex. The product is taken over all vortices in the coherent beamspot. The simulated diffraction patterns shown in figures 2.14(p)-(t) correspond to the Fourier transform of m_x.

2.6 Conclusion

In this chapter we expanded up on the single shot coherent method capable of studying electronic phase heterogeneity. We discussed the background and development of the method from Young's double slit experiment. Then we studied antiferromagnetic $PrNiO_3$ thin films with coherent resonant scattering. We demonstrated that Bragg coherent diffractive imaging can be extended to study the mesoscopic texture of an antiferromagnetic order parameter using resonant magnetic x-ray scattering. We studied the onset of the antiferromagnet transition in

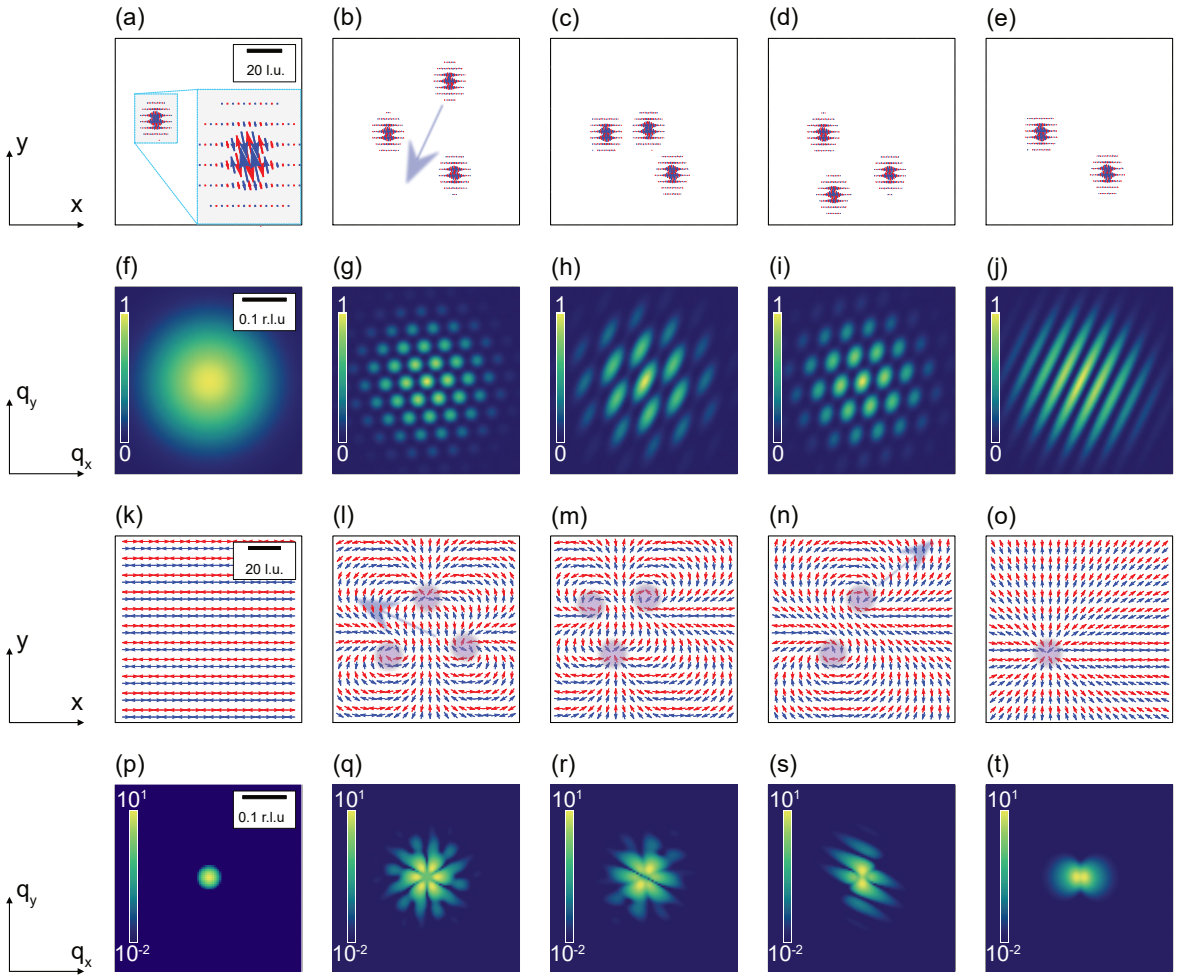

Figure 2.14: **Simulation of RCXD from mobile antiferromagnetic domain arrangements and antiferromagnetic topological spin textures.** (a) Single antiferromagnetic domain in two dimensions. (b)-(d) Three equally-sized antiferromagnetic domains, one moving with respect to the other stationary two. (e) Two equally-sized antiferromagnetic domains. (f)-(j) Absolute value squared of the Fourier transforms of the model domain configurations in (a)-(e). (k) Uniform antiferromagnetism in two dimensions. (l-o) Antiferromagnetic vortices with topological winding number $w = 1$. The centers of the vortices are indicated by a shaded disc. (p)-(t) Absolute value squared of the Fourier transforms of the spin x-component for the antiferromagnetic spin textures shown in (k)-(o). The number of angular nodes corresponds to twice the sum of the winding numbers of all vortices in the beam spot.

$PrNiO_3$, focusing on a temperature regime in which the antiferromagnetic domains are dilute in the beamspot and the coherent diffraction pattern modulating the antiferromagnetic peak is greatly simplified. We demonstrate that it is possible to extract the arrangements and sizes of these domains from single diffraction patterns and show that the approach could be extended to a time-structured light source to study the motion of dilute domains or the motion of topological defects in an antiferromagnetic spin texture.

2.7 Acknowledgements

Chapter 2, in part, has been published in Science Advances, 8, 29, 2022, Martin Bluschke*, Rourav Basak*, Andi Barbour, Ashley N. Warner, Katrin Fursich, Stuart Wilkins, Sujoy Roy, James Lee, Georg Christiani, Gennady Logvenov, Matteo Minola, Bernhard Keimer, Claudio Mazzoli, Eva Benckiser, Alex Frano, Imaging mesoscopic antiferromagnetic spin textures in the dilute limit from single-geometry resonant coherent x-ray diffraction. The dissertation author was the primary investigator and author of this paper. (* indicates equal contribution)

Bibliography

[1] Oleg G Shpyrko. X-ray photon correlation spectroscopy. *Journal of synchrotron radiation*, 21(5):1057–1064, 2014.

[2] Sunil K Sinha, Zhang Jiang, and Laurence B Lurio. X-ray photon correlation spectroscopy studies of surfaces and thin films. *Advanced Materials*, 26(46):7764–7785, 2014.

[3] OG Shpyrko, ED Isaacs, JM Logan, Yejun Feng, G Aeppli, Rafael Jaramillo, HC Kim, TF Rosenbaum, Paul Zschack, Michael Sprung, et al. Direct measurement of antiferromagnetic domain fluctuations. *Nature*, 447(7140):68–71, 2007.

[4] Nelson Hua, Jianheng Li, Stjepan B Hrkac, Andi Barbour, Wen Hu, Claudio Mazzoli, Stuart Wilkins, Roopali Kukreja, Eric E Fullerton, and Oleg G Shpyrko. Discerning element and site-specific fluctuations of the charge-orbital order in fe 3 o 4 below the verwey transition. *Physical Review Materials*, 7(1):014413, 2023.

[5] Jingjin Song, Sheena KK Patel, Rupak Bhattacharya, Yi Yang, Sudip Pandey, Xiao M Chen, M Brian Maple, Eric E Fullerton, Sujoy Roy, Claudio Mazzoli, et al. Direct measurement of temporal correlations above the spin-glass transition by coherent resonant magnetic x-ray spectroscopy. *arXiv preprint arXiv:2002.04259*, 2020.

[6] XM Chen, V Thampy, C Mazzoli, AM Barbour, H Miao, GD Gu, Y Cao, JM Tranquada, MPM Dean, and SB Wilkins. Remarkable stability of charge density wave order in la 1.875 ba 0.125 cuo 4. *Physical review letters*, 117(16):167001, 2016.

[7] L Shen, V Esposito, NG Burdet, M Zhu, AN Petsch, TP Croft, SP Collins, Z Ren, F Westermeier, M Sprung, et al. Interplay between relaxational atomic fluctuations and charge density waves in la 2- x sr x cuo 4. *Physical Review B*, 108(20):L201111, 2023.

[8] XM Chen, C Mazzoli, Y Cao, V Thampy, AM Barbour, W Hu, M Lu, TA Assefa, H Miao, G Fabbris, et al. Charge density wave memory in a cuprate superconductor. *Nature communications*, 10(1):1435, 2019.

[9] K Chesnel, J Nelson, B Wilcken, and S D Kevan. Mapping spatial and field dependence of magnetic domain memory by soft X-ray speckle metrology. 2012.

[10] Peter Wochner, Christian Gutt, Tina Autenrieth, Thomas Demmer, Volodymyr Bugaev, Alejandro Díaz Ortiz, Agnès Duri, Federico Zontone, Gerhard Grübel, and Helmut Dosch. X-ray cross correlation analysis uncovers hidden local symmetries in disordered matter. *Proceedings of the National Academy of Sciences*, 106(28):11511–11514, 2009.

[11] Ivan A Zaluzhnyy, Ruslan P Kurta, Marcus Scheele, Frank Schreiber, Boris I Ostrovskii, and Ivan A Vartanyants. Angular x-ray cross-correlation analysis (axcca): Basic concepts and recent applications to soft matter and nanomaterials. *Materials*, 12(21):3464, 2019.

[12] Run Su, Keoki A Seu, Daniel Parks, Jimmy J Kan, Eric E Fullerton, Sujoy Roy, and Stephen D Kevan. Emergent rotational symmetries in disordered magnetic domain patterns. *Physical Review Letters*, 107(25):257204, 2011.

[13] Yufei Wang, Yilong Zhou, Quanpeng Yang, Rourav Basak, Yu Xie, Dong Le, Alexander D Fuqua, Wade Shipley, Zachary Yam, Alex Frano, et al. Self-assembly of nanocrystal checkerboard patterns via non-specific interactions. *Nature Communications*, 15(1):3913, 2024.

[14] V. Scagnoli, U. Staub, A. M. Mulders, M. Janousch, G. I. Meijer, G. Hammerl, J. M. Tonnerre, and N. Stojic. Role of magnetic and orbital ordering at the metal-insulator transition in $NdNiO_3$. *Phys. Rev. B*, 73:100409, Mar 2006.

[15] A. V. Boris, Y. Matiks, E. Benckiser, A. Frano, P. Popovich, V. Hinkov, P. Wochner, M. Castro-Colin, E. Detemple, V. K. Malik, C. Bernhard, T. Prokscha, A. Suter, Z. Salman, E. Morenzoni, G. Cristiani, H.-U. Habermeier, and B. Keimer. Dimensionality control of electronic phase transitions in nickel-oxide superlattices. *Science*, 332(6032):937–940, 2011.

[16] M. Hepting, R. J. Green, Z. Zhong, M. Bluschke, Y. E. Suyolcu, S. Macke, A. Frano, S. Catalano, M. Gibert, R. Sutarto, F. He, G. Cristiani, G. Logvenov, Y. Wang, P. A. van Aken, P. Hansmann, M. Le Tacon, J.-M. Triscone, G. A. Sawatzky, B. Keimer, and E. Benckiser. Complex magnetic order in nickelate slabs. *Nat. Phys.*, 14(11):1097–1102, 2018.

[17] K. W. Post, A. S. McLeod, M. Hepting, M. Bluschke, Yifan Wang, G. Cristiani, G. Logvenov, A. Charnukha, G. X. Ni, Padma Radhakrishnan, M. Minola, A. Pasupathy, A. V. Boris, E. Benckiser, K. A. Dahmen, E. W. Carlson, B. Keimer, and D. N. Basov. Coexisting first- and second-order electronic phase transitions in a correlated oxide. *Nat. Phys.*, 14(10):1056–1061, 2018.

[18] Jiarui Li, Jonathan Pelliciari, Claudio Mazzoli, Sara Catalano, Forrest Simmons, Jerzy T. Sadowski, Abraham Levitan, Marta Gibert, Erica Carlson, Jean-Marc Triscone, Stuart Wilkins, and Riccardo Comin. Scale-invariant magnetic textures in the strongly correlated oxide $NdNiO_3$. *Nat. Commun.*, 10(1), oct 2019.

[19] Marta Gibert, Pavlo Zubko, Raoul Scherwitzl, Jorge Íñiguez, and Jean-Marc Triscone. Exchange bias in $LaNiO_3$-$LaMnO_3$ superlattices. *Nat. Mater.*, 11:195, Jan 2012.

[20] A. Frano, E. Schierle, M. W. Haverkort, Y. Lu, M. Wu, S. Blanco-Canosa, U. Nwankwo, A. V. Boris, P. Wochner, G. Cristiani, H. U. Habermeier, G. Logvenov, V. Hinkov, E. Benckiser, E. Weschke, and B. Keimer. Orbital control of noncollinear magnetic order in nickel oxide heterostructures. *Phys. Rev. Lett.*, 111(10):106804, sep 2013.

[21] M. Hepting, M. Minola, A. Frano, G. Cristiani, G. Logvenov, E. Schierle, M. Wu, M. Bluschke, E. Weschke, H.-U. Habermeier, E. Benckiser, M. Le Tacon, and B. Keimer. Tunable charge and spin order in $PrNiO_3$ thin films and superlattices. *Phys. Rev. Lett.*, 113:227206, Nov 2014.

[22] M. Bluschke, A. Frano, E. Schierle, M. Minola, M. Hepting, G. Christiani, G. Logvenov, E. Weschke, E. Benckiser, and B. Keimer. Transfer of magnetic order and anisotropy through epitaxial integration of $3d$ and $4f$ spin systems. *Phys. Rev. Lett.*, 118:207203, May 2017.

[23] B. C. Chakoumakos, D. G. Schlom, M. Urbanik, and J. Luine. Thermal expansion of $LaAlO_3$ and (La,Sr)(Al,Ta)O_3, substrate materials for superconducting thin-film device applications. *J. Appl. Phys.*, 83(4):1979–1982, 1998.

[24] M. Sutton, S. G. J. Mochrie, T. Greytak, S. E. Nagler, L. E. Berman, G. A. Held, and G. B. Stephenson. Observation of speckle by diffraction with coherent x-rays. *Nature*, 352(6336):608–610, aug 1991.

[25] Friso van der Veen and Franz Pfeiffer. Coherent x-ray scattering. *J. Phys. Condens. Matter*, 16(28):5003–5030, jul 2004.

[26] S. Eisebitt, J. Lüning, W. F. Schlotter, M. Lörgen, O. Hellwig, W. Eberhardt, and J. Stöhr. Lensless imaging of magnetic nanostructures by x-ray spectro-holography. *Nature*, 432(7019):885–888, dec 2004.

[27] J. M. Rodenburg, A. C. Hurst, A. G. Cullis, B. R. Dobson, F. Pfeiffer, O. Bunk, C. David, K. Jefimovs, and I. Johnson. Hard-x-ray lensless imaging of extended objects. *Phys. Rev. Lett.*, 98(3):034801, jan 2007.

[28] J. Miao, T. Ishikawa, I. K. Robinson, and M. M. Murnane. Beyond crystallography: Diffractive imaging using coherent x-ray light sources. *Science*, 348(6234):530–535, apr 2015.

[29] J. R. Fienup. Reconstruction of an object from the modulus of its Fourier transform. *Opt. Lett.*, 3(1):27, jul 1978.

[30] J. R. Fienup. Reconstruction of a complex-valued object from the modulus of its Fourier transform using a support constraint. *J. Opt. Soc. Am. A*, 4(1):118–123, Jan 1987.

[31] Yu.M. Bruck and L.G. Sodin. On the ambiguity of the image reconstruction problem. *Opt. Commun.*, 30(3):304–308, 1979.

[32] R. H. T. Bates. Fourier phase problems are uniquely solvable in more than one dimension. I: Underlying theory. *Optik*, 61:247–262, 1982.

[33] J.C. Spence, U. Weierstall, and M. Howells. Coherence and sampling requirements for diffractive imaging. *Ultramicroscopy*, 102:149–152, 2004.

[34] X. Z. Yu, Y. Onose, N. Kanazawa, J. H. Park, J. H. Han, Y. Matsui, N. Nagaosa, and Y. Tokura. Real-space observation of a two-dimensional skyrmion crystal. *Nature*, 465(7300):901–904, Jun 2010.

[35] Joseph Barker and Oleg A. Tretiakov. Static and dynamical properties of antiferromagnetic skyrmions in the presence of applied current and temperature. *Phys. Rev. Lett.*, 116(14):147203, apr 2016.

[36] Xichao Zhang, Yan Zhou, and Motohiko Ezawa. Antiferromagnetic skyrmion: stability, creation and manipulation. *Scientific Reports*, 6(1), apr 2016.

[37] S. L. Zhang, G. van der Laan, and T. Hesjedal. Direct experimental determination of the topological winding number of skyrmions in Cu_2OSeO_3. *Nat. Commun.*, 8(1), feb 2017.

[38] Stefanos Kourtis. Bulk spectroscopic measurement of the topological charge of Weyl nodes with resonant x-rays. *Phys. Rev. B*, 94(12):125132, sep 2016.

Chapter 3

Artificial Pattern Formation in Nickelate thin films

3.1 Introduction

In quantum materials oxides hold a special spot with their richness in phenomenology. They host some of the most technologically relevant however least explained phenomena in condensed matter physics such as metal-insulator transition and high-temperature superconductivity. What makes them more exciting is the tunability of the physics they harbor. The ABO_3 perovskite structure is probably one of the most abundant among the different structures stable states of oxides are formed. A wide combination of A and B site ions are used to form the perovskite unit cell which distorts from the simple cubic structure to accommodate the differences in internal stress due to differences in A and B size.

In ABO_3 perovskite phase small structural change perturbs the electronic environment strongly to change the response drastically. We often observe a textured phase diagram with multiple phases competing and co-existing as the structure is tuned. The structural changes from an ideal simple cubic structure can be classified into three main processes: (i) rotations of

the BO_6 octahedra (ii) stretching of the BO_6 octahedra, and (iii) cation displacement. This is schematically shown in 3.1 Epitaxial growth of one oxide of interest on top of the motif provided

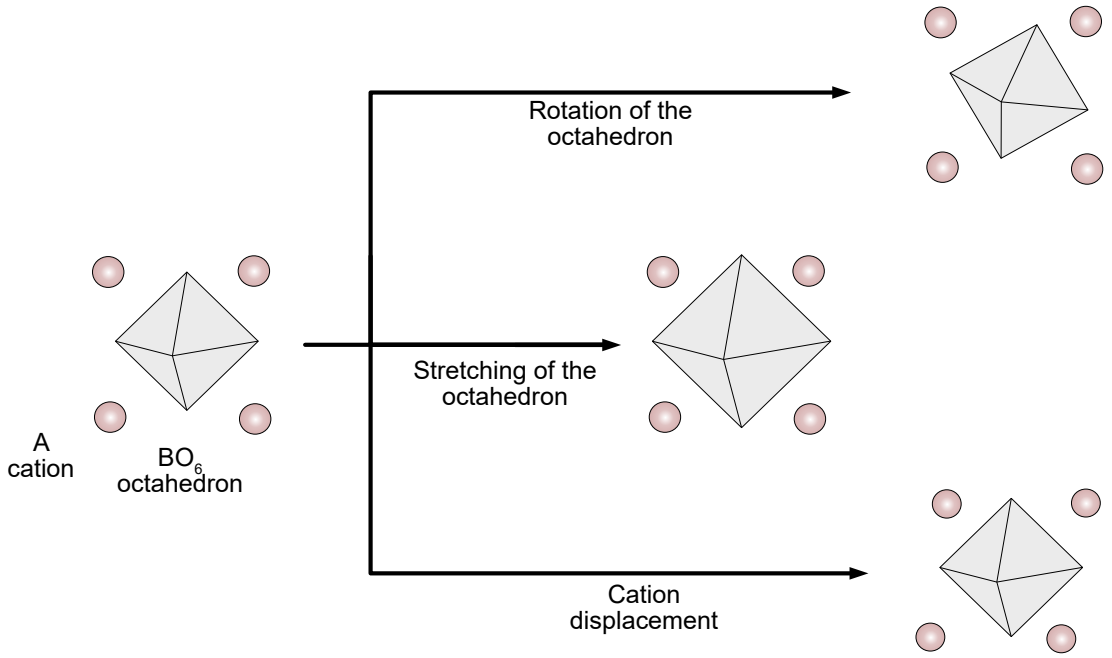

Figure 3.1: **Three primary distortions of ideal simple cubic structures of ABO_3 perovskites**: rotation of the octahedron, stretching and shrinking of the octahedron, and cation displacement

by another perovskite creates further tuning of the overlayer thin film structure[1]. With abundant high-quality substrates available from industrial suppliers and the advancement of thin film growth technology epitaxial strain tuning a perovskite structure for tunable functionality has emerged as a very powerful technique. Although there are many stable phases of substrates available for the misfit strain, a quantity capturing the discrepancy of overlayer and substrate lattice mismatch, they only enable tuning in discrete steps. Thus, this method cannot continually tune the overlayer properties.

Furthermore, a fundamental limitation of strain engineering using strain cells or epitaxial growth comes from the Poisson effect, where accommodating a bi-axial in-plane stress in a thin film always involves modification in all three directions. Such modification inhibits a direct

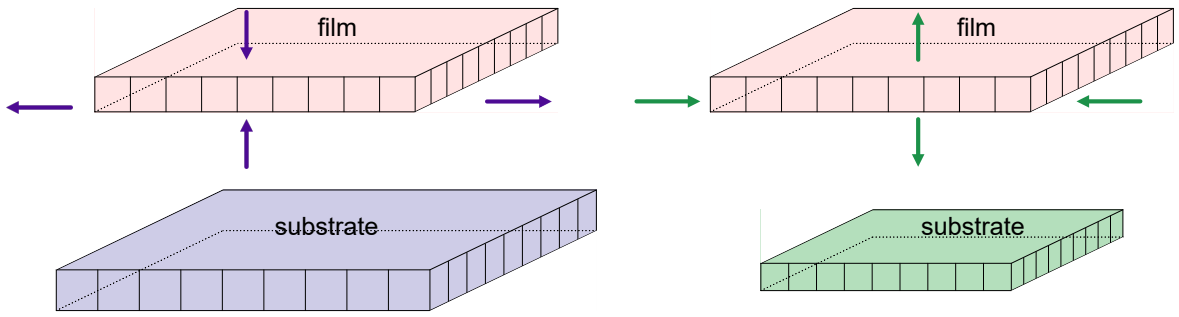

Figure 3.2: **Poisson Effect in epitaxially grown thin films:** (left) A substrate motif having a larger in-plane lattice constant applies a tensile strain on the overlayer film. As a consequence a compressive strain is experienced by the thin film unit cells along the out-of-plane direction. (right) Similarly a compressive in-plane strain generates an out-of-plane tensile strain

experimental way to understand complex physics and further tune it to exact technological needs. This is schematically shown in the figure 3.2 where an in-plane bi-axial compressive strain is accompanied by an out-of-plane tensile strain and vice-versa. In the following section we will show that implantation of noble helium ions provides a method to uni-axially tune the strain on thin films from the chemical pressure of intercalated ions. Since ions get implanted into the unit cell the volume of the unit cell is not preserved anymore.

Finally, as we will see ion implantation provides us with a local tool for strain tuning of the as-grown thin film. Thus taking advantage of the locality aspect we can create lateral heterostructure of implanted and non-implanted regions. Moreover, differently strained perovskite will undergo structural changes accordingly resulting in electronic states that differ from each other. Now if we create a lateral pattern of such implanted and not-implanted regions it may offer us a new paradigm where lateral-interface effects become important. Creating superstructures has non-trivial effects on the electronic bands of the material especially near the Fermi

level which influences the overall property of the material. It is well known how twisting two graphene layers with respect to each other and stacking them on top of each other creates a lateral supermodulation, also known as the Moire pattern. The result is evidenced in the band structure as the weakly correlated material turns into a strongly correlated electron system. With such expectations in mind, we set out to first show that it is possible to create lateral heterostructures of electronic phases in nickelate thin films using a focused helium ion beam. After creating lateral heterostructure we will probe the heterogeneity with Synchrotron-based X-ray techniques which are sensitive to lateral heterostructures of electronic phase.

3.2 Helium Ion beam as a tool for local structural tuning

Ion implantation is a time-tested technique in the semiconductor industry, where high-energy ions are accelerated and directed to form a beam before finally being implanted into the target. It is useed in the semiconductor industry to induce defects as well as dopants into a crystalline material. As soon as it enters the target it collides with the nucleus and electrons of the host material through electro-magnetic interaction and loses its kinetic energy. With successive collisions, it loses some parts of its energy and finally comes to rest at some depth inside the host material. There are two channels of energy loss:

(i) inelastic collision with electrons, and

(ii) elastic collision with the nucleus.

It requires a much greater scope than this thesis to go into the details of high-energy ion kinetics inside the materials. However, we have included a concise discussion in the appendix, complete with references for interested readers. In this section, we will highlight a few key points about the ion kinetics while it slows down inside of the material.

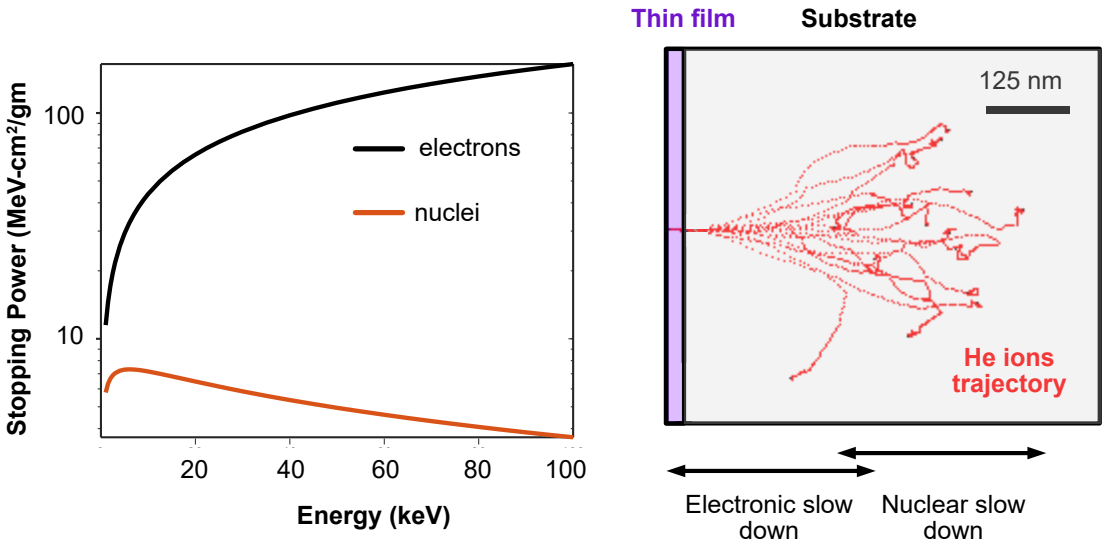

Figure 3.3: **Stopping of helium ions in materials:** (left)Helium stopping power of gold electrons and nuclei as a function of helium ion energy (right) Trajectory of 90keV helium ions in $NdGaO_3$ substrates covered with thin film of $NdNiO_3$, simulated using TRIM simulations

Capturing the ion kinetics: The energy loss of incoming high-energy ions inside the material is dominated by the inelastic collisions with the electrons. The inelastic interaction with the electrons is a complex process however, can be approximately understood as equivalent to a drag force. Thus, just below the surface the ions primarily experience a viscous drag force due to the electrons and lose their energy without much deflection. This continues till the energy drops to a certain limit where elastic collisions with the nucleus become prevalent. We show here the stopping power (Energy loss per unit length of penetration normalized to the density of the material) of electrons and nuclei of gold for an incoming helium ion beam of energy from the ASTAR calculator of the National Institute of Standards and Technology (NIST) which evaluates stopping power by electrons and nuclei of a material for alpha particles (He^{2+}).

Furthermore, transport of ions in matter (TRIM) simulations successfully captures the kinetics of the ions of given energy inside of a material of given composition and density. In the

right panel of Fig 3.3, we have demonstrated the range of electronic slow-down and the nuclear slow-down of energetic ions inside of materials. The noticeable feature of nuclear slowing down is evidenced by the deflection of the ion trajectories deep below the surface. Nuclear collisions are a random process that distributes the ions in all possible directions. A small percentage of the incoming ions back-scatter as well after nuclear collision. Thus a distribution of the implanted ions is seen after all of them come to a stop. The collision with the nucleus creates dislocations of the ions in the material as a result. Such defects are generated inside the material with a Gaussian distribution centered at the stopping range of the ion. This is evaluated using the stopping range of ion in matter (SRIM) simulation tool.

3.2.1 Helium ion implantation:

Following our broad discussion of ion implantation of materials we focus now on the helium ion implantation into oxides. Recent experiments have shown that the implantation of noble helium atoms onto epitaxial thin films after growth provides a means to control selectively and continuously the out-of-plane lattice parameters and hence the strain along the out-of-plane direction, while the film remains locked into the bi-axial in-plane strain provided by the substrate [2]. Annealing at high temperatures in the vacuum undoes this uniaxial strain provided by the helium implantation. The authors implanted He ions of 4keV energy and doses (0, 8, 14, and 21 ions per sq cm) onto 20nm $La_{0.7}Sr_{0.3}MnO_3$ (LSMO) film epitaxially grown on $SrTiO_3$ substrates. As a result, they showed a continuous expansion of the c-lattice parameter of the film with increasing dose followed by a decrease in the paramagnetic-insulator to ferromagnetic-metal transition temperature, and the magnitude of the magnetoresistance. This work showed convincingly that the continuous tuning of out-of-plane lattice strain provided us with a pathway to continuously tune the electronic properties of strongly correlated electron systems. As highlighted by the authors as well as our previous discussion about the stopping power for the case of lightweight high-energy ions such as helium, the majority of stopping power is contributed by

non-nuclear interaction. Thus, they minimize structural damage to the film structure.

The process of He-ion implantation: In the implantation process, He^{2+} ions get accelerated in a static electric field on the order of kV. Using electric fields they are guided towards the grounded film we wish to implant on. The helium current is set corresponding to the dose in ions per square cm (IPSC) we wish to implant the substrate with. Finally, a beam is held at a position for some time (called dwell time) while rastering over a region to match the dose for a given current. Another incredible property of the helium beam is that it can be focused down to 0.5 nm using electro-magnetic lenses providing us with the perfect tool to create lateral heterostructures on the thin film. In the figure 3.4, we are showing the setup of the helium microscope which is also used to create the lateral hetero-structures on oxide thin films. Toulouse *et. al.*[3] showed that using such helium microscope (Orion Nanofab) uni-axial strain tuning can be laterally confined in $BiFeO_3$ thin films epitaxially grown on LSAT and STO substrates. Using a focused ion beam they showed that the uniaxial strain tuning was localized into square regions with sizes ranging from 10×10 to 500×500 μm^2.

Once the helium is in the lattice the stopping of the energetic helium comes from non-nuclear interaction and thus can be modeled using Monte Carlo simulations. Moreover, helium being a noble gas ensures that the sample does not get electron or hole doped. They do not form compounds with the existing ions of the crystal as well. The stability of the implantation exceeds several months without degradation. This has been reported[5], and also tested under the context of the present thesis. The authors studied 20 nm of orthorhombic $SrRuO_3$ coherently grown on $SrTiO_3$ substrates and then exposed to a helium ion beam of 4keV and several doses. They observed that increasing helium dose directly tuned the out-of-plane lattice parameter of the thin film which in turn tuned the rotation pattern of the BO_6 octahedra and resulted in a more tetragonal unit cell structure from an orthorhombic one.

Defect generation due to He-ion implantation: It is well known in the community that ion bombardment can create knock-on damage to the crystal [4]. This ability of high-energy ion

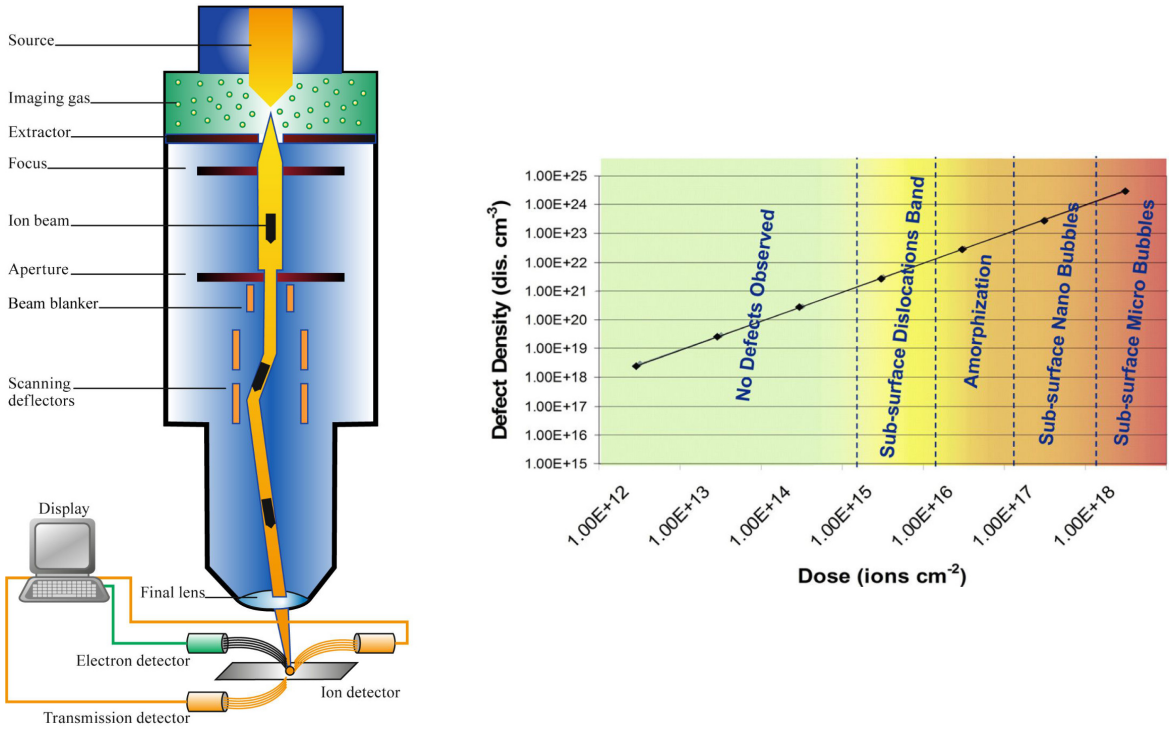

Figure 3.4: **Helium ion microscope and the effect of dose on defect density:** (left) the cross-section of the helium ion microscope showing creation, guidance, and focusing of the high energy helium ion beam before implantation on the sample [4].(right) defect density observed as a function of dose. The intended dose is to be in the limit where no defects are observed. All of our implantation lies in this regime (below 5e15 ions/cm^2).

is readily used in focussed ion beam facilities to cut off a lamella of materials for microscopic study. However, such damages require high energy of helium ion as shown in the figure 3.5, adapted from the topical review [4]. Keeping this plot of defect generation in mind often the dose for structural strain tuning is kept below 50 $\times 10^{14}$ IPSC, above which sub-surface dislocation bands are observed to be created. Furthermore, in this low energy and low dose limit of helium ion implantation functionality of perovskite oxide is seen to be tuned. Hence we look more into the details about the knock-on damages sustained by the helium implanted perovskite structure.

In this energy limit the knock-on damages are hard to observe through structural characterization experiments. Thus, we turn to discuss this from a theoretical point of view following [6].

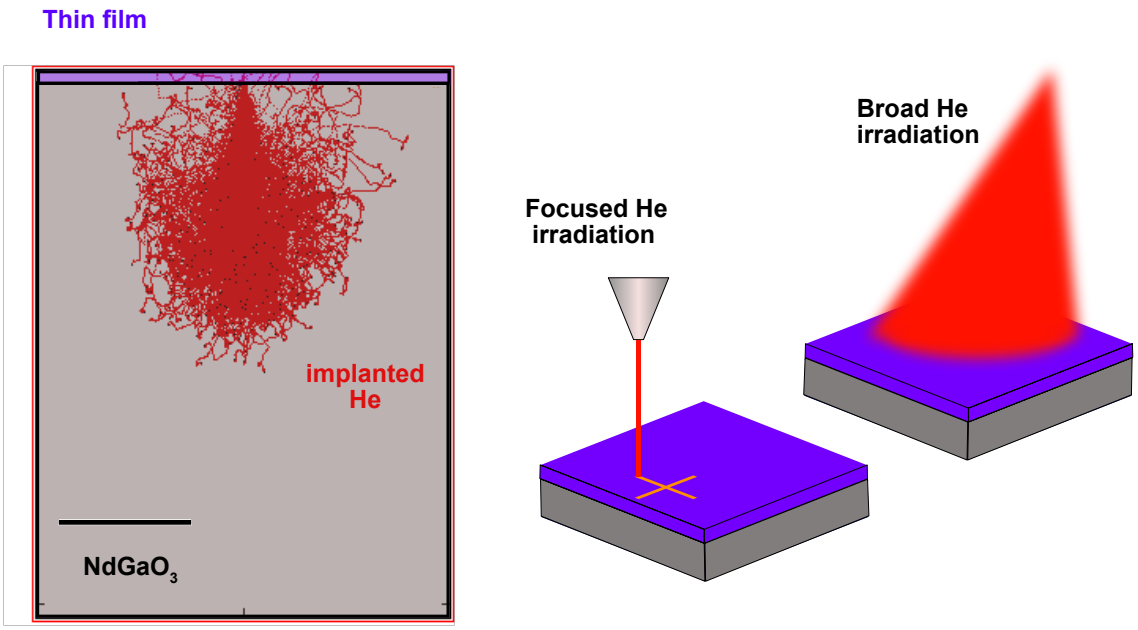

Figure 3.5: Helium ion implantation cross-sectional view of the microscope and two modes of implantation

They used Density Functional Theory (DFT) to evaluate thermodynamic stability point defects that can be caused by helium ion collisions. They considered their evaluation for 4keV ions of helium which will be implanted into thin films of $SrRuO_3$ films of 20nm thickness at a dose of 50×10^{14}IPSC. They considered the helium ions do not propagate into the substrate. Out of three different inherent point defects, (a) vacancy (b) interstitial, and (c) anti-site defects, they found that the lattice parameter expansion along the out-of-plane direction may not have been caused by the He ion interstitial alone. Collisions create cation and oxygen vacancies and the dislodged ions further migrate to interstitial positions. According to the calculation, all of these defects need to be considered as contributing to the lattice expansion.

Setting up the parameter for He ion implantation on the nickelates: For our experiment we developed thin film sof $NdNiO_3$ and $PrNiO_3$ of thickness 15-20 nm on $NdGaO_3$ substrates. We wanted the He ions to go unscattered deep into the substrate and get implanted.

Thus the thin film only experiences minimum damage and the most defect formation happens in the substrate of $NdGaO_3$. To facilitate this, we further considered the energy of the ions to be 90 keV. We used the stopping range of ions in matter (SRIM) simulation to evaluate the mean depth of ion implantation for 90 keV ions. For our purposes, we evaluated the numbers such that the helium ions go deep into the substrate and don't stay inside the thin film. The density used for $NdNiO_3$, $PrNiO_3$, and $NdGaO_3$ are 7.24, 7.39, 7.26 gm.cm^{-3} respectively. The figure above shows the ion trajectory simulated using the transport of ions in matter (TRIM) simulation for the following parameters:

- Thickness of the overlayer ($NdNiO_3$) = 20nm
- Density of the film = 7.24 g.cm^{-3}
- Substrate ($NdGaO_3$) thickness = 1 μm
- Density of the substrate = 7.26 g.cm^{-3}
- He-beam energy = 90keV
- incidence angle = 90° *wrt* surface.

In the following table3.1, we show the stopping range of He ions of different incident energies. This is the mean depth of the ions from the surface and there is a distribution $\sim$40nm at 10 keV, and $\sim$100nm at 90 keV. We see that for any energies above 10 keV the ions comfortably cross the thin film of 20 nm thickness and are implanted into the substrates. We wanted to work on this regime so that the helium directly affects the substrate structure which in turn changes the structure of the thin film through epitaxial relationship.

A hand-wavey way of understanding the effect of helium implantation can be found in analogies to pumping a bike tire. The helium like the air goes inside and provides tensile strain only in the direction outward to the surface. For focused ion implantation we have used 25 keV

Table 3.1: Stopping range of He ions in $NdGaO_3$, $PrNiO_3$, and $NdNiO_3$

Ion energy (keV)	Range in $NdGaO_3$ (nm)	Range in $NdNiO_3$ (nm)	Range in $PrNiO_3$ (nm)
10	46	43	44
25	109	102	105
50	202	188	193
90	327	303	310
100	355	328	337

helium ions however for uniform ion implantation we used a higher energy of 90 keV for 20nm thin films grown on $NdGaO_3$ substrate. We have used the company Kroko inc. for uniform irradiation and used the QB3 facility at UC Berkeley for focused helium ion beam implantation. The energy used for focused ion implantation was limited by the instrument's capability. We have also used samples made by our collaborators of Dynes group at UCSD. These samples were used in the X-PEEM experiment discussed later.

In summary, in this section, we discussed the process of helium ion beam implantation and the incredible uni-axial tuning property it offers. In the following section, we will employ the tuning property to epitaxially grown nickelate thin films and show that lateral heterostructures of electronic states can be created utilizing this tool.

3.3 Phenomenology of Nickelates

In this section, I will first review the physics of rare earth nickelates relevant in the context of the present thesis. In strongly correlated d-electron systems, such as rare earth nickelates the central character is that of the nickel d-electrons near the Fermi level. The short radius of d-electron orbitals makes it the home to strong interactions between electrons who come close to each other. On the other hand, oxygen orbitals are directional and extend from one neighboring d-orbital on one side to the next allowing pathways for electrons and holes to hop around. These

contrasting natures of nickel and oxygen blossom into rich physics in a cubic symmetry such as a perovskite structure where not only the position but the directionality and intermixing of the orbitals play a major role.

In the perovskite rare earth nickelates, the nickels and the oxygens form a corner-shared network of NiO_6 octahedra as shown in figure 3.6a. Although an ideal perovskite maintains cubic symmetry, $RNiO_3$ crystal structure distorts from perfection due to the rare earth ion size. The smaller size of these ions compared to what is needed for a cubic structure prompts a coordinated distortion in the corner-shared network of octahedra, resulting in an orthorhombic *Pbnm* lattice. Furthermore, from La to Lu along the lanthanides in the periodic table the rare earth ion becomes heavier and smaller. To accommodate this, the lattice becomes more and more orthorhombic. In figure 3.6a, we have shown a typical perovskite structure with the distortion where the rare earth ions can be used to define the unit cell (marked by purple dashes).

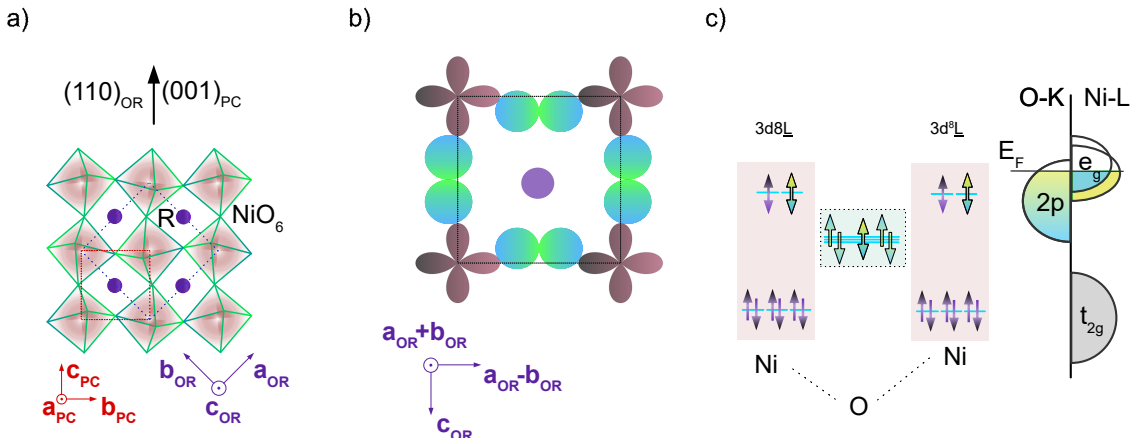

Figure 3.6: **Rich physics of nickelates** a) corner shared octahedra of NiO_6 with the rare earth ions (R) at the octahedral sites forms the unit cell for $RNiO_3$ b) Ni-O-Ni bond angle modulates the overlap between $O-2p$ and $Ni-3d$ orbitals schematically described here using orbitals in x-y plane c) oxygen $2p$ band strongly hybridizes with $Ni-e_g$ orbitals into a covalent $3d^8\underline{L}$ state

The extent of orthorhombic distortion is measured by the tolerance factor, denoted as t, which is calculated as the ratio of the average separation between rare earth and oxygen ions

(d_{R-O}) to the average separation between nickel and oxygen ions (d_{Ni-O}), $t = \frac{d_{R-O}}{\sqrt{2}d_{Ni-O}}$. Ideally, a perfect cubic structure would yield a tolerance factor of 1. However, what's typically observed in the rare earth nickelate family is that this value is often less than 1. Consequently, this leads to a noticeable decrease in the $Ni-O-Ni$ bond angle from its ideal 180°.

Now, when we look closely at the atomic orbital arrangement, adjusting the $Ni-O-Ni$ bond angle away from 180° affects how much the oxygen orbital overlaps with the two nickel orbitals it connects to, thus changing the transfer integral (note 3.6b). On the other hand, the crystal field environment of the nickel ions splits the otherwise degenerate d orbitals into two sets of orbitals: t_{2g} (those who do not point towards the oxygen ligand orbitals, d_{xy}, d_{yz} and d_{zx}) and e_g (those who point towards the ligand orbitals, $d_{x^2-y^2}$ and d_{3z^2-r2} and raises the e_g orbitals to a higher energy. Furthermore, the filling of orbitals follows Hund's rules of maximum multiplicity: all orbitals should be filled with electrons of the same spin before they are paired. Crystal field and Hund's exchange energy determines the filling up of d-orbitals.

In a nominal ionic configuration of Ni^{3+} the orbital occupation would assume a low spin state of $t_{2g}^6 e_g^1$. If only the valence d-electrons were the main driver of physics in the nickelates one could integrate out the oxygen orbitals for the renormalized transfer integral between neighboring Ni sites. In such a scenario a partially filled e_g band will have gapless excitation if the constituent electrons are weakly interacting. If instead, they were strongly interacting with on-site Coulomb repulsion (U_{dd}) the interplay of tunable hopping parameter (t_{dd}) would need to be understood under the light of Mott-Hubbard physics. However, none of these scenarios happen. Neither the nickel ion finds itself in a nominal Ni^{3+} ground state, nor the oxygen orbitals can be integrated out in favor of Mott-Hubbard physics.

Mounting evidence from experiments pointed out that in rare earth nickelates oxygen 2p band energetically lies between the e_g and t_{2g} bands as shown in 3.6c and oxygen $2p$ hybridizes with the nickel e_g bands. The energy required for the Since charge transfer energy (Δ_{pd}) dictates the physics of these materials. Experimentally this is validated by observing the Ni ions in a highly

hybridized $3d^8\underline{L}$ state, where $\underline{L}$ denotes a ligand hole [7] . Thus the ratio of charge transfer energy and the transfer integral becomes a driving parameter according to the Zaneen-Sawatzky-Allen phase diagram for $3d$ Transition metal oxides. Both of these are influenced in a complex way by changing the $Ni-O-Ni$ bond angles.

To summarize, the charge transfer energy (Δ), transfer integral of hopping from $O-2p$ orbital to $Ni-3d$ orbital, on-site Coulomb repulsion, Hund rules, and orbital polarization of the e_g orbital collectively influence the environment of strongly interacting electrons.

What happens if we lower the temperature now?

Phase diagram of rare earth nickelates: As we lower the temperature the high-temperature metallic state transitions into a low-temperature insulating state except for R=La, which remains metallic down to the lowest temperature explored. The transition temperature decreases from Lu to Pr consistently with increasing tolerance factor. The insulating phase is found in a bond ordered and charge ordered state. The bond ordered state forms due to a monoclinic ($P2_1/n$) distortion to the orthorhombic ($Pbnm$) high temperature phase. As a result of this distortion we observe a structural super-lattice formation where nearest neighbor octahedra shrinks and expands respectively from their high temperature metallic state. Furthermore, a concurrent charge order of same ordering wave vector is observed. On the other hand, an antifero-magnetic order emerges in this bond -distorted insulating state if we lower the temperature further for $R\mathrm{NiO_3}$ with $R = LutoSm$. The Neel temperature increases gradually with increasing rare earth size. However, for $\mathrm{NdNiO_3}$ and $\mathrm{PrNiO_3}$ we observe that both metal to insulator transition and paramagnetic to antiferromagnetic transition are coupled making them the most interesting samples to study the complexity of nickelate physics. Here we study $\mathrm{NdNiO_3}$ and $\mathrm{PrNiO_3}$ with helium ion implantation.

There are two fundamental attempts motivated from the two different ends of the phase diagram (high and low tolerance factor) to understand the mechanism of the complex phase transition. One of them considers bond order as the primary order parameter and is called the *site*

selective Mott transition. Here the antiferromagnetic order or the charge order is secondary and is not necessary for the phase transition. In this mechanism a short bond makes the oxygen ligand holes to be shared more with the Ni valence shell making it of $3d^8\underline{L}^2$ character forming a singlet. This effectively makes this octahedra detatch from the network of octahedra. Since the valence band is completely unoccupied or equivalently, occupied with two electrons and two holes this site behaves as part of a band insulator. On the other hand the expanded octahedron gains a $3d^8$ character and the on-site Coulomb repulsion for the half filled valence shell dictates the physics like a Mott insulator. Thus, in this bond ordered phase two neighboring octahedron sites become insulating following two different mechanism [8, 9]. However, we need strong electron lattice coupling to explain the charge order formation as a result of the bond order. Recent works have shown that a free energy of the phase with electronic energy f_{el} and electron-lattice coupling is sufficient to explain the proportional charge order emergent in the low temperature nickelate phase [10, 11]. In such a theory a crucial result is obtained from the free energy analysis which is presented below. The total free energy of the electron-lattice system can be expressed with a harmonic approximation for the lattice energy ($\frac{1}{2}KQ^2$ with Q as the bond order parameter and K is a proportionality constant, along with a coupling term between the electronic charge order and lattice bond order, and a purely electronic term which encodes a first order phase transition in terms of charge order, ΔN. From symmetry consideration of the order parameter we can write, -

$$f(\Delta N, Q) = \frac{1}{2}KQ^2 - \frac{1}{2}gQ\Delta N + \frac{1}{2}\chi_0^{-1}\Delta N^2 + \frac{1}{4}\beta\Delta N^4 + \frac{1}{6}\gamma\Delta N^6, \tag{3.1}$$

We have incorporated different proportionality constant as they required. The stationary solution with respect Q gives us an important result:

$$KQ = \frac{1}{2}g\Delta N \tag{3.2}$$

We will test this relationship as measure of the electron lattice coupling and how it differs

from sample to sample. We consider this picture in the nickelates as a local electron picture where the bond order can influence the electrons locally and modify the electronic correlations. The other limit of this explained by an highly itinerant electron system where they form Fermi surface. For high tolerance factor this limit have been believed to be experimentally realized [12, 13]. In this limit, a Fermi surface instability generates a spin density wave at **q**=(1/2, 0, 1/2) wave vector[14, 15]. We will see during our exploration in nickelates that we are able to change the itinerant versus localized nature of the d-electrons, which in turn changes the character of the magnetism from a localized *site-selective Mott* picture to possibly a *spin density wave* picture. For now we focus on the two specific samples of $PrNiO_3$ and $NdNiO_3$ which act as a reference sample quality. We will implant helium on them to change their electronic character.

3.4 Results: Coupled phase transitions in $NdNiO_3$ and $PrNiO_3$

In this section, we present our experimental exploration of the phase transitions in $NdNiO_3$ and $PrNiO_3$, focusing on the characterization of the ordered phase at low temperatures. To facilitate our discussion, we provide a concise representation of the phase diagram, highlighting the phases under examination. Our aim here is to introduce the phase transitions observed in epitaxially grown rare earth nickelate thin films of $NdNiO_3$ and $PrNiO_3$ on (110)-oriented $NdGaO_3$ substrates, followed by interpreting the observed data in the light of site-selective Mott transition picture with strong electron-lattice coupling.

3.4.1 Charge Disproportionation driven by Bond Order:

Before going into the details of the charge order below the phase transition, let's first introduce the samples and discuss their characteristics. We will discuss their structural details

focusing on how the lattices respond to the strain environment. Then we will establish the high quality of our films being studied from the sharpness of the metal-insulator transition we observe. Finally, we will extract charge order and bond order from these samples as a function of temperature.

Structural Characterization: In our discussions, we primarily utilize epitaxial thin films grown via pulsed laser deposition. For comprehensive information regarding thin film growth, please consult the appendix. We have uniformly produced thin films with a thickness of approximately 22 nm on 110-oriented $NdGaO_3$ substrates for both $NdNiO_3$ and $PrNiO_3$ films. Their structures were characterized using an in-house $four-circle$ diffractometer (make: Huber) operating with Cu-K_α source at room temperature. The specular reflection of (2 2 0) and the off-specular reflection of (2 2 1) were investigated to extract the orthorhombic lattice parameters as shown in the table 3.2 below.

Table 3.2: Bulk lattice parameters of $RNiO_3$ (R = Pr, Nd) compared with measured lattice parameters of $NdGaO_3$ substrate used. In-plane strain value calculated from them is tabulated $\parallel$ or $\perp$ to c direction of $NdGaO_3$ substrate. We used the formula $100 \times (a_{film} - a_{substrate})/a_{substrate} = \%strain$

attributes	$PrNiO_3$ bulk	$NdNiO_3$ bulk	$NdGaO_3$ substrate
a (Å)	5.42	5.39	5.37
b (Å)	5.38	5.38	5.56
c (Å)	7.63	7.61	7.73
$\sqrt{a^2+b^2}$ (Å)	7.64	7.62	7.72
in-plane strain $\parallel$ c	1.31	-1.55	1
in-plane strain $\perp$ c	1.04	-1.48	1

Ideally, one needs at least three mutually orthogonal peaks to refine the six parameters (a, b, c and α, β, γ) that define the structure of a 3-dimensional lattice. However, we get around that by the following crucial assumptions based on the works of Valilionis et al.

- the misfit stress between the substrate and the film is accommodated along the (0 0 1) direction differently than $(1\bar{1}0)$ direction.

- the volume of the unit cell is <u>not</u> preserved to accommodate strain

As a consequence, we need to look at the distortion of the octahedra along the two perpendicular in-plane directions separately. Along the (0 0 1) direction as shown in the figure 3.7 the stress is accommodated by elongating the c lattice parameter of the film. The angles α and β remains equal to 90°. Both of these points are confirmed by checking the epitaxy of the film on the substrate off-specular peak of (2 2 1). On the other hand, in the plane spanned by (1 1 0) and $(1\bar{1}0)$ the angle γ is free to change along with the lattice parameters (a,b) and thus the stress from the substrate is going to be accommodated by all: a, b and γ. Hence with the condition of epitaxy, a, b and γ are the only unknowns.

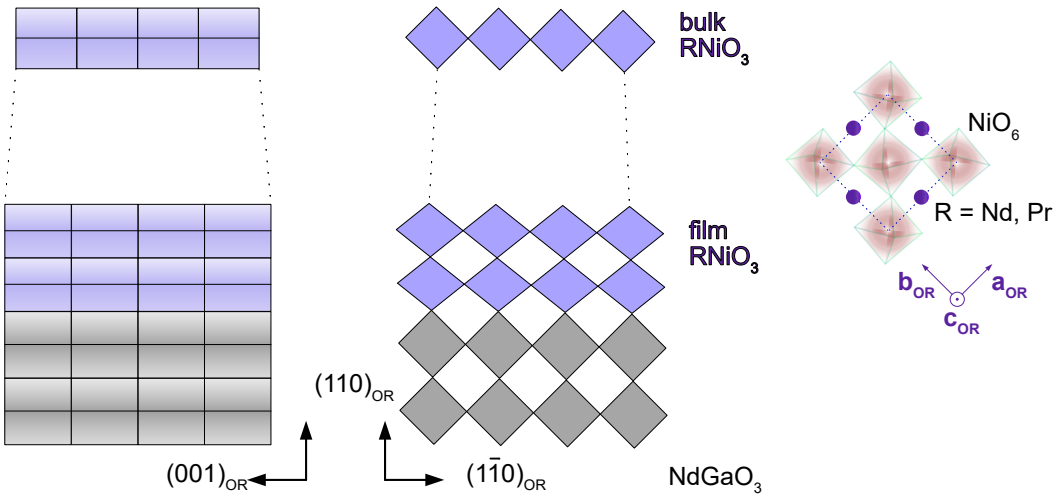

Figure 3.7: Epitaxy changes the lattice parameters a,b,c and γ. The unit cell is shown for continuity

The problem is further simplified by observing the results discussed in where under tensile strain the a and b lattice parameters of the film become equal, $a_{film} = b_{film}$. So finally we have two unknowns a_{film} and γ_{film} in the two equations as follows:

$$\sqrt{a_{film}^2 + b_{film}^2 - 2a_{film}b_{film}cos(\gamma_{film})} = d_{1\bar{1}0\rightarrow substrate},$$
$$\sqrt{a_{film}^2 + b_{film}^2 + 2a_{film}b_{film}cos(\gamma_{film})} = 4 \times d_{220\rightarrow film}. \tag{3.3}$$

Based on the arguments presented above and our measurement of the (2 2 0) and (2 2 1) peaks we find the following lattice parameters for the film and the substrate:

Table 3.3: Bulk lattice parameters of $RNiO_3$ (R = Pr, Nd) compared with measured lattice parameters of $NdGaO_3$ substrate used. In-plane strain value calculated from them is tabulated $\parallel$ or $\perp$ to c direction of $NdGaO_3$ substrate.

attributes	$PrNiO_3$ film	$NdNiO_3$ film	$NdGaO_3$ substrate
a (Å)	5.42	5.4	5.37
b (Å)	5.42	5.4	5.56
c (Å)	7.73	7.73	7.73
$\alpha(^\circ)$	90	90	90
$\beta(^\circ)$	90	90	90
$\gamma(^\circ)$	90.97	91.33	90

The condition of epitaxy along (0 0 1) is confirmed by doing an HKL-scan along (1 1 0) direction (parallel to the growth direction) after aligning to the substrate (2 2 1) peak and finding the film peak at the correct (H, K) coordinates.

Transport Characterization: Four-point van der Pauw measurements were performed to characterize the metal-insulator transition. All of our films discussed in this thesis showed sharp metal-insulator transition with hysteresis loop as expected from $NdNiO_3$ and $PrNiO_3$ samples. This indicates the high quality of coherent thin film growth.

Resonant Hard X-ray Scattering: Now that we have established the quality of the film, and characterized the structure and metal-insulator transition we move to the central investigation regarding charge order. Hard X-ray resonant scattering experiments were carried out to reveal the charge and bond order of the neighboring NiO_6 octahedra as the sample was cooled (*Pbnm* to $P2_1/n$). The experiments were carried out in the 6-ID-B beamline of the Advanced Photon

Source of Argonne National Lab using a six-circle diffractometer. We have seen previously that a Landau theory of strong electron-lattice coupling produced a direct proportionality between the order parameter strength of the bond order and charge order. To test that prediction we set out to measure the relative strength of bond order and charge order as we lower the temperature. As shown in figure 3.8 we consider the deviation from the average Ni-O bond length in each octahedron as the measure of the bond order parameter (Δ). Similarly, the deviation from the average value of charge for neighboring octahedra is considered as the charge order parameter (δ), shown in the figure 3.8 for a nominal charge on Ni ion [16].

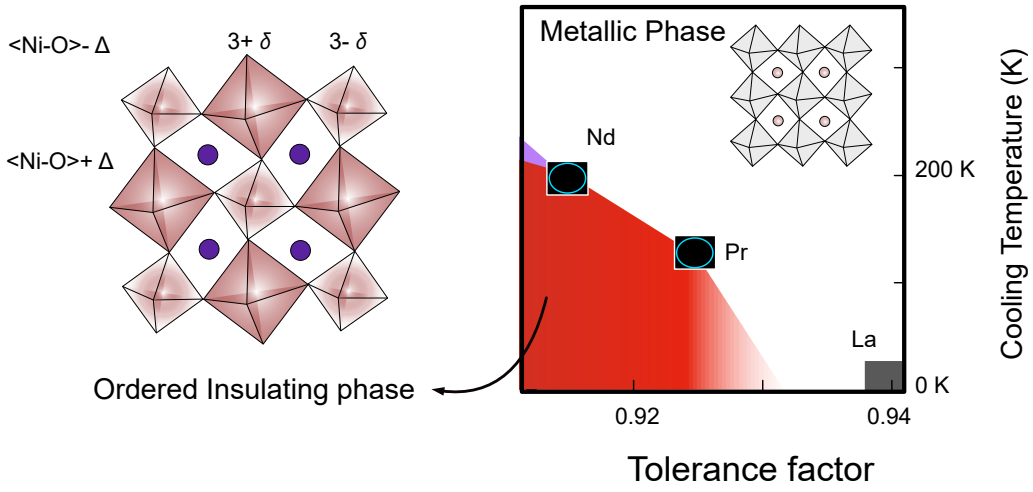

Figure 3.8: Bond order (Δ) and charge order (δ) parameters in the relevant section of the phase diagram for this section

Figure 3.9 shows the schematic experimental setup for the hard X-ray scattering experiment. The incoming polarization was set to σ to increase scattering sensitivity to charge. The scattered beam was not analyzed. We performed fixed-q energy scans around Ni - K edge with an energy resolution of 1eV (comparable to the broadening by core-hole lifetime) while the diffractometer was oriented to the (011) peak. A fixed-q scan updates the diffractometer position for every energy step for the scan. Since the peak is forbidden without charge asymmetry in

nearest neighbor octahedra in the *Pbnm* phase we chose this for maximum contrast during phase transition. However in reality, some monoclinic distortion gives rise to observing this orthorhombic symmetry forbidden peak in the metallic state too but with much lower intensity. Lowering the temperature in these thin films finds a bond and charge-ordered insulating state with a doubling of the unit cell (3.8), thereby allowing the increased intensity of this peak. We measured energy dependence of the intensity of the peak as we cycled the temperature of the sample stage using a Liquid He cryostat with a temperature resolution of $\pm$ 0.1K. For each temperature, after necessary centering and realignment due to thermal drift, we varied the energy of the monochromator and measured the beam current normalized intensity of the peak. The order parameters of the bond order and charge order can be extracted from the energy dependence of this scattering intensity.

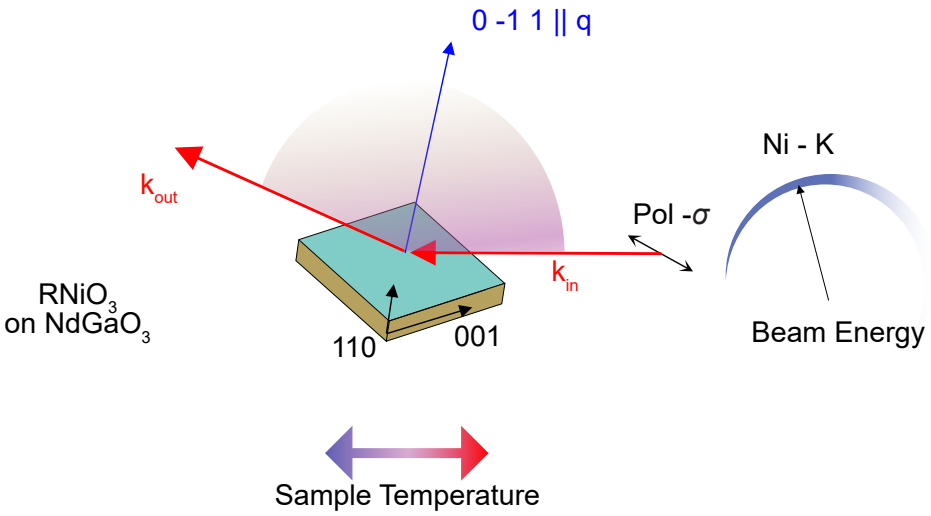

Figure 3.9: Experimental set-up for charge order and bond order determination

Let us focus on the extraction of the relative strength of bond order and charge order from the hard X-ray Resonant Elastic Scattering experiments. Raw data from the energy scans across the Ni-K edge on (0 1 1) reflection for both $NdNiO_3$ and $PrNiO_3$ are shown in figure 3.10 respectively. Only the data for warming is shown for clarity. K edge excitation creates a core

hole in the 1s state and in the dipole approximation, emission lines probe the unoccupied 4p state when that core-hole collapses. Even though the level states are far above the Fermi level, electronic ordering influences the energies of these states in a complex way. Fortunately, this is picked up simply by the 4p density matrix which gets off-diagonal terms due to the monoclinic distortion in a cubic eigenbasis. The scattered intensity observed, $I(\mathbf{q},E) = |F(\mathbf{q},E)|^2$, where $F(\mathbf{q},E)$ is the structure factor and we have neglected the Debye-Waller correction. The structure factor can be expanded as

$$F(\mathbf{q},E) = \sum_i e^{\imath\mathbf{q}\cdot r_i} f_i(\mathbf{q},E)$$

where i runs over all atoms of the orthorhombic or monoclinic unit cell. $f_i(q,E)$ contains energy independent non-resonant($f_i^n r(q)$) scattering and energy-dependent resonant contribution ($f_i^r(E)$). The energy-dependent scattering factor is a complex number and comprises real and imaginary parts as seen previously. The imaginary part of the scattering factor is directly linked to the X-ray absorption spectroscopy (XAS), whereas the real and imaginary parts both influence the scattering cross-section. Since the imaginary component of the non-resonant scattering factor is very small compared to the real component without loss of generality, we consider $f_i^n r(q)$ to be real. Then, the scattering factor expands into its full form as follows:

$$F(\mathbf{q},E) = \sum_i e^{\imath\mathbf{q}\cdot r_i}[f_i^{nr}(q) + Re[f_i^r(E)] + \imath Im[f_i^r(E)]]$$

Now as we sum over the unit cell members every term collects phases. The phases due to translation are accounted for by the phase factor $e^{\imath\mathbf{q}\cdot r_i}$, however, the Ni ions are not only related by translational symmetry. A $(h0l)$ or $(0kl)$ peak with $h,k,l \in Odd$ is forbidden by the translational symmetry of a *Pbnm* lattice. Thus, if we look at the intensity at Ni resonance there should be no contribution due to the resonant contribution. On the other hand, oxygen ions(O) and the rare earth ions (R) contribute to the non-resonant part due to monoclinic distortion present as the cooperative bending of the octahedra even in the *Pbnm* phase.

Let's look closer at the resonant contribution.

In general, $f^r(E) = \sum_{\alpha,\beta=x}^{z} \varepsilon^*_{o,\alpha} \mathcal{F}_{\alpha\beta} \varepsilon_{i,\beta}$, where $\mathcal{F}_{\alpha\beta}$ is the scattering tensor expanded as follows:

$$\mathcal{F}_{\alpha\beta} = \sum_{m=x}^{z} \frac{\langle s|\hat{T}_\beta|p_m\rangle \langle p_m|\hat{T}_\alpha|s\rangle}{E - \delta E + \imath\Gamma/2} \tag{3.4}$$

This denotes that the dipole operator $\hat{T} = (\hat{T}_x, \hat{T}_y, \hat{T}_z)$ acts on the spherical 1s orbital and creates a core-hole pair in the respective 4p orbital. In the monoclinic phase, two neighboring octahedra become inequivalent through bond order and charge order which interferes with the density matrix for the unoccupied 4p shells (to be occupied once we create the core-hole). Thus in the most general consideration, they will contribute a phase factor to the $f^r(E)$ between two neighboring Ni atoms. Since we know the order creates a $2 \times 2 \times 2$ supercell the only phase factor allowed by this symmetry is $e^{\imath\pi} = -1$. Thus, for a unit cell in orthorhombic or monoclinic symmetry, the structure factor for a peak such as the one we investigate (011) becomes:

$$F_{011}(\mathbf{q}, E) = A_{RO}(\mathbf{q}) + \Delta Re[f^r_{Ni}(E)] + \imath\Delta Im[f^r_{Ni}(E)],$$

where $A_{RO}(q)$ contains all the non-resonant contribution from the rare earth and the oxygen ions. Finally when we evaluate the intensity of the peak due to complex conjugation all contributions from $Im[f^r_{Ni}(E)]$ cancel out leaving only $|Im[f^r_{Ni}(E)|^2$ term [17]. On the other hand, the real part survives with the magnitude and the cross terms with the non-resonant part. Assuming $|A_{RO}(q)| >> |Re[f^{r'}_{Ni}(E)]|, |Im[f^r_{Ni}(E)|$ we can simplify the expression to the following:

$$I_{011}(\mathbf{q}, E) \approx |A_{RO}(\mathbf{q})|^2 + A_{RO}(\mathbf{q})\Delta Re[f^r_{Ni}(E)]$$

Main Result: $\Delta f^r_{Ni}(E)$ is extracted for our case from the raw data using E_{NRes} = 8356 eV (black arrow) as the non-resonant energy and shown in figure 3.10 for $NdNiO_3$ and $PrNiO_3$ respectively. The first column shows the raw intensity as measured during the experiment. The

second column corresponds to the extracted $\Delta Re[f^r_{Ni}(E)]$. We then note that at the resonance peak (noted by the green arrow) the intensity is mostly dominated by the Ni electronic states. However, at off-resonance (blue arrow) majorly crystal structure determines the intensity of the peak. Thus, we extract the bond order parameter from the raw intensity counts at the non-resonance position below the resonance peak(E_{NR}). It is interesting to note that even the $\Delta[f^{r'}_{Ni}](E)$ below the resonance peak is significantly influenced by the bond order. However, above the resonance energy, it doesn't.

Thus, an estimate for the charge order can be extracted from plotting $\Delta f'_{Ni}(E_{Res})$ as a function of temperature while subtracting the high-temperature value. Similarly, we extracted the bond order strength using the temperature evolution of the $\sqrt{I(E_{NR})}$. This is shown for both the warming and cooling cycles as indicated by the color-graded arrows in the last column of 3.10.

Discussion: From the plots of Fig 3.10 (e-f) it can be seen that the bond order and charge order in the $NdNiO_3$ film appear simultaneously as expected from the strong electron-lattice coupling. In line with the expectation, the phase transition is sharply first-order in nature with a hysteresis loop of 15K. We contrast this temperature dependence with the temperature dependence of $PrNiO_3$ where a smaller hysteresis loop, of about 5K, opens and the orders set in more gradually indicating a weaker first-order nature of the coupled phase transition. Furthermore, the strength of the order parameters is much lower for $PrNiO_3$ compared to $NdNiO_3$.

Before discussing the comparison, it is worth highlighting a few points here. The order parameters are extracted relative to their high-temperature value. Thus effects of background, difference in incoming flux, and detector sensitivity can be ignored. Although we kept incoming flux and detector sensitivity identical for both samples. Furthermore, we used the same non-resonant energy to extract the resonant energy evolution of $\Delta[f^{r'}_{Ni}]$ to have them comparable to each other. In other words, both of the orders are expressed in the same units even though the unit is not $\AA$ for the bond order or fraction of electron charge for the charge order. Hence, we have

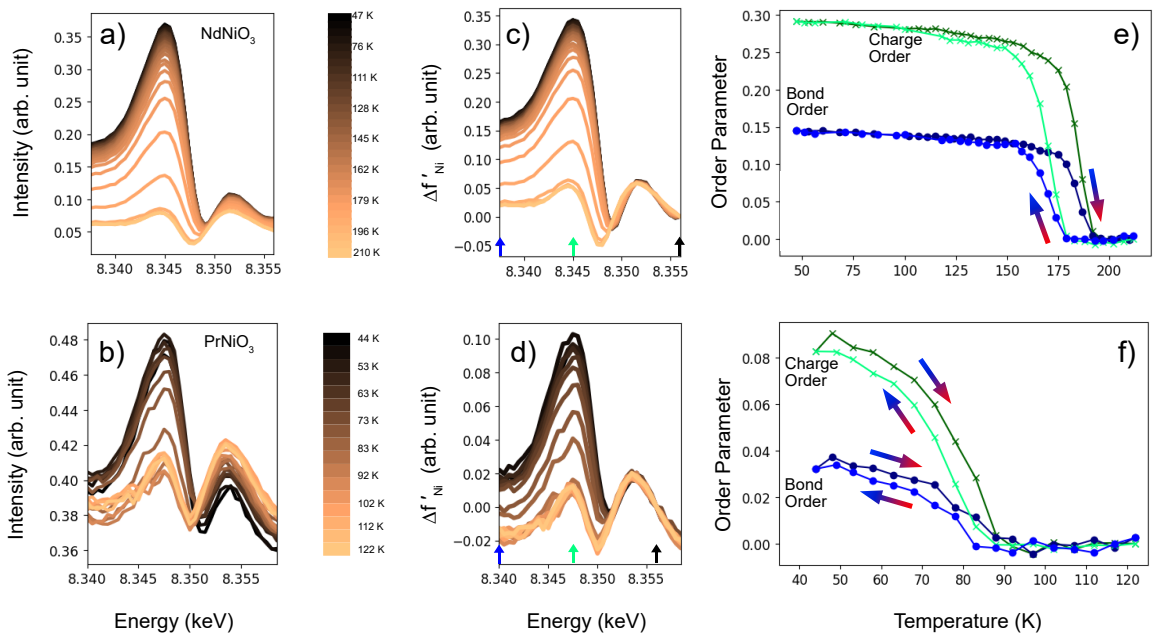

Figure 3.10: **Experimental result extracting bond order and charge order evolution with temperature** The top row is for $NdNiO_3$ and the bottom row is for $PrNiO_3$. The left-most columns show raw data. The middle columns show extracted $\Delta f'_{Ni}$ whereas the right-most column shows the extracted bond order and charge order for both warming and cooling cycle

plotted the charge order strength to the bond order strength of respective systems in Fig 3.11.

We first note the linear relationship observed by the bond and charge order indicating strong electron-lattice coupling as suggested by and observed by in $NdNiO_3$-NAO superlattice. Both $NdNiO_3$ and $PrNiO_3$ show the linear dependence although the proportionality constant is slightly larger for $PrNiO_3$. In the view of the model laid out by [18] this could mean a lower coupling between electron and lattice. For a more itinerant d-electron system of $PrNiO_3$ it is expected to have lower electron-lattice coupling. However, our results indicate that even though it is weaker in amplitude than $NdNiO_3$ charge order, it still follows a linear relationship with the bond order.

Secondly, we have extracted the critical exponent of the phase transition shown in figure 3.12. We did a time scan, i.e. we parked the detector on the (011) peak and let the temperature

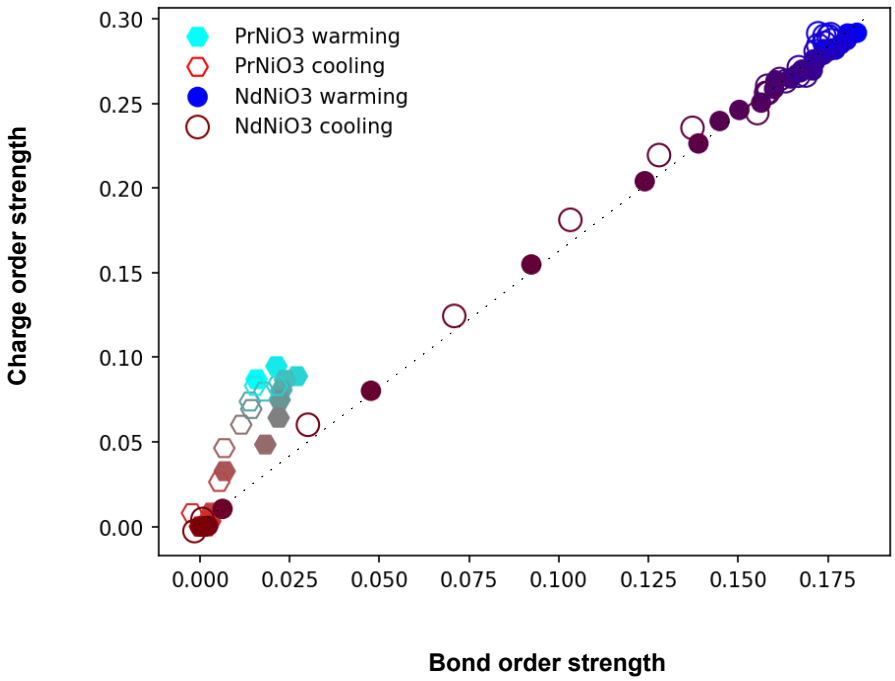

Figure 3.11: Bond order and charge order parameter co-dependence: for both $NdNiO_3$ and $PrNiO_3$ we observe a linear relationship between the bond order and the charge order extracted

rise. We made sure that our region of interest in the area detector captured the peak. The thin films were large enough to ensure that the cryostat expansion during this measurement did not alter the sample-beam intersection. For a first-order phase transition, the critical exponent can be related to the percolation of the nucleating phase. We subtracted the high-temperature intensity ($Intensity(T_{High})$, where T_{High} is well above the transition temperature) from the raw counts and then fit the result to the expression $(1-\frac{T}{T_C})^{2\beta}$ to extract both T_c and β. The β also differ significantly between $NdNiO_3$ and $PrNiO_3$. This may indicate that the phase texture evolution in $NdniO_3$ is different than $PrNiO_3$.

Thus, from this discussion, we conclude that $NdNiO_3$ hosts a stronger electron-lattice coupling and thus electronic behavior can be tuned if we can tune the lattice. Thus, $NdNiO_3$ is an immediate choice for strain tuning via helium implantation. In the case of $PrNiO_3$, this is

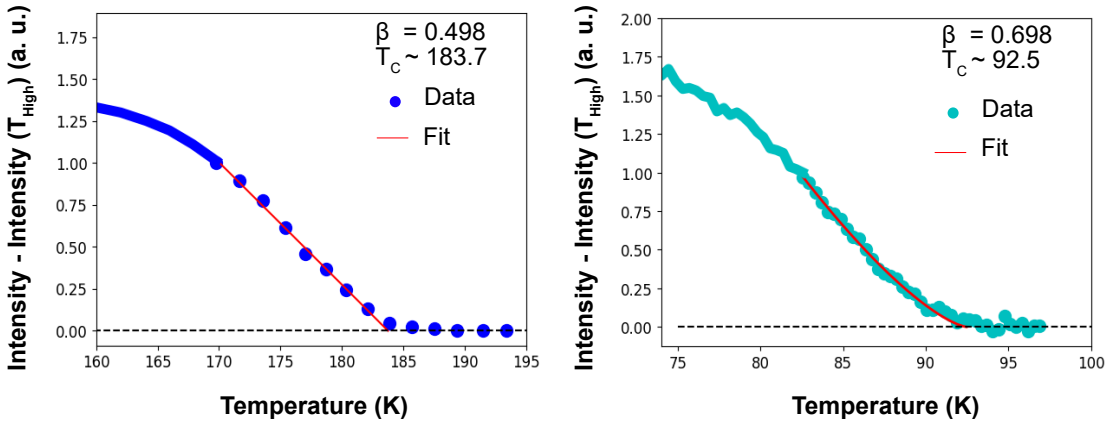

Figure 3.12: Critical exponent of the phase transition: (left) $NdNiO_3$ (right) $PrNiO_3$

complicated and will be harder to control since a small bond order change resulted in a relatively stronger charge order change. This may indicate other mechanisms such as a Pierels instability arising from spin density wave in an orthogonal symmetry are at play. We speculate that such a mechanism is on top of the site-selective Mott transition causing the increased charge order observation. With this insight, we move to the next section where we highlight soft X-ray scattering investigations done on these samples.

3.4.2 Antiferromagnetism:

Both of our $NdNiO_3$ and $PrNiO_3$ films transition into a low-temperature non-colinear antiferromagnetic phase with an ordering vector of $(\frac{1}{2}, 0, \frac{1}{2})$, consistent with the phase diagram (figure 3.13). To characterize the magnetic phase and subsequently compare the two magnetic phases between $NdNiO_3$ and $PrNiO_3$ we conducted soft X-ray resonant scattering. In this case soft X-ray energy was tuned to the Ni-L3 edge. Soft X-ray magnetic scattering was carried out in a Kappa-diffractometer of 29-ID-C beamline of Advanced Photon Source of Argonne National Lab. Kappa-diffractometer can be directly mapped into a four-circle diffractometer with

constraints. On these thin films, we have also performed soft X-ray absorption spectroscopy in total electron yield mode for Ni-L3 and O-K edges towards a complementary understanding of the electronic structure in the beamline of 4.0.2 in Advanced Light Source of Lawrence Berkeley National Lab.

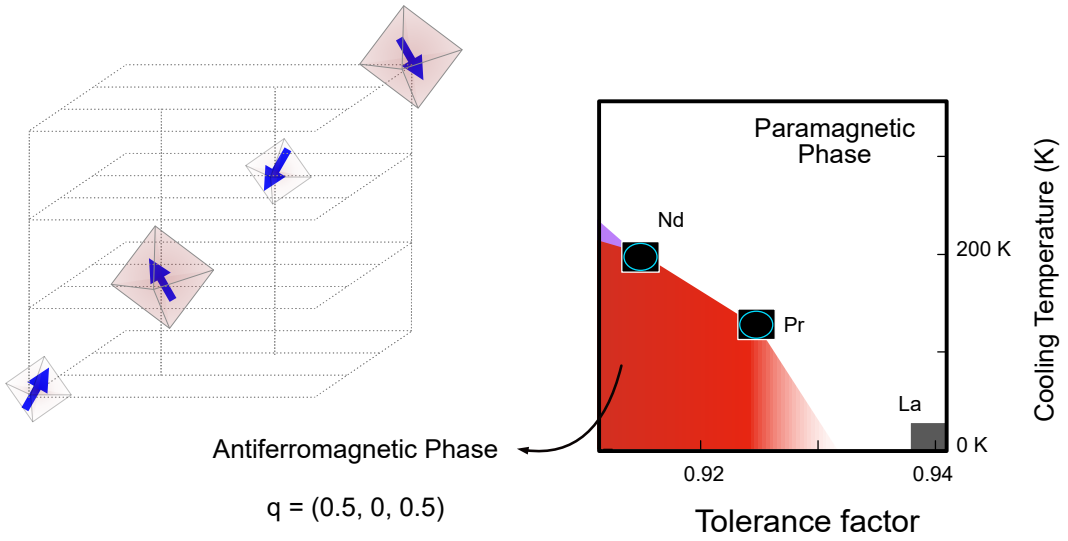

Figure 3.13: Schematic of the phase diagram and the low-temperature antiferromagnetic phase with a spiral structure

An antiferromagnetic order such as the one observed in nickelates can be characterized by (i) the temperature dependence of the magnetic order parameter, *m* (ii) the correlation length of the order (iii) the energy dependence of the magnetic order, and (iv) its magnetic moment orientation. Here we have explored the first three for all of our films. Before we discuss the results, let us first go through the experiment methodology.

This begins by finding the in-plane orientation of the substrate. First, we figured out the (001) direction from finding the (221) peak. Usually one of the edges of the as-bought substrate is parallel to the (001) direction. Then, we remounted the thin film in the diffractometer with $(1\bar{1}0$ in the scattering plane. Next, we resolved $(\bar{1}10)$ from $1\bar{1}0$ by finding the (240) and (420) respectively. Now that we have confirmed the orientation we took the samples to the Kappa

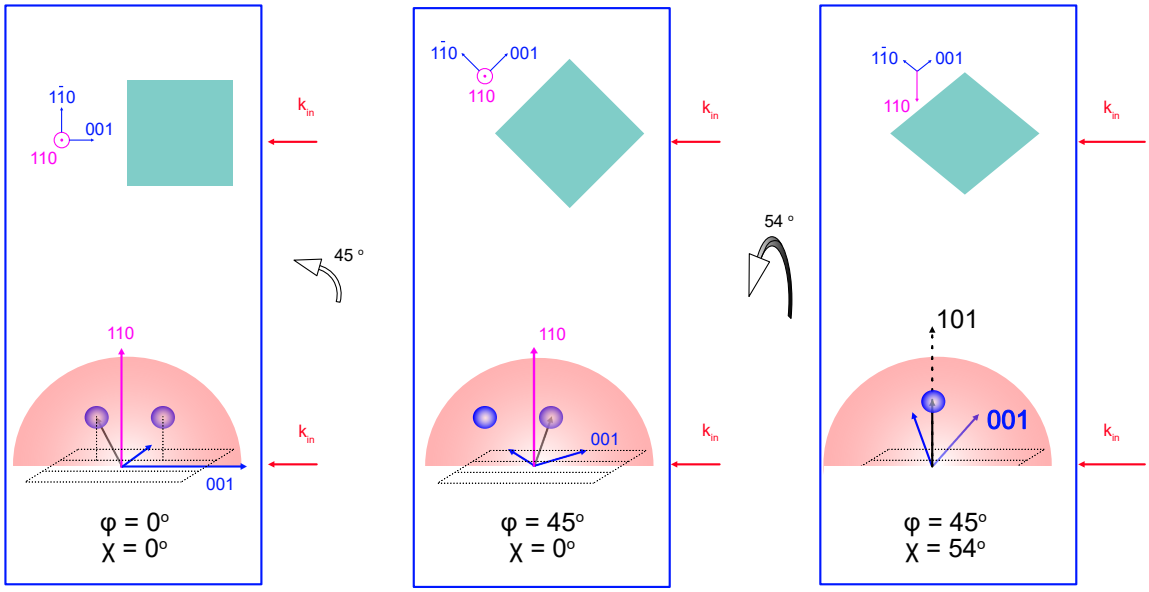

Figure 3.14: Experimental method to do the resonant scattering experiment: each step from left to right shows how the sample is rotated in real space (top row) and as a result how the peaks in the reciprocal space get oriented with respect to the scattering plane. After the last column we change 2th to 110° and theta to 55° to observe the magnetic peak

diffractometer in 29-ID-C. Finally, we mounted them with (001) pointed towards the beam at th = 0°, and sample normal pointed towards 2th = 90° detector position. At low temperature and Ni-L3 resonance with phi rotated by 45° and chi by 54° we could see the magnetic peak on our detector. This is schematically shown in figure 3.14. Note, after the ϕ rotation a $-54°$ of χ rotation would not have brought any one of the magnetic peaks into the scattering plane. The Kappa diffractometer had chi and phi-motor equivalent motion, otherwise, the standard practice is to make a wedge of 54° and mount the sample phi-rotated by 45°. This way at the resonance condition the magnetic peak is found in symmetric mode at 2th = 110°. We should mention that apart from this symmetric mode there can be many asymmetric ways ($th \neq 2th/2$) of finding the peak. However, we stick to this mode for simplicity from the geometrical consideration of the Kappa diffractometer.

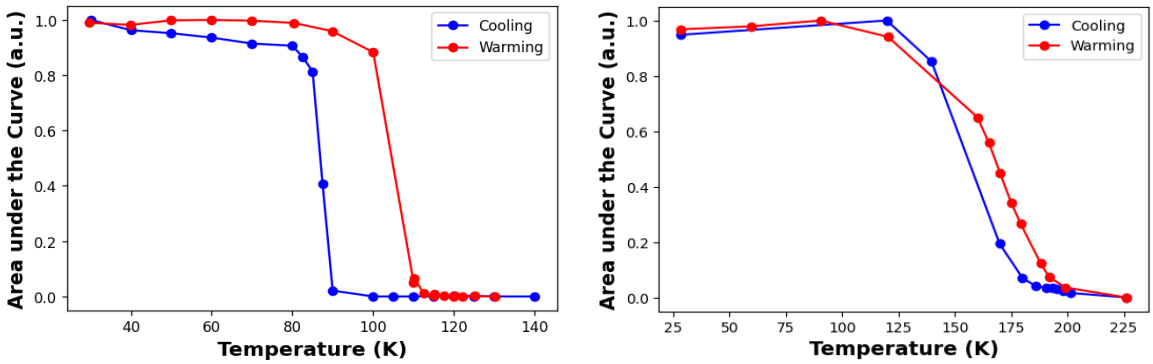

Figure 3.15: **Antiferromagnetic order evolution with temperature** in (left)$PrNiO_3$ and $NdNiO_3$: Both transition shows a first order nature with clear hysteresis loop.

Result and Discussion: Once we found the magnetic peak, we measured the temperature dependence by taking rocking curve scans after aligning to the peak at each temperature. We used a Si diode detector with an angular span of 3°. The response was measured by an Ammeter connected to the diode. For every scan, we evaluated the area under the curve after subtracting the background and fitting the signal with a Gaussian peak. The result of the measurement is shown in figure 3.16. Consistent with the metal-insulator transition and bond order-charge order transition the coupled antiferromagnetic transition also occurs around 90K for $PrNiO_3$ and around 210K for $NdNiO_3$. The correlation length for $NdNiO_3$ is significantly larger than the correlation length of $PrNiO_3$ indicating a more rigid antiferromagnetic phase. The correlation length was observed to be 45nm for $NdNiO_3$ and 29nm for $PrNiO_3$. The observed antiferromagnetic correlation length is similar to studies conducted elsewhere.

Energy response of the magnetic peak: Next, we turn our attention to the spectroscopic information that we harnessed from the samples. First, let's discuss the energy dependence of the magnetic peak. Similar to the measurement done at the Ni-K edge, here we also varied the energy while the diffractometer was set at the momentum transfer condition $\mathbf{q} = (\frac{1}{2}, 0, \frac{1}{2})$. In other words, for every energy we re-oriented our diffractometer to match the diffraction condition

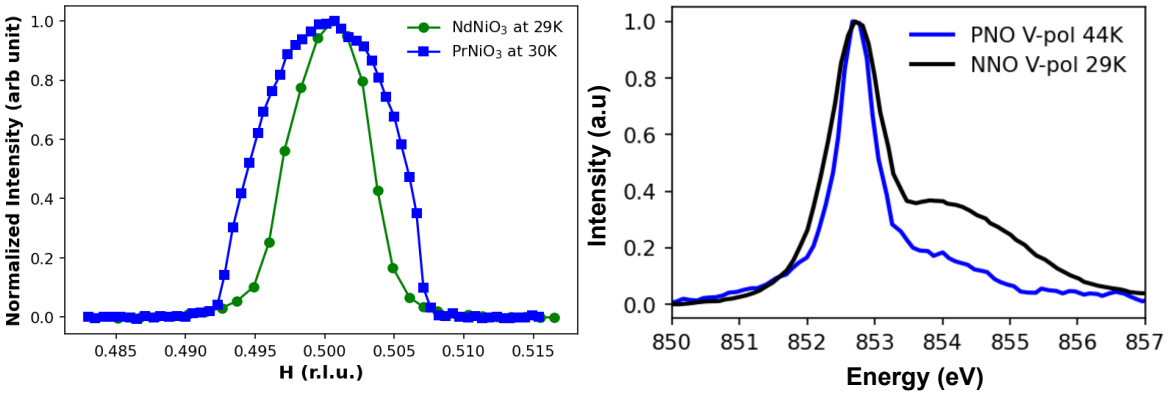

Figure 3.16: **Magnetic order characterization:** (left) rocking curve scans on the peak projected onto the H axis is used to extract the correlation length. (right) fixed-q energy scan on the magnetic peak

for the magnetic Bragg peak for the given energy. The energy dependence revealed a clear Ni-L3 resonance as shown. Moreover, on closer inspection, we see that the energy dependence shows a two-peak structure. We fit the energy dependence with a large Lorentzian (peak A) and a small Gaussian peak (peak B). In the table below we summarize the characterization of the magnetic peaks for both films. Neel temperature is mentioned for the cooling cycle. The correlation length mentioned is along the $q_\perp$ direction.

Table 3.4: Characterization of the magnetic order

Thin film	along $q_\perp$ Correlation Length (nm)	cooling Neel Temp (K)	$E_B - E_A$ (eV)	Amplitude ratio (B:A)
$PrNiO_3$	29	90	1.4	0.09
$NdNiO_3$	45	210	1.7	0.2

Authors in have thoroughly discussed the response of the magnetic peak energy dependence as a function of the bond distortion. It has been suggested from the calculations that the two peak structure primarily comes from the two different sites where the bond disproportionation drives the effective spin moment on each octahedron. The long bond sites create an effective spin moment close to $S = 1$ whereas the short bond sites host an effective spin moment close to $S = 0$.

With an increased bond distortion, the short bond site contributes most to the second peak (peak B) and the long bond to the lower energy peak (peak A). The effect of decreasing bond order is manifested by the short bond peak moving to a lower energy and the long bond peak moving to a higher energy resulting in a decrease in the peak separation. For lower bond order in $PrNiO_3$, we also observe a decrease in the peak separation. The peak amplitude ratio also decreases in the case for $PrNiO_3$ where it is worth noting that we are using vertical polarization to compare the energy dependence. A difference in spin orientation will lead to a decrease in intensity for a given incoming polarization on a given geometry of scattering. This is probably a remnant of what was previously observed.

X-ray absorption spectroscopy: Finally, we explore X-ray absorption spectroscopy collected from the samples in Total Electron Yield (TEY) mode with the energy of the incoming beam around Ni L-edge and O K-edge and a resolution of 100meV. We alternated the polarization between Horizontal and Vertical polarization for each measurement at a given temperature. In the grazing incidence with an angle of 20 deg the horizontal polarization was mostly perpendicular to the surface of the film while the vertical polarization was entirely in-plane. We measured the ground current and normalized it to a mesh current collected just before the beam entered the chamber. The measured data after background subtraction and averaged over polarization are shown in figure 3.17 where we discuss the difference in absorption spectra at those edges between $PrNiO_3$ and $NdNiO_3$ well above and well below the transition temperature.

In the absorption spectra of O-K edge ($1s \rightarrow 2p$), we focus on the pre-peak structure centered around 527.8 eV. The area of the peak is associated with oxygen projected $3d^8\underline{L}$ states and thus an indicator of the Ni-O covalency [19, 1]. With decreasing rare earth atom size and decreasing tolerance factor (La $\rightarrow$ Lu) the Ni-O-Ni angle decreases from 180°, and so does this peak. Furthermore, it was reported that as $NdNiO_3$ and $PrNiO_3$ undergo the metal-insulator transition the peak area decreases on the high energy side of the peak [19]. The metallic state of $PrNiO_3$ has slightly more Ni-O covalent character than $NdNiO_3$ metallic phase. For both $NdNiO_3$

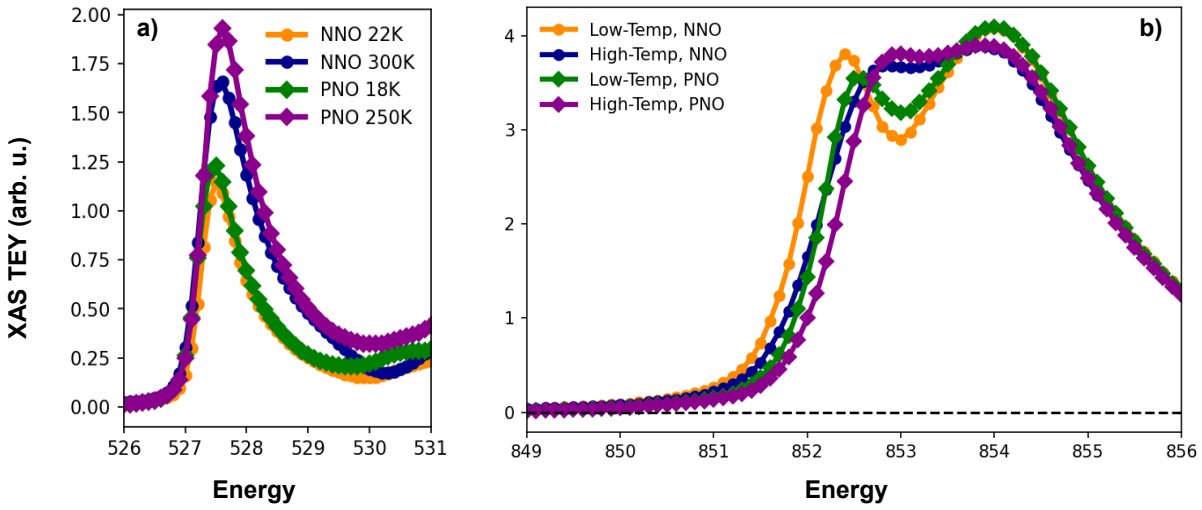

Figure 3.17: **X-ray absorption spectroscopy(XAS) in total electron yield (TEY) mode:** (left) O-K edge pre-peak, and (right) Ni-L3 edge for $NdNiO_3$ (NNO) and $PrNiO_3$(PNO) for above and below the transition temperature(T_{MIT})

and $PrNiO_3$, we observe that the pre-peak area under the curve in the insulating state decreases to almost 60% of its high-temperature value. This is interesting since the bond order and charge order in $PrNiO_3$ is much less than that of $NdNiO_3$. This may indicate that the change in the spectral weight during the phase transition in nickelates is independent of the bond order strength.

On the other hand, the Ni edge spectra are consistent with the interpretation that bond order plays a significant role in changing the electronic environment. The primary feature of the spectroscopy data from a nickel L3 edge($2p \rightarrow 3d$) is that it shows a clear two-peak structure. The peaks are less separated at high temperatures but they appear significantly discernible at low temperature insulating state of the sample. We have tabulated the salient features of the Ni-L3 edge in table 3.5 after fitting two peaks to the structure. We fit the spectra in the range 851, 855 two Gaussians. Since X-ray absorption spectroscopy is a surface-sensitive technique we are also sensitive to the dirt that the sample has on the surface and which contributes to the background of the measurement.

From the table, we focus on the parameters ΔE, $A : B$, and the width of each peak which

Table 3.5: Ni-L3 edge characteristics in nickelates thin films: $E_{A(B)}$ - center of the A(B) peak, $\Delta E = E_B - E_A$, $A : B$ = E_A/E_B, $FWHM_{A(B)}$ = full-width at half maximum of peak A(B)

attributes	$NdNiO_3$ 22 K	$NdNiO_3$ 300 K	$PrNiO_3$ 18 K	$PrNiO_3$ 250 K
E_A	852.3	852.6	852.5	852.7
E_B	854.0	853.9	854.0	854.0
ΔE	1.7	1.3	1.5	1.2
$A : B$	0.65	0.35	0.47	0.37
$FWHM_A$	0.8	1.0	0.8	0.9
$FWHM_B$	2.4	2.8	2.6	2.6

are independent of the beamline calibration and background subtraction. To carry out the analysis and subsequent interpretation of data we follow the work by Disa *et. al.* [20]. They have similarly characterized the data and found qualitative agreement through charge-transfer multiplet modeling. However, it should be noted that the charge transfer multiplet effects can not cover the peak broadening effects entirely[19]. As the authors noted the splitting of the Ni-L3 XAS can be directly related to the charge transfer energy between the O-2p and Ni-3d orbitals. A charge transfer energy as discussed before relates to the increase of an electron at Ni-e_g orbitals from O-p orbitals and drives the central physics of the nickelates. This creates a ligand hole ($\underline{L}$ in the ligand orbital which remains covalently shared with the Ni-orbital it overlaps with. Such a situation can be interpreted similarly to the Zhang-Rice singlet states in the cuprates and responsible for the conductivity.

If the charge transfer energy is increased it becomes easier for the system to remain covalent. The effect is evidenced by the peak splitting between the two peaks of the Ni-L3 XAS. We name them as *A* peak(852.7 eV) and *B* peak (at 854 eV). In the metallic state, the

two peaks considerably overlap indicating a high covalent state of the NiO_6 octahedra. We further note from our extracted value that not only does the peak separation increase but also the A-peak becomes comparatively sharper as the respective nickelates undergo the metal-insulator transition. We can interpret this result from the site-selective Mott transition picture where two neighboring octahedra assume a short bond and a long bond structure. This in turn influences the electronic character from $3d^8\underline{L} + 3d^8\underline{L} \rightarrow 3d^8 + 3d^8\underline{L^2}$. Thus, a decrease in covalency increases the energy separation between the two features corresponding to the two states and makes a more prominent$3d^8$ state observed as the A-peak in our XAS spectra. The increased separation in $NdNiO_3$ can be attributed to the increased bond order observed in this material which will enforce more decrease in covalent component.

Thus, it is clear from our measurement that the effect of bond order is to decrease the covalency of the NiO_6 octahedra. This is evidenced by the loss of high energy spectra in the O-K edge XAS pre-peak and the increased splitting in Ni-L3 edge XAS. In the L2 edge, a similar low-energy shoulder is observed to be formed due to the metal-insulator transition, in line with the L3 edge. However, since the L2 edge is significantly weaker than the L3 edge we show the L3 edge here for characterization. Furthermore, the change in the electronic configuration may not be discrete and is more continuously tunable as evidenced by the low-temperature XAS ΔE between $NdNiO_3$ and $PrNiO_3$. Furthermore, we note the remarkable similarity between the peak separation of the magnetic peak energy response and the X-ray absorption spectroscopy. We consider that such similarity is a first hint that the effective spin moments of the two Ni sites depend on the bond order[21]. Following Hund's rule, for the $3d^8$ and $3d^8\underline{L^2}$ states the expected moment are $S = 1$ and $S = 0$ respectively. Hence the ligand holes antiferromagnetically couple with the Ni-holes. As the bond order tunes the covalency of the Ni-O continuously so does the effective spin moment change continuously from a $(\frac{1}{2}, \frac{1}{2})$ configuration to $(0, 1)$ in the short-bond and long-bond sites. A gradual tuning from $3d^8$ configuration may result in intermediate spin configurations where the moments are somewhere in between.

Thus, we have explored the charge order, bond order, and magnetic order in rare earth nickelate materials where the phase transitions are maximally coupled. We find that the magnetic order in $NdNiO_3$ has a longer correlation length compared to $PrNiO_3$. In the energy response of the magnetic peak, we observed the influence of bond order further providing evidence for a lower bond order in $PrNiO_3$.

3.5 Results: Tuning the phase transition with He implantation

In this section, we will discuss the effect of helium implantation on the nickelate thin films. Strong electron-lattice coupling in the nickelates was clearly evidenced in the previous section where a decreased bond order in $PrNiO_3$ compared to $NdNiO_3$ resulted in observing slightly different energy response from the total electron yield data of the X-ray absorption spectroscopy and the fixed-q energy scans of the magnetic order. Since both of these systems show more or less similar characteristics we study them both under helium implantation. Helium implantation is expected to change the out-of-plane lattice parameter in the thin film and through this strong lattice-electron coupling we expect to see a change in the electronic configuration and its temperature response. To the best of our knowledge, there has not been a study on nickelates exploring the effect of the uniaxial strain. We will see that indeed the helium implantation suppresses the coupled phase transition gradually.

3.5.1 Uniform helium irradiation in $NdNiO_3$:

To study this we have identically grown epitaxial thin films of $NdNiO_3$ on 110-oriented $NdGaO_3$ similar to the one discussed above. Then we uniformly irradiated the thin films with helium ions of 90 keV energy. The energy was set to make sure that the ion completely penetrates the thin film and gets implanted deep into the substrate. We exposed different films to different degree of helium ion dose or fluence: 0, 1, 4, 8. and 30 ions per sq. cm. (IPSC) For comparison,

we need at least 10^{17} ions per sq cm to create dislocations and damages. Thus, in this limit, the helium will be simply implanted into the substrate.

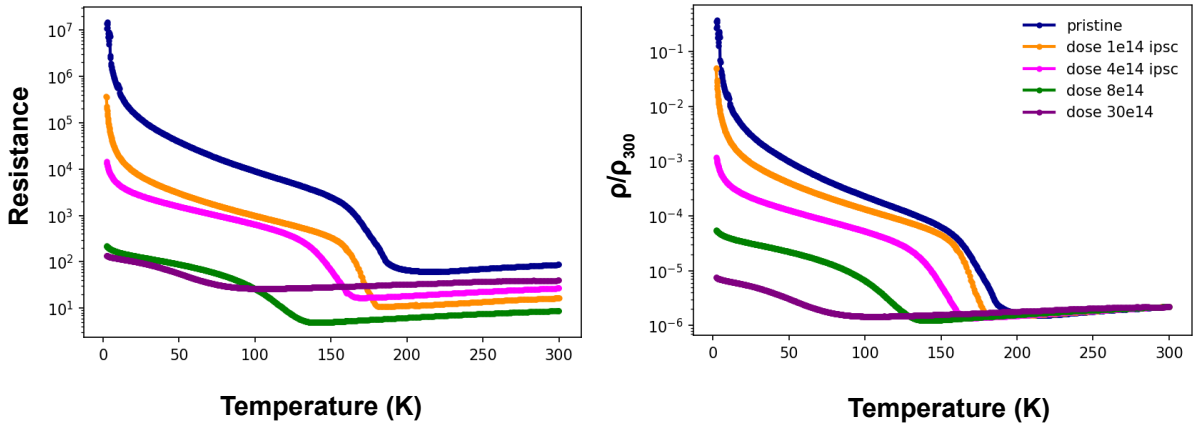

Figure 3.18: **Tuning metal-insulator transition in $NdNiO_3$ films:** Four point Van der Pauw measurement on the helium implanted thin films show a gradual suppression of metal-insulator transition. (left) as measured resistance in units of Ω shows the room temperature resistance drops for the first 4 doses. (right) normalized resistivity with respect to the high temeperature shows the slope of the high temperture metallic state remains same for the first four doses.

Tuning of Metal-Insulator Transition:

The first important result is shown in figure 3.18 where the resistance and resistivity normalized by room temperature resistivity is plotted for the sample temperature when the sample was warmed from 2K to 300K. We measured the transport following the same methodology as the pristine sample discussed above. A gradual lowering of T_{IMT} is observed from the transport data. We note that the slope of the metallic state remains indifferent to increasing helium dose. Also, initially, the raw resistance value at room temperature decreases with increasing dose up to 8e14 IPSC indicating a tuning of the conductivity without introducing defects. Probably we introduce some structural defects with a dose of 30e14 IPSC where the room temperature resustance is observed to go up.

In the table below we have listed the transition temperature for the cooling cycle and the warming cycle along with the width of the hysteresis loop for comparison.

Table 3.6: Transition temperatures as extracted from transport measurements

samples ‘	T_{MIT}	T_{IMT}	width (ΔT)
pristine NNO 17	215	225	20
dose 1e14 NNO 13	155	180	15
dose 4e14 NNO 12	145	170	15
dose 8e14 NNO 11	120	140	15
dose 30e14 NNO 10	100	100	5

We see that the width of the hysteresis loop also remains the same up to 8e14 IPSC. Thus, even with helium implantation, the phase transition remains first order. At the dose of 30e14 IPSC even though the loop width severely decreases we can still see a clear separation of the warming and cooling trajectories.

Structural Order: We investigated the structure of the helium-implanted thin films before and after the helium implantation. Identically grown samples of $NdNiO_3$ hosted identical structures, to begin with. We also used the substrates of the same batch to ensure defect density in the substrate is also roughly similar among the samples. The effect of the helium implantation is similar to the ones reported To characterize the structure we carried out X-ray diffraction on the helium implanted samples using our lab X-ray four circle diffractometer (make Huber) with Cu-K source. The results are shown in figure 3.19

X-ray diffraction: Here we are showing the reciprocal space map of the peak (221) in HHL plane spanned by the sample normal direction of (HH0) and in-plane direction of (00L). We aligned the substrate peak with the lattice parameters of the pristine sample. The doses increase from left to right. The primary observation is that the thin film peak decreases its HH position without changing the L value as the dose increases. We interpret this as the out-of-plane d-spacing change while the thin film remains epitaxial. Also, note that the main substrate peak doesn't change its position in line with our choice of lattice parameters. Thus, the thin film remains

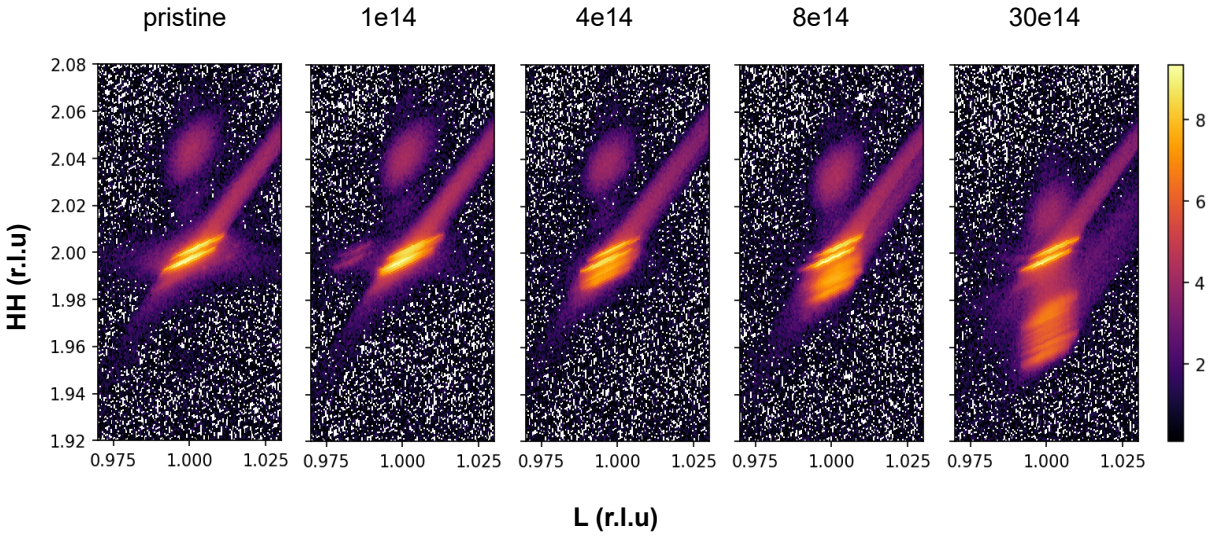

Figure 3.19: **X-ray diffraciton on the (2 2 1) peak of the substrate and the thin film:** The thin film peak continually decreases in out of plane direction (HH) but remains unchanged in the in-plane direction (L). On the other hand apart from the main substrate peak a distortion peak emerges correlated with increasing helium implantation dose. The doses are marked on top of each panel in units of ions.cm^{-2}

epitaxial in the in-plane directions but changes considerably in the out-of-plane direction. Thus, we are applying a uni-axial strain along (1 1 0) direction.

Furthermore, we note that a new 'distortion' peak shows up below the substrate peak. With increasing dose this peak gains intensity and sinks lower in HH value while also remaining fixed to the L value. *Other references have also reported this*. The helium-implanted layer of the substrate possibly contributes to this intensity while the deep pristine substrate layer remains untouched by the incoming helium from the top, which contributes to the intensity of the original pristine substrate peak position. Since with Cu-K$_\alpha$, our penetration is much higher we see both of them. To test this hypothesis we do a depth resolve X-ray diffraction on 4e14 IPSC implanted thin film.

Depth resolved X-ray diffraction: The penetration depth of X-rays in the material depends on the energy, angle of incidence, and composition of the material. For a given material increasing the energy increases the penetration depth. We did a longitudinal scan (th2th scan)

on the specular peaks. Both (110) and (220) are symmetry-allowed peaks for the substrate. On the left panel, the data is taken in a soft X-ray chamber of 29-ID beamline of the Advanced Photon Source (APS) whereas the data on the right is collected from a hard X-ray scattering setup at beamline 17-2 of the Stanford Synchrotron Radiation Lightsource (SSRL). Increasing energy increases the penetration depth in general. We evaluated the exact penetration depth for the incidence angles as 350 nm, 440nm, 620 nm and 2125 nm from the online database for the energies 1700 eV, 2000 eV, 2500 eV, and 8500 eV, respectively.

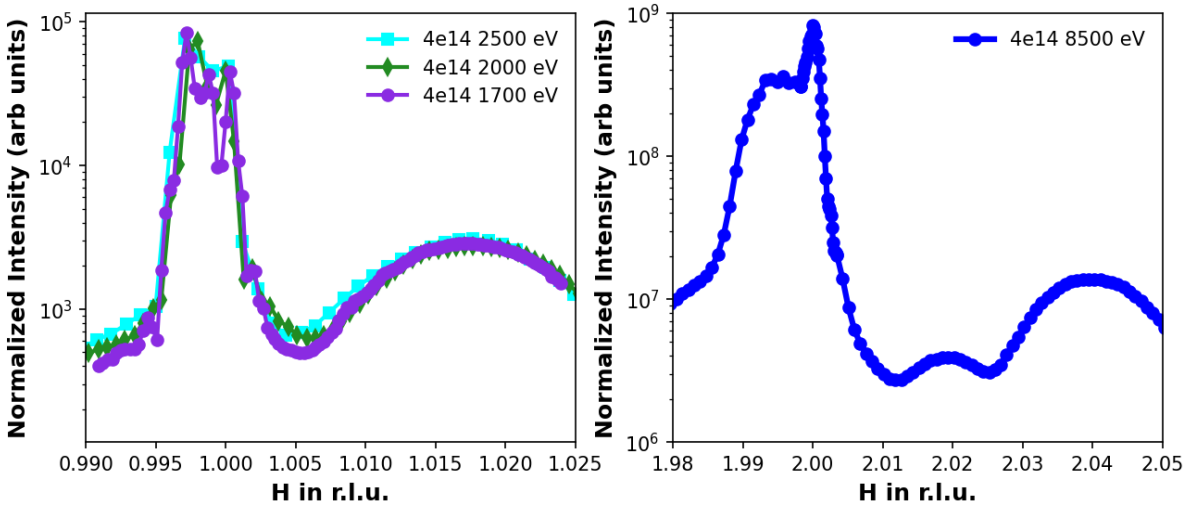

Figure 3.20: **Depth resolved X-ray diffraction on the specular peaks** (left)data taken in beamline 29-ID of the APS on the (110) peak of the substrate (right) data taken in the beamline 17-2 of the SSRL on the (220) peak of the substrate. In both scans the film peak is also visible

Here we show that as we increased the penetration depth of the X-rays the amplitude ratio of the distortion peak to the untouched substrate peak decreased. This confirms the hypothesis we formed from the simulation of ion trajectory. Helium gets implanted near the top of the substrate and modulates the lattice parameters of that substrate layer. To evaluate the helium implanted region near the top surface we plot the ratio of the maximum of the distortion peak amplitude to the substrate peak amplitude which shows up at the integer location of the reciprocal lattice unit. The ratio is a direct measurement of the percentage of helium implanted substrate region to

the otherwise unaffected substrate regions. The ratio decreases linearly indicating an increase in unaffected substrate percentage as we go deeper. Furthermore, the ratio is approximately 1 about the penetration of 1250nm. To a linear approximation, then the top 600nm of the substrate hosts the implanted helium. Our depth-dependent measurement doesn't exclude the thin film as a host to the helium. However, it is less likely for a high-energy 90 keV helium to be stopped within the overlayer following our discussion in Sec 3.2.

Our result from the depth-dependent measurement of the depth of helium implantation matches the simulation estimate as well. Since only a thin layer suffers from the helium implantation the in-plane lattice parameters are kept intact by the rest of the bulk substrate. Moreover, the depth-dependent XRD already shows that the helium implantation effect is inhomogeneous. As the 1700eV X-ray probes $\sim$350 nm of the top part of the sample which is well below the range of helium implantation depth, it still records a measurement from the pristine contribution apart from the distortion peak. We will explore the inhomogeneity further.

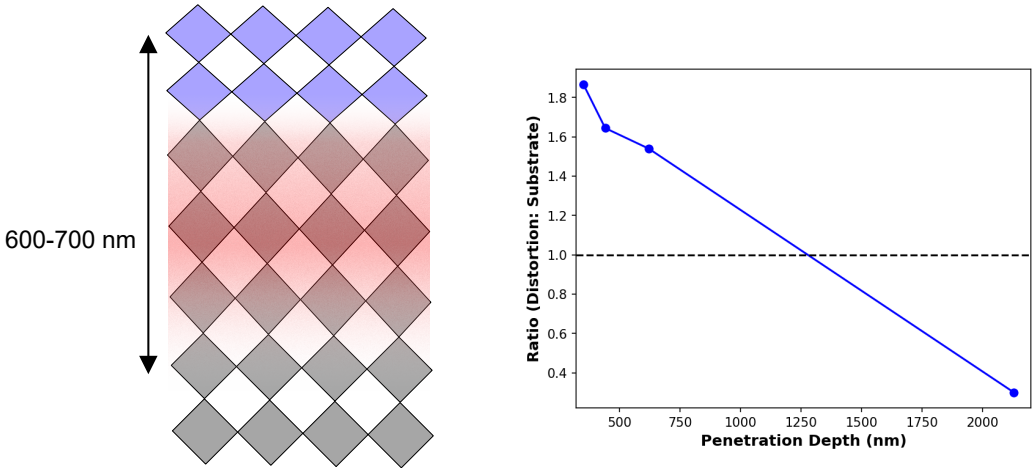

Figure 3.21: **Schematic of structural changes brought about by helium Implantation:** (left) a concentrated helium layer is found near the top 600-700nm surface of the substrate. From the depth-resolved measurements the ratio of distortion peak to substrate peak for different probing energy is plotted to find a linear relationship. Where the ratio is 1, half of the scattering volume will correspond to the implanted layer.

We have seen so far that the helium gets implanted into the substrate approximately down to 600nm from the surface however, the epitaxial relationship remains unperturbed. Thus, under the tensile strain, we expect the distortion in the substrate layer will only change the lattice parameter a and γ. In this case, the d-spacing increases so γ must decrease. The bending distortion to change γ will propagate along the strain direction into the thin film layer due to the cooperative bending of the connected octahedra. As a result, there will be a subsequent decrease in the γ of the nickelate film resulting in a change in the d-spacing along the out-of-plane direction of (1 1 0). This is observed in the data as the film peak sinks lower in the reciprocal space maps with an increased dose of helium implantation. This is schematically shown in the following figure 3.22. We have shown only the lattice plane where the chemical pressure provided by the helium implantation is mostly adjusted by the co-operative bending and stretching of the octahedra. On the plane spanned by (110) and (001) a stress is managed by changing the c-axis lattice parameter. From the reciprocal space maps it is clear that the c-axis lattice parameter does not change.

To quantify the structural changes experienced by the thin films in this way we extract the out-of-plane d-spacing on the peak (220) similar to the previous section. Since the helium-implanted substrate layer and the film both remain epitaxial to the untouched substrate layer and under tensile stress we can use equation 3.1. The results are tabulated below and also in Fig :

We note that to accommodate the uniaxial strain the γ angle continuously decreases towards 90° whereas the lattice parameters a and b increase. This is schematically shown in Fig 3.22. To quantify the amount of uniaxial strain we assume the definition $strain = \frac{d'-d}{d} * 100$, where d' and d are the d-spacing along 220 for the implanted and bulk $NdNiO_3$, respectively. We summarize the change in lattice parameter and strain along the out-of-plane direction in the figure 3.23 below:

Thus we conclude on the following observations:

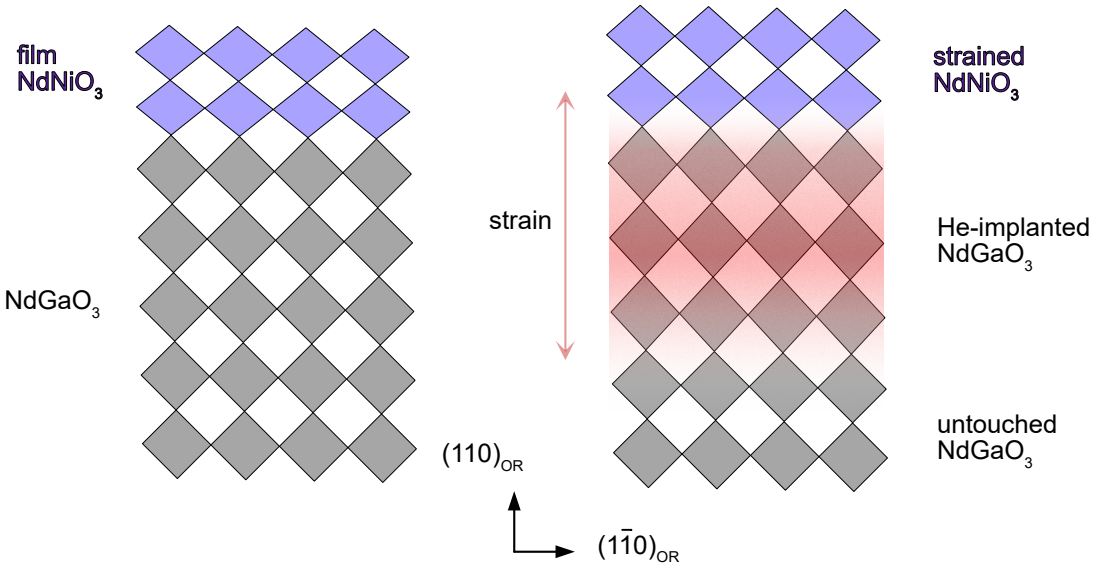

Figure 3.22: **Sub surface helium Implantation generates uniaxial strain:** The epitaxial relationship between the substrate and the film helps to propagate the uniaxial strain through cooperative bending of the corner shared octahedra across the interface

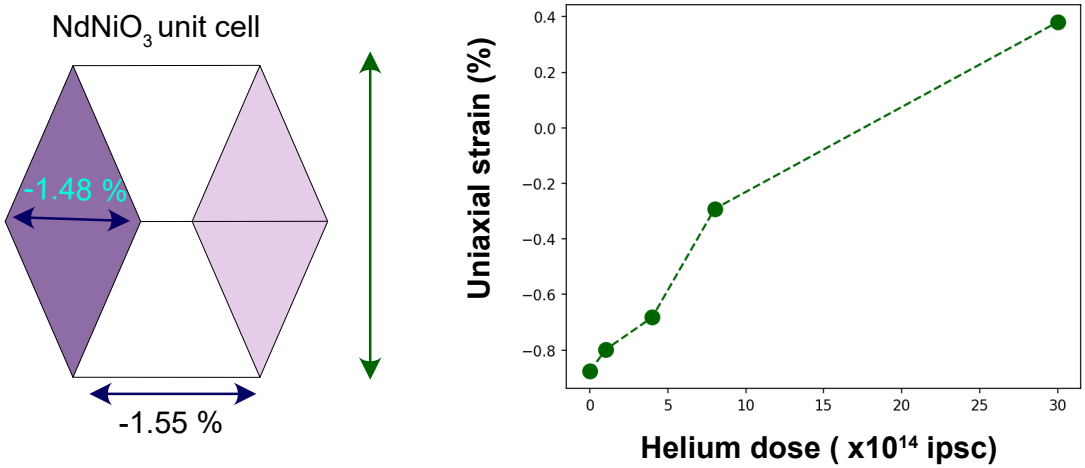

Figure 3.23: **Uniaxial strain tuning by helum implantation:** (left) a schematic of strain experienced by a $NdNiO_3$ unit cell. The uniaxial strain corresponding to the green arrow plotted on the right panel as a function of helium implantation. We observe a clear linear relationship.

Table 3.7: Tuning lattice parameters with helium implantation

attributes	pristine	1e14	4e14	8e14	30e14
2th (220)	48.16	48.12	48.06	47.86	47.52
a (Å)	5.402	5.404	5.407	5.418	5.436
b (Å)	5.402	5.404	5.407	5.418	5.436
c (Å)	7.73	7.73	7.73	7.73	7.73
$\alpha(^\circ)$	90	90	90	90	90
$\beta(^\circ)$	90	90	90	90	90
$\gamma(^\circ)$	91.36	91.31	91.25	91.02	90.64

- Helium implantation creates a distorted although epitaxially strained layer of the substrate
- Since this layer is in direct contact with our film it changes the strain environment for the film in the out of plane direction only
- To accommodate the change in the out-of-plane direction the lattice parameters of the $NdNiO_3$ film change. However, in this process, the unit cell volume doesn't remain conserved.
- The strain along the out-of-plane direction becomes increasingly compressive ultimately switching sign for the dose of 30e14 IPSC.

Bond Order and Charge Order: Since we tuned the strain environment and the lattice parameters an imminent curiosity is how it effects the bond order and consequently the charge order formation in the nickelates. A hint of decrease is expected from the lowering of the transition temperature and the low-temperature resistance of the insulating phase.

To follow up, we investigate bond order and charge order formation in helium implanted $NdniO_3$ using the methodology described in the previous section. We studied the same pristine and helium-implanted samples with doses of 1e14, 4e14, and 8e14 ions per sq cm(ipsc). Due to time contraint, we could not study the sample with helium dose of 30e14 ipsc. However, the data we gathered is sufficient to observe the trend due to the uniaxial strain modulation.

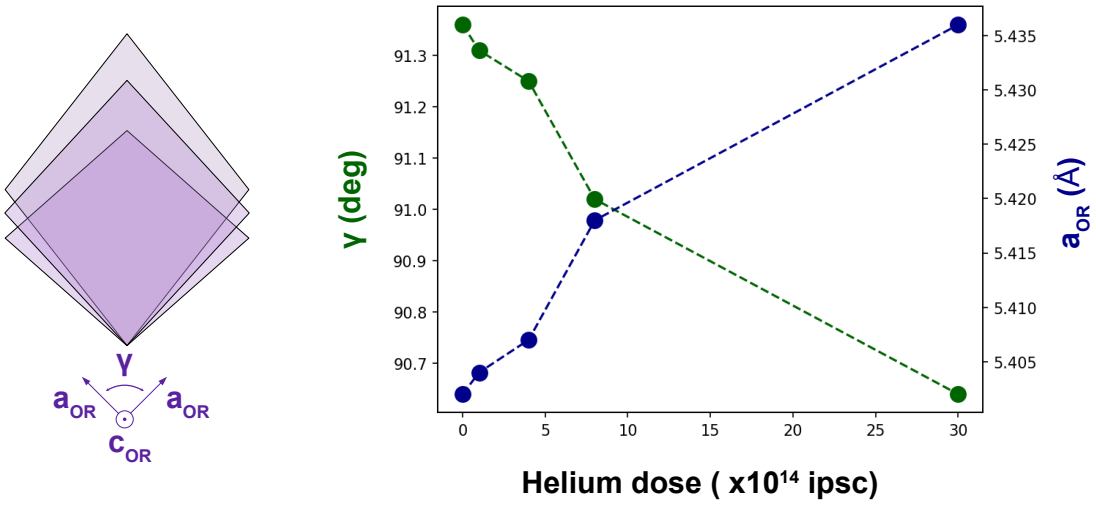

Figure 3.24: **Strain modulates the lattice parameter of $NdNiO_3$ film:**(left) a schematic of the effect of the uniaxial strain on the unit cell shape projected on the c lattice parameter. (right)The lattice parameters evolve continuously with increasing helium dose

We observe a continuous tuning of the transition temperature of the coupled bond order and charge order transition. The transition temperature decreases continuously. The strength of the bond order also follows a continuous trend with the only outlier of 4e14 IPSC. However, the strength of the charge order doesn't follow a continuous trend even though they decrease by 8e14 IPSC dose. We tabulated here the transition temperature measured from the warming of the samples along with the insulator-metal transition as observed from the transport data.

Table 3.8: Bond order transition temperature

samples	T_{BO}	T_{IMT}
pristine NNO 17	190	225
dose 1e14 NNO 13	175	180
dose 4e14 NNO 12	155	170
dose 8e14 NNO 11	120	140

The following figure 3.25 summarizes the entire dataset for the warming cycle on each sample under investigation. We note that the data for the sample implanted with 8e14 ipsc helium shows a sharp artifact around 8.35 keV and possibly due to multiple scattering from the sample.

We have collected the cooling cycle data as well which do not differ in general from the warming data, except it is shifted due to hysteresis. For clarity, we have only shown the warming cycle here.

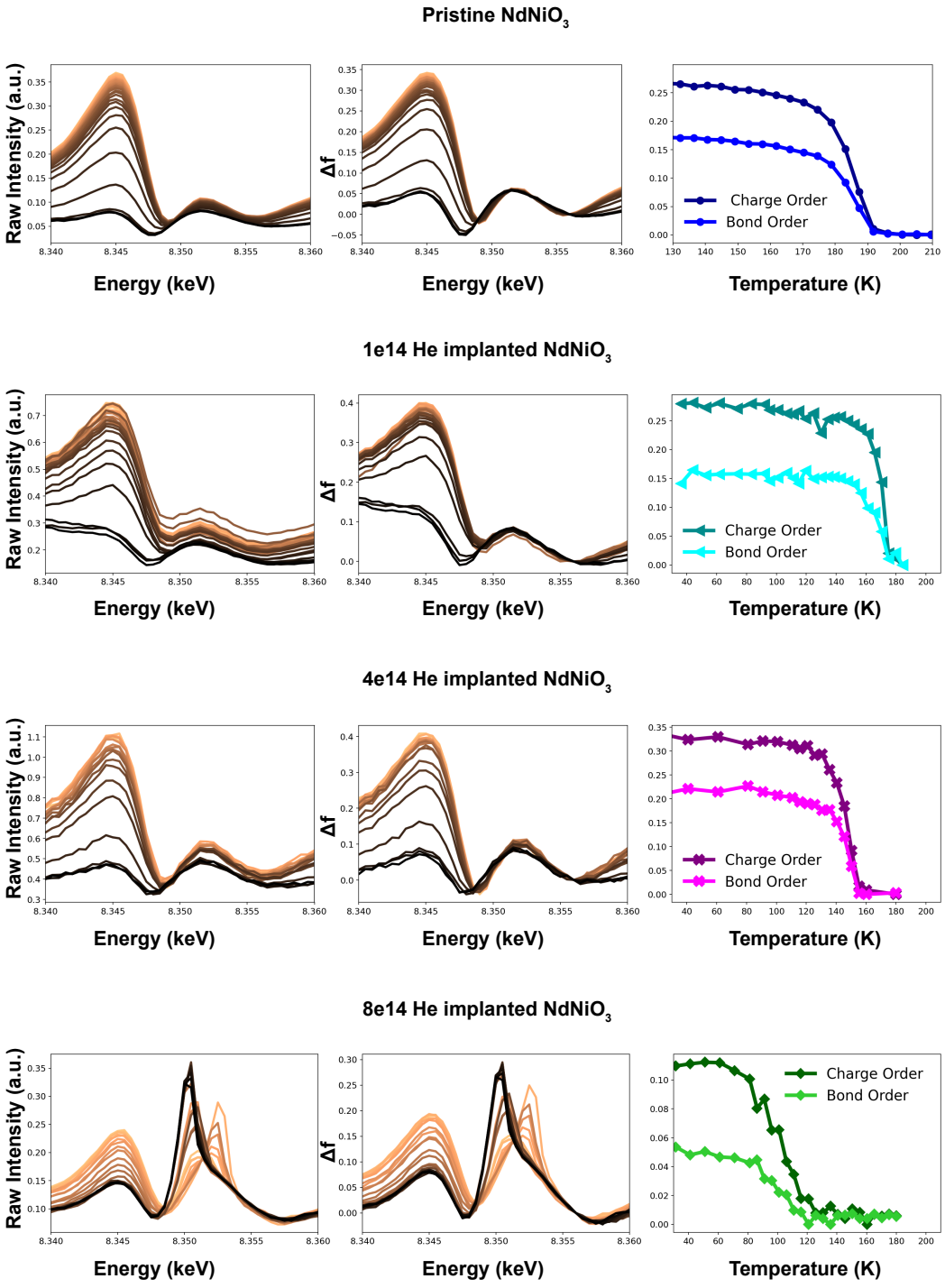

Figure 3.25: **Energy response of the bond order and the charge order and their interrelation:** we extracted the bond order and charge order from raw energy response of the $(011)_{OR}$ peak(left most panel) and extracted $\Delta f'$ (middle panel). The temperature evolution of the order parameters are plotted on the right most panel for damages 0,1,4, and 8e14 IPSC. Due to time limitation we could not measure 30e14 sample

We first note that the peak shape of the energy response doesn't change much at the low temperature. This could mean that the structure factor relationship between nearest neighbors giving rise to the observed energy modulation remains unchanged, except for their amplitude. The apparent decrease of separation between two peaks in the energy response of the 8e14 ipsc implanted sample is possibly due to the influence of the multiple scattering peaks and hence regarded as an artifact. Furthermore, we tested the linear relationship of bond order and charge order to test the strength of electron lattice coupling as a function of the strain we provided. We see that the linear relationship is well maintained down to the highest dose measured. Thus, we conclude that the strong electron-lattice coupling in $NdNiO_3$ also remains unperturbed by the uni-axial strain tuning due to helium implantation.

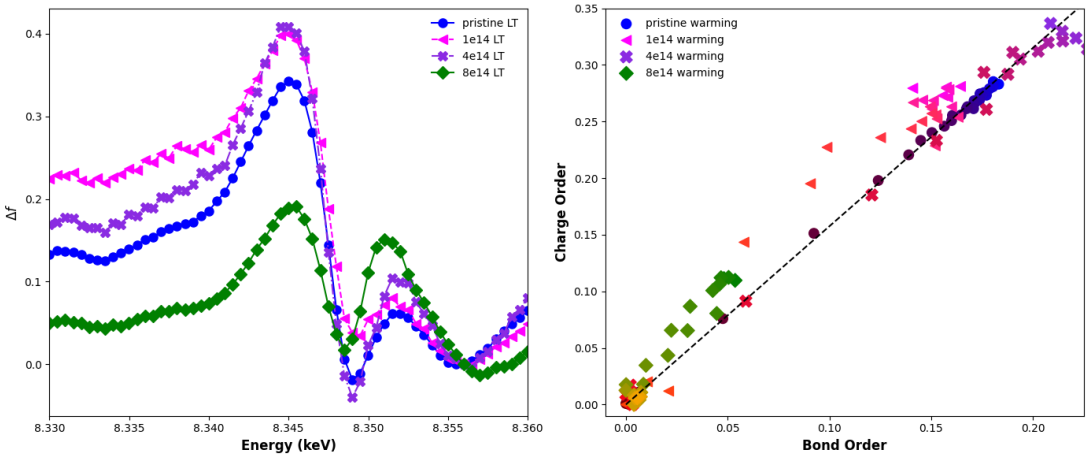

Figure 3.26: **Characteristics of the bond order and charge order** (left)energy response of the resonant contribution $\Delta f'(E)$ (right) bond order relative to the charge order for evolution for each temperature measured for the warming cycle shows the linear relatinship remains valid upto the highest dose investigated indicating that the strong electron lattice coupling is unperturbed

We followed the same energies to extract Δf from the raw data and subsequently evaluate charge order from it. We have also used the same energy to extract the bond order strength from the raw intensity. We note an overall decrease of bond order with increased uniaxial strain, except for the sample with dose 4e14 ipsc where both bond order strength and charge order strength

increase comparatively. This indicates an incoherent control over bond order by uniaxial strain manipulation. To illustrate this point, we have shown below the temperature evolution of the bond order and the charge order to the uniaxial strain calculated in the previous section.

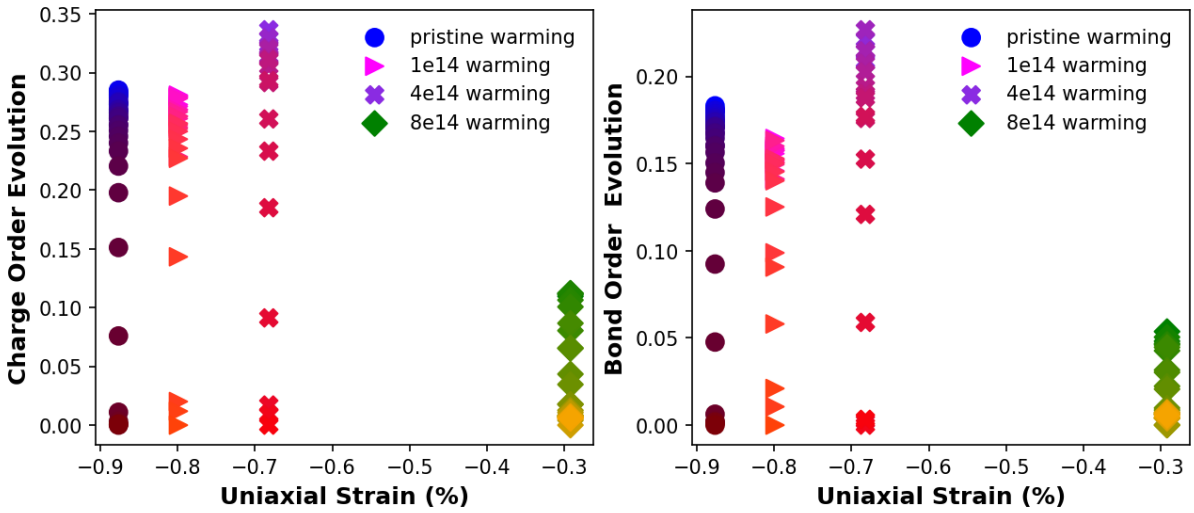

Figure 3.27: **Evolution of bond order vs charge order with helium implantation:** (left) Charge order (right) bond order evolution for the warming cycle for the corresponding uniaxial strain

The decrease in transition temperature however indicates that it becomes harder for the system to be in a bond-ordered and charge-ordered phase. Hence, a gradual decrease in the overall strength of bond order fits naturally. If we compare this with the bond-ordered phase of $PrNiO_3$, we note that the slope of charge order to bond order was higher in $PrNiO_3$ and the maximum strengths of charge and bond order were lower. Thus, even though the transition temperature decreases to become like $PrNiO_3$ the electronic configuration must be different from the pristine $PrNiO_3$. This is one of the first evidence we highlight which indicates that a uniaxial strain tuning deviates from the phase space of the nickelate phase diagram in an independent manner. In the following sections, we will find further confirmation of this point.

Finally, we conclude with the following observations from the charge order investigation:

- As expected the bond ordering temperature decreases with an increase in helium dose. This indicates that it becomes harder for the lattice to lower the energy through bond ordering. We observe the strength of the bond order lower with increased uniaxial strain with only the anomaly of 4e14 IPSC.

- Charge order follows a similar trend as bond order with less prominence. The linear relationship is followed by the charge order as a function of the bond order supporting evidence for strong electron lattice coupling in the nickelate thin film even with the helium implantation in the substrate.

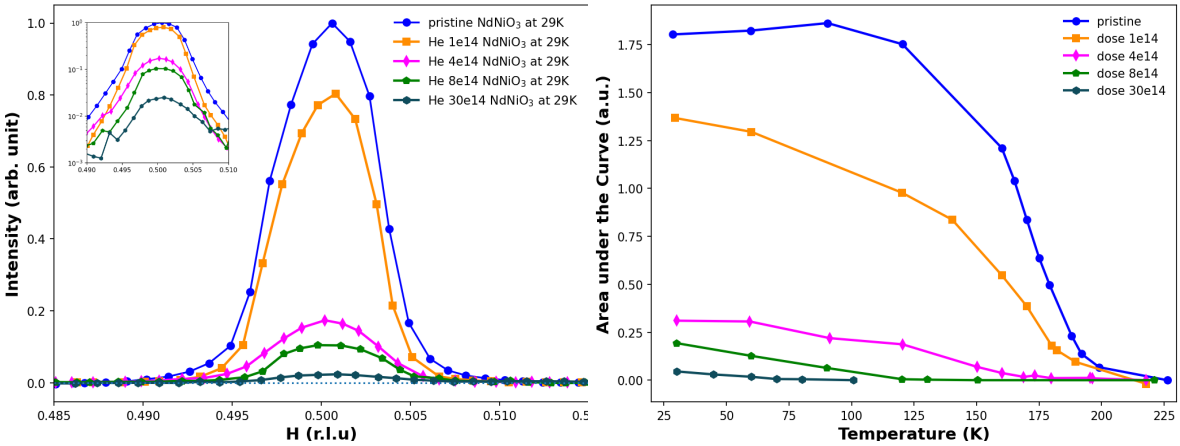

Figure 3.28: **Magnetic peak evolution with increasing helium dose:** (left) rocking curve scan on the magnetic peak shows a decrease in magnetic order strength but relatively unchanged full-width at half max (right) temperature evolution of the magnetic peak shows a gradual decrease in Neel temperature with increasing helium dose, as expected

Magnetic Order: Contrasting to the bond order evolution with damage, magnetic order shows a gradual tuning of transition temperature as well as the magnetic order strength. Such coherent control of magnetism provides significant evidence for spin-lattice coupling in $NdNiO_3$ films. Figure 3.28 a) shows the lowest temperature magnetic peak as was observed through

a rocking curve scan on $q_{AFM} = (\frac{1}{2}, 0, \frac{1}{2})$ in the Kappa-diffractometer chamber of 29-ID of Advanced Photon Source in Argonne National Lab following the same experimental method explained above. With the detector gain remaining fixed the beam current normalized intensity of the magnetic peak for films exposed with different doses clearly shows a gradual decrease in the magnetic order parameter. We continued to measure the rocking curve scans as we cycled the temperature through the transition temperature on each film. The temperature evolution of the magnetic peak shows a continuous tuning of the Neel temperature as evidenced in 3.28b. Remarkably the correlation length of the magnetic phase doesn't change.

To extract the correlation length of the magnetic order, we fit a Gaussian to extract the correlation length along the transverse direction to the momentum transfer and it was roughly 40-45 nm for all. However, the transition temperature continuously decreases. We show these extracted data in figure 3.29. We interpret the result as follows: the domain sizes do not change with increased helium dose but the moment size for each participating atom changes. This interpretation is supported by the decrease in the scattered intensity on the peak which is proportional to the square of the antiferomagnetic order. The antiferromagnetic order in turn is proportional to the individual moments. On the other hand, the decrease in transition temperature indicates a change in exchange interaction strength between the Ni atoms. To explore more about the change in exchange interaction we focus on the energy space.

We measured the energy dependence of the magnetic peak at the base temperature of 29K with fixed-q energy scans. The energy resolution was 0.1 eV. Fig 3.30 a) shows the energy dependence normalized by the maximum of the detector intensity to highlight the features. We used the right circular polarization to also consider the possibility of spin reorientation due to the change in the electronic environment. Similar to what we observed for the pristine samples the energy response of the magnetic peak is comprised of two peaks: a Lorentzian and a Gaussian. We observe that the peak ratio and the width of the peaks change with increased helium dose.

Firstly, we measured the intensity of the magnetic peak through rocking curve scans

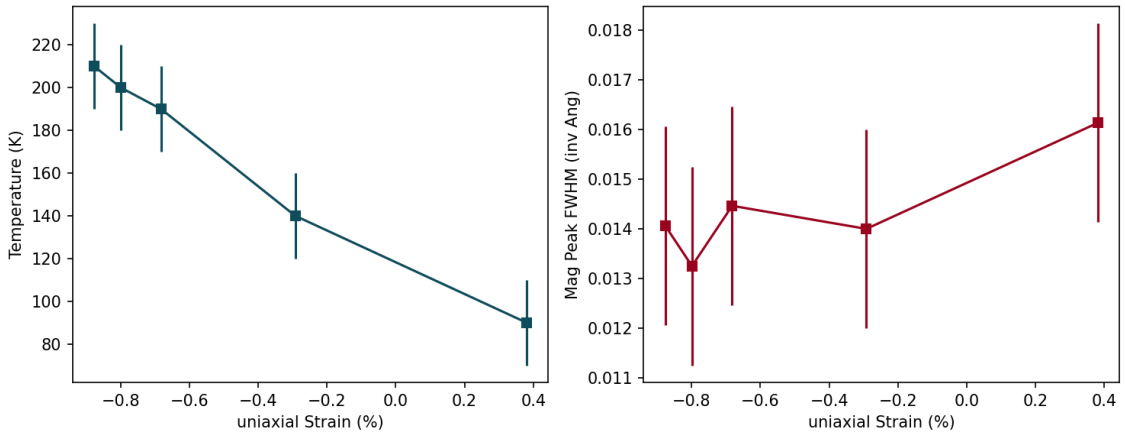

Figure 3.29: Effect on Helium damage on T_{Neel} and the correlation length

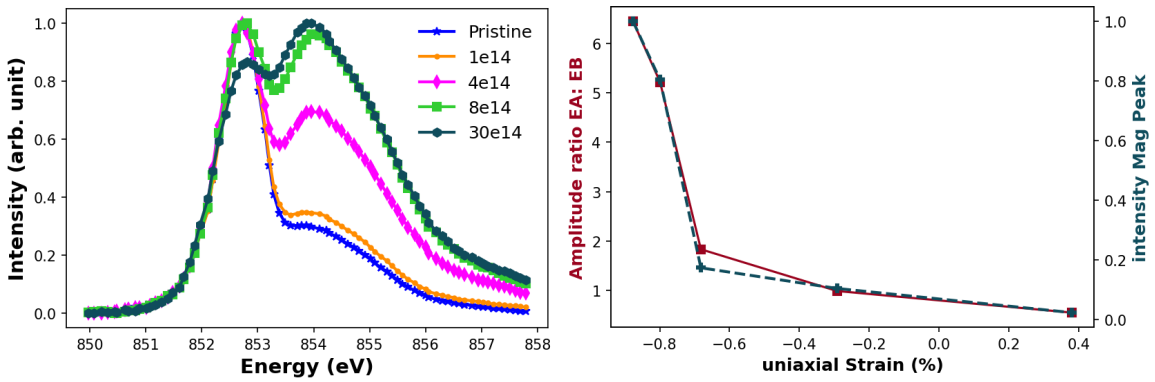

Figure 3.30: **Energy Dependence at low temperature:** (left) energy dependence on the magnetic peak normalized to the maximum of the intensity clearly shows two peak structure we call the first peak peak A and the second broad one peak B(right) intensity from the rocking curve scans plotted together with the ratio of the peaks A:B directly correlates indicating the drop of the magnetic intensity is correlated with the relative change in the energy distribution

with energy tuned to the first peak (E_A) at 852.7 eV. Fig. 3.30 b) shows the amplitude of the magnetic peak evolution from such rocking curve scans for the uniaxial strain due to the helium implantation. We see the fall of the magnetic peak intensity with decreased uniaxial strain. We simultaneously show the ratio of the two peaks from the fixed-q energy scans. They perfectly match indicating the fall of the first peak (at 852.7 eV) is correlated with the rise of the second

peak at 854 eV.

On closer investigation, we find that the amplitude of the second peak increases slightly while the intensity of the first peak drops sharply. Neither matches the magnetic peak evolution but their ratio. While the peak at E_A becomes smaller and sharper, the peak at E_B becomes broader and stronger. The spread of the energy peaks as extracted from fitting the plots indicates that the broadening of each peak exchanges values as we reach the highest dose measured from the pristine sample.

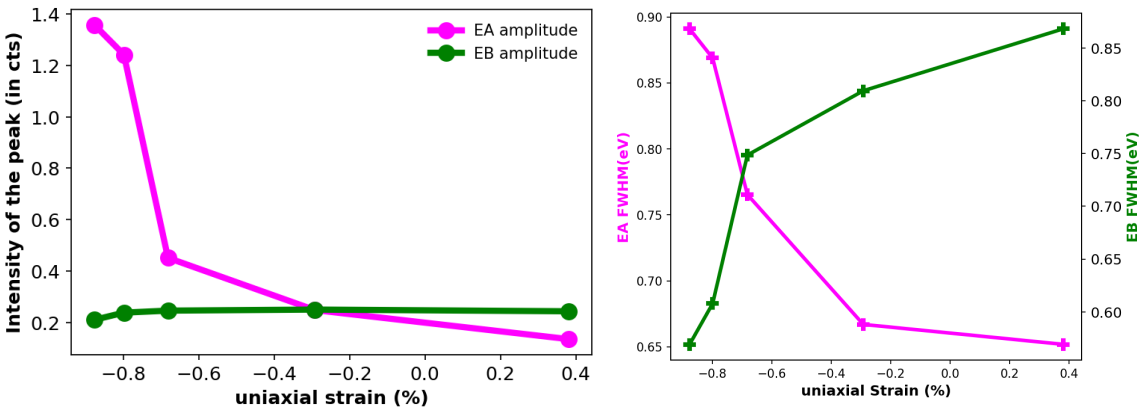

Figure 3.31: **Extracted fit parameters from the energy scans:**(left)Amplitude and (right)FWHM evolution of the energy peaks as a function of uniaxial strain corresponding to the helium dose

The continual evolution of the energy response is quite fascinating and demands further investigation. Green *et.al*. thoroughly discussed the energy response from a double cluster model involving two distorted NiO_6 octahedra cluster, based on the site-selective Mott transition picture [21]. The model captures the essential features of the insulating and magnetic phases of the nickelates with negative charge transfer, bond and charge disproportionation, orbital degeneracies, and on-site Coulomb interactions. On top of this, they considered inter-cluster Ni-ligand hopping in their Hamiltonian explicitly. They found that the ligand hole couples with the Ni-hole spin of the e_g orbitals antiferromagnetically and tends to shift to the compressed (short bond) octahedra as the breathing distortion is increased. This continually tunes the effective spin on the neighboring

Ni sites driving the short bond site towards $S = 0$ while the long bond site towards $S = 1$. We have experienced the aspect of continuous tuning of the magnetic moment from our measurement on pristine $NdNiO_3$ and $PrNiO_3$ magnetic order. However, there is a dynamic charge fluctuation which gets prominent as the bond order is lowered.

As discussed with a strong bond order the ligand holes accumulate at the short bond sites in a tunable manner with the bond order towards the limiting configuration as (4,2) where the first number in the conjugate pair refers to the total number of holes in the short-bond site and the second number refers to the total number of holes in the long-bond site. Although even at the strongest bond order this is not the pure configuration. Due to dynamical charge fluctuations, there is a non-zero configuration weight for the state (3,3) with a significant configuration weight found to be (4,2). As we lower the bond order the fluctuations dominate. At lower bond order, the (4,2) and (3,3) can become equal in configuration weight while the (2,4) also becomes non-zero. At the zero bond ordered phase, (3,3) state dominate with considerable weight shared by (4,2) and (2,4) states. The effect of the charge fluctuation was further found in the energy response of the magnetic peak. The authors showed that even in the limit of zero bond order the charge fluctuations can give rise to a strong magnetic circular dichroism signal. Their calculated energy response shows that increased inter-cluster hopping of the Ni-ligand hole shows up as a split peak structure in the magnetic circular dichroism signal. As the hopping parameter is tuned to be stronger, the peak at the peak position similar to the E_A increases in strength. The resonant magnetic diffraction signal can be found from the magnetic circular dichroism through Kramers-Kronig transformation, which in general preserves the peak positions. Thus for low bond-ordered samples with a high dose of helium implantation, the two peak structures could be explained by increased charge fluctuations.

They have also found that with non-zero bond order, the long bond site contributes to the E_A peak position and the short bond site to the E_B position. As the bond order strength decreases the two peaks from two different sites come closer until they become indistinguishable at zero

strength of the bond order parameter. At this limit, the two peak structure, peak separation, and their relative intensities are found to be maintained by the inter-cluster hopping parameter. Thus, from this discussion, we form the insight that with decreasing bond order inter-cluster hopping and charge fluctuation may take over the electronic configuration in the helium-implanted nickelates and drive the phase transition. However, we do not yet see direct evidence of increased charge dynamics. To see that we will turn towards soft X-ray emission and absorption spectroscopy.

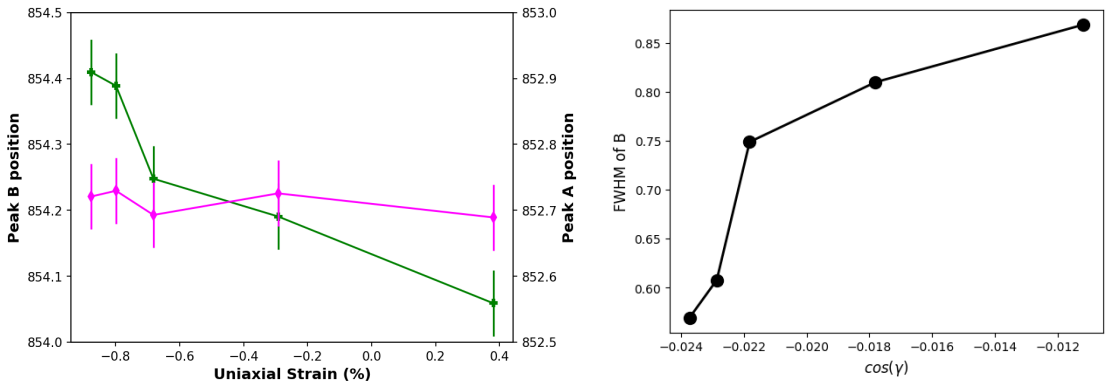

Figure 3.32: **Further characterization of the fits:** (left) peak B position continually decreases and comes closer to peak A position but peak A remains relatively static (right) FWHM of peak B as a function of $cos(\gamma)$

Before turning towards the investigation of inter-cluster hopping we tie a few loose ends. We note that the peak position of the peak at E_B moves to lower energy with a decrease in the bond ordering strength. However, the peak position at E_A does not change as shown in 3.32. Following the analysis of [21] we note that if the bond order decreases the two peaks come closer with their energy gap decreasing. On the other hand, the inter-cluster hopping doesn't considerably influence the E_A peak position. Thus, we can consider a smooth changeover from a strong bond-ordered phase to a high inter-cluster hopping phase. As a result of the shrinking bond order the E_B peak lowers in energy however, with the increased inter-cluster hopping the E_A peak is sustained. With more strain even the inter-cluster hopping starts to decrease when the Ni-O-Ni distance increases beyond a limit. At this limit, the E_A peak might fall below the E_B

peak as seen in double-cluster simulations and the case of damage of 30e14 IPSC.

However, with this evidence, we realize that the electronic environment of the nickelates changes completely with the strain. From a bond order-driven site-selective Mott transition the magnetic order is driven by charge fluctuations and inter-cluster hopping. In this limit of a highly itinerant hole system, the effect of the Fermi surface becomes important. We plotted the increase in the full-width at half-max (FWHM) of the peak at E_B with respect to the $cos(\gamma)$ for each sample and see a correlated relationship. The exact fit for both the FWHM of the peak at E_A and E_B are found and shown in figure 3.33. The double cluster simulation does not explicitly discuss the effect on the full-width half max of each peak. Furthermore, the broadening of a peak in a many-body quantum system is influenced by many parameters such as core-hole lifetime, spin and charge fluctuation, coupling to phonon, etc. It is not clear to us if a single parameter or multiple parameters influenced the broadening of the peaks. However, since we consider that the inter-cluster hopping dominates with increasing dose we can further take the broadening as a signature of the increased hopping. The relationship with $cos(\gamma)$ may not be surprising considering in nickelates Ni-O-Ni bond angle significantly influences the physics.

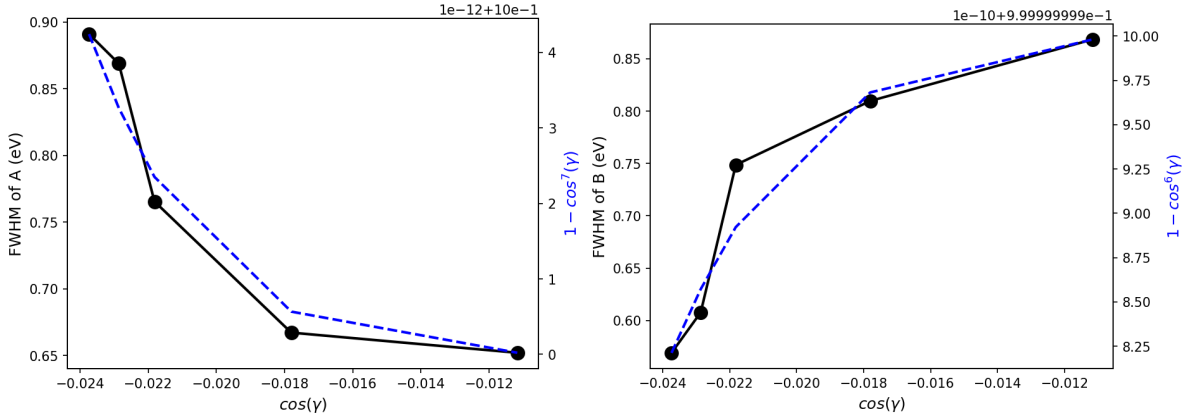

Figure 3.33: FWHM fits and its dependence with $cos(\gamma)$

Absorption and emission spectroscopy: After we have probed the order parameters of the ground state of nickelates with temperature for each helium implanted sample we observed

that the helium implantation generated uniaxial strain tuned the coupled paramagnetic-metal to bond and charge-ordered antiferromagnetic-insulator transition. From the energy dependence of the magnetic peak, we realized that the electronic character of the transition is also changing from a site-selective Mott transition (where strong bond order drives the transition) to a transition where bond order is low and dynamic charge fluctuation is high. To investigate further about the electronic configuration we investigate here room temperature and low temperature X-ray absorption spectroscopy (XAS) in total electron yield (TEY) mode. The experiments were carried out in Beamline 4.0.3 of the Advanced Light Source (ALS) and followed the methodology described in the previous section for the pristine samples.

The raw data were similarly background subtracted and normalized to produce the plot in figure 3.34 where we have plotted the room temperature XAS TEY for O-K edge pre-peak and the Ni-L3 edge. From the O-K edge we see that the pre-peak shrinks with increased helium implantation. Since this pre-peak is considered the oxygen orbital projected $3d^8\underline{L}$ states and an indicator of the Ni-O covalency. Thus we have direct evidence that with helium implantation we are changing the electronic configuration of the nickelate even at the room temperature metallic state. The change in the Ni-L3 edge is more subtle.We have multiplied the polarization-averaged background-subtracted spectra with a series of numbers to show that the intensity of peak A increases slightly.

We have further extracted the quantities that describe the peaks in the above XAS and shown in the figure 3.35 below. Firstly, the area under the O-K pre-peak within energy 526 eV to 530 eV is discussed first. We can see that the area decreases to $\sim$60% of the pristine state. For pristine $NdNiO_3$ and $PrNiO_3$, we observed such shrink in the area under the O-K edge pre-peak for metal-insulator transition. However, that was accompanied by the peak splitting of the Ni-L3 edge upto 1.7eV gap between the two peaks. We see that ΔE from the pristine 1.3 ev value decreases by 0.06 eV only. We note here that the resolution for the measurement was $\sim$0.1 eV and thus the shift falls below the resolution of the measurement. Thus even the room temperature

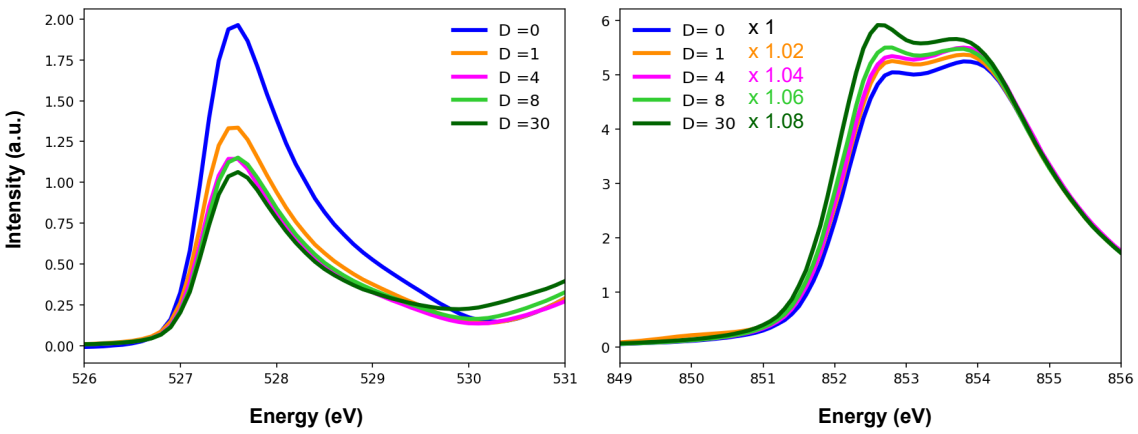

Figure 3.34: X-ray absorption spectroscopy on helium implanted samples Room temperature (left) O-K edge pre-peak (right) Ni-L3 edge

state of the helium-implanted sample is unique. Thus the tuning with helium implantation has opened a new dimension of phase space for the nickelates.

Secondly, from the fit of two Gaussian to the Ni-L3 XAS intensity we note that the full-width at half-max(FWHM) for peak A roughly remains constant or decreases ever so slightly, whereas the peak B FWHM increases indicating a broadening. For any helium-implanted sample including the pristine, there is no bond order at room temperature and we observed a decrease in the $3d^8\underline{L}$ state thus the change in the peak ratio must be brought in by the increased charge transfer energy accompanied by the decrease in covalency. However, the increase is comparatively lower than what we observed in the insulating state again providing support for a distinct state compared to the pristine metallic or insulating state of the sample. In this state describing the physics locally is not enough.

Finally, we extracted X-ray linear Dichroism (XLD) and from that, we extracted the hole ratio between the out-of-plane and in-plane d orbital. We note that there is a slight change in the hole distribution but eventually with a higher helium dose the distribution becomes isotropic.

Next, we turn our attention to the electronic configuration of the unoccupied states as

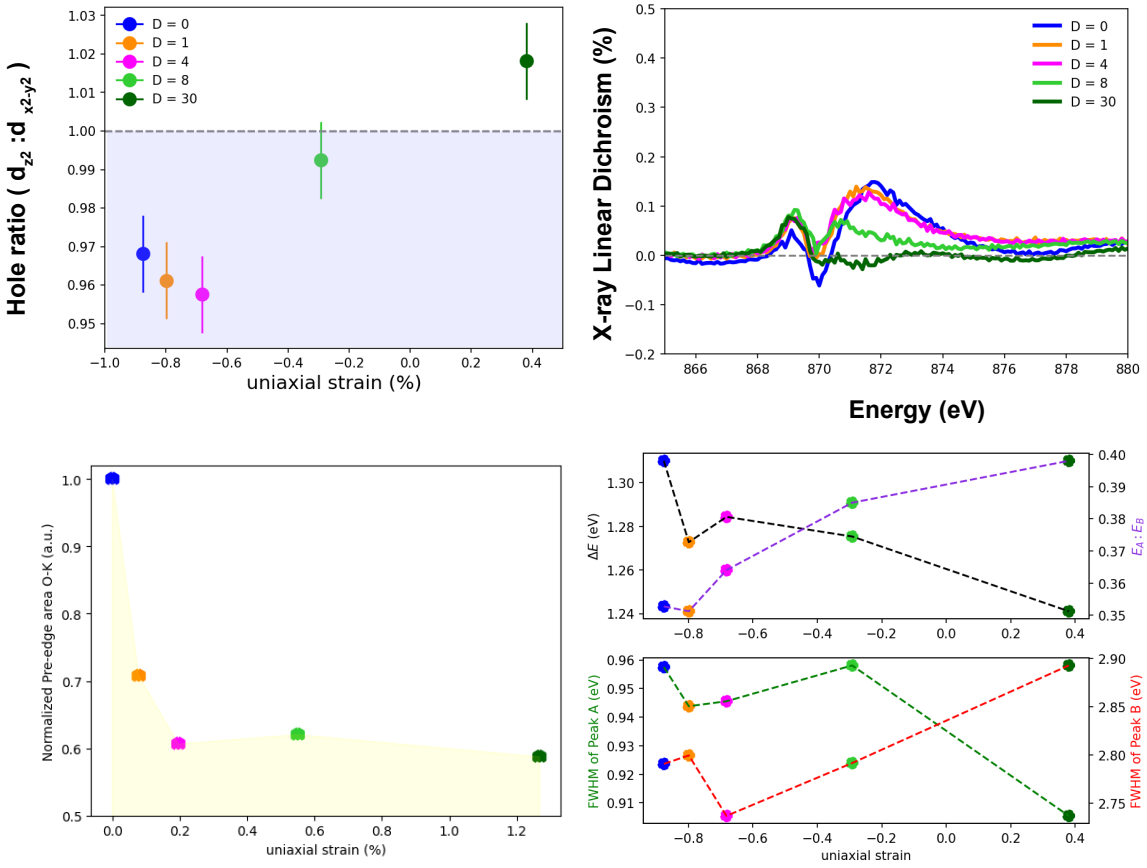

Figure 3.35: Peak characteristics extracted from the room temperature XAS

we lower the temperature. All of the samples undergo a metal-insulator transition however at a different temperature. Increased doses result in lower transition temperatures. we have collected the data at 22K where all samples are insulating according to the transport measurement.

We see that the O-K edge pre-peak shrinks even further. The extracted area under the curve is shown in figure 3.36 along with the room temperature data. The area under the curve for any sample at any temperature is normalized by the low-temperature pristine data. It is interesting to observe that as the implanted sample undergoes the transition they decrease the covalency further to an extent that is similar to the pristine phase transition. Without the bond order, it seems the system tries to find the ground state by decreasing the covalency. As if it knows only one way

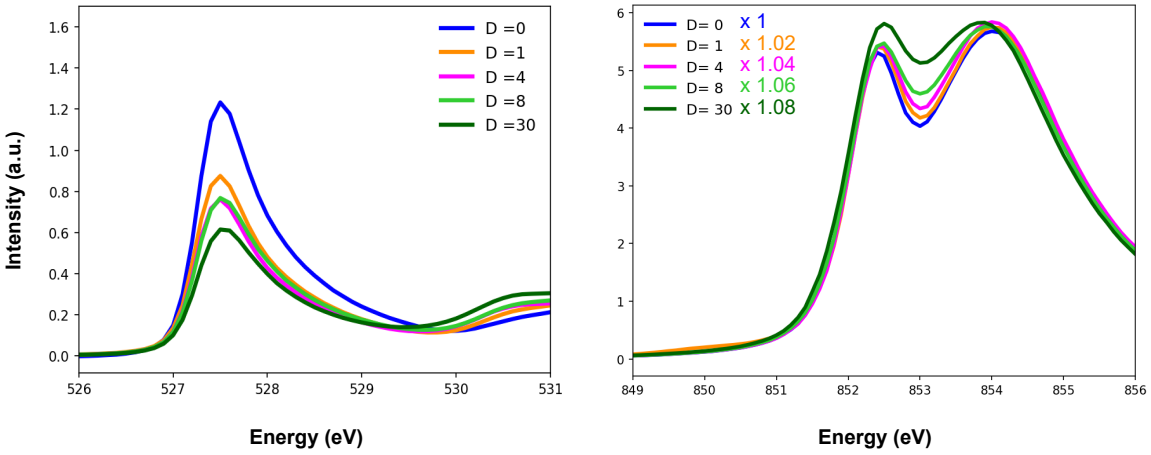

Figure 3.36: X-ray absorption spectroscopy on helium implanted samples Low temperature (left) O-K edge pre-peak (right) Ni-L3 edge

to decrease the overall energy however one question remains: what means does it take to decrease the covalency as bond order is unavailable?

On the other hand, we observe familiar two-peak splitting for the low-temperature Ni-L3 edge peak; as expected from decreased covalency and increased charge transfer energy. With increased helium dose and hence uniaxial strain the peak splitting decreases slightly. Both peak A and peak B broaden and the peak ratio of $A : B$ decreases. If we compare the high temperature ΔE with low temperature ΔE we realize the change is the largest for the pristine sample and decreases continuously upto the highest helium dose we explored. Thus, even though the O-K edge pre-peak shrinks similarly the peak separation at the Ni-L3 edge does not undergo similar change due to the metal-insulator transition. Furthermore, we observe the sharpness of the separated peak decrease with increased uniaxial strain from the implanted helium. There is intensity between the two peaks which increases in weight as helium implantation increases. The existence of these new states is echoed in the increased broadening of the peaks and decreased peak ratio. In the table below we summarize the detailed finding of the XAS data for both temperatures.

X-ray absorption spectroscopy told us that the room-temperature state and the low-

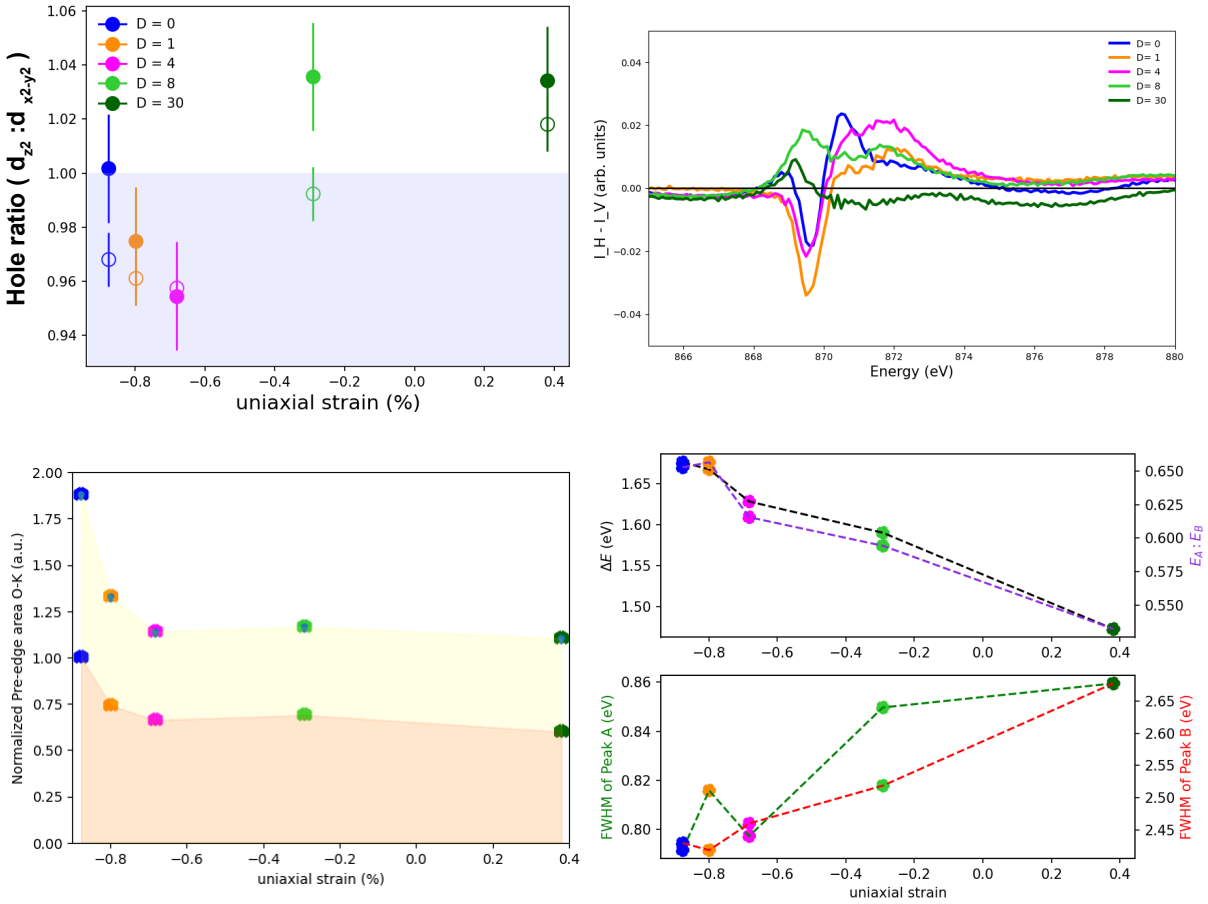

Figure 3.37: Peak characteristics extracted from the low temperature XAS

temperature state both differ significantly from the pristine metal and insulator state in terms of electronic configuration. Furthermore, the calculations of local approximations seem to fail to explain the evolution of the XAS with helium implantation such as the pre-peak of the O-K edge decrease but the Ni-L3 edge doesn't split simultaneously. Thus, it is imperative to investigate the occupied electronic states near the Fermi level for Ni valence shells. We thus conduct an energy resolved X-ray emission experiment at the resonance edge of the Ni-L3 also known as Resonant Inelastic X-ray Spextroscopy (RIXS).

To conduct the experiment we mounted all of the samples simultaneously on the sample holder. The incident angle of the incoming beam was set to 30° and the scattering angle was

fixed at 150°. Emitted photons passed through a grating before being recorded by a CCD detector (make Andor) of 2048 X 128 pixels. The energy of the emitted is resolved along the long direction and the short direction is summed over for statistics. Before the start of the experiment, we tested the instrument resolution using elastic scattering from carbon tape in the energy range we intend to collect the data. The overall energy resolution was found to be ∼700 meV at 50μm exit slit size. The energy resolution is slit size-dependent. We obtained a lower resolution at ∼500 meV however the intensity dropped quite a bit and for the sake of limited time, we decided to continue with the 700 meV resolution.

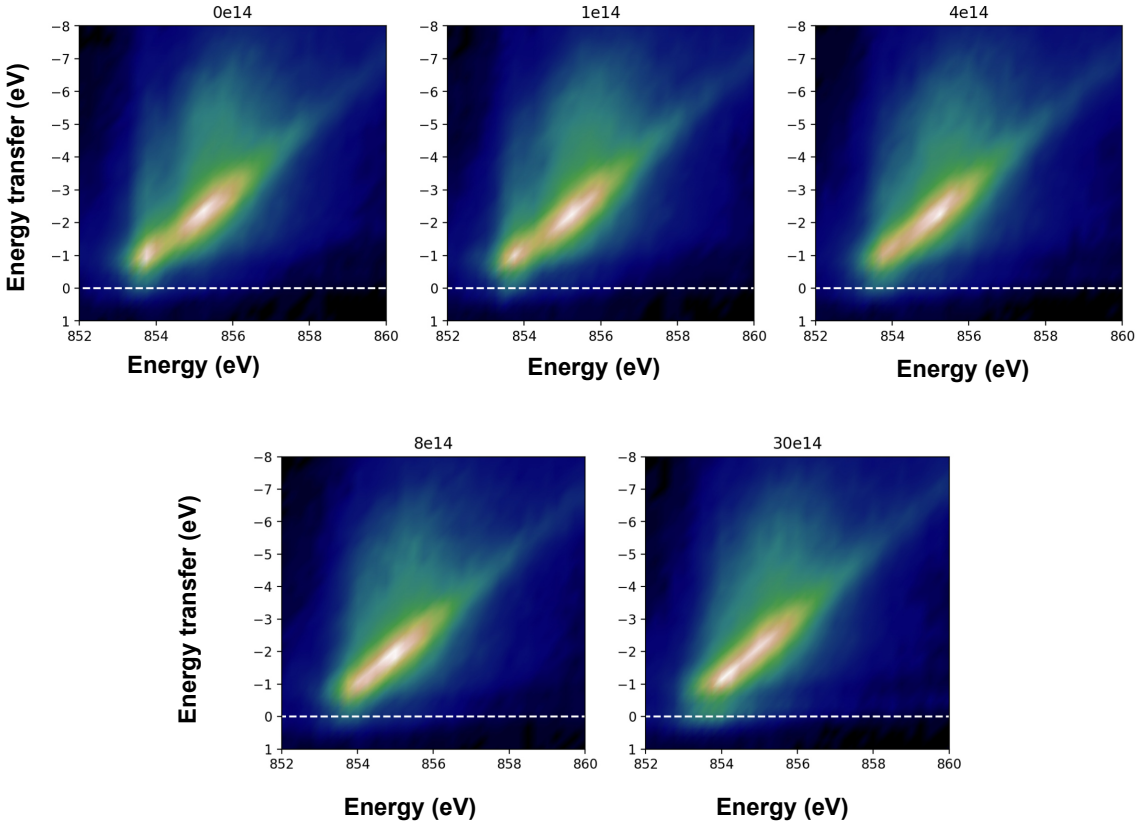

Figure 3.38: **Resonant inelastic X-ray scattering (RIXS) measured at 80K.** The dd excitation becomes increasingly delocalized for higher helium ion implantation and merges with the charge transfer excitation. This also increases the low energy excitation between 0 to -1 eV indicating a poorer insulating phase for the helium implanted samples.

At this scattering geometry described above we vary the energy of the incident beam from 852 eV to 861 eV with a step size of 250 meV. From the collected spectra we subtracted the incident energy to plot the energy transfer to the sample versus incident energy, called energy map. This data is shown for all of the helium implanted $NdNiO_3$ samples. We begin the discussion of the energy map following the pioneering work of Bisogni *et.al*. [7].

In the low-temperature insulating state, two distinct excitations were found in similarly epitaxial $NdNiO_3$ thin film: localized *dd* excitation around 1eV energy transfer, and charge transfer excitation around 2-3 eV which was reported to have an itinerant component. The itinerancy of an excitation can be read from the energy map if with increased excitation the energy transfer linearly increases. For the pristine sample, we reproduce the result of Bisogni *et.al*. only with lower resolution. despite the resolution, the primary features can be immediately seen. The localized *dd* excitation is found around 1 eV quite separated from the charge transfer excitation around 2 eV which has an itinerant component. The incredible observation comes from the subsequent energy maps where increasing the helium implantation the localized component of the *dd* excitation starts to merge with the charge transfer excitations. The gradual tuning of the delocalization of the *dd* excitation continues up to the highest explored implantation dose where both excitations merge along the itinerant line and no clear distinction exists any more between the charge transfer excitation and the *dd* excitation. This precisely provides evidence that the low-temperature insulating state is very distinct in the electronic configuration of the implanted samples. They continue to become different with increasing doses. Furthermore, this explains the states in between the A-peak and B-peak which were observed in the XAS TEY measurement.

The figure 3.38 provides further direct evidence about the increased itinerant character of the nickelate physics. The calculation by [21] showed that bond order competes with charge fluctuation thus with increased bond order we did not see the itinerant component of the nickelate physics. One limit of the physics was suggested by [22] where an itinerant component of the Hamiltonian results in a Fermi surface where a spin density wave instability exists. As we have

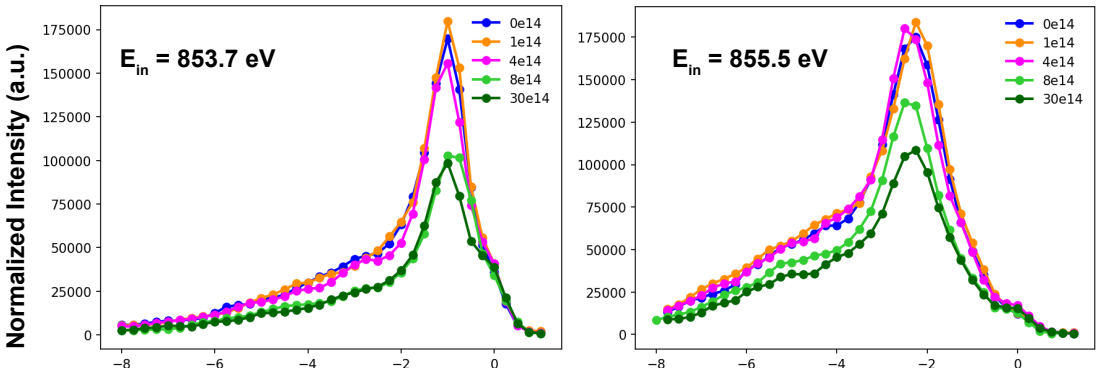

Figure 3.39: Decrease in dd excitation energy and FL and CT energy

seen previously such an evaluation correctly extracts the wave vector of the antiferromagnetic order. Furthermore, in systems with more itinerant characters, such an explanation seems to prevail. For example, in $PrNiO_3$-$PrAlO_3$ superlattice a weakly metallic state with strong antiferromagnetic order but weak charge order was reported, which could be readily explained by the density wave theory which considers antiferromagnetic order as the primary order parameter and charge order as a result of the magnetic order. For such an explanation, the existence of bond order is not necessary. With the increased itinerant character of the d-electrons of Ni, we might as well be in this configuration space where the phase transition can be explained by the emergence of a spin density wave order.

Finally, we end this discussion by pointing out that the itinerant character of the d-electron increases while the low energy excitations below the 1eV energy line get more weight with increased implantation. It becomes visibly clear in the energy map of 30e14 IPSC. Thus not only do the high-energy excitations change the characteristics, but previously absent low-energy excitations show up as a result of uniaxial tuning. We have taken slices of the energy map at the incoming energy aligned to the *dd* peak location and to the center of the charge transfer excitaition. For the doses of 8e14 and 30e14 IPSC the increase in low energy excitation below the *dd* excitation and above the elastic line can be seen. The broadening of the high energy excitation

to the low energy side makes the system more metallic. Thus with considerable broadening of the high energy excitation we can expect a metallic system with antiferromagnetic order. Since bond order was stronger in $NdNiO_3$ to reach the limit with low helium dose such that we remain inside the region where defects are experimentally not observable, we use $PrNiO_3$ as the tunable material.

3.5.2 Uniform helium irradiation in $PrNiO_3$:

Now that we have realized the effect of helium ion implantation effect on $NdNiO_3$ we look for the applicability in the case of $PrNiO_3$, where the bond order in the pristine state was weaker than $NdNiO_3$. In $PrNiO_3$ the lattice electron coupling was strong so the strain tuning is expected to similarly tune the electronic state of the sample. We were successful in suppressing the phase transition however the decrease of transition temperature was not smooth and collapsed rapidly. Ultimately in the process of tuning the phase transition, we discovered metallic antiferomagnetism in $PrNiO_3$ thin films.

Results We highlight the tuning of the metal-insulator transition in 22nm $PrNiO_3$ thin films epitaxially grown on 110 oriented $NdGaO_3$ substrates through figure 3.40 where we have shown that the coupled paramagentic-metal to antiferromagnetic-insulator is supressed. However it took much less helium dose to supress the transition completely. By the dose of 30e14 IPSC (the highest dose for the case of $NdNiO_3$) the sample was completely metallic with no antiferromagnetic order at $\mathbf{q} = (1/2, 0, 1/2)$. For a dose of 4e14 IPSC we observed no antiferromagnetic peak as well. Thus we realize for $PrNiO_3$ the control by helium implantation becomes more difficult.

We considered in the low bond ordered pristine state the overlayer lattice might not be rigid enough to sustain tunability by the uniaxial strain helium implantation provided. We then tried a new thing. We decreased the thickness of the overlayer to make the epitaxial strain from the substrate more homogeneous on the $PrNiO_3$ film. A thinner film has a stronger epitaxial

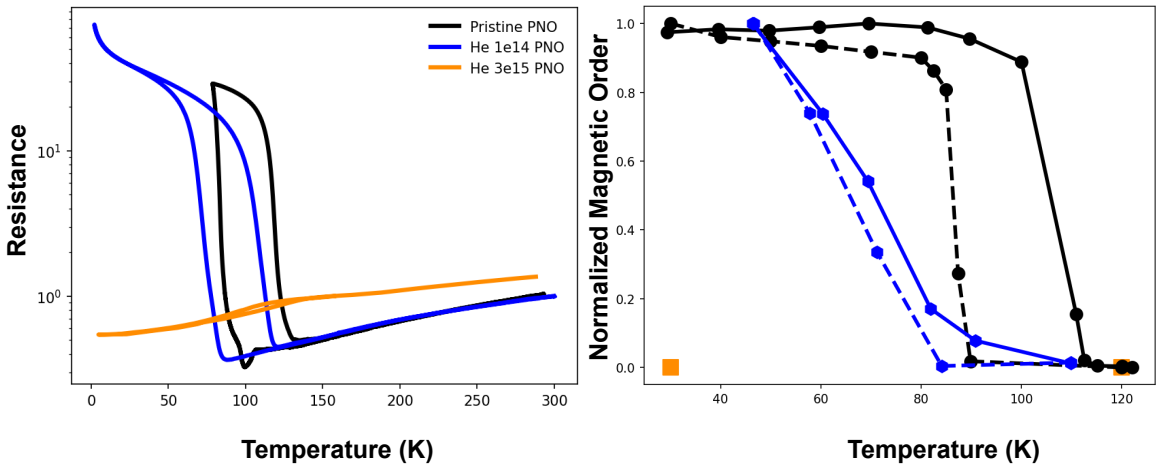

Figure 3.40: Metal-insulator transition and paramagnetic to antiferromagnetic transition both are simultaneously suppressed

relation with a decreased strain gradient compared to a thicker one. The trick helped us to tune the metal-insulator transition in $PrNiO_3$ thin films of 15nm thickness. We implanted those 15nm thick $PrNiO_3$ films with helium with doses of 0, 1, 2, 3, 4 and 5e14 IPSC. We show the result of continuous tuning of the metal-insulator transition in these films in figure 3.41. The four-point van der Pauw transport measurement showed a continuous tuning of the phase transition. Although we could continuously tune the transition temperature the control was not as nice as $NdNiO_3$. We see that room temperature normalized resistance suddenly jumps for the dose of 3e14 IPSC only to sufficiently collapse for the next higher dose of 4e14 IPSC. Remarkable the resistance of the sample with 5e14 IPSC dose does not change the slope of the resistance versus temperature curve down to the lowest temperature deeming it as a metal. However, the resonant soft X-ray scattering measurement finds an antiferromagnetic peak in this sample. The control over antiferromagnetic transition showed an incoherent control similar to the transport measurement. Thus the sample implanted with 5e14 IPSC shows undeniable evidence of being an antiferromagnetic metal.

antiferromagnetic metal: Let us focus our attention towards the sample implanted with 5e14 IPSC which appears to be a metal from the transport measurement and an antiferro-

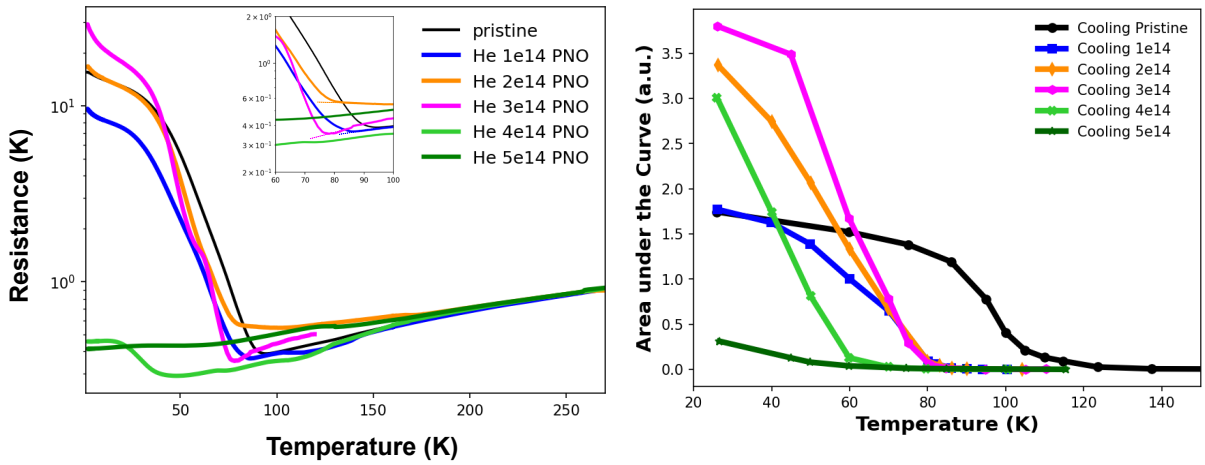

Figure 3.41: Gradual Tuning of the phase transition in 15nm thick $PrNiO_3$: (left) transport characterization (right) antiferromagnetic order

magnet(AFM) with $\mathbf{q}_{AFM} = (1/2, 0, 1/2)$ from the resonant soft X-ray elastic scattering. We further characterized the AFM peak with rocking curve scans. The extracted full-width at half-max(FWHM) is plotted along with the rocking curves in figure 3.42. We have also shown the continuous evolution of the Neel temperature with increased helium dose. Similar to the $NdNiO_3$ sample we observe the correlation length ($\sim \frac{1}{FWHM}$ remains unchanged with increased doses of helium implantation. All of the changes in the magnetic order are thus accounted for by the lowering of the magnetic moment at each Ni site. The transport characterization for complex material like nickelates can be misleading. For instance, if the sample has inhomogeneous domain distribution at low temperatures without filling the volume of the thin film then scattering from the sample will show an antiferomagnetic peak. However, there can be conducting pathways avoiding the insulating domains. It is worth noting that the magnetic domain sizes do not differ from the pristine sample indicating such domain arrangement leading up to a metallic behavior is not applicable for the $PrNiO_3$ sample. We still look for a local electronic signature that will prove beyond doubt the metalicity of the sample. We have collected fixed-q energy scan data on the magnetic peak of the sample. Moreover, while collecting this data we have collected

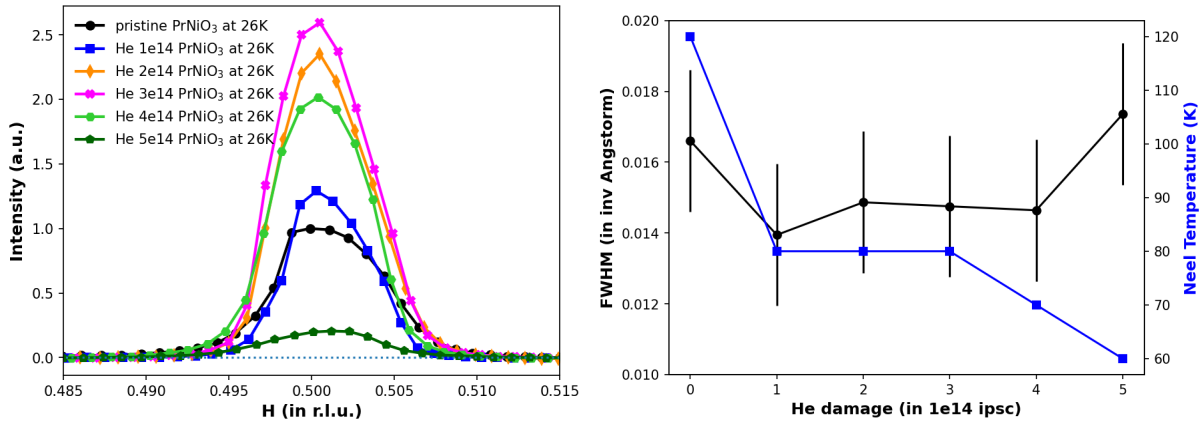

Figure 3.42: Evolution of the antiferromagnetic order with increased helium implantation

the Total Electron Yield through the Ammeter connected to the sample. This data is shown in Fig 3.43. In the energy scan of the magnetic peak, we observe an initial sharpening of peak A with a gradual lowering of peak B intensity. However, after the dose of 3e14 IPSC, the trend reverses finally reaching the metallic sample of 5e14 IPSC helium dose where both peak are of equal intensity. Corresponding TEY measurement shows the signature two peak structure of the insulating nickelate state for samples upto 3e14 IPSC dose. It decreases for 4e14 IPSC and for 5e15 IPSC implanted sample we do not see the two peak structure of the XAS. Instead, we see a response usually observed in the metallic state of $PrNiO_3$.

Thus, similar to compressively strained $PrNiO_3$-$PrAlO_3$ superlattice we consider the sample implanted with 5e14 shows a metallic spin density wave state.

3.6 Results: Pattern formation using focused ion beam

Once we have realized the robust effect we bring into the nickelates uniformly implanted with He ions we move to the ultimate challenge of creating mesoscale textures of electronic states

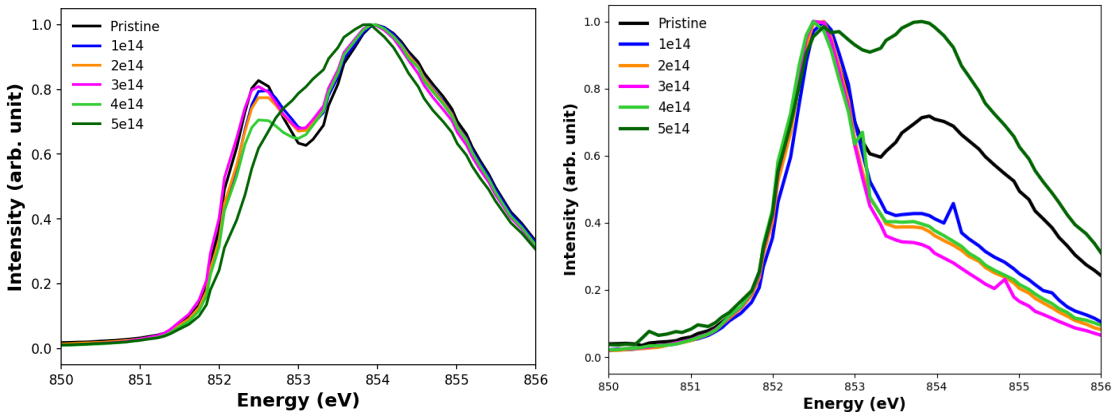

Figure 3.43: Energy response measured on the antiferromagnetic peak (left) total electron yield (right) fixed-q energy scan

using a focused ion beam of helium. We used a helium ion microscope to implant the helium onto the substrate. We will show that the focused ion beam successfully tunes the local structure of the substrate and the uniaxial strain remains localized to the thin film in the implanted region only. Since the uniaxial strain changes the electronic character and the phase transition of the nickelate film, we will see by local implantation of helium ions we will be able to create artificial mesoscale electronic structures.

We used a dose of 30e14 IPSC for both $PrNiO_3$ and $NdNiO_3$ film. For the $PrNiO_3$ film, this dose completely suppressed the transition down to liquid helium temperature, but for the $NdNiO_3$ sample, it drives the transition temperature below 90K. The only difference we have from the uniformly implanted case is that the energy of the helium ion beam is limited to 25 keV from the helium microscope specification at QB3 of UC Berkeley. According to our previous SRIM simulation, this is sufficient energy for the ions to pass the thin film and get implanted into the substrate. Thus we do not expect any different behavior.

We first discuss the pattern we created on the $PrNiO_3$ sample. For any investigation related to a mesoscopic pattern, we need to help with creating a map of the sample. Often these

are done through several marks which are called fiducials. During the X-ray experiments, they help us find the tens of micron-scale patterns in a milimeter scale thin film. Thus, after growth and characterizing we created fiducial marks on the sample depending on the experiment at hand. For the $PrNiO_3$ sample we investigated the success of electronic pattern creation using X-ray photo-electron emission spectroscopy (X-PEEM). Since as per our above discussion even the room temperature state is different in electronic configuration we utilize that to create contrast in the photoemission signal.

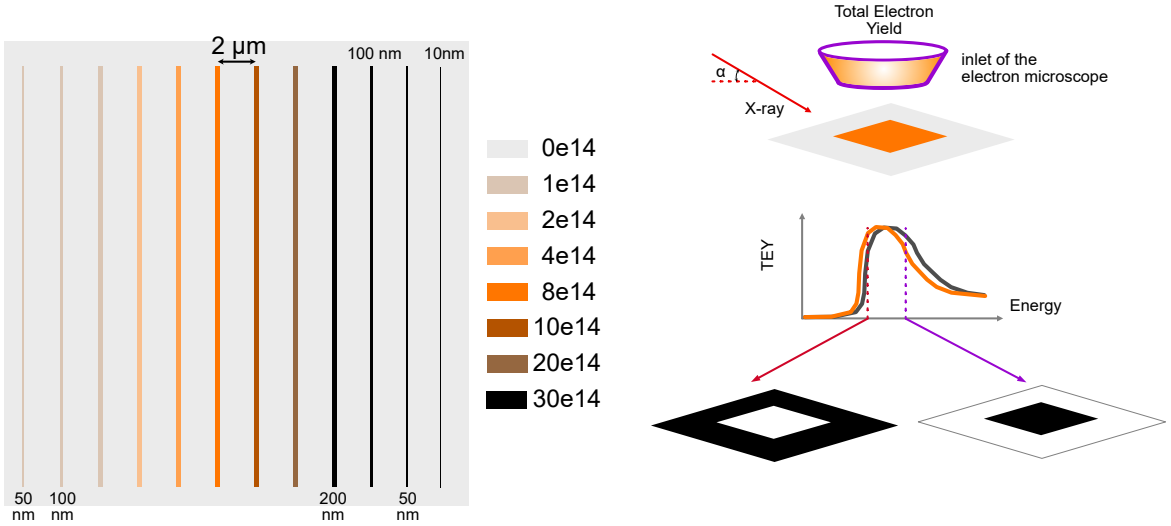

Figure 3.44: X-ray photo-electron emission microscopy (left) sample design (right) schematic of contrast mechanism

3.6.1 Resonant X-ray photo electron emission microscopy:

Resonant photoemission ejects a core electron from an occupied level. Ejection of the corre electron creates a core hole which is further quenched by an electron from the continuum or an electron from the higher valence shells. If the core hole is filled with an electron from a higher valence shell another electron is ejected in the process. Such secondary electron emission is known as the Auger effect. All of these electrons come out of the surface of the sample exposed to the resonant radiation. The total electron yield can be parallelly measured connecting

a ground wire from the sample through an ammeter. This current is recorded in X-ray absorption spectroscopy experiment. Thus, in resonant photoemission, we focus directly on the electrons instead of the replenishing current. However, they are directly related.

The electrons have a small mean free path in the sample. Thus, only the electrons very close to the surface $\sim$2-10nm make it out of the surface for detection. In the microscopy mode of this experiment, we set an external electric field perpendicular to the surface of the sample. For our experiment, it was set at 18 keV. Right after ejection the electrons are subjected to this field and accelerated towards the objective lenses. At the focus of the objective lenses, a two-dimensional electron detector is placed to record the distribution of the electrons in real space. This way we get an image of the electron-emitting parts of the sample under focus for a given energy. The brightness of the pixel is directly related to the count of the electrons leaving that position on the sample for a given energy.

Contrast Mechanism: A typical X-PEEM experiment relies on finding the contrast of the sample surface as a function of energy. This is schematically shown in the Fig. To design a contrast, we first study the TEY of the XAS on the sample and focus on the energies where they deviate in intensity. For our sample, we know that near peak A the intensity in TEY is slightly higher for helium-implanted samples, which can be utilized to create the contrast. At this energy, electrons emitted from the regions with different electronic configurations due to the helium implantation will be higher in number than in a different position in energy where the pristine ejects more electrons. Thus if we take an image with incoming energy near peak A the implanted regions will appear brighter. we can further increase the contrast by utilizing images taken at two energies. If we divide the image taken at the first energy by the image taken at the second energy the image will appear brighter where the electronic configuration is changed due to helium implantation.

Sample preparation and Mounting: We carried out the XPEEM experiments in beamline 11.0.1.1 of the Advanced Light Source of the Lawrence Berkeley National Lab. The lowest

temperature we could achieve was 150K and hence we explored the electronic phase heterogeneity in the metallic phase on samples where we developed line patterns of different thicknesses and helium doses. The schematic of the sample is shown in the Fig. The highest dose we explored is 30e14 IPSC similar to the uniform helium implantation. Each line was separated from the other by 2μm. In the central region, we wrote the pattern with an equal thickness of 200 nm but varying helium dose. Both ends on the other hand had lines with varying thickness for damages 30E14 IPSC (200nm, 100nm, 50nm, and 10nm), and 1e14 IPSC (200nm, 100nm, and 50nm). From the uniform helium implantation, we know that at this dose the film remains metallic down to the lowest temperature. The objective of this experiment was to first confirm that we can write electronically heterogeneous patterns with a focused helium ion beam and then characterize the patterns written.

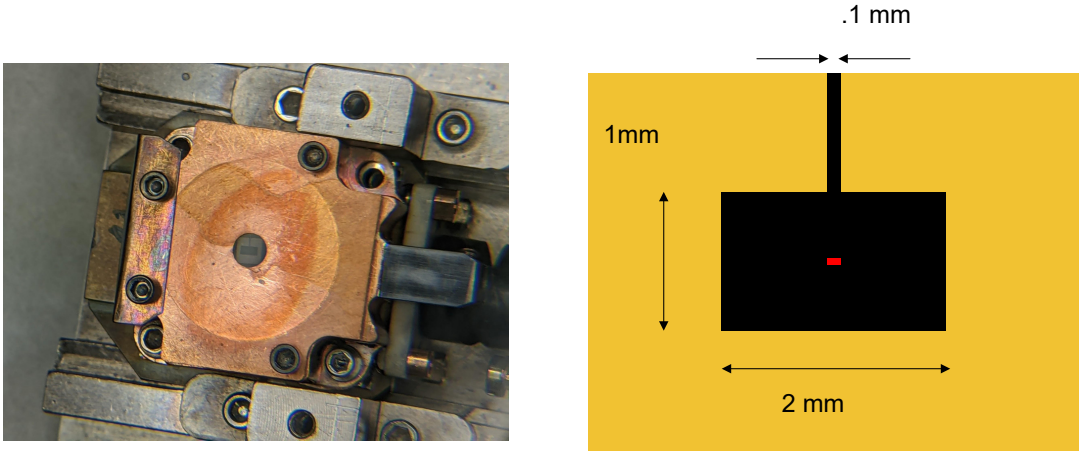

Figure 3.45: Sample design and sample mount the central red box contains all the pattern

The samples were prepared by our collaborators from the Dynes lab of the University of California San Diego and developed in the helium microscope of the University of California Riverside. Helium dose was varied from 1e14 IPSC to 30e14 IPSC in multiple steps to check if the pattern forms similarly among different doses. We also varied the thickness of the lines

to check if it affects the quality of the patterns drawn. The helium beam was focused down to 0.5 nm and the resolution of the XPEEM experiment was 30nm. We further developed a fiducial pattern which is shown in the Fig along with the sample mounting set up in the XPEEM chamber. It can be seen that the sample sits under a Cu cover. This puts a design consideration where the pattern to be investigated must be drawn at the center of the sample away from the Cu rim. The fiducial design was developed by depositing 40nm Ti/Au with a custom-designed mask. The empty channel in the gold deposition is intended as a guiding direction to find the pattern at the center. The channel thickness was kept at 100 μm similar to the length of the pattern to ease the search process.

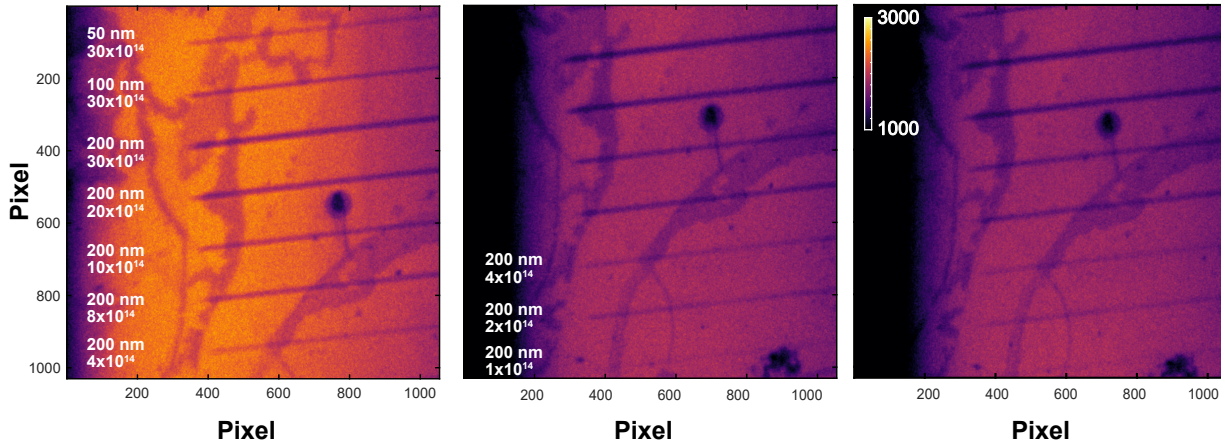

Figure 3.46: XPEEM images showing features and beam damage with exposure

Exposure control: One main consideration while doing an XPEEM experiment is to control the exposure. Extremely high brilliance beam is focused to a small micron size spot increasing the resonant flux density extremely high. Resonant X-rays tune to the valence electrons and can damage the film for such high flux density. thus at the beginning of the experiment, we found a region to test our exposure and find the optimum exposure such that the sample electronic environment is not altered while we have sufficient count to discern 30 nanometer scale features which is the instrument resolution. We found that for our film both pristine and helium-implanted region are damaged with long exposure. By trial and error, we found that a slit

opening of 80×500 μm with 0.5 s exposure was optimum. To increase the statistics we repeated each scan 8 times at a given input energy. The beam was incident on the sample at an angle of 45° and an Au foil was inserted in the beam path to further decrease the flux. To make sure we have not damaged the sample while collecting data we collected a reference image before and after the spectro-microscopy scan. In the region of interest, we collected more images after the data collection to show the effect of X-ray radiation. From left to right the exposure time increases and the photoelectron count drops. All panels are scaled to the same colormap to highlight this feature. Furthermore, we realized that at low temperatures the beam damages are sustained better by the sample. Thus, we cooled the sample down to ∼160K while collecting data.

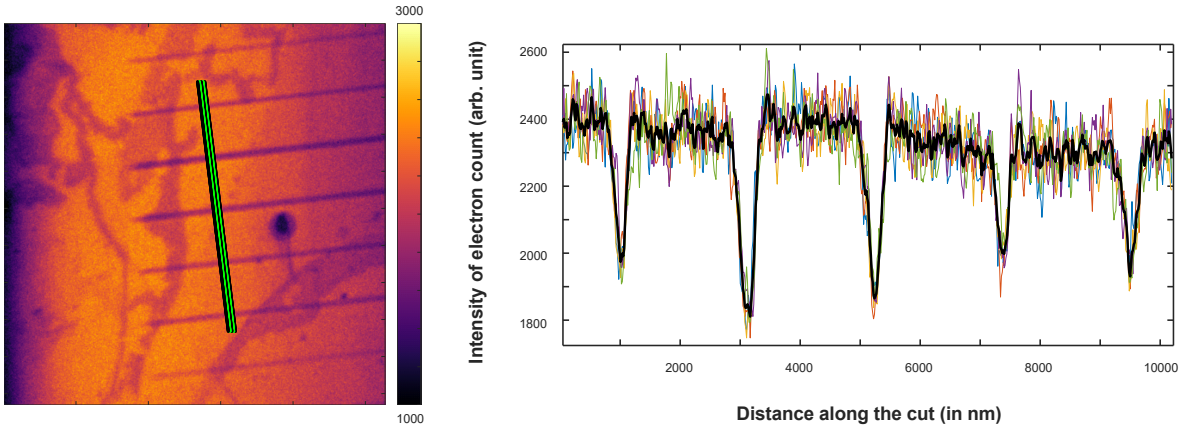

Figure 3.47: Taking cuts on the X-PEEM images and verifying widths

Result: The figure 3.46 provides the first evidence of our ability to write localized patterns of a different electronic state. The sample is not etched but only the substrate underneath is implanted with helium. We observe that the pattern written with a helium dose of 30e14 IPSC is the most prominent. The image is taken with the Ni-L3 resonance of energy which we had been referring to as peak B. Thus the implanted regions appear dark. We have taken multiple

cuts along the perpendicular direction to the elongation of the stripe. We averaged the cuts to smoothen out the fluctuations and extract the width of each artificially patterned electronic feature. the extracted data and the intended design is shown in the table below:

Table 3.9: Extracted width compared with intended design of the artificial electronic pattern

dose	intended thickness (nm)	extracted thickness (nm)
8e14	200	210
10e14	200	210
20e14	200	225
30e14	200	255
30e14	100	180

We extracted the width of each line from the full width at half-max of the intensity profile. It is worth noting that the intensity from the helium-implanted regions increases with lower dose thereby decreasing the contrast. To understand this we conduct a spectroscopy experiment with resolution of 28nm. the intention to compare the the total electron yield from the uniformly implanted sample with a localized implanted region. We want to make sure that the region implanted with 30e14 IPSC behaves electronically similar to the sample we studied in previous section.

We have so far shown that the focused helium implanted region is electronically different from the pristine region. The continually decreasing trend of the contrast from the cuts in the previous figure is a first hint that they are different from each other as well. However, we want to confirm if the continuous tunability of the electronic phase observed during the uniform helium implantation still survives in the focused implantation limit. We compared the XAS TEY measured on the uniformly implanted samples with the total count from a well-defined region as we ramped the energy of the incoming beam. Thus they should be directly comparable. Furthermore, we set the polarization to be vertical and with 45° incidence angle we have an equal contribution from the in-plane and out-of-plane components. For the tey measured in the uniformly implanted samples we have also averaged the polarization for direct comparison. Since

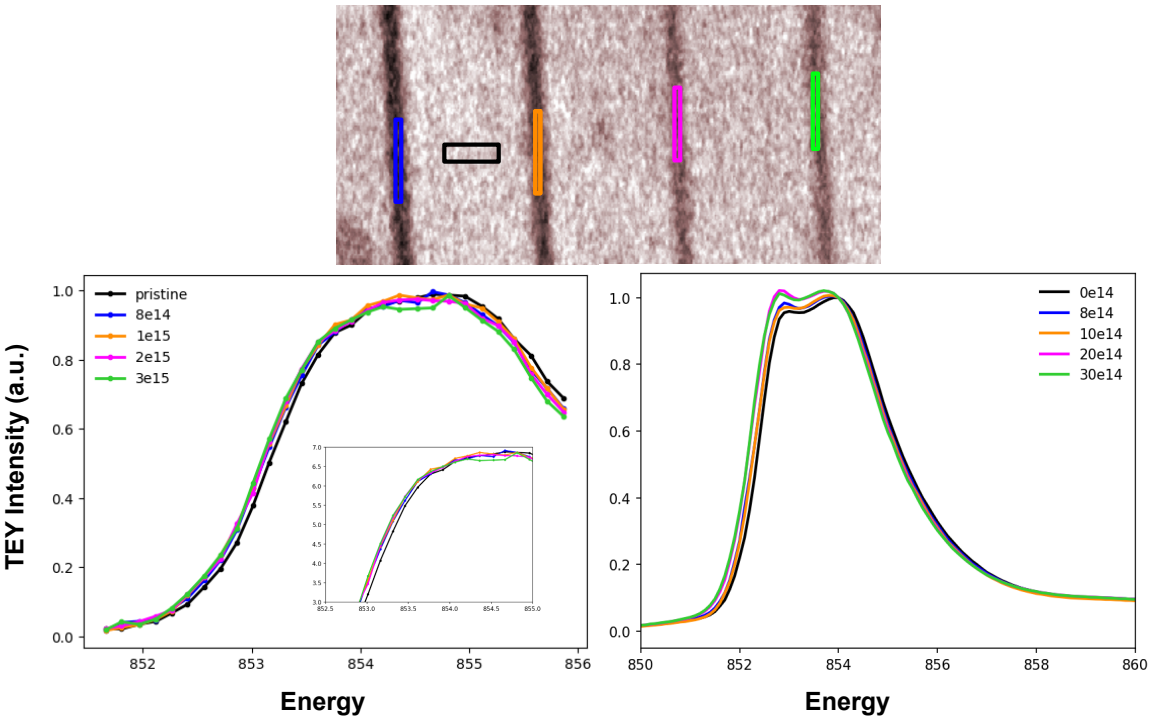

Figure 3.48: X-ray Absorption characterization confirming electronic phase tuning

the energy resolution in XPEEM is poorer than the energy resolution of the XAS beamline we only see a qualitative match. This is shown in the Fig below where we have shown side by side the XAS collected from the $PrNiO_3$ samples implanted with uniform dose of 0,8,10,20, and 30e14 IPSC with the XAS extracted from defining an region of interest as the small boxes and averaging the count in the boxes for each energy. We see an increase in weight for the states near the E_A peak with increasing helium dose for both uniformly and focused helium implantation. This result proves that the focused helium implantation changes the electronic configuration similar to a uniform helium implantation. Thus, the suppression of the phase transition will be observed in this localized region. This is precisely what we wished for. If we lower the temperature on this sample the helium-implanted region will not turn into an antiferromagnetic insulator whereas the pristine region will become antiferromagnetic creating an artificial lateral antiferromagnetic

texture.

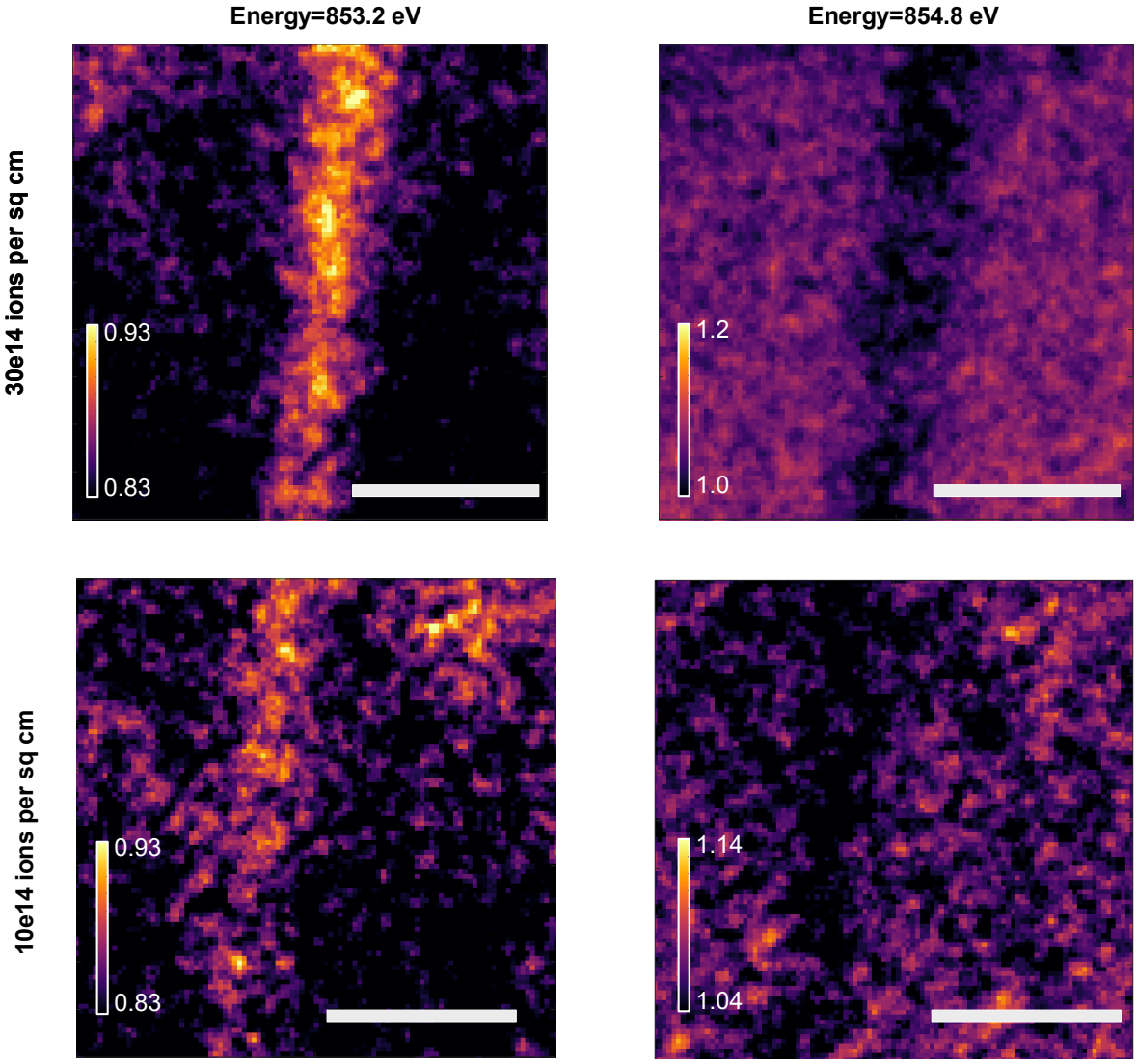

Figure 3.49: Spectromicroscopy observed on the 30e14 and 1e14 IPSC lines showing a greater spread but better uniformity for the 30e14 IPSC lines.

Before we move onto that final step of this project of creating and verifying antiferromagnetic texture, we note the heterogeneity of the pulsed laser deposited samples which can be seen in the spectromicroscopy images taken at the B-peak in the Ni-L3 resonance profile. that heterogeneity survives inside the implanted region indicating that the individual grains of the thin

film remain undisturbed by helium dose as high as 30e14 IPSC. From the width evaluation, we found that for the dose of 30e14 IPSC may the feature spreads more than the intended dimension however that dose provides us with the cleanest line profile as seen from the comparative figure 3.49. This is also evidenced by the smooth drop of the line profile in Fig 3.47.

3.6.2 Resonant Coherent soft X-ray scattering:

We have confirmed so far that with helium implantation we can locally tune the electronic configuration of the nickelates. The room temperature electronic state was found similar between the locally tuned and uniformly implanted sample. Since the electronic state at high temperature was similar to the uniformly implanted sample we expect that it will undergo the coupled phase transition similarly. Thus, for the selected implantation dose of 30e14 IPSC the helim implanted $PrNiO_3$ film should not undergo the coupled phase transition down to liquid helium temperatures whereas, the implanted $NdNiO_3$ film should show an antiferromagnetic transition around 90K. Thus if we set the temperature above 100K we expect to observe implanted regions to remain paramagnetic while the pristine region will turn into antiferromagnet.

The pattern we created along with the sample fabrication details is shown in the figure 3.50 below. The intention was to implant the lines of helium equally spaced over a region on the order of 20μm. We patterned two regions: one with 500nm wide implanted regions separated by 200nm pristine region, and the other with 1000 nm wide implanted regions separated by 200 nm pristine region. We used a dose of 30e14 IPSC. We wanted to create an antiferromagnetic grating which will leave the signature of its periodicity on the reciprocal space reflection on the magnetic peak as a small-q modulation. The spatial parameters were motivated from forward modelling the scattering outcome discussed below. With these considerations we set out to fabricate the focused ion implanted samples.

Sample fabrication: As deposited thin film samples were used to developed patterns at helium microscope of Quantitative Biosciences at UC Berkeley (QB3-Berkeley). The implantation

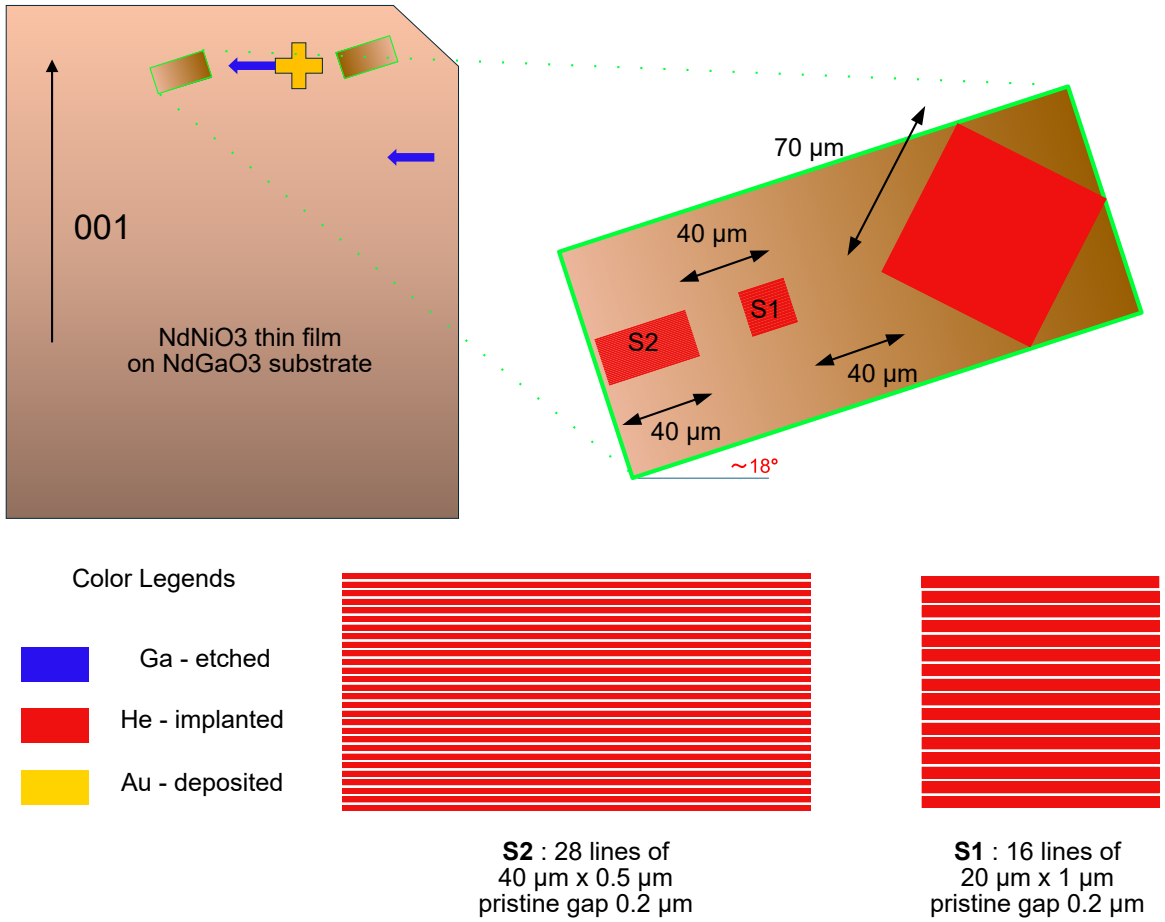

Figure 3.50: Sample fabrication: focused helium beam implanted $NdNiO_3$ thin film with grating like pattern S1 and S2. Detailed dimensions are shown in the figure along with the fiducial marks. The pattern is rotated by 18° with respect the edge to have the grating modulation along perpendicular direction to scattering plane.

energy was 30 keV. From our evaluation this is sufficient for the ions to pass through the thin film and get implanted into the subtrate about 100 nm below the interface. Such high energy helium was focused on the sample plane using the electro-magnetic lenses. The beam current was set at 3.36 pA with a dwell time of 1 μs which deposited 30e14 IPSC in a region. Before taking the sample to the helium facility we deposited gold fiducial according the experiment at hand. Unlike the XPEEM experiment, nano-diffraction experiment usually demands creating microstructures

to be investigated near the edges of the sample due to the limitation from zone plate optics.

Fresnel zone plate is used to focus the beam on the sample for nano-diffraction measurements which is discussed in detail in chapter 6. However for the present discussion we note that an order sorting aperture is required for the zone plate and is placed between the zone plate and the sample. For example, at CSX-23 ID beamline where we investigated the helium implanted patterns the approximate separation between the zone plate and the OSA was approximately 8.6 mm for a focal length of the zone plate at 10.3114 mm with a depth of focus of 6 μm at 852 eV. Thus the sample to OSA separatio is only about 1.72 mm. Thus, if we have a sample which requires the zone plate-OSA assembly to move 2mm downstream to focus on a point 2mm inside the edge of the sample, then the assembly would crash. This mechanical limitation motivates us to design patterns near the edge of the sample so that we have sufficient room for the zone plate assembly.

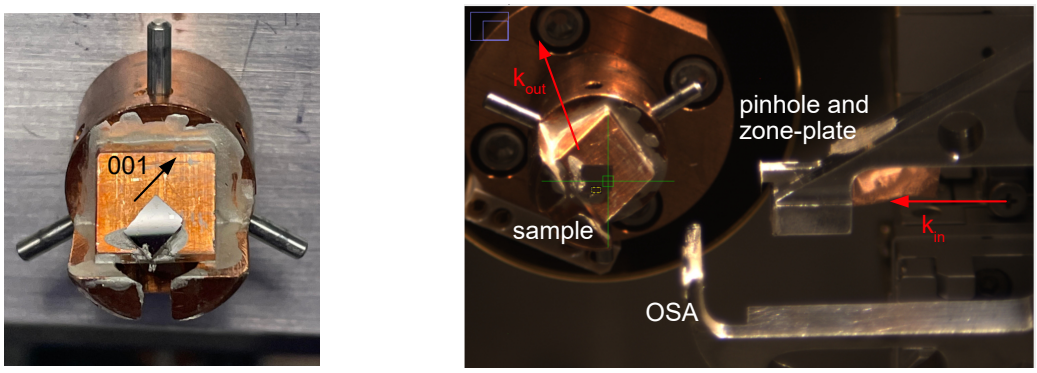

Figure 3.51: Experimental set up and mounting of the sample: (left) We mounted the sample rotated by 45° in ϕ and on a wedge to provide the χ tilt of 54° (right) the beam propagation direction along with the optics assembly used for this experiment. The optics assembly can move along the beam or perpendicular to the beam. During nano-diffraction we scanned the zone plane and OSA together in the plane perpendicular to the beam propagation.

In nano-diffraction measurements it is useful to write different scales of fiducial from microscopic length scale to the length scale of intended feature so that at every step of zooming in we have fiducial marks to act as guides. This is what we describe here. We deposited a gold

cross of $\sim$ 250 μm followed by a Ga etched arrow of similar dimension. We later realized during the experiment that the Ga etching was not required. Then we implanted a region of 70 x 70 μm^2 on both sides of the gold cross. Right next to the helium implanted region we drew the patterns. Each pattern contains one region of 16 lines of implanted regions with dimensions of 1μm$\times$20μm with 200 nm spacing in between (S1), and 28 lines of of implanted regions with dimensions of 0.5μm$\times$40μm with 200 nm spacing in between (S2). The implanted regions will remain paramgnetic below the transition with the pristine regions becoming antiferromagnetic. Thus S1 and S2 will have 200 nm wide line of antiferromagnetic regions separated by 1000 nm and 500 nm of paramagnetic regions, respectively. Thus, if we see the modulation in the scattered intensity due to the antiferromagnetic grating the modulation will have different spatial frequency. We further developed M1 to M4 which are implanted regions of 4x4 μm^2 area with a pristine square hole of 100nm to 500nm side-length at the center. However, due to time limitations we could not finish our investigation on them. **Coherent resonant soft X-ray scattering:** The

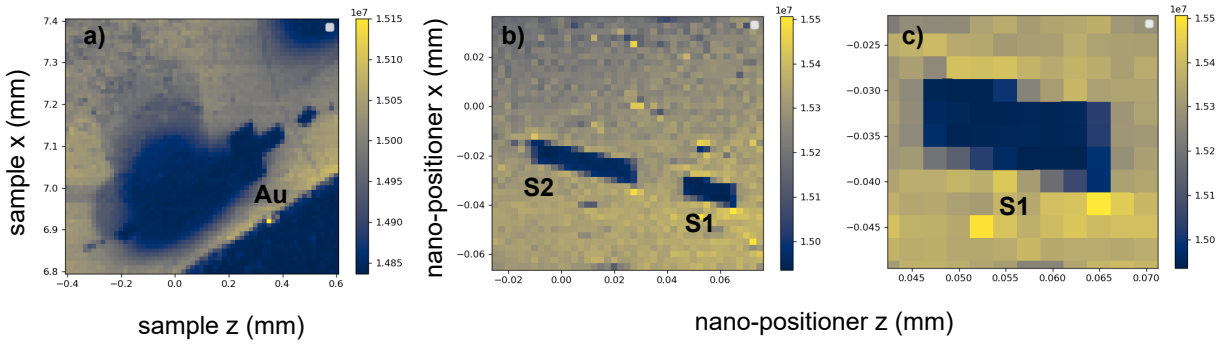

Figure 3.52: Finding the pattern through guidance by the fiducial. (left to right) We find a feature at a scale and zoom in to find the next feature on that scale till we reached S1

samples were created right before the experiment date and was not heated or treated by anything other than acetone coated wipe to clean the surface. The sample was then mounted on a wedge similar to the experimental conditions decribed in Chapter 3. With the sample mounted like

that we set the polarization to π and energy to the Ni-L3 edge at 853 eV. All other experimental conditions pretty much resembled the experiment described in the previous chapter with only one crucial difference: we used Fresnel zone plate with OSA and not a pinhole. We lowered the temperature to 112 K where the pristine sample showed a clear AFM peak at $(\frac{1}{2}, 0, \frac{1}{2})$. We know from our investigation of the uniformly implanted sample that at this temperature the implanted $NdNiO_3$ must remain metallic-paramagnet. We killed the feedback correction to the diffractometer motors after aligning the diffractometer properly to the antiferromagnetic peak so that it does not influence our positioning. For the rest of the experiment we moved the sample position or rastered the beam using nano-positioners which can move the optics over the beam to move the focus on the sample.

Since the depth of the focus of the zone plate is roughly 6 μm at the diffraction condition of $\theta = 55^\circ$, $\phi = 45^\circ$, and $\chi = 54^\circ$ (where the last two angular motion were provided by how we mount the sample on a wedge) it is very easy to become out of focus if we are traversing the beam on the sample. Thus it is important to fix the distance of the zone plate-OSA assembly by rastering over a known feature on the sample and making sure that the contrast of the feature is the best for the selected distance among many other choices. This optimization of the zone plate is an added condition for zone plate based coherent scattering. For our experiment, we checked the contrast on the antiferromagnetic gratings (S1 and S2) to be investigated to fix the distance of the zone plate-OSA assembly. We conducted the experiment in two different modes both effectively showing the same information. First we conducted a nano-diffraction experiment which is a scanning mode experiment to investigate the texture. At the diffraction condition set to the AFM peak we scanned the beam on the sample using nano-positioners. Here we measured the total scattered intensity for every point the beam landed on the sample. We scanned with a resolution of 100 nm steps with the a focus size where the contrast of the features were maximum. The nano-diffraction measurements on the patterns S1 and S2 crealy showed the beam spot convoluted intensity modulation due to the the grating pattern we intended to create. This is a clear proof

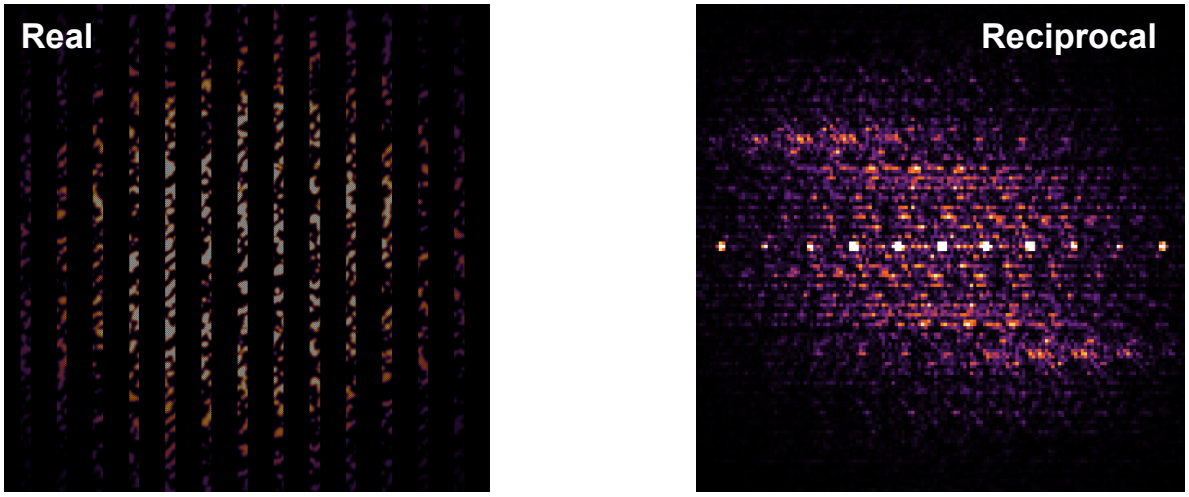

Figure 3.53: Modelling of the experiment and expectation from the grating pattern for a defocused coherent illumination. The reciprocal space pattern is just the amplitude Fourier transform of the left panel. We see super-modulation due to the artificial grating structure imposed on the natural antiferromagnetic domain formation.

that at low temperature the implanted areas remains paramagnetic but the pristine areas become antiferomagnetic. From our measurement we can also find the separation between the pristine regions and see that it is approximately double for the S1 pattern as expected.

Another way we find the signature of the AFM grating is on the single shot scattered intensity recorded on the detector. This is a remnant of the discussion we had in chapter 3 where meso-scale dilute patterns leave its mark on the intensity modulation on the Bragg peak. When the zone plate position is not optimal the beamspot is not tightly focused on the sample and we have a broad beam covering multiples of the fringes and we see a clear supermodulation on the scattered intensity as shown in the figure below. The frequency of modulation(Δq) is inversely related to the separation of two antiferromagnetic strips. Since S1 has twice the separation in real space than S2, the separation of fringes on the AFM Bragg peak is lower by a factor of 2.

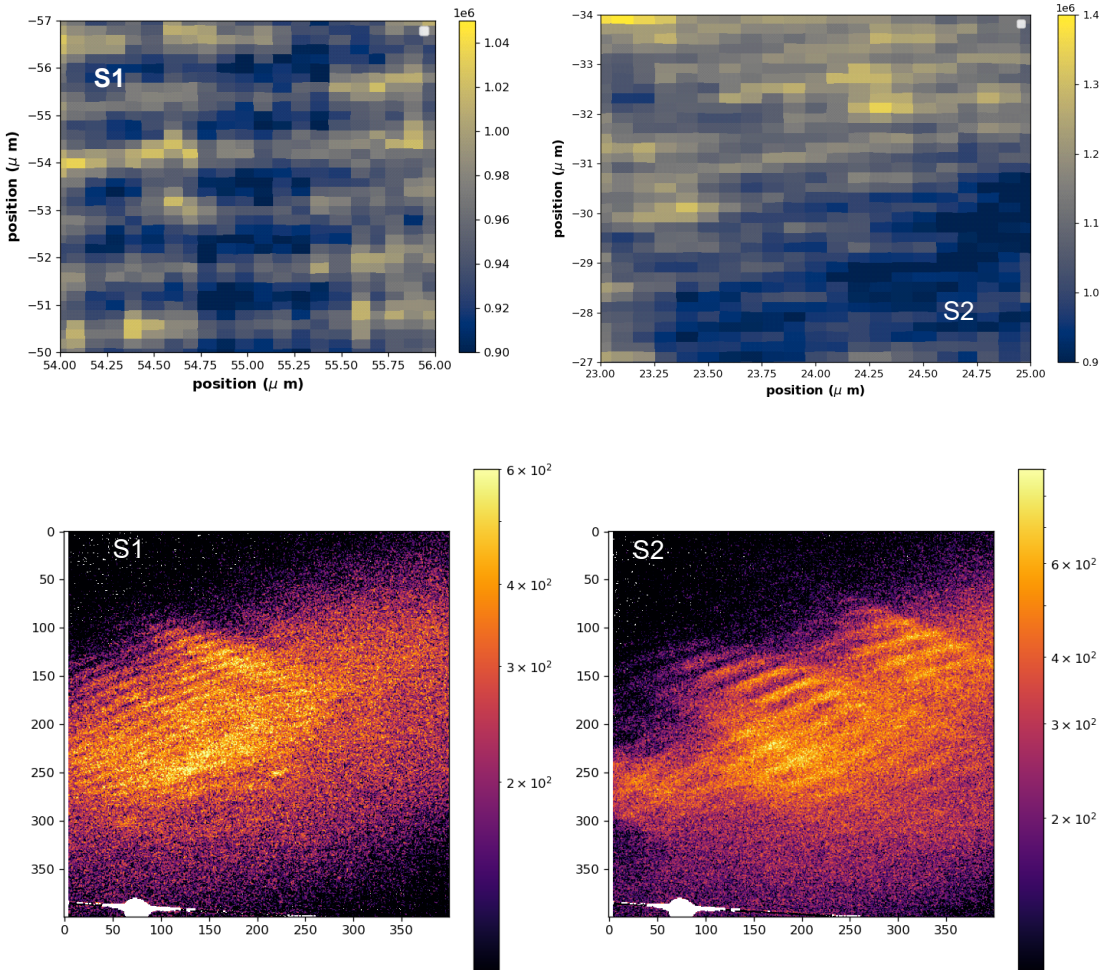

Figure 3.54: Nano diffraction measurement (top row) and Coherent resonant scattering on the AFM grating (bottom row) the bottom row is shown in pixels

Thus we comprehensively prove the existence of an antiferromagnetic grating structure created artificially in a strongly coupled antiferromagnetic thin film using focused helium ion implantation.

3.7 Conclusion

In this chapter we achieved tuning electronic character of a strongly correlated electronic system through strong-electron lattice coupling. We modified the lattice and through which changed the electronic character by helium implantation. We showed here that implantation of helium ion into the substrates changes the uniaxial out of plane strain for the epitaxial film while keeping the in-plane biaxial strain unperturbed. We also observed that the helium implantation did not change the electron-lattice coupling and we could increase the itinerant character of the d-electron by tuning the strain along the out-of-plane direction only. We monitored the change in bond order, charge order, transport and magnetic order of the sample.

The magnetic order revealed a change in character of the magnetism. Following the change in the localized character and decrease in the Bond order we believe we gradually changed the electronic environment for the d-electrons from a *site selective Mott transition* to *Fermi surface guided density wave transition*. This is continually tunable and proportional to the helium dose we offer. This way we have shown a controlled mechanism of strain tuning on rare earth nickelates and tuned the nature of electronic correlation. Such degree of control in tunability post growth of epitaxial nickelate can be used to further expand the phase diagram like we did here. For example, we can employ the same techniques on oxygen deficient nickelates or hole doped nickelates to check for the effect. From our X-ray absorption spectroscopy measurement we showed that the high temperature electronic state was also modified in this process. Thus we have shown that we can change the correlation in a bad metal state by the uniaxial strain tuning, which can be further employed other relevant materials.

We can further follow up on the project by studying the fluctuations in the implanted samples by X-ray photon correlation spectroscopy. How the fluctuation changes as we increase the helium implantation and relates to electronic phase can be an important study characterizing the dynamic charge correlation in this material. In [21], the authors numerically found significant

evidence for dynamic charge correlation which can influence the magnetic energy response. We observe the magnetic energy response to change as a function of the helium dose. Thus, to complete the story a follow up work can correlate and highlight the relevance of dynamic charge correaltion measuring it directly.

Furthermore, taking advantage of helium microscope this strain can be tuned locally to create lateral heterostructures. Utilizing experimental methods sensitive to local electronic states we were able to image the lateral heterostructures that we artificially created. We have effectively created a metastable phase of a complex material. Since the implanted region is highly itinerant it will be a curious investigation to follow the effect of two implanted lines on the pristine layer between them. We can study the fluctuation on an ordered peak such as the magnetic Bragg peak measured on a patterned region. This will be an interesting problem in mesoscopic physics of such complex materials. With promise of so many interesting physics question around the new physical system we have created we conclude this section.

Bibliography

[1] S. Middey, J. Chakhalian, P. Mahadevan, J. W. Freeland, A. J. Millis, and D. D. Sarma. Physics of Ultrathin Films and Heterostructures of Rare-Earth Nickelates. *Annual Review of Materials Research*, 46(Volume 46, 2016):305–334, July 2016. Publisher: Annual Reviews.

[2] Hangwen Guo, Shuai Dong, Philip D. Rack, John D. Budai, Christianne Beekman, Zheng Gai, Wolter Siemons, C. M. Gonzalez, R. Timilsina, Anthony T. Wong, Andreas Herklotz, Paul C. Snijders, Elbio Dagotto, and Thomas Z. Ward. Strain doping: Reversible single-axis control of a complex oxide lattice via helium implantation. *Phys. Rev. Lett.*, 114:256801, Jun 2015.

[3] C Toulouse, J Fischer, S Farokhipoor, L Yedra, F Carlà, A Jarnac, E Elkaim, and P Fertey. Patterning enhanced tetragonality in BiFeO3 thin films with effective negative pressure by helium implantation. *PHYSICAL REVIEW MATERIALS*, 2021.

[4] Frances I Allen. A review of defect engineering, ion implantation, and nanofabrication using the helium ion microscope. *Beilstein Journal of Nanotechnology*, 12:633–664, July 2021.

[5] A. Herklotz, A. T. Wong, T. Meyer, M. D. Biegalski, H. N. Lee, and T. Z. Ward. Controlling Octahedral Rotations in a Perovskite via Strain Doping. *Scientific Reports*, 6(1):26491, May 2016. Publisher: Nature Publishing Group.

[6] Vinit Sharma, Andreas Herklotz, Thomas Zac Ward, and Fernando A. Reboredo. Designing functionality in perovskite thin films using ion implantation techniques: Assessment and insights from first-principles calculations. *Scientific Reports*, 7(1):11166, September 2017. Publisher: Nature Publishing Group.

[7] Valentina Bisogni, Sara Catalano, Robert J. Green, Marta Gibert, Raoul Scherwitzl, Yaobo Huang, Vladimir N. Strocov, Pavlo Zubko, Shadi Balandeh, Jean-Marc Triscone, George Sawatzky, and Thorsten Schmitt. Ground-state oxygen holes and the metal–insulator transition in the negative charge-transfer rare-earth nickelates. *Nature Communications*, 7(1):13017, October 2016. Publisher: Nature Publishing Group.

[8] Hyowon Park, Andrew J Millis, and Chris A Marianetti. Site-selective mott transition in rare-earth-element nickelates. *Physical review letters*, 109(15):156402, 2012.

[9] Bayo Lau and Andrew J Millis. Theory of the magnetic and metal-insulator transitions in r nio 3 bulk and layered structures. *Physical Review Letters*, 110(12):126404, 2013.

[10] Alexandru B Georgescu and Andrew J Millis. Quantifying the role of the lattice in metal–insulator phase transitions. *Communications Physics*, 5(1):135, 2022.

[11] Oleg E Peil, Alexander Hampel, Claude Ederer, and Antoine Georges. Mechanism and control parameters of the coupled structural and metal-insulator transition in nickelates. *Physical Review B*, 99(24):245127, 2019.

[12] Matthias Hepting, Matteo Minola, Alex Frano, Georg Cristiani, G Logvenov, E Schierle, M Wu, M Bluschke, E Weschke, H-U Habermeier, et al. Tunable charge and spin order in prnio 3 thin films and superlattices. *Physical Review Letters*, 113(22):227206, 2014.

[13] A Frano, E Schierle, MW Haverkort, Y Lu, M Wu, S Blanco-Canosa, U Nwankwo, AV Boris, P Wochner, G Cristiani, et al. Orbital control of noncollinear magnetic order in nickel oxide heterostructures. *Physical Review Letters*, 111(10):106804, 2013.

[14] SungBin Lee, Ru Chen, and Leon Balents. Landau theory of charge and spin ordering in the nickelates. *Physical review letters*, 106(1):016405, 2011.

[15] SungBin Lee, Ru Chen, and Leon Balents. Metal-insulator transition in a two-band model for the perovskite nickelates. *Physical Review B*, 84(16):165119, 2011.

[16] Jong-Woo Kim, Yongseong Choi, S. Middey, D. Meyers, J. Chakhalian, Padraic Shafer, H. Park, and Philip J. Ryan. Direct Evidence of the Competing Nature between Electronic and Lattice Breathing Order in Rare-Earth Nickelates. *Physical Review Letters*, 124(12):127601, March 2020.

[17] Y. Lu, A. Frano, M. Bluschke, M. Hepting, S. Macke, J. Strempfer, P. Wochner, G. Cristiani, G. Logvenov, H.-U. Habermeier, M. W. Haverkort, B. Keimer, and E. Benckiser. Quantitative determination of bond order and lattice distortions in nickel oxide heterostructures by resonant x-ray scattering. *Physical Review B*, 93(16):165121, April 2016.

[18] Alexandru B. Georgescu and Andrew J. Millis. Quantifying the role of the lattice in metal–insulator phase transitions. *Communications Physics*, 5(1):1–14, May 2022. Publisher: Nature Publishing Group.

[19] John W. Freeland, Michel van Veenendaal, and Jak Chakhalian. Evolution of electronic structure across the rare-earth RNiO3 series. *Journal of Electron Spectroscopy and Related Phenomena*, 208:56–62, April 2016.

[20] Ankit S. Disa, Alexandru B. Georgescu, James L. Hart, Divine P. Kumah, Padraic Shafer, Elke Arenholz, Dario A. Arena, Sohrab Ismail-Beigi, Mitra L. Taheri, Frederick J. Walker, and Charles H. Ahn. Control of hidden ground-state order in NdNi O 3 superlattices. *Physical Review Materials*, 1(2):024410, July 2017.

[21] R. J. Green, M. W. Haverkort, and G. A. Sawatzky. Bond disproportionation and dynamical charge fluctuations in the perovskite rare-earth nickelates. *Phys. Rev. B*, 94:195127, Nov 2016.

[22] SungBin Lee, Ru Chen, and Leon Balents. Landau Theory of Charge and Spin Ordering in the Nickelates. *Physical Review Letters*, 106(1):016405, January 2011.

Chapter 4

Phase Competition in Fe intercalated NbS_2

4.1 Introduction

Phase competition and phase coexistence are ubiquitous in strongly correlated electronic systems. When multiple electronic degrees of freedom such as spin, orbital, charge, and lattice couple to each other a spatially inhomogeneous ground state often emerges. Such textured material unsurprisingly deviates from linear behavior and small perturbations are met with large responses. High-temperature superconductors are one such example which remains enigmatic to this day. Small tuning of electron or hole doping percentage completely changes the electronic character of the material. Moreover, the superconducting state emerges competing and often coexisting with a charge density wave state. Thus, understanding the phase competition and phase coexistence is attributed to the mystery of understanding the high-temperature superconducting phase of cuprates

To understand phase competition and phase coexistence we need tools to characterize electronic heterogeneity and its evolution under perturbation. Coherent resonant scattering perfectly fits the requirement. On one hand, the resonance condition makes it sensitive to the electronic states, and on the other coherence makes it sensitive to the real space textures. Here we

will explore the potential of coherent resonant scattering to understand phase competition in a highly tunable magnetic material: Fe intercalated NbS_2.

We first discuss previous works that have inspired us to conceive the project: starting with the strange phenomenology of resistance switching observed in this material and subsequent in-depth study of highly tunable magnetic ground state explored by neutron scattering . Then we discuss our discovery of a concomitant charge order state that couples to an external magnetic field providing us with sufficient evidence for a strongly coupled electronic environment. Finally, we characterize phase competition in such a system using coherent resonant soft X-ray scattering.

4.2 Phenomenology of Fe_xNbS_2

$Fe_{\frac{1}{3}+\delta}NbS_2$ is formed intercalating transition metal ions of Fe into van der Waals bonded layers of NbS_2. NbS_2 belongs to the large class of transition metal di-chalcogenides (TMDC, TA_2) with $T = Nb, Ta, V, Mo$ and $A = S, Se$. Two-dimensional TMDCs host coupling of electronic degrees of freedom making them attractive not only for studies of basic physical phenomena but also for technological applications. These materials are a prototypical example of the charge density wave phase emerging from the Fermi surface instabilities of weakly interacting itinerant electrons at low temperatures. They also host phonon-mediated superconductivity at lower temperatures. However, NbS_2 stands out of the pool by being the only TMDC to host superconductivity without a charge density wave state indicating a different electron correlation environment.

Structure: Including Fe atoms in between chalcogen layers increases the electronic correlation in this system. For TMDCs there are two thermodynamically stable phases: 2H or trigonal prismatic and 1T or distorted octahedral, categorized following the stacking of transition metal and chalcogen atoms (see Fig). For stoichiometric intercalation of $x = \frac{1}{3}$ in the formula unit of Fe_xNbS_2 the Fe atoms arrange into a stacked bilayer arrangement of $\sqrt{3} \times \sqrt{3}$ super-lattice in

between layers of 2H-NbS_2. Such an arrangement breaks the inversion symmetry of the crystal unit cell which results in a spin splitting of the electronic bands driven by spin-orbit interaction.

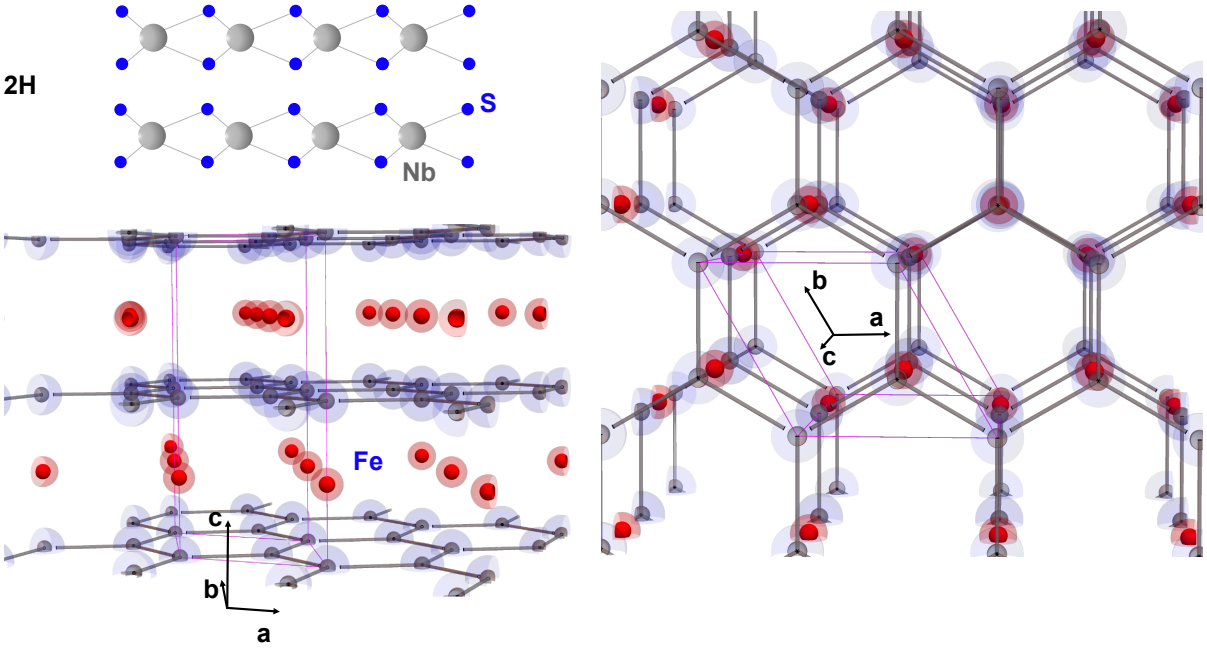

Figure 4.1: Structure of $Fe_{1/3}NbS_2$

Thermodynamic Characterization: Firstly, the intercalation supresses the superconducting transition of the parent compound, NbS_2. From room temperature down to 2K the system remains metallic (Fig). On the other hand, magnetic susceptibility measurement shows two magnetic transitions: at $T_{N1} = 45K$ and $T_{N2} = 41K$, both of which host an antiferromagnetic state below the transition temperature. The in-plane resistivity and susceptibility (in-plane and out-of-plane) are shown in Fig 2. Contrasting the in-plane susceptibility measurement with the out-of-plane direction it was expected to have the moments of the spins in the antiferromagnetic order aligned along the [001] direction.

The broken inversion symmetry of the unit cell makes it an ideal candidate for spin-orbit

coupling, and subsequently for spintronic applications. To understand the role of inversion symmetry let's consider an electron in a magnetic field $\mathbf{B}$ moving with a momentum $\mathbf{p}$. Then the force experienced by the electron is $\mathbf{F} = \frac{-e}{m}\mathbf{p} \times \mathbf{B}$. We can interpret this as an effective electric field experienced by the electron in its rest frame as

$$\mathbf{E}_{eff} = \mathbf{p} \times \mathbf{B}/m$$

By electromagnetic duality transformation ($\mathbf{E} \to c\mathbf{B}$ and $c\mathbf{B} \to -\mathbf{E}$) then an electron in an electric field $\mathbf{E}$ will experience in its rest frame an effective magnetic field of strength

$$\mathbf{B}_{eff} = \mathbf{E} \times \mathbf{p}/(mc^2)$$

The Zeeman splitting due to this magnetic field will include a term in the Hamiltonian describing such system. Thus, in its rest frame where the electron experiences this magnetic field, the energy level will be split for two different spins of the electron with the symmetry allowed spin-orbit Hamiltonian $H_{SO} \propto \mathbf{E} \times \mathbf{p} \cdot \sigma$, where σ is the spin Pauli matrix. Since this term in Hamiltonian must preserve time-reversal symmetry, under which $\sigma \to -\sigma$ and $\mathbf{p} \to -\mathbf{p}$, the term involving the momentum must also change its sign, i.e. $\mathbf{E} \times (-\mathbf{p}) = -\mathbf{E} \times \mathbf{p}$. Hence in general for $H_{SO} = f(\mathbf{E}, \mathbf{p}) \cdot \sigma$, $f(\mathbf{E}, \mathbf{p})$ must then be an odd-function of $\mathbf{p}$. This necessitates breaking the spatial inversion symmetry. Now that our set-up is ready to discuss the incredible spintronic phenomenology we dive straight into it.

Electrical Switching: The expected charge-spin coupling in this system is evidenced when the application of a direct current pulse switches the resistance of the material in its low-temperature antiferromagnetic ground state between two stable states. The experiment was conducted on an eight terminal device as shown schematically in the figure. The horizontal and vertical pathways were used for DC pulsing the crystal where an AC source of 100 μA fed current through one of the 45° channels. From the perpendicular channel to the AC channel voltage was

measured to extract resistance. For a DC pulse of $5.4 \times 10^4 Acm^{-2}$ density for a duration of $10ms$ across the blue electrodes the authors observed a drop in resistance. A subsequent pulse across the red electrodes revived the resistance.

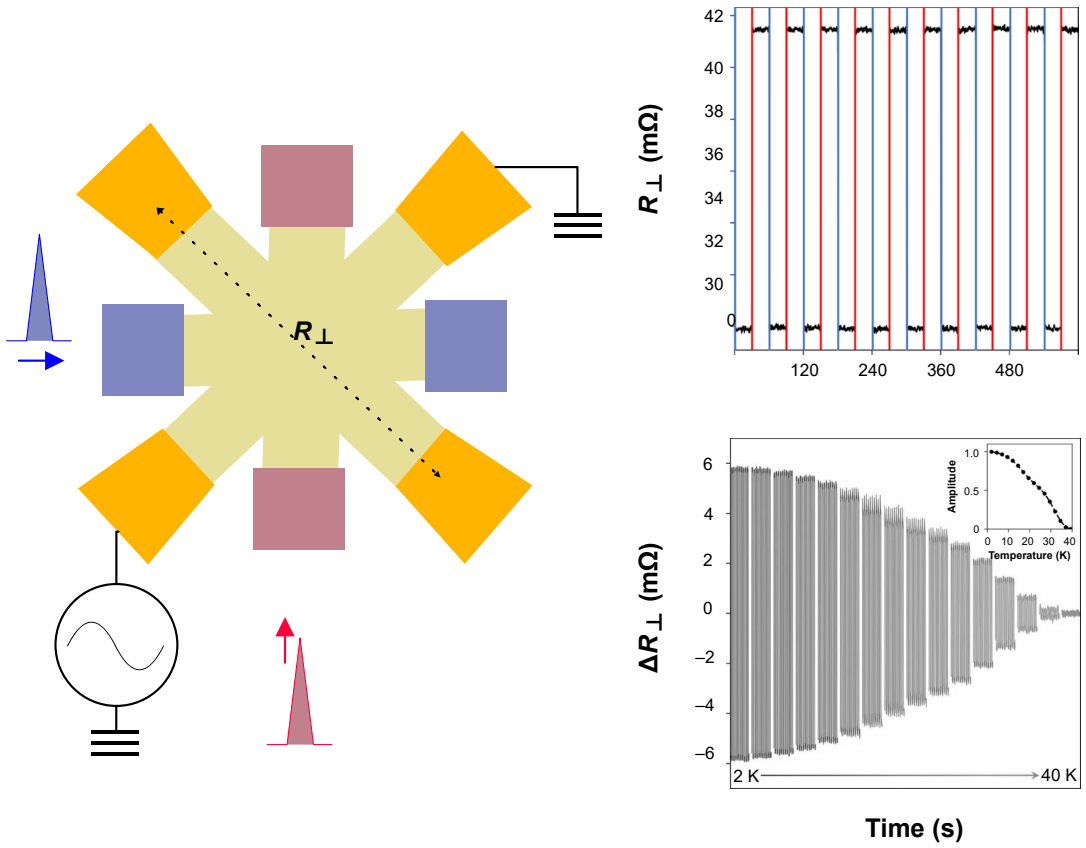

Figure 4.2: **Electrical Switching of FNS coupled to the antiferromagnetic phase**: (left) The eight-pronged device used to measure $R_\perp$ by the authors [1]. They pulsed along the blue pads and the red pads. (right-top) shows the result of the DC pulses on the measured value of $R_\perp$. This resistance switching data is collected at 2K in the stoichiometric sample with x $=\frac{1}{3}$ (right-bottom) we have plotted the switching amplitude as a function of temperature (also inset) showing the collapse of switching above the Neel temperature of the sample

Technologically this was an important step towards antiferromagnetic spintronics and memory application. However, the phenomenon itself posed a scientific challenge to decipher the mechanism of switching. As the system was warmed up above the Neel transition temperature the switching amplitude gradually decreased to 0. Coupling to antiferromagnetic order is thus

crucial for the phenomena. Understanding the antiferromagnetism in this material became of the highest importance. Out of many other possible mechanisms that involved the coexistence of spin glass phase with antiferromagnetic order, it was also suggested that the application of the DC pulse may serve to switch the sample between two distinct anti-ferromagnetic ground states that correspond to the two different resistance values in the measurement.

Antiferromagnetic Order: The out-of-plane susceptibility showed hints of the puzzle where it appeared to have two antiferromagnetic transitions. To gain a thorough understanding of the magnetic phase neutron diffraction measurements along with structural and magnetic susceptibility measurements were carried out on single crystal samples of high quality. However, on top of the stoichiometric sample this time the authors explored off-stoichiometric samples with iron site vacancies (x = 0.32) and interstitials (x=0.35). The stoichiometry was confirmed with energy-dispersive X-ray measurements.

Whereas magnetic defects are usually expected to suppress magnetic correlation and lower the transition temperature, highly tunable long-ranged magnetic phases were discovered as the Fe concentration was varied [2]. The wave vector of the under and over-intercalated samples differed from each other while the stoichiometric samples showed coexistence and competition of those phases. For the under-intercalated sample, the wave vector of the AFM order was found to be $\mathbf{k}_{stripe} = (0.5, 0, 0)$ and termed as the 'stripe' phase for the arrangement similarity of the Fe moments in a layer with stripe pattern. For the over-intercalated sample the wave vector was $\mathbf{k}_{sigzag} = (.25, .5, 0)$ and the AFM phase was named 'zigzag'. We will follow the same naming conventions in this thesis. The neutron diffraction measurements were carried out on individual single crystals with high crystalline quality. Fig shows the complex ground state phase diagram with the stripe and the zigzag phase dominating down to the lowest temperature near under-intercalated and over-intercalated samples respectively. The magnetic moment arrangement in real space is depicted using a magnetic unit cell in three dimensions as well as shown in the triangular Fe lattice planes in between the TMDC layers.

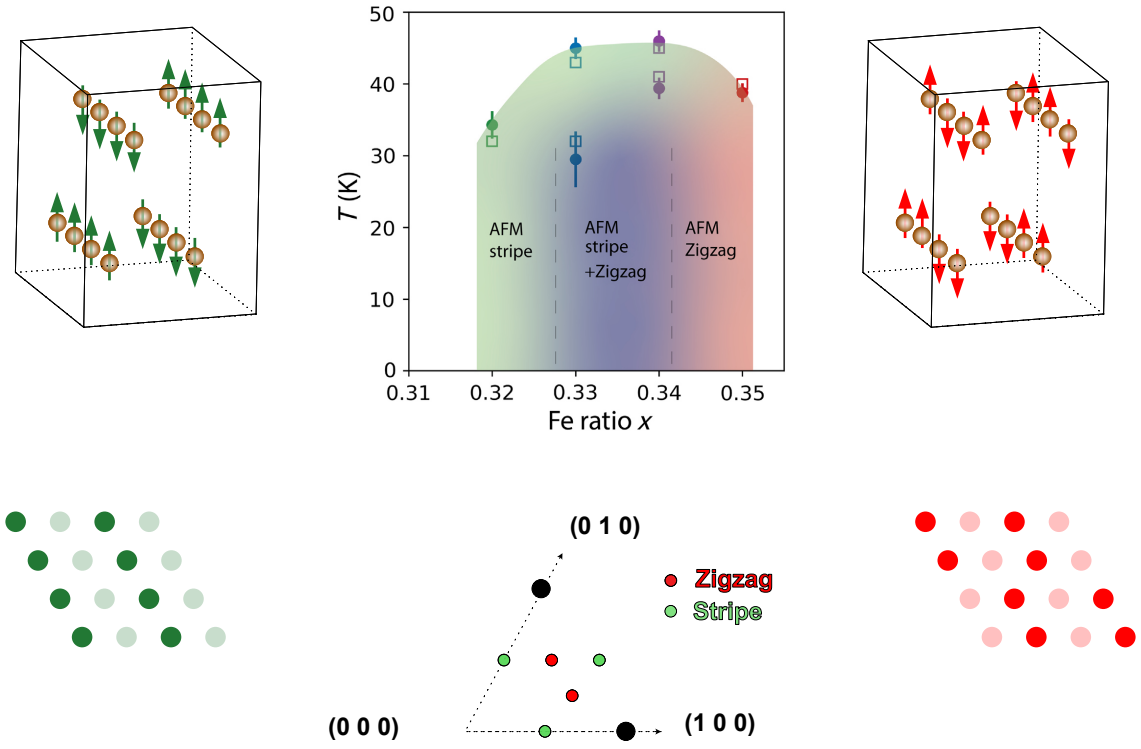

Figure 4.3: **Phase Diagram of Fe_xNbS_2 from neutron scattering:** (top-left) and (bottom-left) shows the spin configuration in the 'stripe' phase on the Fe atoms. Similar diagram is shown for the 'zigzag' phase on the (top-right) and (bottom-right). The dark(light) circles represent spin up(down). (top-middle) panel shows the phase diagram as a function of temperature and Fe itercalation ratio, x adapted from [2]

For the stoichiometric sample, they indeed observed both of these antiferromagnetic states. Around 45K first the stripe phase emerges and then around 41K the peaks related to the zigzag phase also show up. The emergence of the zigzag phase is met with a decrease in the intensity of the AFM peaks related to the stripe phase, indicating a phase competition for the real estate in the sample. This is consistent with the thermodynamic measurements where the out-of-plane susceptibility measurements saw indications of two antiferromagnetic transitions. We show here the key data from the publication where the temperature evolution of the magnetic peaks was measured. The peak positions for the magnetic peaks are shown in the figure along with their temperature evolution. The widths of the peak in all directions were instrument resolution-limited,

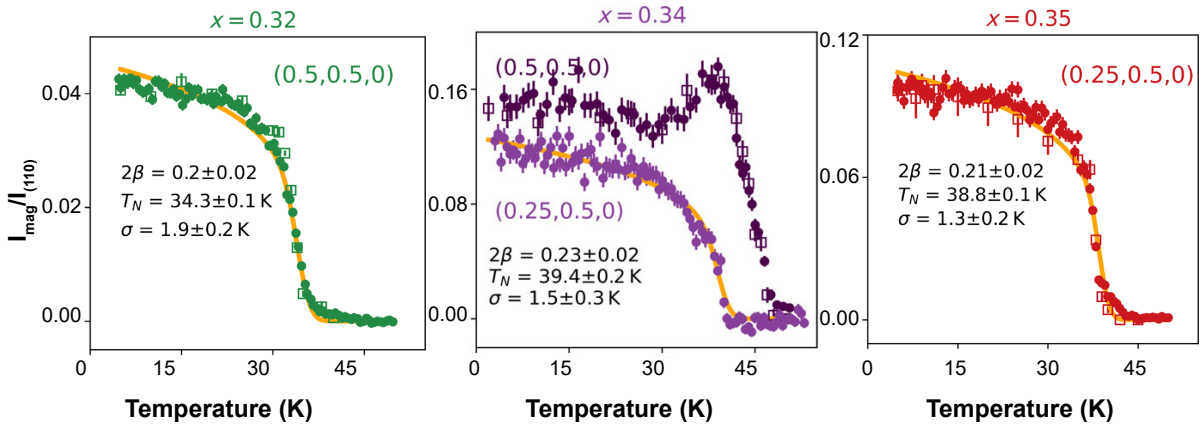

Figure 4.4: Neutron Scattering result

affirming the three-dimensional structure of the magnetic domains. The authors also confirmed that the three-dimensional correlation remains preserved in the stripe phase even with phase competition with the zigzag phase in the $1/3$ intercalated samples. This means that the decrease in intensity observed in the stripe phase peak is not due to the correlation changing from a 3D to a 2D peak shape.

Furthermore, all of the phase transitions were continuous phase transitions. Extracted critical exponent β from the temperature evolution of the magnetic peak intensity showed consistency with 2D Ising model. Below we tabulate their findings about the antiferromagnetic phase in each stoichiometric sample. We also tabulate their lattice parameters for completition. We see that the effect of intercalation only changes the out-of-plane lattice parameter.

The neutron scattering also revealed that the Fe-spin moment orientation is along the c-axis for all samples with negligible in-plane components. This ruled out the spin-glass mediated switching mechanism proposed since an in-plane directionality of the spin-orbit torque would not be able to switch one domain to the other both having moments along out-of-plane direction.

In summary, this sample hosts a strong charge carrier to antiferromagnetic order coupling where the antiferromagnetic phase itself has two possible ground states: stripe and zigzag. They dominate the low-temperature ground state for under-intercalated and over-intercalated samples,

Table 4.1: Key results from the neutron scatteing study [2]

attributes	$x < \frac{1}{3}$	$x \approx \frac{1}{3}$	$x > \frac{1}{3}$
T_N (K)	34	$\sim 45(1^{st})$ $\sim 41(2^{nd})$	39
β	.2	.23	.21
k_{AFM}	(.5, 0, 0)	(0.5, 0, 0)-1^{st} (0.25, 0.5, 0) - 2^{nd}	(0.25, 0.5, 0)
a = b (Å)	5.76	5.76	5.76
c (Å)	12.13	12.15	12.19
space group	$P6_322$	$P6_322$	$P6_322$

respectively. However, for the stoichiometric sample, they compete and coexist. Thus in these samples, an external DC pulse may switch the configuration in favor of one phase switching the resistance.

This brings us to the central question we will try to answer using coherent resonant soft X-ray scattering:

How do the two low-temperature phases compete with each other where the two phases break the high-temperature symmetry differently in a strongly correlated environment?

But we start the discussion, let us first visit the concomitant charge ordering phenomenon associated with the spin ordering in these samples to fully unveil the complexity of these materials.

4.3 Discovery of Charge Order and coupling to AFM phase

With the strong spin-charge coupling observed in this material and suppression of superconductivity with intercalation, we asked the obvious question of whether the antiferromagnetic order could stabilize any charge order. The parent compound is peculiar in the family of TMDCs by not exhibiting any charge density wave order. It was suggested that the anharmonic fluctuation

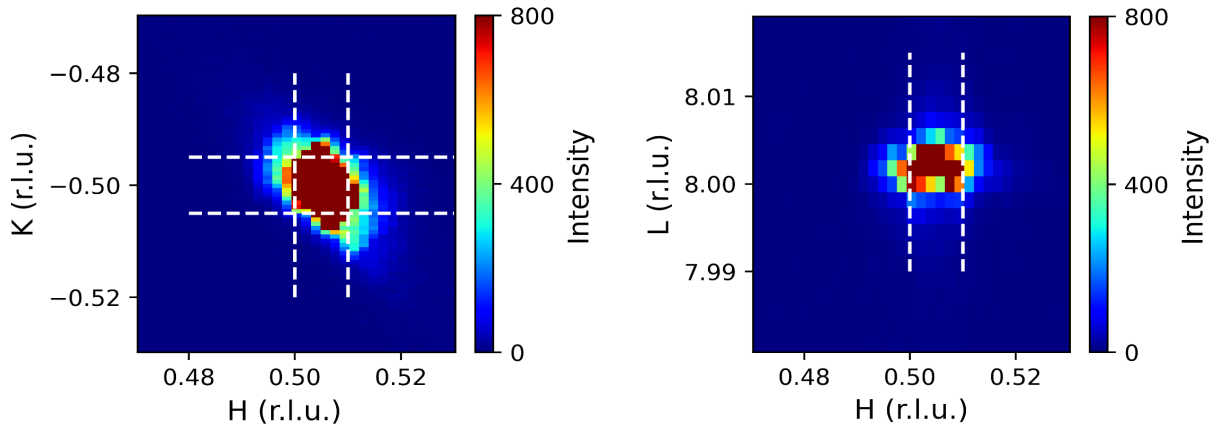

Figure 4.5: **Observed Charge Order peak in the detector** (left) The intensity of the superlattice peak sampled on the HK plane (righ) on the HL plane

of the lattice destabilizes the charge order in the parent compound , which was otherwise close to an instability to charge order due to many-body effects involving competing Coulomb and electron-phon interaction . Furthermore, a recent experimental investigation of diffuse scattering of hard X-rays showed faint charge order peaks at M points i.e. (0.5, 0, 0) wave vector positions attributed to either Friedel oscillations around impurity or extremely faint charge density wave order . We were further lured to search for charge order in intercalated compounds due to the small resistivity kink observed at the Neel transition temperature and optical polarimetry measurement showed three-state nematicity related to the measurement of optical birefringence.

Hard X-ray Scattering experiments were carried out using the psi-circle diffractometer of the 6-ID-B beamline at the Advanced Photon Source, Argonne National Laboratory with an incident photon energy of 10 keV and σ -polarization. The scattered beam was detected with a Dectris Pilatus 100K area detector without polarization analysis. We used high-quality single crystals with Fe ratio of $x = 0.32$ and 0.35, previously measured with neutron scattering . Their mosaicity was determined to be 0.15° in peak width (full width at half maximum, FWHM) on the $(1,0,7)$ atomic Bragg peak. For the $x = 0.32$ sample, we also examined a second small crystal

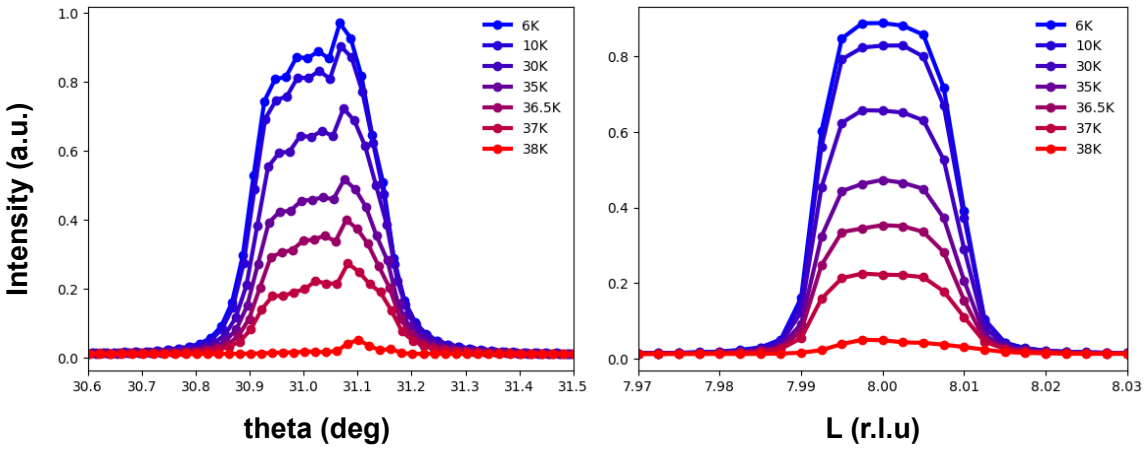

Figure 4.6: **Temperature evolution of the emergent charge order** (left) rocking curve scans on the (0.5, -0.5, 8) peak (right) L-scans to understand the out-of-plane correlation length on the same peak.

with better mosaicity, with FWHM $= 0.02^{\circ}$. The samples were glued to a Cu-post using silver paint and mounted one at a time on the closed-cycle cryostat with Be domes for the X-rays to pass through. The temperature was changed between 5.6 K to 50 K with an instrument resolution and control of 0.1 K.

We first studied the X-ray scattering on the $x = 0.35$ sample, which with neutron diffraction showed a zigzag order with a magnetic wave vector k_{m2} = (0.25, 0.5, 0) below T_N = 38 K. At T =6 K, we observed new superlattice peaks at Q = (0.5, 0, L) and (0.5, 0.5, L) (L = integer values) as seen from the detector image in figure 4.5. We measured six equivalent momentum positions for each Q and confirmed a series of superlattice peaks with half-integer in-plane indices and integer L. At $T = 45$ K, all those peaks disappear, revealing a temperature-dependent behavior. We recognize these super-lattice peaks as the charge order peaks. In what follows we will characterize the intensity to justify our recognition.

Firstly, we note that the peak showcases a three-dimensional correlation. In figure 4.6 we demonstrate the melting of this super-lattice peak from rocking curve scans and L-scans at the peak position of (0.5, -0.5, 8) taken at different temperatures as we warmed the sample from

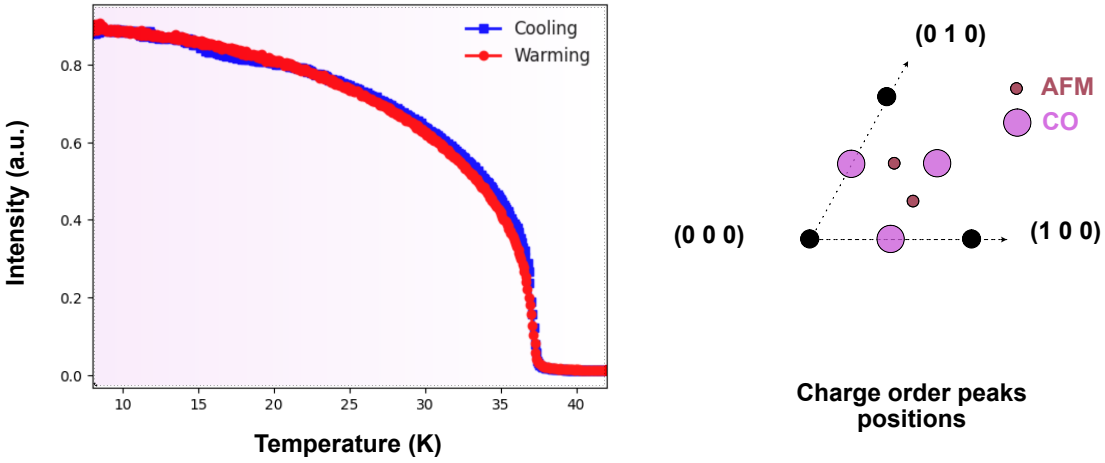

Figure 4.7: **Temperature evolution and Reciprocal location:** (left) warming and cooling on the charge order peak showing no hysteresis and the phase transition to be continuous in nature. The onset temperature is exactly same as the Neel temperature of the sample indicating an antiferromagnetic origin of the charge order (right) position of the charge order peaks and the AFM peaks below the transition temperature along with the Bragg peaks for over-intercalated samples.

base temperature. A well-defined FWHM along the L direction provides further evidence of the three-dimensionality of the charge order.

To characterize the three-dimensional correlation length of the super-lattice order. We have taken reciprocal cuts of a representative peak (0.5, -0.5, 8) equivalent to the (0.5, 0, L) peaks along different high-symmetry directions as shown in figure 4.8. To evaluate the domain size from these cuts we have taken the values of the ends of the FWHM positions on the peak and evaluated $\Delta q = |(H,K,L)_{end2}| - |(H,K,L)_{end1}|$. Then we converted it into real space measurements using $2\pi/\Delta q$. The extracted values are tabulated below and shown in figure.

We observe that the in-plane correlation lengths are longer by a factor compared to the out-of-plane correlation length. It is not surprising that the out-of-plane correlation length is smaller. Furthermore, these peaks with half-integer in-plane indices are visible at both even and

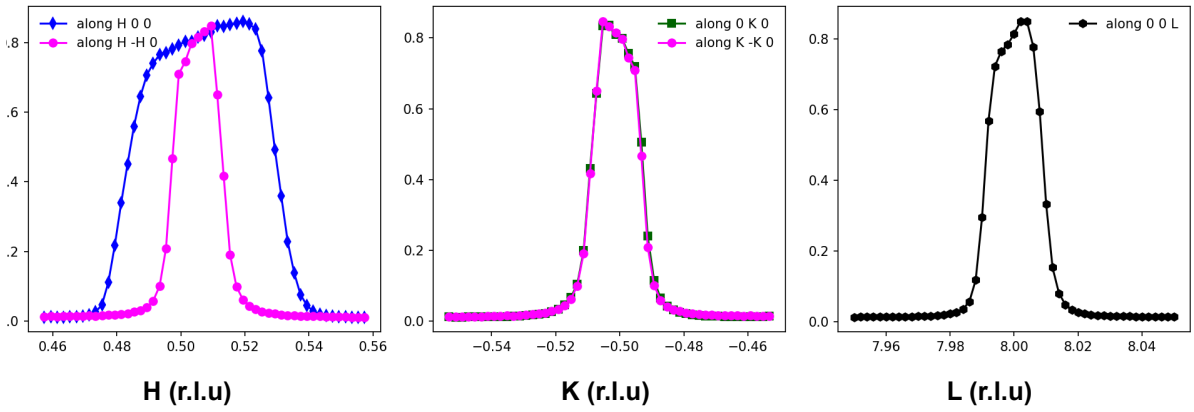

Figure 4.8: **Correlation length along different high symmetry direction of the emergent charge order** different cuts along the (0.5, -0.5, 8) peak is shown in the panels and used to extract the correlation length along these direction. The correlation is three dimensional but highly ansiotropic.

Table 4.2: Correlation length of the charge order evaluated from 4.8

	Δq (Å^{-1})	Real space size (nm)
along (100)	0.0039	162.3
along (010)	0.0014	436.7
along (1-10)	0.0028	224.2
along (001)	0.0084	74.8

odd values of L, contrary to the selection rule of odd L values for the zigzag and stripe magnetic phases, where two adjacent Fe layers stack anti-parallel. Thus the superlattice order is equally present in every layer of the unit cell. What is more surprising is that the in-plane correlation lengths are also not identical along the high-symmetry directions. As shown in the table and visualized in the figure 4.9. There seems to be a preferential direction for a longer correlation length.

We contrast the temperature evolution of this superlattice peak with the intensity of a Bragg peak of equivalent d-spacing. After alignment to the Bragg peak we collected rocking curve scans on the peak as we changed the temperature and observed no significant change in the peak as shown in the figure 4.10. We have also checked the intensity at the antiferromagnetic

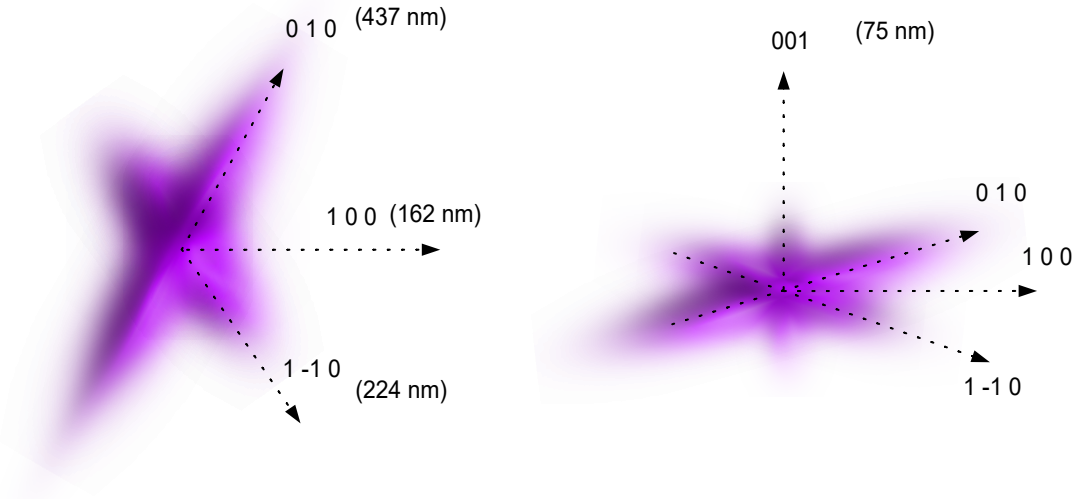

Figure 4.9: **Anisotropic correlation length of the charge order:** (left) top view (right) isometric view of an average correlation

peak location to no avail. We scanned over other high symmetry positions with wave vectors $(n/3,m/3,L),(n/3,0,L),(n/4,m/4,L)$, and$(n/4,0,L)$ with $n,m \in \mathbb{Z}$ and $L = 7,8$ at the lowest temperature with the same polarization of incoming beam but we did not find any other super-lattice peak.

Secondly, to investigate the electronic origin of the super-lattice peak. We moved to the energy space. We performed fixed-q energy scans on the peak at Fe-K edge and Nb-K edge with incoming polarization set to σ. Also, we analyzed the scattering signal to disentangle the charge component of scattering from the spin. These experiments were carried out at the 4-ID beamline of National Synchrotron Light Source-II of the Brookhaven National Lab. We used a six-circle diffractometer in four-circle mode with fixed phi and a point detector to collect the scattered signal. We normalized the energy-integrated scattered intensity but resolved the polarization of the scattered beam using an analyzer crystal of Al-660 for Nb-K edge and Cu-220 for Fe-K edge.

We note that almost all of the scattered signal is observed in the $\sigma - \sigma$ channel, i.e. where the incoming and outgoing beam are σ polarized. This channel is dominated by the charge scattering component. A change in polarization will indicate spin contribution to the scattered

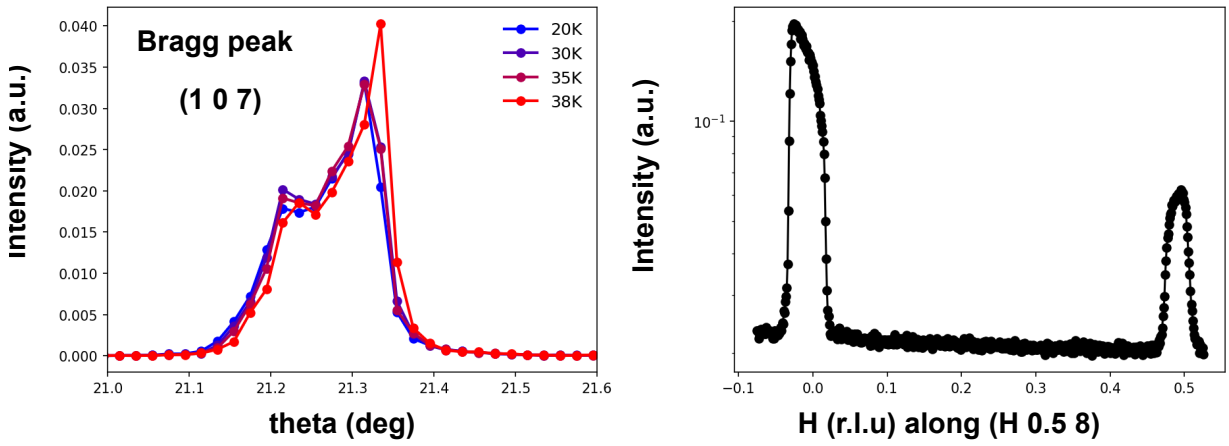

Figure 4.10: **Temperature evolution of the Bragg peak and null intensity at the stripe order peak position of (0.25, 0.5, 8)**

signal. The absence of the peak intensity in the $\sigma - \pi$ channel thus excludes the magnetic origin of the super-lattice peaks.

In the same figure 4.11, we have also shown the fixed-q energy scan on a Bragg peak around Fe-K edge of 7.12 keV. During fixed-q energy scans the energy was varied using a double crystal monochromator of Si(111). The energy resolution is 1 eV at 10 keV. At the resonance, the intensity only decreases reflecting absorption by the layers close to the surface which decreases the scattering volume and hence the intensity. This is a usual response at resonance energy conditions if there is no electronic origin of the peak, such as the Bragg peak we investigate here. The spectra don't change below the transition temperature as well. We observe similar responses at the charge order peak as discussed below denoting a lack of electronic origin such as valence or orbital ordering.

The low-temperature energy responses across Fe-K edge at 7.12 keV or Nb-K edge at 19keV, are identical with the energy response of the Bragg peak. Above the transition temperature, there are no peaks. However, when we scanned at the peak location the intensity now increased

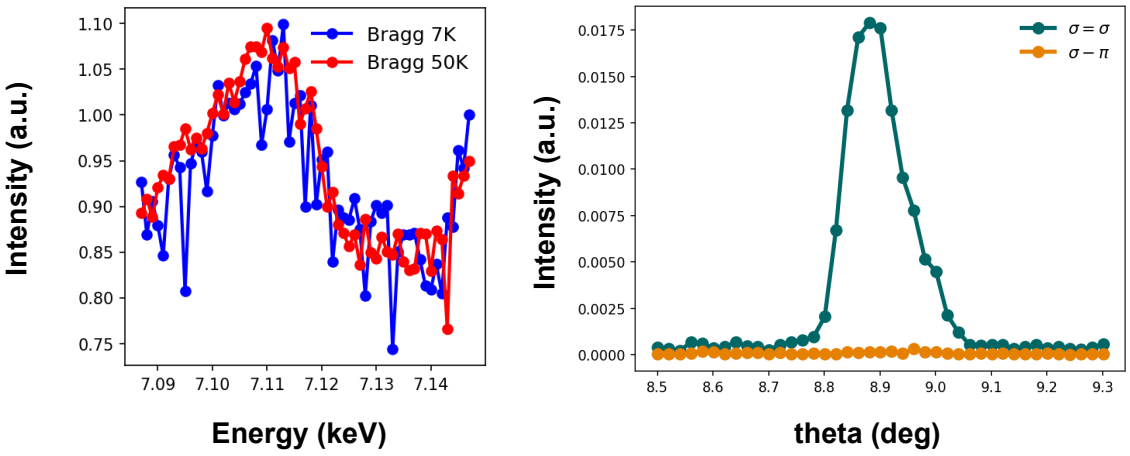

Figure 4.11: **Energy dependence of the Bragg peak and Polarization dependence of the charge order peak** (right) the charge order peak clearly sensitive to the $\sigma - \sigma$ channel proving a charge origin to the superlattice peak

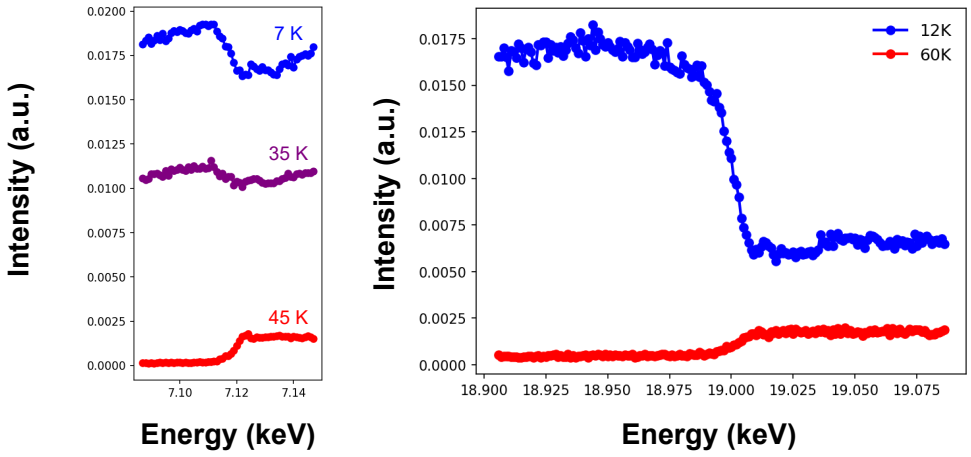

Figure 4.12: **Energy dependence of the charge order peak near Fe-K edge and Nb-K edge as we changed the temperature**(left) we measured both energy dependence with incoming polarization selected as σ and the temperature was varied. The measurement was done with fix-q energy scan on the peak location. The high temperature measurements do not host a Bragg peak and thus mimic the fluorescence data

across the Fe-K edge or Nb-K edge due to an increase in the fluorescence yield. In both of these cases, we created a core hole at the 1s state and let it collapse. we observed the photon emitted in the process of the core-hole collapse. A lack of energy modulation near the Fermi level by the valence environment (like we saw in the case of nickelates) may mean that the electrons in the cations do not participate in the charge ordering.

It is worth asking the question: why didn't we observe the charge order peak in neutron scattering investigation? Where the relative intensity of the magnetic peaks was about 50% of the Bragg peak intensity, the half-integer peaks on the other hand were found to be approximately 3 orders of magnitude smaller than the Bragg peak intensity. Thus, these peaks may have produced a negligible relative intensity above the background level in neutron scattering. That is probably one of the reasons for not seeing the peaks in neutron scattering. A strong charge ordering influences structural distortion resulting in a shift of the whole atom, like a bond distortion in nickelates. We have reasons to believe that the valence electrons of the cations do not participate in the process. Then the cations are more likely to scatter the neutrons strongly but do not undergo the distortion required and as a result, this peak doesn't show up. In hard X-ray scattering, we scatter from the electrons and the electronic modulation shows up as a Bragg peak.

In contrast, we did not observe any additional temeprature-dependent super-lattice peaks in the samples with x=0.32 that host the magnetic 'stripe' phase. We scanned over roughly 36 peaks with half-integer in-plane indices, as well as other high-symmetry directions, including $(n/4,m/4,L),(n/3,m/3,L),(n/4,0,L)$ and $(n/3,0,L)$ (n,m = integers, L = 6,7). We studied two $x = 0.32$ samples: one neutron sample with a comparable mosaicity to the $x = 0.35$ sample (FWHM = 0.15°), and the second one with a sharper peak width (FWHM = 0.02°). Both samples did not reveal any apparent temperature-dependent peak features. The superlattice peak at (0.5,0.5,L) persists up to room temperature (see Fig. S1 (b)), most likely due to a small portion of the Fe occupancy at 2b sites in the under-intercalated samples. Given the surveyed momentum positions, the invisibility of charge ordering in $x = 0.32$ is plausibly related to the highly tunable

magnetic structures with respect to Fe ratio x, which will be discussed later.

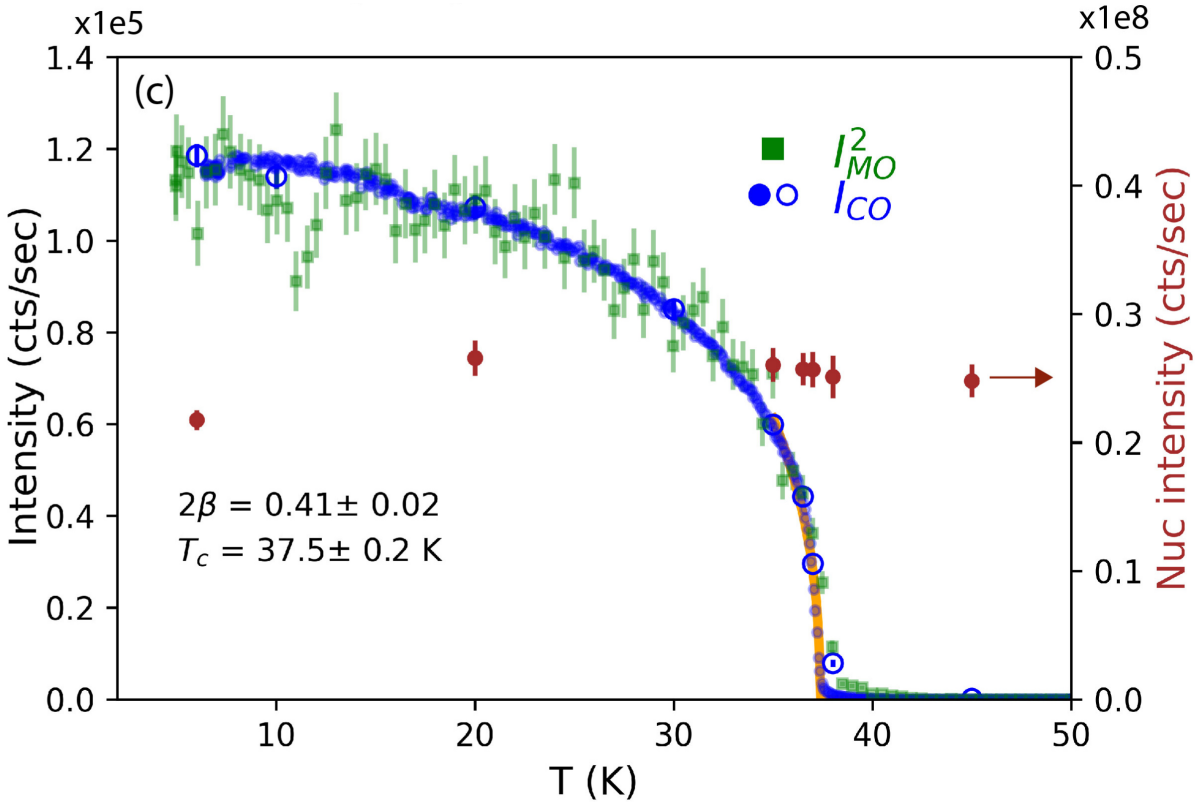

Figure 4.13: **Correspondence between magnetic and charge order intensity** we show here the charge order and square of the magnetic order parameter with varying temperature. They correlate exactly indicating a direct proportionality. Contrasting with these temperature evolution the structural Bragg peak does not change with temperature.

The magnetic link: A surprising connection of charge order to magnetism was found from the temperature dependence of the magnetic order. Our argument follows the temperature dependence of the charge order peak in the sample with x=0.35. We determined the transition temperature for the charge order phase by fitting the order-parameter curve with a power law exponent in the temperature range above 30 K. Th order parameter plot was collected by warming or cooling the sample at a constant rate while recording the charge peak intensity in so-called, timescan. The data is shown in Figure 1b). The fit yielded a charge order transition temperature of T_C = 37.5(2) K and a power law exponent for the charge ordering of 2β = 0.41(2). From the magnetoelastic model to be discussed below, this value implies a 2β value of 0.21 for the

magnetic ordering, consistent with the 2D Ising model value of $2\beta = 0.25$. The value of T_C is in good agreement with the magnetic order transition temperature, suggesting a strong connection between charge and magnetic order.

The charge order in the zig-zag phase is clearly driven by the antiferromagnetic order. To further understand the intimate relation between the charge and magnetic orders, we compared the temperature-dependent intensities of the two orders. Interestingly, the square of the magnetic intensity I_{MO}^2 matches perfectly with the charge order intensity I_{CO} after scaling by a constant factor. This correlation can be attributed to the charge modulation from magnetoelastic coupling between the lattice and magnetism [3], which induces uniform strain ε via the coupling term:

$$\sum \varepsilon_{i,j} m_i m_j. \tag{4.1}$$

The free energy for the magnetic order is in the form of

$$\mathcal{F}(m) = -a_m(1 - \frac{T}{T_N})m^2 + b_m m^4, (a_m, b_m > 0) \tag{4.2}$$

. Because of the magnetoelastic coupling, there is an additional term $\Delta\mathcal{F}$ in the free energy [4],

$$\Delta\mathcal{F} \sim -\gamma\rho m^2 + \frac{1}{2}\rho^2, \tag{4.3}$$

where m is the magnetic moment, γ is the coupling strength and ρ is the modulated charge density, which is a secondary order parameter. This coupling leads to the charge scattering intensity from minimizing the free energy (Fig. 4.14 (b)) as :

$$I_{CO} \sim \rho^2 \sim m^4 \sim I_{MO}^2. \tag{4.4}$$

This agrees with the empirical intensity relationship in our data.

In Q-space, the free energy can be expressed as:

$$\sum_{k_1,k_2} \rho(-k_1-k_2)m(k_1)m(k_2)+\frac{1}{2}\rho^2 \tag{4.5}$$

This formula implies that the wave vector of the charge order, k_{CO}, would be the sum of two magnetic wave vectors, k_m. As shown in Fig. 4.14(c) in the $x = 0.35$ sample, 12 equivalent magnetic wave vectors are assigned to three magnetic domains (denoted by three symbols). Within one domain, two k_{m2} (red vector) can generate one charge wave vector k_{CO2} (blue vector), leading to a total of six equivalent wave vectors associated with (0.5, 0.5, 0). This naturally explains the observed peak positions with half-integer in-plane indices considering the momentum positions $Q_{CO2} = \tau \pm k_{CO2}$ (τ is the atomic Bragg position).

For the stripe phase, the magnetic wave vector occurs at half-integer values (Fig. 4.15 (right)). Any charge scattering originating from the magneto-elastic coupling would be orders of magnitude weaker than the regular Bragg scattering from the crystal lattice. Doubling of k_{m1} causes the charge order peaks to appear at the atomic Bragg peak positions, making them undetectable in the experiment. Consequently, we are unable to determine if any magnetoelastically induced charge ordering in the x = 0.32 stripe phase sample.

The magnetic order induced charge ordering in $Fe_{0.35}NbS_2$ is different from that of other pristine TMDs exhibiting incommensurate charge-density-wave order, such as 2H-$NbSe_2$. 2H-$NbSe_2$ was reported to display the low-energy Fermi surface nesting [5, 6, 7, 8, 9, 10, 11]; but later the CDW formation was found to be attributed to the electron-phonon coupling mechanism [12, 13]. In $Fe_{0.35}NbS_2$, our ARPES measurements did not reveal any clear evidence of CDW features via auto-correlated Fermi surface analysis [14] (see Fig. S3). In addition, our spectra have revealed a strong photon energy dependence of the electronic structure caused by the Fe intercalation, distinct from the quasi-2D electronic band in bulk NbS_2 [15]. These results confirm that the charge order here is not a simple low-energy electronically driven transition, but rather

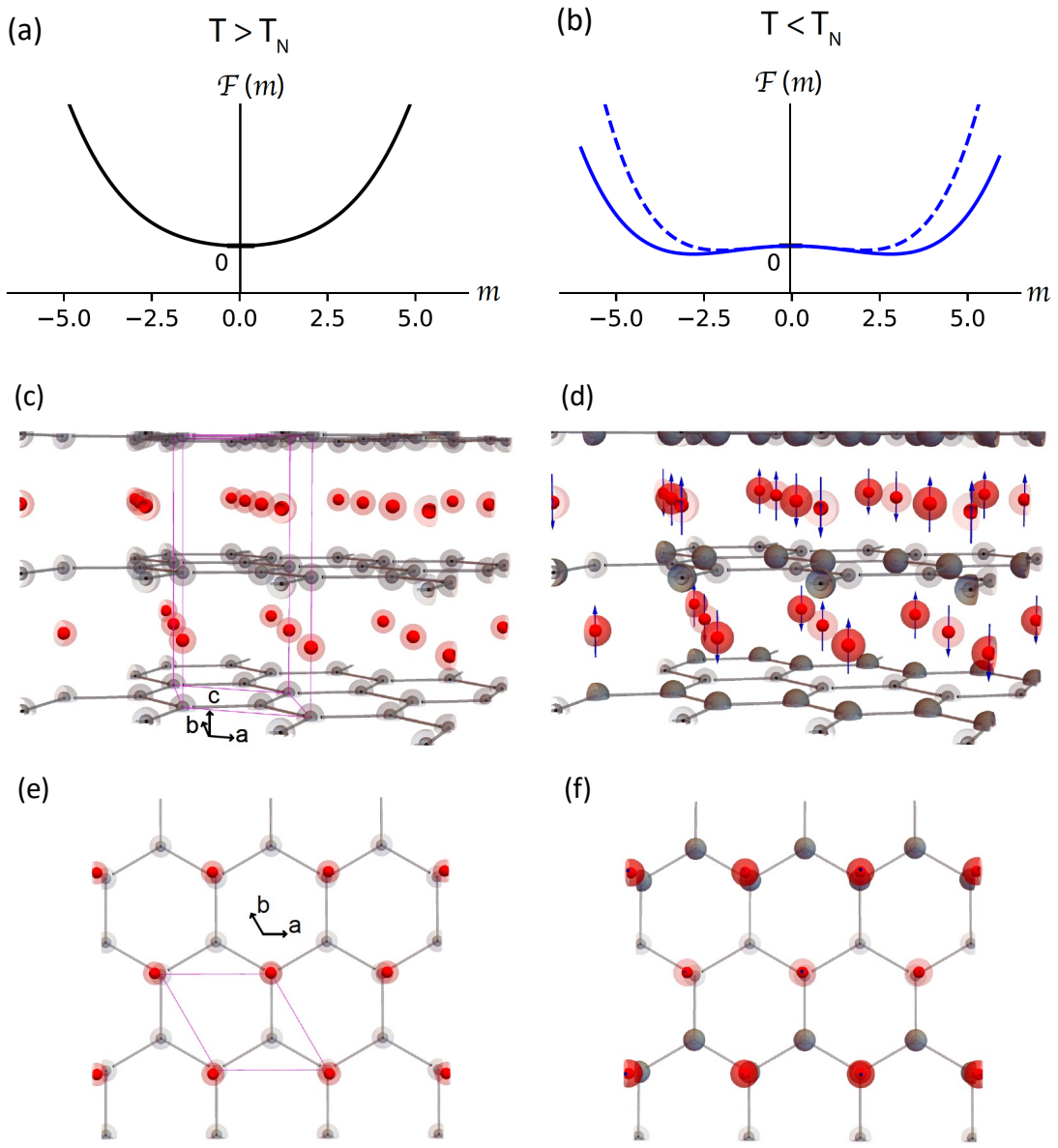

Figure 4.14: Schematic illustrations of the free energy for (a) $T > T_N$ and (b) $T < T_N$. In panel (b), the dashed blue line is the free energy for the antiferromagnetic order considering it undergoes a continuous phase transition. The solid blue line includes the change of the free energy $\Delta\mathcal{F}$ due to magneto-elastic coupling, lowering the ground state energy. (c) & (e) High temperature ($T > T_N$) lattice showing only Fe (red) and Nb (dark) atoms in three-dimensional and *ab*-plane projections, respectively. The pink line denotes the unit cell. (d) & (f) Illustration of the 3D charge ordering ($T < T_N$), accompanied by the zig-zag spin ordering in three-dimensional and *ab*-plane projections, respectively The dark and light red (grey) spherical clouds denote the charge density modulation localized on Fe and Nb sites, and blue arrows mark the spin structure of Fe.

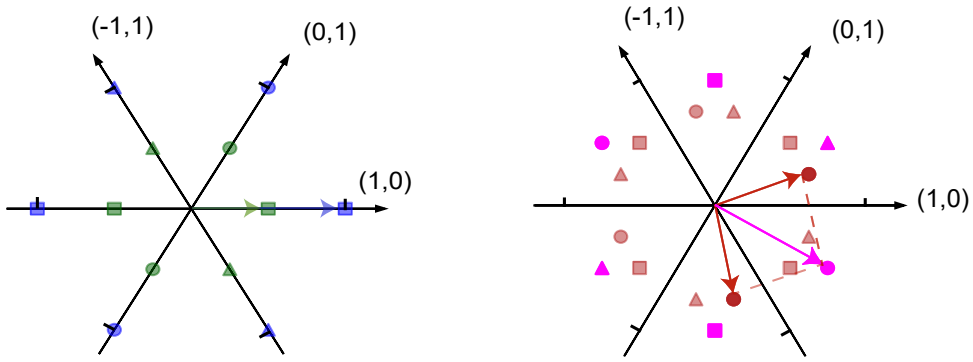

Figure 4.15: **Charge Order and Magnetic order relationship in reciprocal space:** different shapes of the peaks corresponds to different domains (left) the charge order and magentic order peaks for the under-intercalated samples. The relationship places the charge order peaks exactly on top of the Bragg peaks (right) the charge order peak for a 'zigzag' phase can be found by adding the wave vectors of two magentic peaks

the intra/interlayer magnetic exchange coupling involving Fe is a vital factor.

Magnetic Field Dependence of the Charge Order: An obvious consequence of the coupling of charge order and magnetic order parameter is that charge order parameter should respond to the external magnetic field. To experimentally verify this consequence we conducted magnetic field dependence hard X-ray scattering. We conducted these experiments at the P09 beamline of Petra-III light source in DESY-Hamburg. Field-dependent X-ray scattering constrains the accessible Ewald sphere due to the experimental geometry and access to the scattered beam through the magnet. At this beamline, we have a 14T superconducting magnet which provides the field in the vertical direction in a horizontal scattering plane. The scattered intensity was recorded using an area detector. To set up for the experiment we had to build a sample holder and mount the samples beforehand to meet with the dimensions of our samples. We mounted the 0.35 intercalated sample which we investigated in neutron and hard X-ray scattering. We showed in the figure our mounting schema and the sample holder with multiple sample assemblies. The diffractometer was essentially a two-circle diffractometer with no χ and Φ motor. Investigation on other samples was time-restricted so we present here the data from the 0.35 sample only.

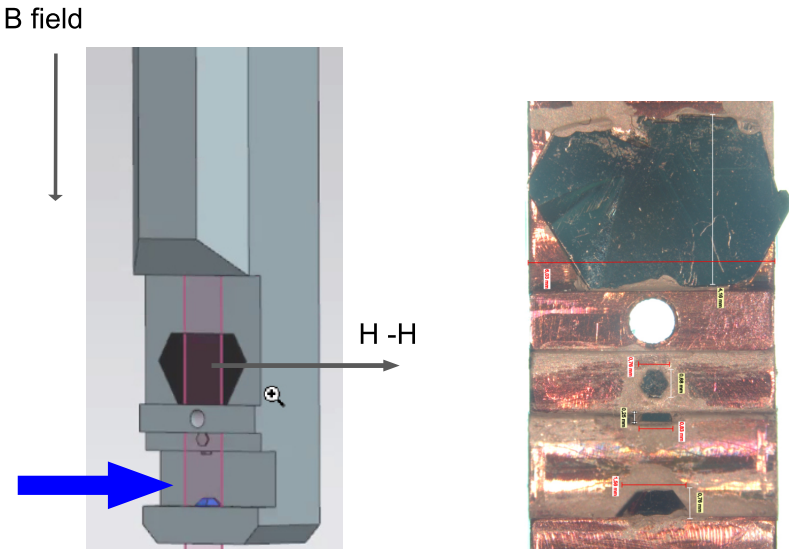

Figure 4.16: **sample holder for field dependence of the charge order** (left) schematic of the scattering set-up with the exernal field pointing along the in-plane direction. (right) actual samples mounted before putting into the diffractometer

At the Bragg condition, we accessed the (0.5, 0, 8) peak at the base temperature. The endstation offered a base temperature of 3K. Incoming polarization was set to σ and energy was set to 10keV. Firstly from the temperature evolution, we observed a previously unforeseen decrease in intensity at the lowest temperature. Maximum intensity was observed around 15-20 K. Secondly, the correlation length also changes by 34% indicating a melting of the charge order. We need further measurements to test the reproducibility of these low-temperature phenomena.

We followed this measurement up with field-cooled charge order formation and then observed the temperature dependence of the charge order while keeping the field on. Figure 4.17 shows various of such field cooled and field warmed measurements. For each temperature, we collected rocking curve scans and L scans on the peak. The intensity plotted here is the area under the curve of the beam-current normalized signal for the L scans. The rocking curve measurements show identical development. They follow the same intensity evolution until 5T, however, we

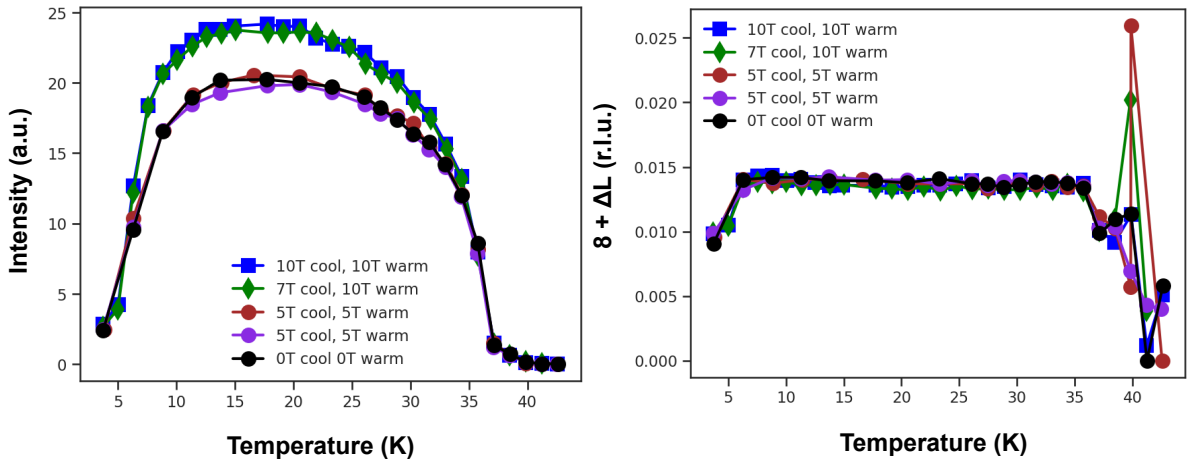

Figure 4.17: **Field Cooling of the Charge Order** We have shown here multiple temperature cycle with different external field as mentioned. With external field the transition temperature does not change indicating the short range correlation remains preserved. On the right panel we see the correlation length in the out-of-plane direction for different field cooling showing identical correlation length for all.

observe an increase in intensity without any change in out-of-plane correlation length denoting the amplitude of the order parameter changes as we expected from the coupling term.

Then we wiped the remnant of field dependence on the order parameter by warming and cooling without an external field. Finally, we set the temperature at 20K where the order parameter was maximum during the temperature cycle, ramped the field slowly to a desired field, and held it fixed when we collected data. We collected rocking curve scans at every data point shown in the figure 4.18. Finally in the figure we plotted the area under the curve which also showed field-dependent intensity change.

Finally, we have unfolded the complete complexity of this material. There are two magnetic phases 'stripe' and 'zigzag' that compete with each other at the stoichiometric sample. Furthermore, the charge order phase couples with the magnetic order phase. The magneto-elastic coupling term fixes the charge order peak position in the reciprocal space. For the 'zigzag' phase we find half-order peaks whereas the 'stripe' phase only allows charge-order peaks to coincide

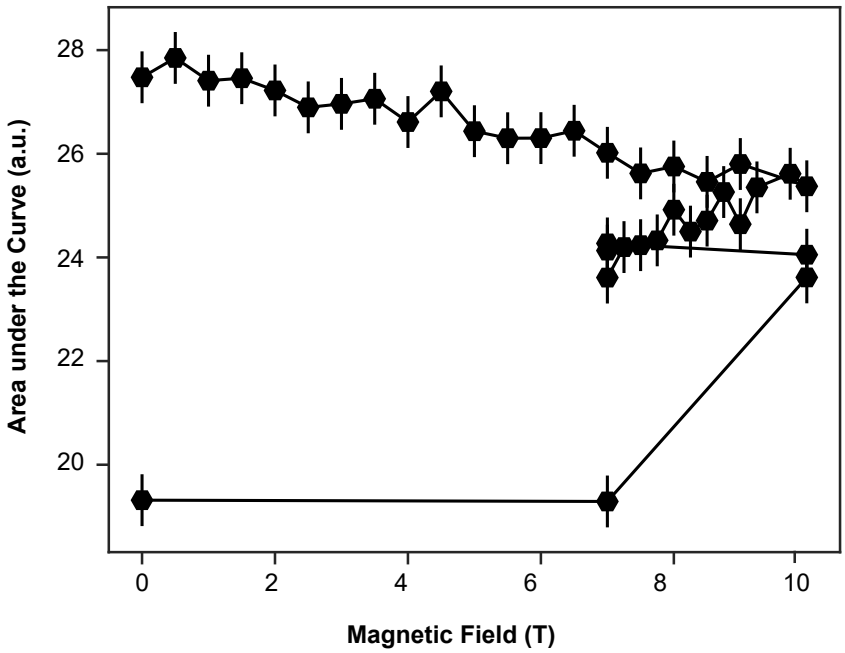

Figure 4.18: Field dependence of the charge order at 20K. Increasing the field increases the area under the curve of the charge order. The two different points at 10T is found when we increased the field upto 12T after the lower intensity point. Field is pointed perpendicular to the scattering plane

with the Bragg peak positions.

4.4 Phase Competition from Coherent Scattering

To explore the phase competition between two anti-ferromagnetic orders we carried out coherent resonant soft X-ray scattering on a sample with x=0.327. We determined the intercalation ratio from an average of 10 measurements of energy dispersive X-ray measurements. Since resonant coherent scattering is sensitive to the phase texture of electronic order, under competition a change in phase texture will be reflected on the speckle pattern to be analyzed to characterize the competition. The experiments were carried out in the beamline of 23ID

CSX at National Synchrotron Light Source-II of Brookhaven National Lab. The scattering chamber is identical to the one discussed in chapter 3. To do the resonant scattering we tuned our incoming beam to the resonance of Fe-L3 edge. However, at this low energy, the accessible reciprocal space is very small. Even though we could access the (0.5, 0, 0) peak i.e. the stripe phase antiferromagnetic peak, the 'zigzag' peak at $q = (0.25, 0.5, 0)$ peak stayed out of range. Hence, for the soft X-ray resonant scattering experiment we will focus only on the 'stripe' phase antiferromagnetic order. We will follow the evolution of its phase texture to understand the melting of this phase.

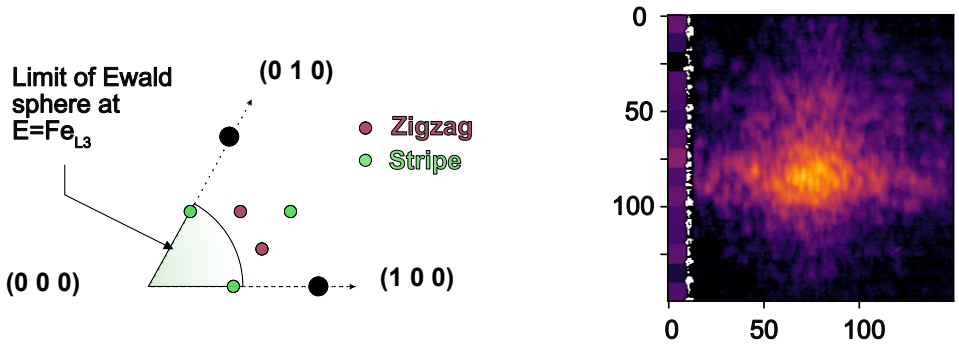

Figure 4.19: **Restricted Ewald Sphere at Fe-L3 edge and Speckle pattern** we show both 'zigzag' and 'stripe' phase peak locations with the shaded section indicating the Ewald sphere at Fe-L3 edge. We can access some 'stripe' phase peaks but can not access any 'zigzag' phase peak. (right) the speckle pattern on the detector for the Stripe phase at 41.2 K

To be certain of the position we are measuring we had to adapt some sample design. Sometimes there are sample features, such as defects on the surface which act as a position marker. However, it is always a better idea to create one which will not change as we will change the temperature. To create the marker we used gold wires of 25 μm gauge. First, we fixed the sample on a gold-plated Si substrate and then tied the gold wires to the plating after tightly winding over the sample. We wound two straight wires to make it look like axes as shown in the figure 4.20. We used the crossing of the wires as the origin of the sample positioning.

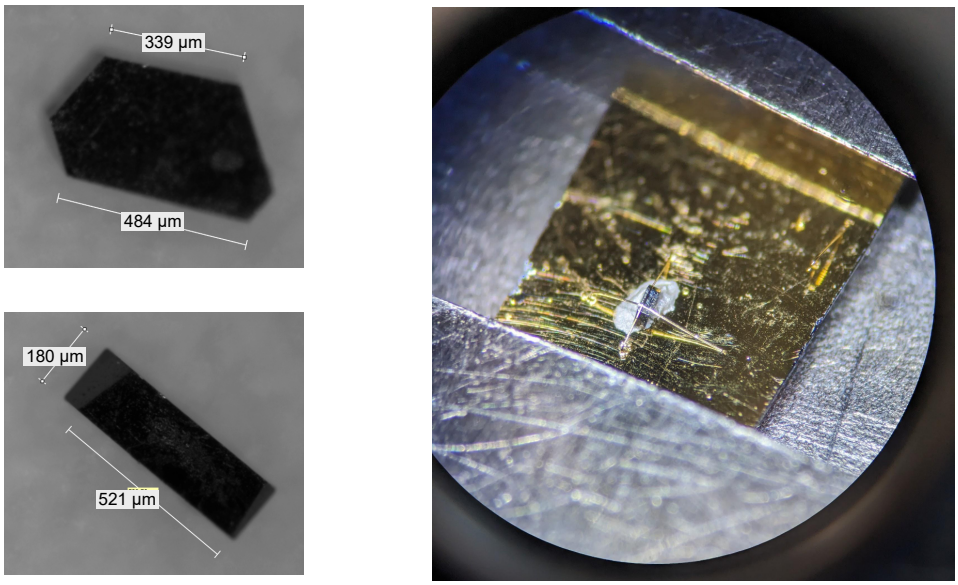

Figure 4.20: **Sample preparation:** Left two panels show the dimension of the sample we investigated in the coherent soft X-ray scattering experiment. The right panel shows the gold wire tied over the sample which acted as fiducial

4.4.1 Melting of the Stripe Phase:

The 'stripe' phase melts in two ways: firstly, as we warm up it melts due to thermal fluctuation, and secondly, as we cool down it melts due to competition with 'zigzag' phase. From the susceptibility measurements, we know that the stripe phase sets in at T_{stripe} = 45K, whereas the 'zigzag' phase sets in at T_{zigzag} = 41K. We set the liquid helium flow to reach the base temperature of 20K and then used a heater to go to the desired sample temperature. The temperature control was accurate down to $\pm$5K.

The first question we ask: *Are the two melting similar?*

To illustrate this point we show here a schematic of an antiferromagnetic domain which first forms as we lower the temperature. For a continuous phase transition, the fluctuations are long-range correlated at the transition temperature. This is evidenced by the susceptibility divergence at T_C. As we lower the temperature this correlation length decreases to a finite value

and the ordered patch expands. Thus under thermal fluctuations, we expect the ordered patch to melt from the boundary. For a complex order parameter field, even though the amplitude fluctuations stabilize below T_C the phase factors remain free to fluctuate.

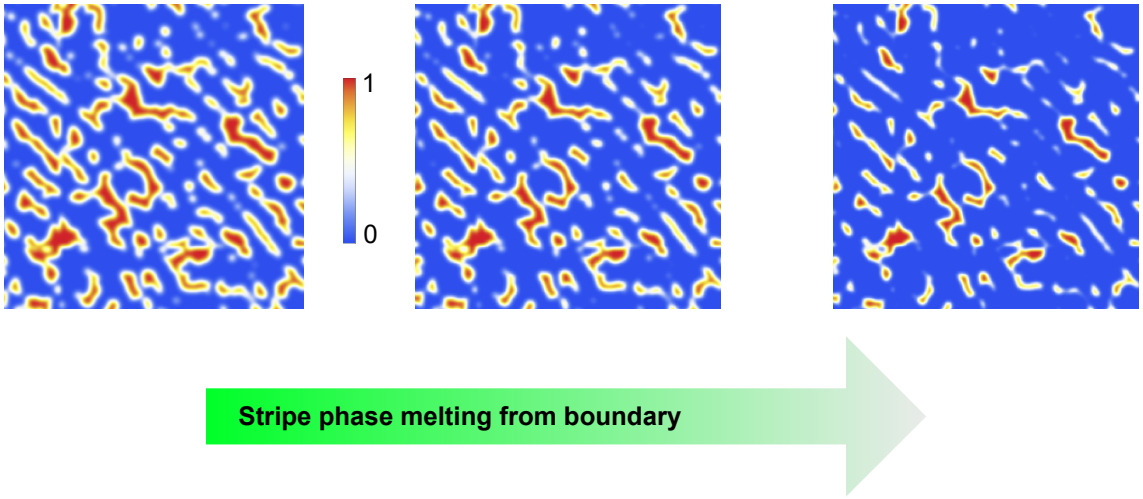

Figure 4.21: Schematic of Domains melting from boundary

On the other hand, melting due to phase competition can happen either from the boundary or the core of the patch. For a melting from the boundary, the 'zigzag' phase will nucleate at the domain walls of the 'stripe' phase. It will look like thermal melting of the 'stripe' phase. Recently the authors of [16] have shown that domain walls of a quasi-2D charge density wave order with wave vector (0.5, 0, 0) can nucleate a superconducting phase known to compete with the charge density wave phase. Unless there is a specific way the new phase nucleates and grows, this melting will appear identical to thermal melting in terms of the phase texture of the initial phase.

Another possibility is that phase fluctuation away from the criticality may induce topological defects such as dislocations. Now if one order nucleates as a topological defect in the other order then it is likely to be created in the core of the ordered patch where the amplitude of the order parameter is strong and more or less uniform. Thus the phase fluctuation governs the

phase texture. We have shown schematically how such a melting can occur in practice. Since we are sensitive to only the stripe order both disordered and 'zigzag' phases appear invisible to the resonant X-ray scattering we employ.

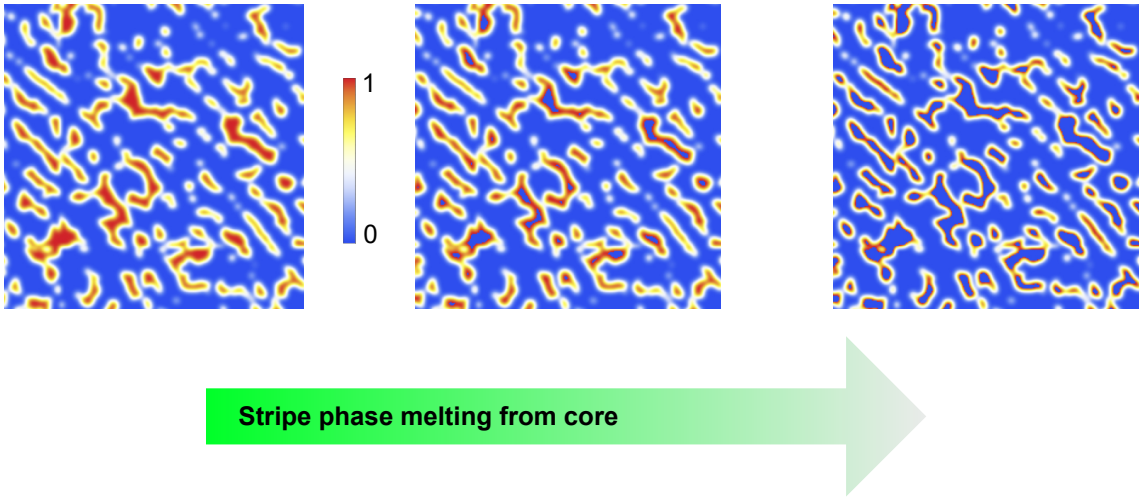

Figure 4.22: Schematic of Domains melting from core

To carry out the investigation we mounted the sample inside the scattering chamber with the c-axis perpendicular to the scattering plane. Then we tuned the polarization of the incoming beam to π polarization and energy to the Fe-L edge at 707 eV. With the spin moments mostly pointing along the c-axis a π polarized incoming beam is going to be highly sensitive to the spin component of the scattering factor. On the other hand, the σ polarized beam will be least sensitive to the spin texture. We have illustrated the experimental setup in the following figure. Our $2th$ angle was 123° and *theta* was 41° at such scattering angles the detector almost looks directly at the sample surface.

First, we show the temperature evolution of the integrated intensity of the antiferromagnetic peak. This data is continuously collected as we ramped the temperature while keeping the diffractometer aligned to the peak position of 41K. We integrated the intensity of the peak and showed here as a function of the sample temperature. As expected, the antiferromagnetic order

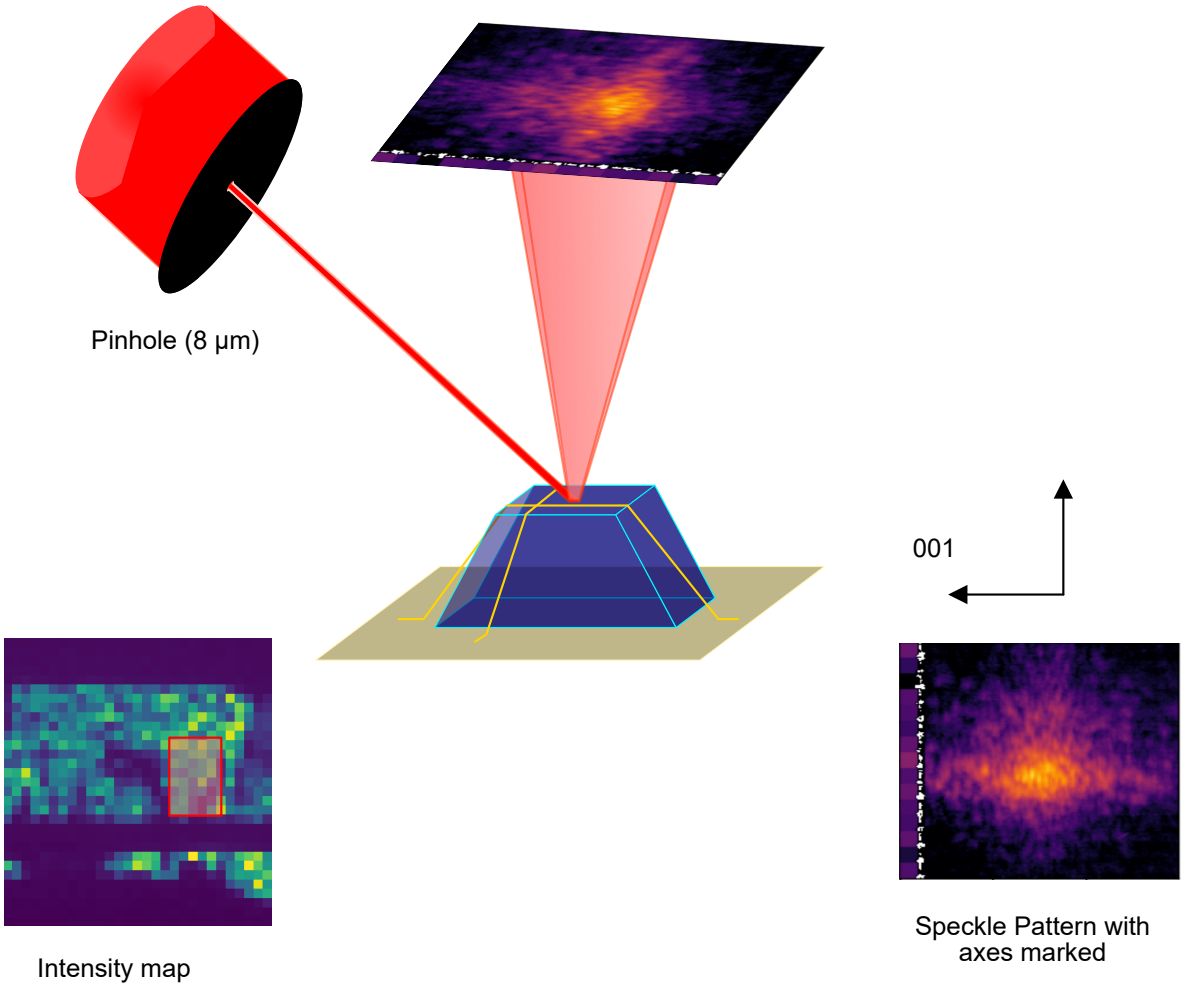

Figure 4.23: **Details of the Experimental Schematic** The schematic shows the pinhole selecting a small section of the beam incident on the sample. The left-bottom panel shows the integrated intensity of the peak on different part of the sample collected by rastering the beam. We investigated the red patch with coherent resonant soft X-ray scattering as we cycled the temperature.

emerges at 47.5K and peaks around 41K where the 'zigzag' phase emerges. We see an immediate and sharp decrease in the 'stripe' phase intensity. We selected 5 temperatures including 41K to collect the speckle pattern as marked in the figure and elaborated below. Contrasting with the neutron experiment we note that the intensity of the 'stripe' phase decreases significantly. This could be explained considering that the neutron scatters from the entire sample whereas we are

scattering only from a region of $\sim 10\mu$m.

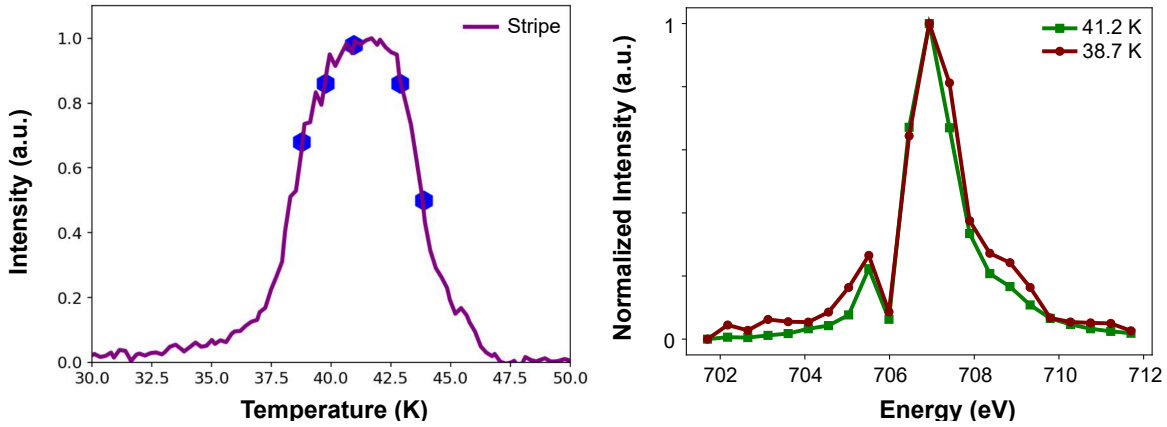

Figure 4.24: **Temperature and Energy Dependence:** Incoherent data on the 'stripe' peak showing temperature evolution (left) and energy dependence (right) in 'stripe' (41.2K) and 'zigzag' phase (38.7K)

From the energy response, we note that the peak position doesn't change with the 'stripe' phase melting under competition. We set our incoming beam energy to the peak of the energy response at 707 eV. We note a slight change in the energy response below 41K however the overall peak shape remains similar highlighting an identical electronic correlation at the scale of nearest neighbor physics of the Fe atoms. The energy resolution of the incoming beam focusing optics is about 0.1 eV setting the longitudinal coherence length on the order of 1μm which is considerably higher than the penetration depth of the soft X-rays at the resonance condition ($\sim$ 80nm). Thus the entire scattering volume scatter coherently during the measurement we are about to discuss.

As seen in the figure above, the magnetic peak as observed in the fast CCD detector exhibits complex speckle patterns: a fingerprint of the spatial texture of the 'stripe' phase. At a given position we captured the speckle pattern as we changed the temperature. However, this task was far from trivial and required us to use the gold wires as a homing device at each temperature as discussed below.

4.4.2 Ensuring positional accuracy:

As we change the temperature, the cryostat elongates. The motion is reflected as a change in the area illuminated under the beam. This potentially jeopardize the experimental accuracy. Aligning ourselves at every temperature to the gold wires helps us rehome to the original position before changing the temperature. Two orthogonally oriented gold wires serve as two axes of a 2D coordinate system. Using the edge of the gold wires we aligned ourselves accurate upto the size of the beamspot of $\sim 10\mu$m determined by the pinhole diameter of the same size.

We illustrate the experimental procedure of recalibration of the origin of the sample positioning coordinates under temperature change in the following figure. Each pixel in the intensity map is the integrated intensity on the 2D detector. It is easy to identify the gold wires as the linear dark regions. Right next to the dark horizontal line from the gold wire, we mark the region we explored to track the speckle pattern under temperature evolution with a translucent red patch.

After setting up the origin we moved to the center of the region by moving the sample motors. Then we waited long enough for the system (sample, sample motors, and the cryostat) to reach equilibrium and did not move anything on the diffractometer after that. Then we moved only the pinhole using a nano-positioner to scan the beam on the sample. During the mapping of the sample using the nano-positioners of the pinhole we took 8μm steps. To ensure sub-beamspot size accuracy of positioning between two temperatures we utilized features on the sample such as the one next to the region investigated. This feature had a single pixel giving off intensity enclosed by dark regions. Thus it served as a nice homing beacon.

Finally to ensure that at every temperature we are measuring the same position we also mapped the identical region using σ polarization. Unlike the π polarization, this is dominated by charge scattering. Thus the speckle pattern reflects structural features such as cracks or distortions on the surface and does not change with temperature. We used the speckle pattern generated from σ polarized incoming beam as the final check on our methodology to go to the original

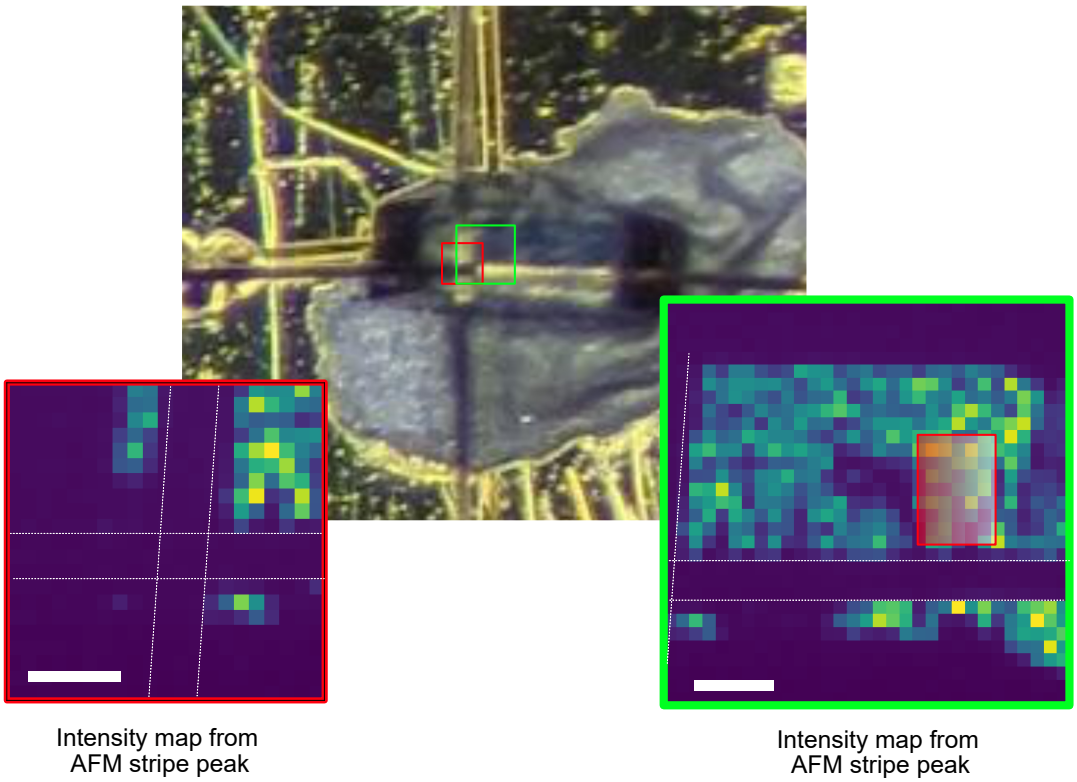

Figure 4.25: Another intensity map showing the fiducial finding and referencing the nanp map measurement area with respect to the gold wires for positioning at different temperature

position. The figure below shows the speckle pattern from σ polarized incoming beam at different temperatures we explored. The 'streaks' coming off from the peak are fingerprints of the structural distortions present at that location. We consider this as a convincing proof of location match between different nano map measurements at different temperatures.

As an aside, we would like to draw readers' attention to the fact that we could see a (0.5, 0, 0) peak with σ polarization, which is a forbidden Bragg peak. It is an allowed charge order peak for 'zigzag' phase. However, for under-intercalated samples that host the 'stripe' AFM phase, we observe a temperature-independent distortion peak at this location. Furthermore, this soft X-ray scattering beamline has a second harmonic contamination to the incoming energy. That may be responsible for a weak Bragg peak at this diffractometer position. However, as the 'zigzag' phase

sets in the peak intensity is supposed to increase with lowering of temperature which we did not observe. This might be another piece of evidence that the charge-order doesn't form on Fe-atoms.

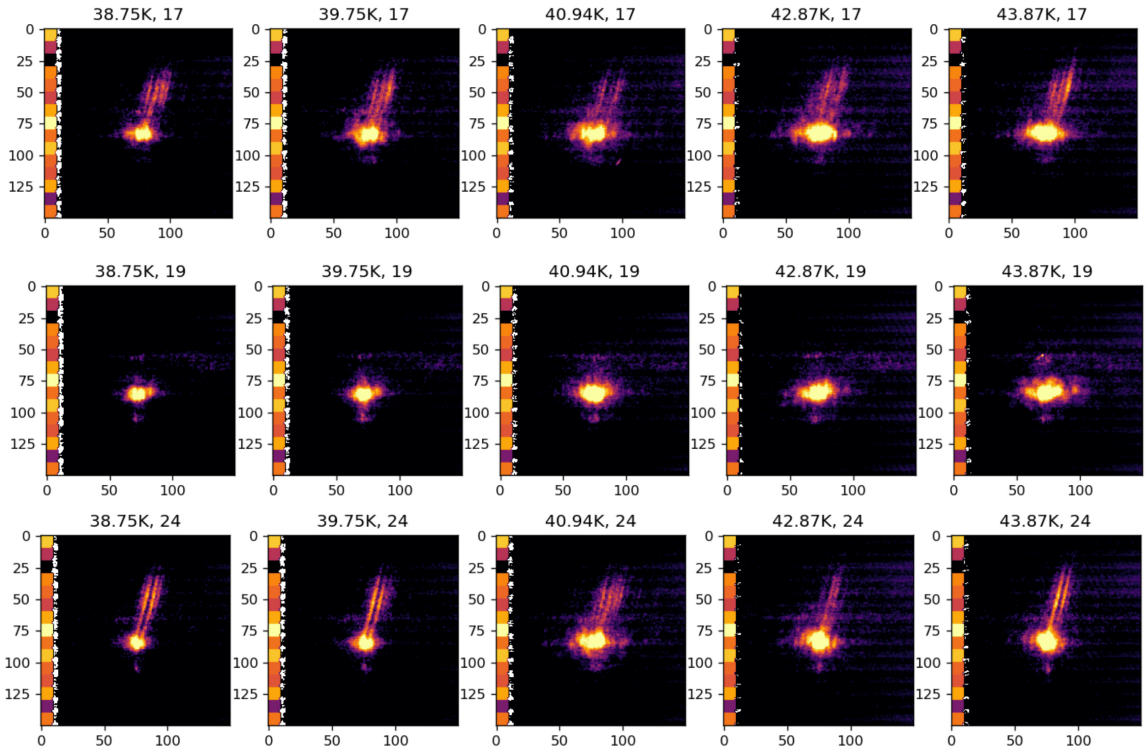

Figure 4.26: **Speckle pattern at horizontal polarization:** Since the horizontal polarization is not sensitive to the spin moments the intensity pattern serves as a fingerprint of the position. Here we show horizontal intensity pattern for three such positions (indexed on top of each panel) showing the similarity of intensity pattern for every temperature visited on that spot

4.4.3 Analysis of Speckle Pattern:

Now that we have established that we were certain of collecting the speckle pattern from the identical location to an accuracy of 8μm. We move on to discuss the data. In the figure below we show the π polarized speckle pattern of the 'stripe' phase texture. We have collected speckle patterns from a 11x11 grid. We ensured the data quality of each point and disregarded points that showed low intensity to discern the speckle pattern. We first note that the contrast is quite low indicating a highly incoherent background, either due to fast dynamics or a large fluorescence

background. Our preliminary X-ray Photon Correlation Spectroscopy measurement indicated a slow fluctuation convincing us of the latter as the reason.

We had more than 42 positions where the intensity was good enough to ensure high-quality speckle pattern analysis. As we discussed in the introductory chapters for a complex speckle pattern with low contrast we resort to correlation analysis for the understanding of the speckle pattern. We show below the speckle pattern of a representative position and note the evolution of the speckle pattern at the temperatures 38.75 K, 39. 75K, 41 K, 42.87 K, and 43.87 K: two above and two below the peak saturation of the 'stripe' phase intensity.

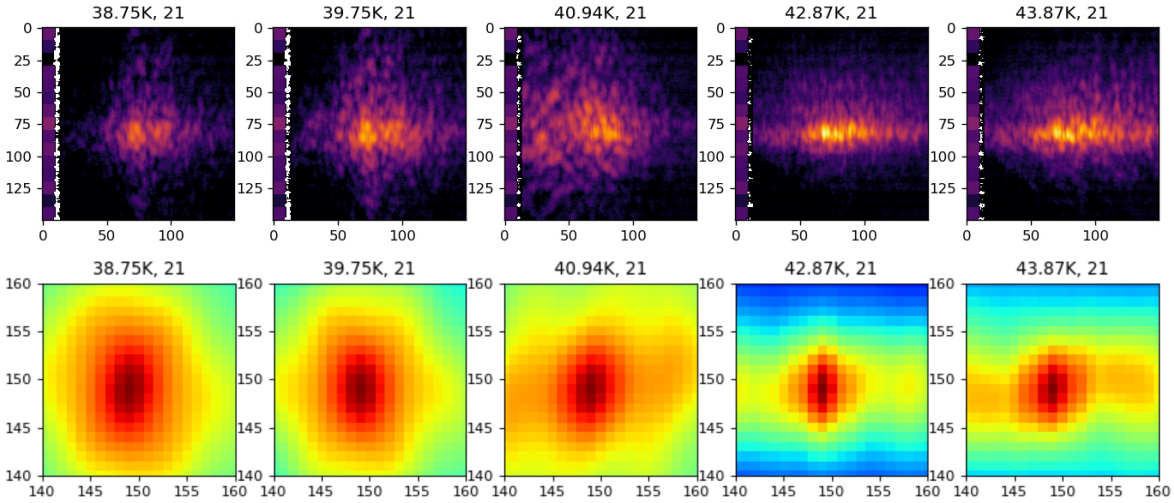

Figure 4.27: **Vertical Polarization and auto-correlation:** selecting vertical polarization for the incoming beam makes us sensitive to the antiferromagnetic order and hence the speckle pattern (top row) is a signature of the texture of the 'stripe' phase for every temperature sampled and mentioned on top of each panel. The bottom row on the other hand measures the auto-correlation to extract the average speckle size which we use later to extract the incoherent background

To analyze the data we follow the procedure laid out by, where we first evaluate the autocorrelation function of each pattern. Each auto-correlation pattern is a two-dimensional intensity distribution twice the size of the region of interest from the detector we selected. At the center of the intensity distribution lies a sharp peak on top of a gaussian background. This

peak is the coherent contribution to the auto-correlation intensity and its size tells us the average speckle size. The extracted average speckle size in pixel units are 4×8, 4×8, 4×8, 2×4, and 3×4 in pixel units. This sharp peak sits on top of a broad Gaussian peak which comes from the incoherent part of the signal. We also note that the anisotropy of the correlation peak of the coherent portion is similar to the anisotropy of the individual speckle spots observed in the detector image.

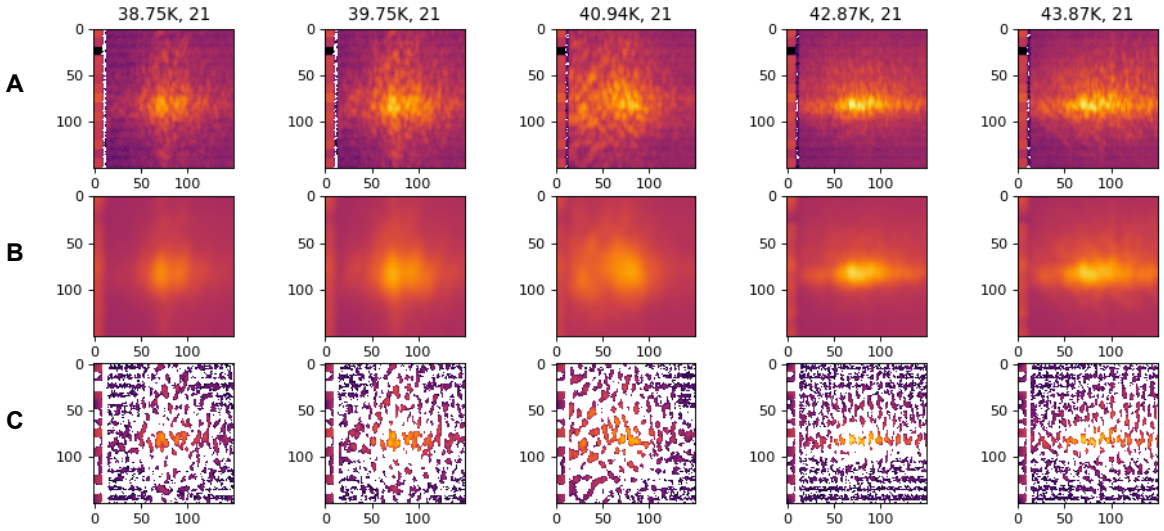

Figure 4.28: **Incoherent background and Coherent signal extraction**: From row A we evaluate the auto-correlation function to extract the average speckle size which we use as the Gaussian filter size to find the incoherent background shown in row B. Finally the row C is extracted by subtracting each column of B with respective A panel.

Next, we utilize the average speckle size to evaluate the incoherent background from the speckle pattern. We subtracted the incoherent background from the raw data to get the coherent scattering data. We used a Gaussian filter of the same size as the average speckle size to wash out the intensity modulation. This gives us an incoherent background as shown in the figure 4.28.

However, the incoherent data holds valuable information such as the correlation length of the order. We note that the vertical direction on the detector is mostly parallel to the (010) direction whereas the horizontal direction is parallel to the (001) direction of the crystal reciprocal

lattice. We took cuts of the intensity along the horizontal and vertical directions and subsequently fitted them with a Gaussian signal. We observe that along the vertical direction, we have a single Gaussian intensity distribution. However, along the horizontal direction, we have two intensity maxima which we fit with a single Gaussian too. Our fit matches with the average of both intensities to extract the average correlation length along the direction. With their reciprocal lattice marked, we conclude that the out-of-plane correlation length increases slightly as the stripe phase melts. But, the correlation length along the 010 direction decreases approximately by a

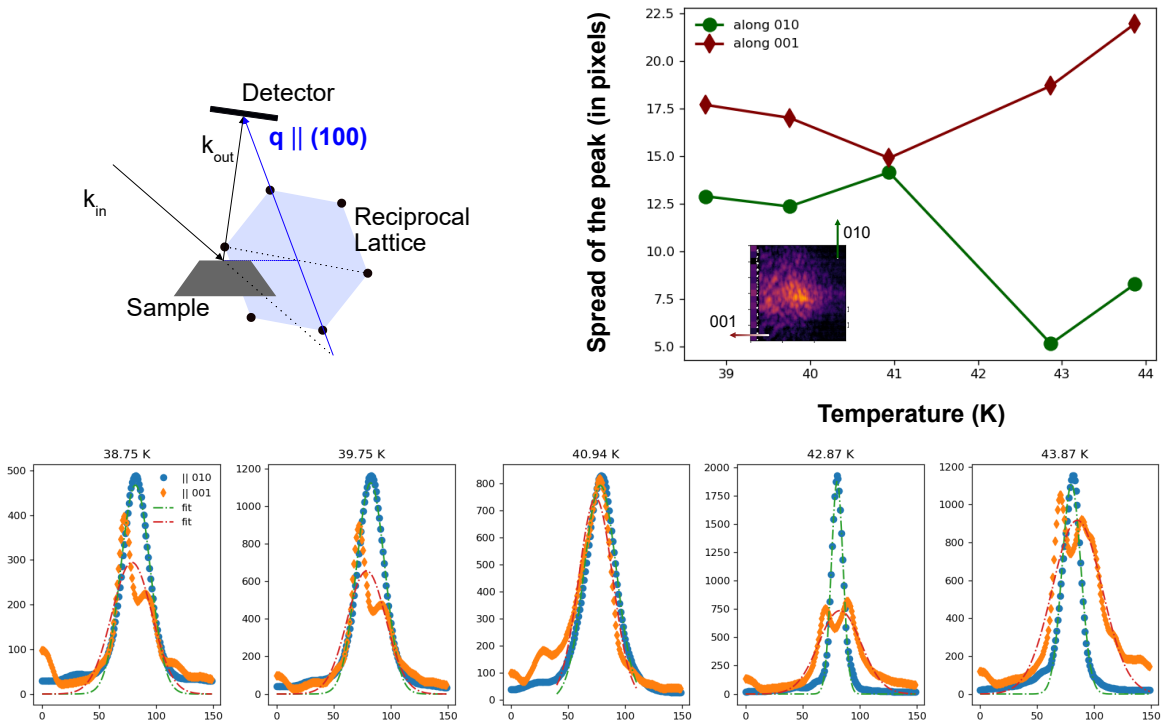

Figure 4.29: Evolution of FWHM in the incoherent envelope on the speckle patterned 'stripe' peak. The crystallographic direction on the detector is extracted from the figure on the top-left. The FWHM of the peak along these high symmetry direction is extracted and fitted with Gaussian to find the evolution of the FWHM. Notably, we see that along (010) the FWHM doubles.

factor of 2 right at the boundary where 'zigzag' phase sets in. We show in the inset the directions on the detector. The figure on the left is used to show that the vertical direction of the detector

is mostly parallel to the 010 direction whereas the horizontal direction which is parallel to the 001 direction can't be seen in the figure. The decrease in correlation length by a factor of 2 saturates as we lower the temperature further. However, we notice that the overall peak intensity decreases significantly. We interpret this result as disorderliness in correlation central to the amplitude-correlated domain structures. This is our first hint at solving the problem of phase competition.

Once we have filtered out the incoherent signal we employ cross-correlation between the speckle patterns of two different temperatures. The cross-correlation between the speckle pattern taken at T_i and T_j is called as C_{ij}, and defines as follows:

$$C_{ij} = \sum_{m=1}^{N} \sum_{n=1}^{N} A(m,n) \times B(m-i, n-j) \tag{4.6}$$

Here A and B are $N \times N$ matrices of the intensity distribution of the speckle pattern for T_i and T_j, respectively. Physically, this is equivalent to shifting one speckle pattern on the other by (i, j) and multiplying the overlapping pixels together. This way we extract the intensity-intensity correlation between two temperatures resulting in a four-point correlation function. The cross-correlation matrix is a symmetric matrix with diagonal elements as the auto-correlation of each image.

Interestingly the cross-correlation also shows complex patterns. However, we will focus on the central intensity peak which captures the similarity between the two images. We are following here the methodology for two-time correlation evaluation for X-ray photon correlation spectroscopy. Instead of two-'time' we are finding the four-point correlation between two temperatures.

Finally, we evaluated normalized cross-correlation between two images which serves as a

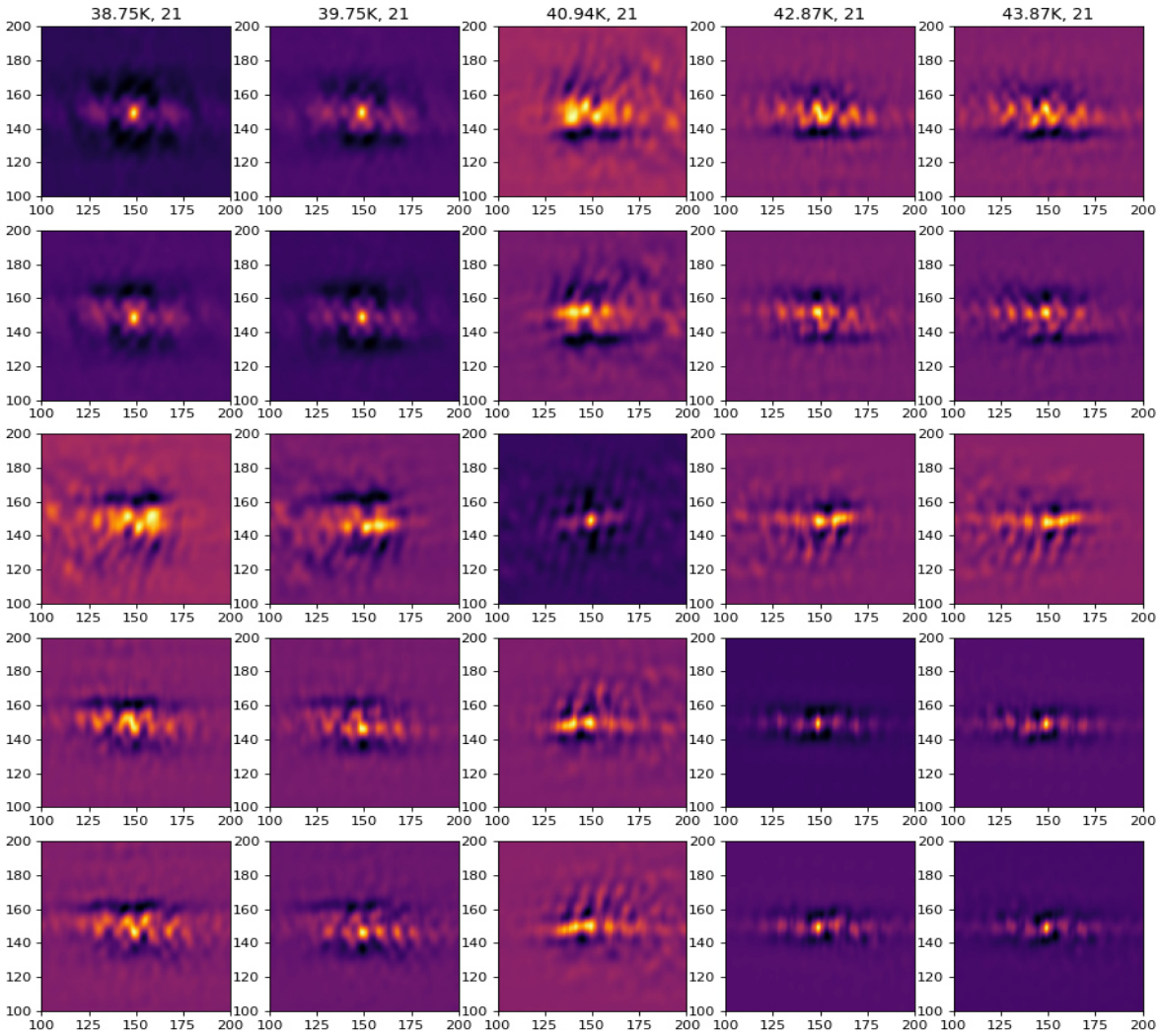

Figure 4.30: **Cross correlation evaluation between two temperature speckle patterns:** we evaluated the two temperaure cross correlation by convolution one speckle pattern with another. The diagonal entries are auto-correlation matrices

similarity index of the speckle pattern. This is defined as:

$$\rho_{ij} = \frac{\sum_{x,y} C_{ij}}{\sqrt{\sum_{x,y} C_{ii} \sum_{x,y} C_{jj}}} \tag{4.7}$$

This is a number between 0 to 1. If two images are identical the similarity index will be 1,

whereas a completely anti-correlated image will yield 0. We carried out the sum in an 8×8 pixeled region centrally. In the figure below we show the similarity index matrix or two-temperature correlation for the 5 temperature points measured.

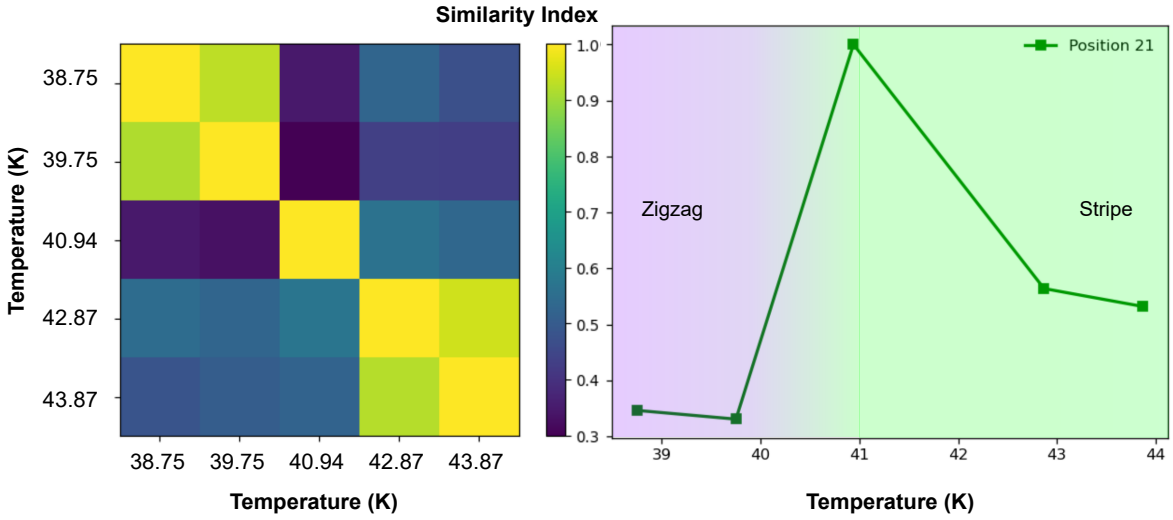

Figure 4.31: (left)Similarity Index between two temperature speckle pattern (right) similarity of different temperature speckle pattern with 41.2 K speckle pattern.

We observe a block diagonal form where the two low-temperature speckle patterns match highly with each other and the two high-temperature speckle patterns match. However, neither of these sets match the 41K. Since the low-temperature speckle patterns do not match with the high-temperature speckle pattern we have a clean first evidence that the melting of the antiferromagnetic 'stripe' phase due to thermal fluctuation is different from the melting due to phase competition with the 'zigzag' phase.

The mismatch with the 41K speckle pattern is elaborately shown in the right panel. This plot can be thought of as a line cut through the central row or central column of the two-dimensional matrix shown on the left. Contrary to the high-temperature side where the similarity drops gradually, it drops rapidly on the low-temperature side. The change of intensity is relatively similar for these two temperatures even though the overall speckle correlation differs significantly. The relative high similarity between two temperatures can happen if the ordered regions grow or

melt from the boundary. Since the speckle pattern observed after scattering is the power spectrum of the Fourier transform, a boundary expansion or shrink operation on each domain retains the principle component of the spatial distribution of the domains and thus the principle component of the speckle pattern. This is observed for the two end-points on the temperature axis in each side. To illustrate how two speckle patterns may match while the overall intensity decreases we resort to modeling.

4.4.4 Modelling the Melting:

Here we show the cross-correlation among the speckle pattern generated from two situations we discussed an order phase patch would melt: (a) melting from the boundary, and (b) melting from the core.

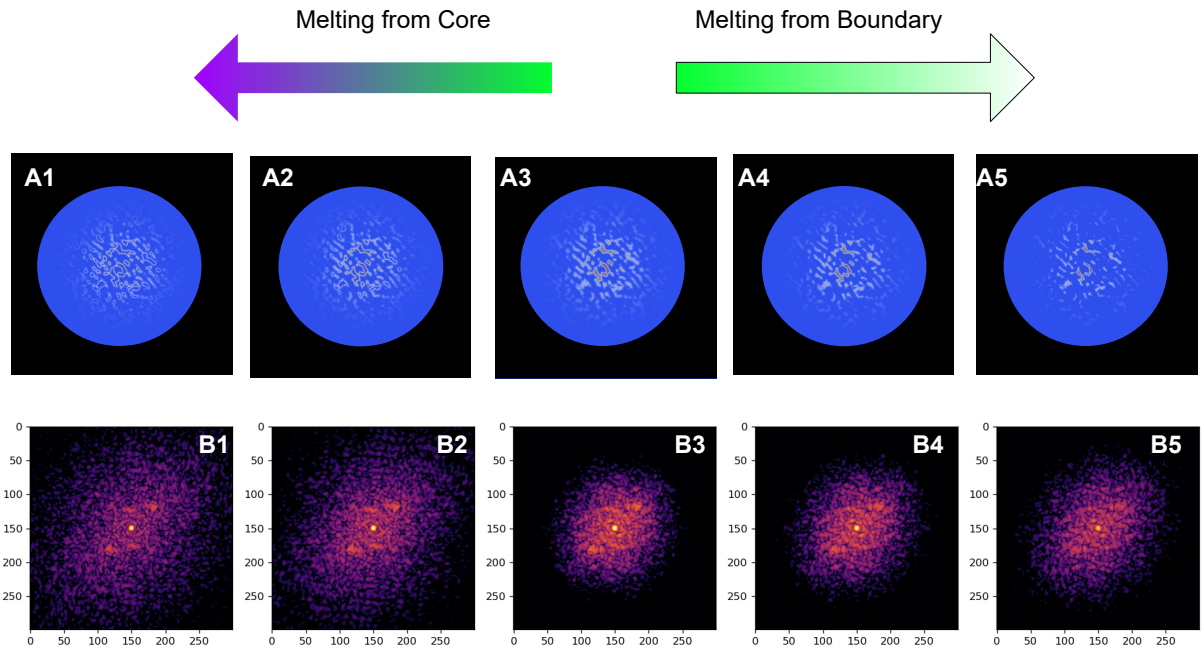

Figure 4.32: Similarity Index between two temperature speckle pattern

On the top row (A1-A5) of the figure we a circular beam spot illuminating a region on the sample with an arbitrary representative heterogeneous distribution of antiferromagnetic phase. The bottom row (B1-B5) is the amplitude Fourier transform of this illuminated domain distribution which looks like a complex speckle pattern. We considered a Gaussian beam illumination and thus multiplied the domain distribution with a Gaussian envelope to generate the real space scenario similar to what we had during the experiment. For the reciprocal space data, we just took the power spectrum of the Fourier transform of the domain distribution. Let us navigate this figure from the middle column (A3 and B3) which represents a situation in the phase transition where the stripe phase is at its maximum strength.

From this condition, we consider the two pathways of melting. The melting from the core begins from the second column from the left and progresses towards the left (A2 to A1). Whereas the melting from the boundary scenario is illustrated on the right two panels (A4 to A5). At first glance we note that the Gaussian envelope of the intensity distribution in reciprocal space for the first two panels (B1 and B2) shows an increase in FWHM, denoting a sudden decrease in the correlation length. This sudden decrease in correlation can also be seen in our experimental data between 42.87 K and 40.94 K suggesting a similar stripe phase mesoscopic texture evolution between those two temperatures. On the other hand, melting from the boundary decreases the amplitude correlation length gradually. We focus first on the melting evolution from A3 to A5. The overall intensity decreases since the scattering volume decreases.

Next, we focus on the fine details. The speckle patterns on the Gaussian envelope were extracted similarly and then evaluated with equation 5.3. In the figure below we show the speckle pattern after the incoherent background subtraction and zoomed into a region of interest on the peak. The incoherent background comes from the average correlation length discussed above. The speckle pattern on the other hand tells us about the domain organization. Before quantifying the similarity index of the speckle pattern, we qualitatively discuss this point.

If we follow the speckle pattern from C3 to C5 we identify large structures that retain

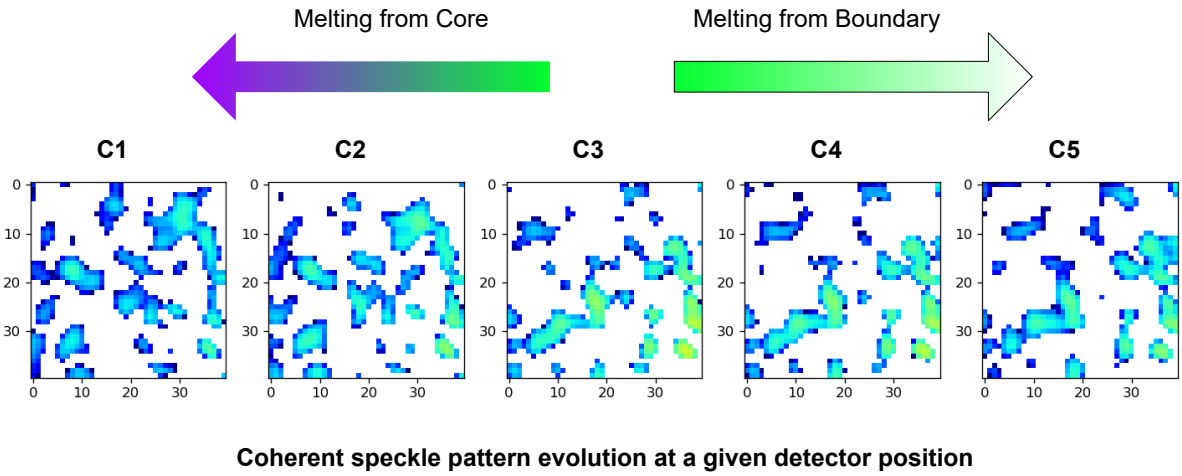

Figure 4.33: Speckle pattern from the melting simulation

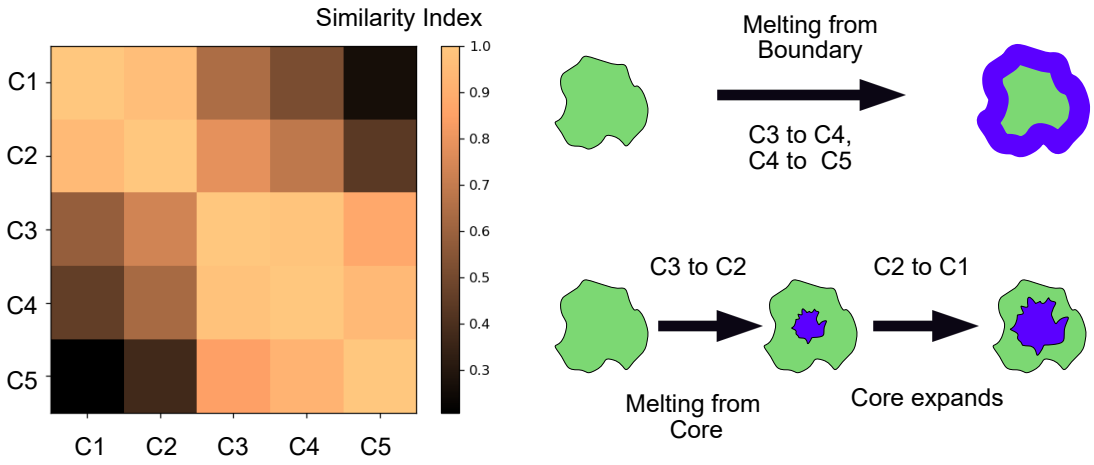

Figure 4.34: Speckle pattern from the melting simulation

position, intensity, and shape similarity among the panels. Low-intensity small structures are the ones to become dissimilar first. The similarity index between two such speckle patterns will be found high. A similar evolution of speckle pattern is observed between C2 to C1. Thus we argue that in later stages of melting from the core, the evolution of the speckle pattern indicates a melting from the boundary for the annular domain areas which hosts a phase decorrelated core

in the middle. However, the speckle pattern completely reorganizes between C2 and C3, which indicates that the nucleation phase of phase decorrelated core will completely reorganize the speckle pattern. The similarity index between two such speckle pattern will be low. Once the cores are established and their further evolution involves growing in volume, the similarity index between two such speckle patterns will be high.

4.5 Discussion

In light of the previous argument, we revisit the similarity index matrix from our data. The block diagonal structure now can be understood as temperature regions where melting from the boundary is the dominant mode of melting. So from 39.75 K to 38.75 K, and from 42.87 K to 43.87 K the stripe phase domains melt from the core boundary and domain boundary, respectively. However, the similarity index among the speckle patterns of 42.87 K, 40.94 K, and 39.75 K are quite low. We conclude that between 42.87 K to 40.94 K the core regions of the stripe domains start to disappear. We consider that the cores are replaced by the zigzag phase since the low-temperature melting of the 'stripe' phase is associated with the phase competition with the 'zigzag' phase. Between 40.94 K to 39.75 K, the 'zigzag' phase continues to populate the real space by further nucleation and the growth of existing ones.

Following the methodology discussed we analyzed all of the positions in question to gain statistical significance. This leads us to a conviction that the observed behavior of melting is not special for the representative case. It happens all over the region we investigated.

Thus we conclude that the melting due to the 'zigzag' phase below 41K happens from the core of the stripe patch, as if the 'zigzag' phase is nucleated as a topological defect of the 'stripe' phase. With the help of coherent resonant soft X-ray scattering, we have found the key relationship between the two phases. Following our understanding firstly, we show below schematically how the 'zigzag' phase can be viewed as a topological defect for the 'stripe' phase. Then, we discuss

a phenomenological theory that encompasses the essential physics of the system.

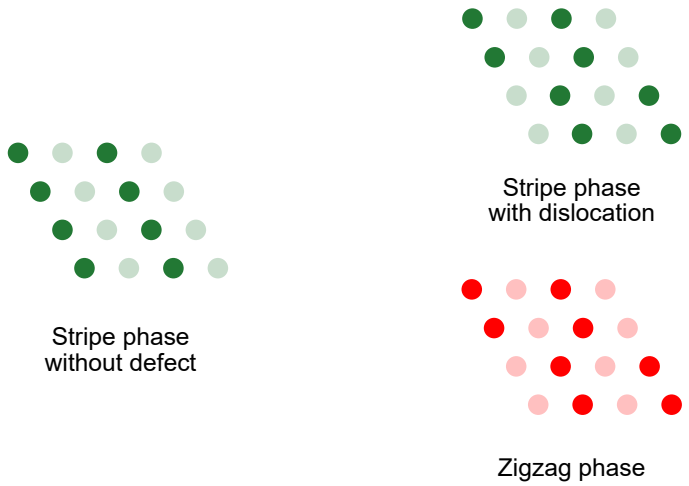

Figure 4.35: **Correlation between stripe phase and zigzag phase:** Here we show that for a given domain orientation a stripe phase with dislocation looks identical to a zigzag phase spin arrangement

Fig 4.35 captures the relationship between the order parameters schematically. There are three equivalent wave vectors for the stripe phase related by a 120° where we have shown the relationship for only one of them. Let us consider the magnetic moment at a site $\mathbf{r_i}$ is

$$\mathbf{M}(\mathbf{r_i}) = e^{\imath \mathbf{q_{stripe}} \cdot \mathbf{r_i}} M,$$

where $\mathbf{q_{stripe}}$ is the reciprocal lattice vector of the magnetic order and M is the order parameter. Now the topological defect in this field can be defined similarly to Burger's vector as

$$\oint_C \nabla \mathbf{M} \cdot d\mathbf{r}$$

taken around a loop C. If C does not enclose a dislocation defect in the stripe phase, the path runs over lattice spacing to yield 0. If, however, it encircles a defect the integration yields $\imath 2\pi M$, which

is equivalent to the winding number. On the other hand same path of integration is followed in the zigzag phase where

$$\mathbf{M}(\mathbf{r_i}) = e^{\iota \mathbf{q}_{\mathbf{zigzag}} \cdot \mathbf{r_i}} M,$$

the dot product for the entire loop cancels out and we find the order is defect free. Since the two antiferromagnetic phases are very close in energy space and they are related by a dislocation defect a phase fluctuation may result in nucleating the zigzag phase in the stripe phase as a topological defect of the latter.

To capture this into a phenomenological theory we borrow inspirations from the McMillan-Ginzburg-Landau model of commensurate to incommensurate charge density wave (CDW) transition through discommensuration [17, 18] . The second-order transition from commensurate to incommensurate is seen on transition metal dichalcogenide 2H-$TaSe_2$. The discommensuration is defined as the phase of the complex order parameter of the CDW commensurate phase which differs from $2\pi/3$ effectively unlocking the CDW from the crystal lattice. The discommensuration thus is a phase defect in the commensurate CDW field. Following the solution of the free energy minimization for a constant amplitude but varying phase of the complex order parameter the authors show that discommensuration nucleates well separated from each other and eventually span the space with decreasing temperature.

Let us redefine the magnetic moment at a site as

$$\mathbf{M}(\mathbf{r_i}) = e^{\iota \mathbf{q}_{\mathbf{stripe}} \cdot \mathbf{r_i}} \psi,$$

where ψ is a complex order parameter defined in real space as $\psi(\mathbf{r}) = \phi(\mathbf{r}) e^{\iota\theta(\mathbf{r})}$. The phase quantifies the deviation from an order parameter of a certain wave vector. Then the McMillan free energy functional can be written as

$$f = \tau|\psi^2| + \xi^2|(\iota\nabla + \mathbf{q}_\delta)\psi|^2 - \frac{E}{2}(\psi^2 + \psi^{*2}) + G|\psi^4| \tag{4.8}$$

where τ is the reduced temperature and G,E>0. ξ is the characteristics length scale of correlation and $\mathbf{q}_\delta$ is a reciprocal space vector such that

$$\mathbf{q_{stripe}} + \mathbf{q}_\delta = \mathbf{q_{zigzag}}$$

. We did not consider any coupling to external fields or the charge order term to keep the equation to the bare minimum terms necessary to explain the phenomena. Including them does not change the fundamental structure of the argument presented here. Furthermore, this free energy density is only for a single domain where one of the order parameters manifests out of three possibilities, ψ_1, ψ_2, and ψ_3 rotated 120° to each other. A full free energy density will include such terms for every ψ_i and the symmetry-allowed coupling terms. Now replacing ψ with $\phi e^{\iota\theta}$ in the equation 4.8 we get:

$$f = \tau\phi^2 + \xi^2[(\nabla\phi)^2 + \phi^2(\mathbf{q}_\delta - \nabla\theta)^2] - \frac{E}{2}\phi^2 cos(2\theta) + G\phi^4 \tag{4.9}$$

The reduced temperature term decides if the ground state energies will have an order with non-zero ϕ however the wave vector for the order parameter is decided by the subsequent terms. The second term minimizes the free energy when $\nabla\theta = \mathbf{q}_\delta$ or, $e^{\iota\theta} = e^{\iota\mathbf{q}_\delta\cdot\mathbf{r}}$. On the other hand, the third term minimizes the free energy the most when $\theta = n\pi$ with n as an integer. Thus the term does not alter the ordering vector of the moments but changes the overall phase by ± 1. Through the free energy density description we have incorporated the emergence of the 'zigzag' phase and 'stripe' phase as per the phase(θ) term of the complex order parameter field. In the limit when $T << T_C$ and the order parameter is established to a constant the free energy density is dictated by the phase term as we considered previously.

The Euler-Lagrange equation for the phase term can be found from the minimization of the functional

$$\frac{\delta f}{\delta\theta} = 0 = \nabla^2\theta - \frac{2E}{\xi^2} sin(2\theta) \tag{4.10}$$

This is in the form of the Sine-Gordon equation, which allows soliton-like solutions for the phase. From a complex order parameter field following the McMillan-Ginzburg-Landau energy functional we have found that a significant value of E favors the formation of the 'stripe' phase along with soliton-like solution for the phase term(θ) of the complex order parameter field. We have also identified such soliton-like solution for the 'stripe' phase as the 'zigzag' phase. This explains the nucleation of the 'zigzag' phase in the 'stripe' phase as soon as the amplitude fluctuations(ϕ) are diminished and phase (θ) fluctuation becomes the main driver of the physics.

Solving the Sine-Gordon equation we come to the solution for the phase(θ) term as it evolves over space.

$$\theta(r) = C * tan^{-1}(e^{\pm\frac{2\sqrt{E}}{\xi}r}), \tag{4.11}$$

where r is the distance along a direction in the lattice plane perpendicular to the c-direction and C is some constant. We show in the Fig 4.36 how the solution varies for $\xi = 2$ and $E = 0.1, 0.7, 4,$ and 25. We see that high E value stabilizes θ to integer multiples of π which allows the 'stripe' phase. As a solution of the Sine-Gordon equation, we observe the 'zigzag' phase emerge as a defect. As the value of E decreases this phase increases in expanse and wipes the 'stripe' phase out.

We conclude that we have found a qualitative similarity between the phenomenological model and the experimental model based on the observation. McMillan-Ginzburg-Landau functional captures the essential physics of the system which we have realized from the observation of the coherent resonant scattering outcome. Tracing the speckle pattern evolution during the melting of the stripe phase during competition and thermal melting showed the intricate interrelation between the two phases. The E term in the functional is dimensionless and is explained by McMillan as the phase coupling to the structure in this model, termed as lock-in energy. This is possibly the manifestation of the magneto-elastic coupling discussed in relation to the concomitant charge order in this material. We know from the phase diagram that the term can be

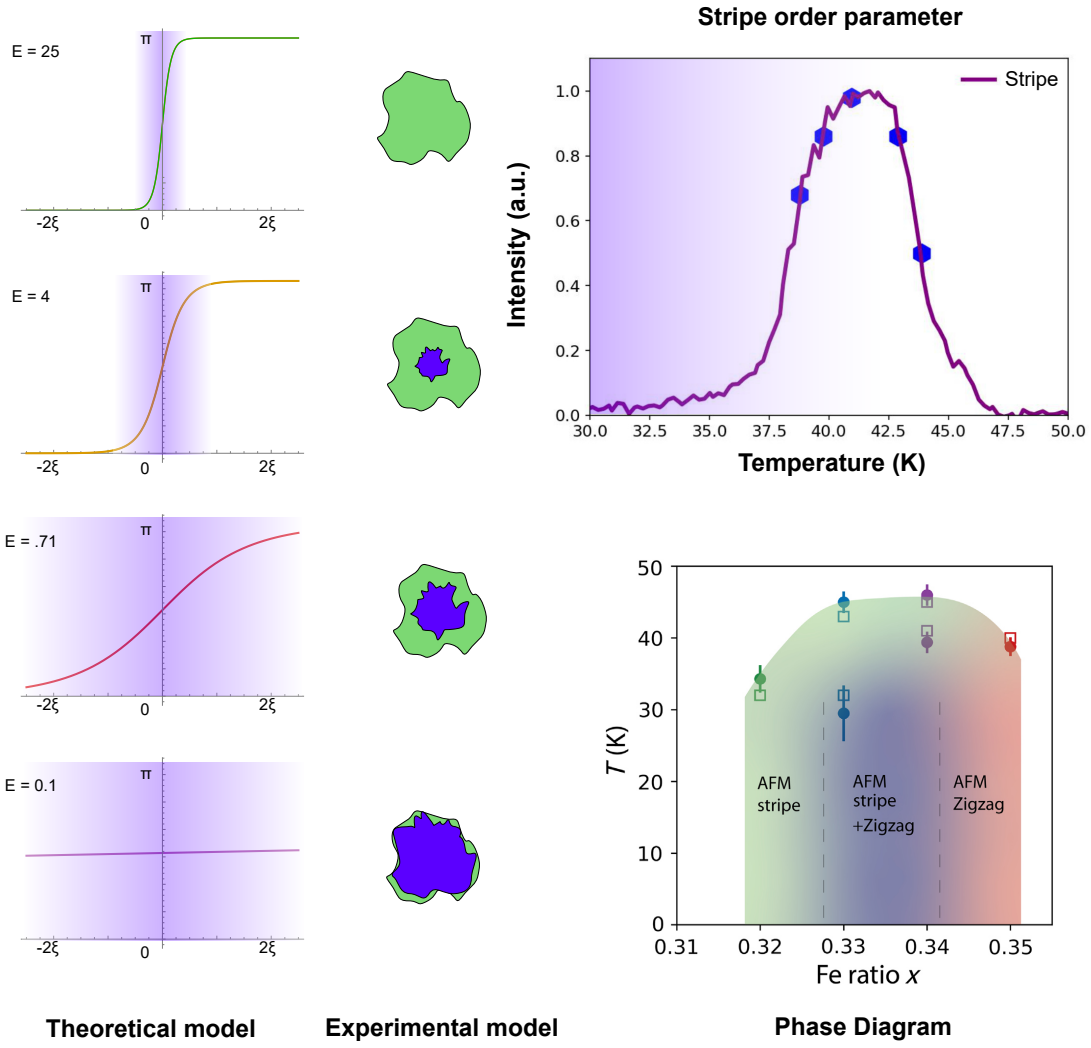

Figure 4.36: Conclusion of melting of the stripe phase and comparison of theoretical and experimental models to capture the inter-relation between the two phases as the phase texture evolves

modulated by intercalation ratio. For a lower intercalation ratio than the stoichiometric one, it results in a higher value of E realizing the 'stripe' phase as the low-temperature ground state. With increasing intercalation the value switches to a lower value and we observe the 'zigzag' phase. Around the stoichiometric ratio, we observe a temperature-dependent evolution that nucleates the 'zigzag' phase inside the 'stripe' phase and allows it to expand with decreasing temperature. The temperature dependence of the E term may result from the small thermal expansion in this

strongly correlated system.

Outlook: Physics of strongly correlated magnetic systems is fascinating. In this chapter, we have explored one such system. We studied the evolution of the antiferromagnetic texture to identify the physics using coherent resonant soft X-ray scattering. In the outlook section, we discuss a few loose ends and how we are approaching to resolve them.

Charge order in under-intercalated sample Even though the Landau theory term indicated the existence of a charge-ordered phase concomitant with the antiferromagnetic order in the under-intercalated sample we have not directly observed it. An indirect way to observe could come from exploring coherent hard X-ray scattering. Critical slowing down during phase transition is a universal phenomenon in continuous phase transition. We can study the fluctuation dynamics of the structural domains and domain walls as the sample undergoes a phase transition using X-ray Photon Correlation Spectroscopy (XPCS). The time scale of the dynamics tells us the energy separation between two fluctuating states of domain configuration. Thus, by tuning to a diffuse scattering in the tail of a Bragg peak we can monitor the time dynamics at different temperatures. A critical slowing down will indicate the existence of an emergent charge order. We can simultaneously study the inelastic X-ray scattering which will show the softening of the phonon mode associated with the charge order formation.

short range interaction: Coherent scattering explored the long wavelength physics of the material. To explore the nearest neighbor coupling term we can perform a resonant inelastic soft X-ray scattering experiment. Furthermore, we can study the absorption spectroscopy of the sample to understand the unoccupied electron levels.

In-operando measurements: Now that we have an understanding of the phase evolution in the sample in thermal equilibrium we can extend it to studying the non-equilibrium physics during resistive switching phenomena which originally got us interested. In such a measurement we can use Dark Field X-ray Microscopy (DFXM) measurement to image the melting of the associated charge order phase and re-emergence through the switching cycle. We can also study

the domain fluctuation dynamics on the charge order through XPCS as we vary the switching frequency.

4.6 Conclusion

We observed a remarkable antiferromagnetic phase in intercalated NbS_2 samples. The antiferromagnetism couples to a charge-ordering phenomenon. The origin of the charge order remains unknown. However, we have resolved the relation between two magnetic phases that show up in this material with coherent resonant soft X-ray scattering. we can clearly distinguish between the melting of the stripe phase under thermal fluctuation and under phase competition. Furthermore, the phase competition indicates an interesting relationship between the two magnetic phases where one phase is a topological defect of the other phase. From this relation, we developed a phenomenological model based on McMillan-Ginzburg-Landau model which qualitatively agrees with the experimental observation of the 'stripe' phase melting under phase compeition. The methodology employed using resonant coherent soft X-ray scattering can be employed elsewhere similarly where an order parameter of a phase melts in competition with another phase.

4.7 Acknowledgements

Chapter 4, in part, has been published in Physics Review Letters, 131, 186701, 2023, Shan Wu*, Rourav Basak*, Wenxin Li, Jong-Woo Kim, Philip J. Ryan, Donghui Lu, Makoto Hashimoto, Christie Nelson, Raul Acevedo-Esteves, Shannon C. Haley, James G. Analytis, Yu He, Alex Frano, and Robert J. Birgeneau, Discovery of Charge Order in the Transition Metal Dichalcogenide FexNbS2. The dissertation author was the primary investigator and author of this paper. (* indicates equal contribution)

Bibliography

[1] Nityan L. Nair, Eran Maniv, Caolan John, Spencer Doyle, J. Orenstein, and James G. Analytis. Electrical switching in a magnetically intercalated transition metal dichalcogenide. *Nature Materials*, 19(2):153–157, 2020.

[2] Shan Wu, Zhijun Xu, Shannon C Haley, Sophie F Weber, Arani Acharya, Eran Maniv, Yiming Qiu, AA Aczel, Nicholas S Settineri, Jeffrey B Neaton, et al. Highly tunable magnetic phases in transition-metal dichalcogenide fe 1/3+ δ nbs 2. *Physical Review X*, 12(2):021003, 2022.

[3] Earl R. Callen and Herbert B. Callen. Static magnetoelastic coupling in cubic crystals. *Phys. Rev.*, 129:578–593, Jan 1963.

[4] Q. J. Harris, Q. Feng, Y. S. Lee, Y.-J. Kim, R. J. Birgeneau, and A. Ito. A synchrotron x-ray study of the phases and phase transitions in the mixed ising-xy magnet $Fe_xCo_{1-x}TiO_3$. *Zeitschrift fur Physik B Condensed Matter*, 102(2):163–182, Mar 1997.

[5] T. Kiss, T. Yokoya, A. Chainani, S. Shin, T. Hanaguri, M. Nohara, and H. Takagi. Charge-order-maximized momentum-dependent superconductivity. *Nature Physics*, 3(10):720–725, Oct 2007.

[6] S. V. Borisenko, A. A. Kordyuk, V. B. Zabolotnyy, D. S. Inosov, D. Evtushinsky, B. Büchner, A. N. Yaresko, A. Varykhalov, R. Follath, W. Eberhardt, L. Patthey, and H. Berger. Two energy gaps and fermi-surface "arcs" in $nbse_2$. *Phys. Rev. Lett.*, 102:166402, Apr 2009.

[7] D. J. Rahn, S. Hellmann, M. Kalläne, C. Sohrt, T. K. Kim, L. Kipp, and K. Rossnagel. Gaps and kinks in the electronic structure of the superconductor $2h$-$nbse_2$ from angle-resolved photoemission at 1 k. *Phys. Rev. B*, 85:224532, Jun 2012.

[8] Th. Straub, Th. Finteis, R. Claessen, P. Steiner, S. Hüfner, P. Blaha, C. S. Oglesby, and E. Bucher. Charge-density-wave mechanism in $2H-nbse_2$: Photoemission results. *Phys. Rev. Lett.*, 82:4504–4507, May 1999.

[9] K. Rossnagel, O. Seifarth, L. Kipp, M. Skibowski, D. Voß, P. Krüger, A. Mazur, and J. Pollmann. Fermi surface of $2h-nbse_2$ and its implications on the charge-density-wave mechanism. *Phys. Rev. B*, 64:235119, Nov 2001.

[10] T. Valla, A. V. Fedorov, P. D. Johnson, P-A. Glans, C. McGuinness, K. E. Smith, E. Y. Andrei, and H. Berger. Quasiparticle spectra, charge-density waves, superconductivity, and electron-phonon coupling in 2H−nbse$_2$. *Phys. Rev. Lett.*, 92:086401, Feb 2004.

[11] D. W. Shen, Y. Zhang, L. X. Yang, J. Wei, H. W. Ou, J. K. Dong, B. P. Xie, C. He, J. F. Zhao, B. Zhou, M. Arita, K. Shimada, H. Namatame, M. Taniguchi, J. Shi, and D. L. Feng. Primary role of the barely occupied states in the charge density wave formation of nbse$_2$. *Phys. Rev. Lett.*, 101:226406, Nov 2008.

[12] F. Weber, S. Rosenkranz, J.-P. Castellan, R. Osborn, R. Hott, R. Heid, K.-P. Bohnen, T. Egami, A. H. Said, and D. Reznik. Extended phonon collapse and the origin of the charge-density wave in $2h$−nbse$_2$. *Phys. Rev. Lett.*, 107:107403, Sep 2011.

[13] F. Weber, R. Hott, R. Heid, L. L. Lev, M. Caputo, T. Schmitt, and V. N. Strocov. Three-dimensional fermi surface of $2h-NbSe_2$: Implications for the mechanism of charge density waves. *Phys. Rev. B*, 97:235122, Jun 2018.

[14] M. Hashimoto, R.-H. He, J. P. Testaud, W. Meevasana, R. G. Moore, D. H. Lu, Y. Yoshida, H. Eisaki, T. P. Devereaux, Z. Hussain, and Z.-X. Shen. Reaffirming the $d_{x^2-y^2}$ superconducting gap using the autocorrelation angle-resolved photoemission spectroscopy of bi$_{1.5}$pb$_{0.55}$sr$_{1.6}$la$_{0.4}$cuo$_{6+\delta}$. *Phys. Rev. Lett.*, 106:167003, Apr 2011.

[15] Zakariae El Youbi, Sung Won Jung, Christine Richter, Karol Hricovini, Cephise Cacho, and Matthew D. Watson. Fermiology and electron-phonon coupling in the $2h$ and $3r$ polytypes of Nbs$_2$. *Phys. Rev. B*, 103:155105, Apr 2021.

[16] Sangjun Lee, John Collini, Stella X-L Sun, Matteo Mitrano, Xuefei Guo, Chris Eckberg, Johnpierre Paglione, Eduardo Fradkin, and Peter Abbamonte. Multiple charge density waves and superconductivity nucleation at antiphase domain walls in the nematic pnictide ba 1- x sr x ni 2 as 2. *Physical review letters*, 127(2):027602, 2021.

[17] W L McMillan. Theory of discommensurations and the commensurate-incommensurate charge-density-wave phase transition.

[18] V N Moura. McMillan-Ginzburg-Landau theory of singularities and discommensurations in charge density wave states of transition metal dichalcogenides. *PHYSICAL REVIEW B*, 2024.

Chapter 5

Beyond : Multiple beamspot coherent scattering

5.1 Introduction

With the ability of coherent resonant X-ray scattering laid out we observe that it can be used to

- image first formed domains of antiferromagnetic order during nucleation of a first order phase transition
- image artificially fabricated lateral hetero-structures of mesoscale antiferromagnetic patterns in a paramagnetic background
- distinguish between the melting of an antiferromagnetic order to phase competition and thermal fluctuation and identify the competing phase as the topological defect of the antiferromagnetic order.

We want to highlight that even though we showed the results for antiferromagnetic order, the method is not specific to antiferromagnetic order. Any electronic order such as charge order,

density wave order, or orbital order is observable by the coherent soft-Xray resonant scattering. As long as the peak is broad in reciprocal space and we have enough contrast so that the Bragg peak hosts a speckle pattern we can unearth information about the mesoscale structure and dynamics.

However, at the outset, the method appears to be complex. This is because of the complex speckle pattern associated which doesn't provide us with a direct real-space picture but hides the information in the correlations as we saw in the previous chapter. At its core, the complexity rises from the multiplicity of the domains under the beam spot as shown in Ch3[1]. Only in the dilute limit, does the speckle pattern become easy enough to 'guess' the spatial distribution of the domains correctly. Here we want to leverage this 'diluteness' aspect and show its potential to study the physics of systems under dynamic equilibrium.

Even if the domain distribution is not dilute, diluting the beam footprint on a random domain distribution will have the same simplifying effect on the speckle pattern. This is our key argument and is shown here schematically in Fig 5.1for a random domain distribution. As seen previously the simplification offers to extract the spatial distribution of domains from a single shot of the speckle pattern. Tracking the time evolution of the speckle pattern under experimental conditions will reveal the spatio-temporal structure of domains if and when it changes.

To help dilute the beam footprint we will use the modifications to the already employed X-ray optics in the scattering chambers of soft X-ray resonant coherent beamlines, specifically the Fresnel zone plate. All of the figures shown here are simulations to illustrate the point in question. Also through the process, we will show the designs that have been developed to create multiple coherent beam spots of illumination. In the following section, we will discuss this in detail. Once we have established the design schema for the modification we will discuss science questions that can be addressed with it.

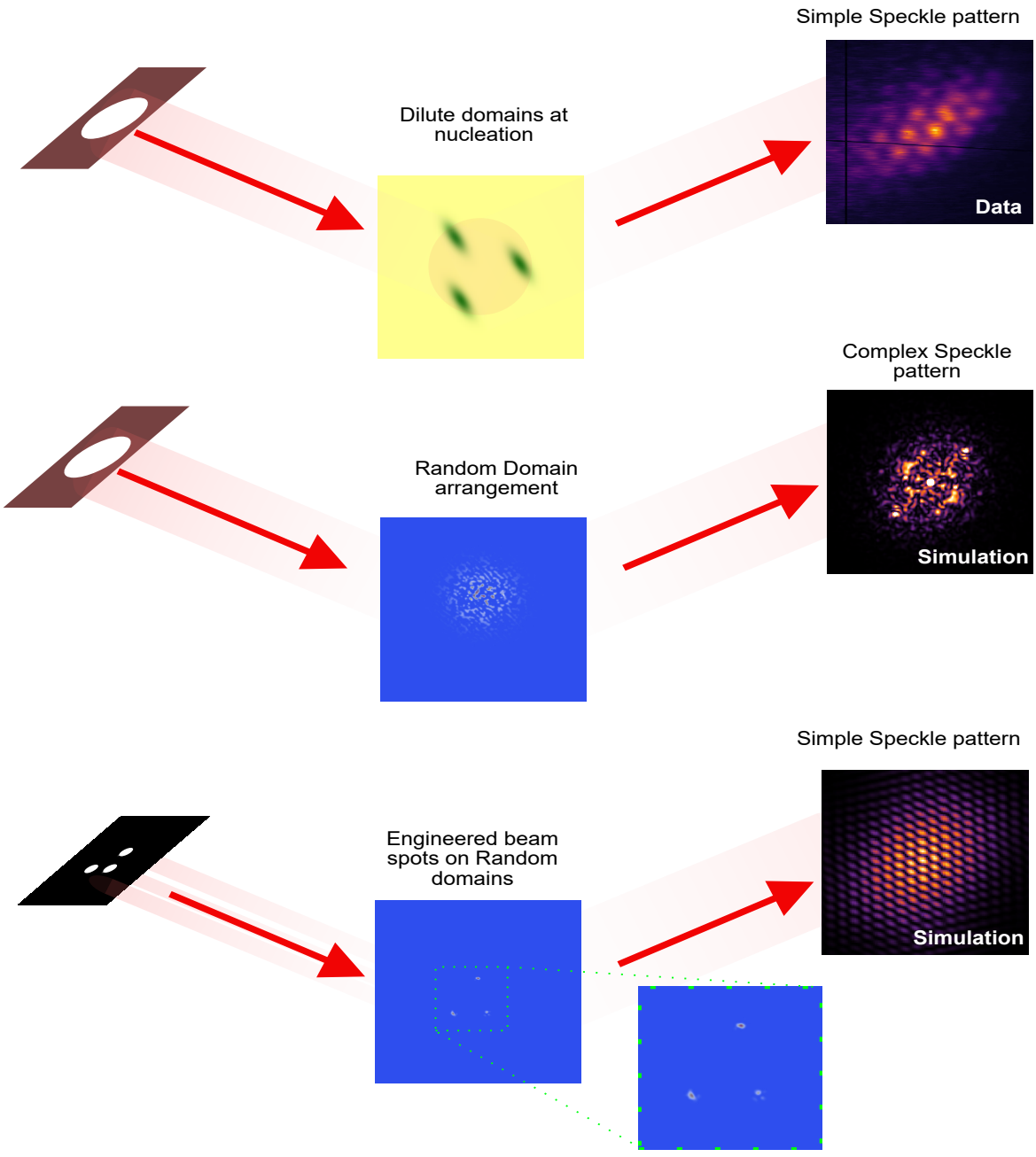

Figure 5.1: Diluting the beam spot simplifies the speckle pattern. The top row shows our results of imaging dilute nucleating antiferromagnetic domains using pinhole scattering. The second row demonstrates the increased complexity of the speckle pattern with more domains. The speckle pattern, an amplitude Fourier transform of the random domain arrangement, is simulated using [2] as a mask. Finally, in the last row, we propose diluting the beam spot into multiple, carefully arranged beam spots (three in this case) to restore the symmetry and simplicity of the speckle pattern.

5.2 Results: Beamspot Engineering

Creating a coherent beam spot from an extended source requires focusing. There are multiple ways to focus X-rays such as Kirkpatrick-Baez mirrors, kinoform lens, compound refractive lens, and Fresnel zone plates. We will briefly mention the others before we focus on the main element of discussion: Fresnel zone plate. Kirkpatrick-Baez mirrors are probably the most widely used method to image the source at a desired focal spot. This is an assembly of two orthogonal cylindrical mirrors set in grazing reflection conditions. Apart from reflective optics, refractive optics are also used to focus X-rays, known as compound refractive lenses. In this case, it is an assembly of concave lenses prepared by drilling aligned holes. However, both reflective and refractive optics work better at hard X-ray energies, above 5 keV. In the soft X-ray regime, the absorption of X-rays by elements increases drastically thus only diffractive optics can help modify the beam propagation.

5.2.1 Fresnel zone plate:

A Fresnel zone plate is a circular diffraction grating that focuses light similar to a lens[3]. The operating principle of a Zone plate is based on interference in the near field limit. Before we discuss zone plate technically we discuss the design in simple terms. If light passes through a circular hole it produces annular interference fringes. Now if we back-propagate the wave from the rings of constructive interference the phases must constructively match at the center of the hole. Thus they will create a focus. Thus if we illuminate a circular diffraction grating with a plane wave it is going to create focus by constructive interference. This is the basic idea which we will elaborate.

Fresnel zone plate acts in the near-field limit, where we must consider the curvature from the secondary wavefronts and can not consider propagation from the sources as plane waves. Circular zones of a Fresnel zone plate are indexed by n up to N for the outermost zone. Let us

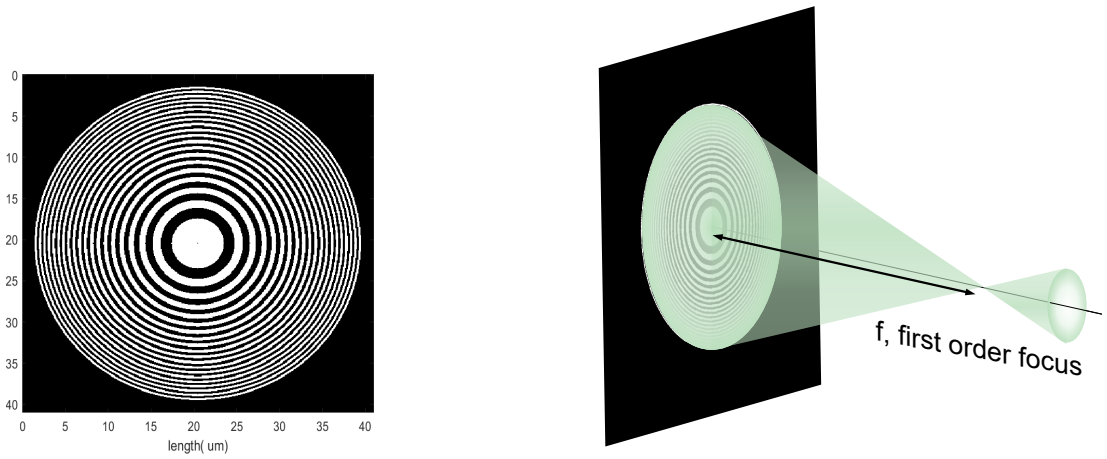

Figure 5.2: Characteristics of Zone plate. (left) A typical zone plate (right) zone plate focuses the incoming beam into a tight focus spot. Here we have shown the beam propagation upto the first order focus and beyond

consider that such a zone plate is illuminated by a plane wave of wavelength λ and has a focal length of f. Neighboring zones differ by a path length difference of $\lambda/2$. Let us also consider that nth zone has a radius of r_n with a width of Δr_n. Then we have,

$$\sqrt{(r_n)^2 + f^2} - f = \frac{n\lambda}{2} \tag{5.1}$$

Expanding the square root and neglecting terms above second-order for a small zone plate we obtain,

$$r_n^2 = n\lambda f \tag{5.2}$$

Here we have neglected the spherical aberration i.e. the fourth order term but this is a functional description of the zone plate. This is sufficient to see that the zone plate is inherently chromatic: every wavelength has a different focus. Thus zone plate as a focusing optics is perfectly suited for coherent scattering chambers where high longitudinal coherence length

requires filtering of wavelengths. The transverse coherence length on the other hand is achieved by focusing through constructive interference. The interference condition ensures phase matching of the incoming wave fronts and thus by construction they are coherent. Therefore, we focus on the zone plate as the element to work on for multiple beam-spot creation.

The above equation allows for the zone plate to have multiple foci along the principal axis of beam transmission. The mth order foci are to be found at $f/|m|$, with $n \to n|m|$, where $m \in \mathbb{Z}$. Thus along the axis zone plate creates cones of focused light propagating for each one of the focus and an unfocused beam for the 0^{th} order. To have a single focused beam spot we must filter out the other cones of different order. This is achieved by an order sorting aperture which simply allows the desired order and blocks the other. Thus, a transmission Fresnel zone plate always comes with an order sorting aperture. The full setup is shown in the Fig 5.3.

Simulation of a Zone plate wave propagation:

As discussed previously in Chapter 3 the propagation of a monochromatic coherent beam can be evaluated using scalar diffraction theory. Here we wish to simulate the beam profile propagation along the propagation axis for a given zone plate design illuminated by a coherent monochromatic beam. Rayleigh-Sommerfield equation as was discussed in context of equation 2.9 will be used again and rewritten here as follows

$$F(u,v) = \frac{\imath}{\lambda} \int_A f_{ZP}(x,y) \frac{e^{\imath \mathbf{k}\cdot\mathbf{r}}}{r} dx dy$$

Here $r = \sqrt{r_0^2 + (u-x)^2 + (v-y)^2}$ is the distance from a secondary source point in the zone plate (x,y) plane to a point in the sample plane or the observation plane (u,v). If we expand r in the limit where r_0 is considerably larger than the zone plate dimensions

$$F(u,v) = \frac{\imath}{\lambda} e^{\imath k r_0} \iint_{ZP} e^{-\imath \frac{\pi}{r_0 \lambda}(x^2+y^2)} e^{-\imath \frac{\pi}{r_0 \lambda} ux} e^{-\imath \frac{\pi}{r_0 \lambda} vy} f_{ZP}(x,y)\, dx dy \tag{5.3}$$

The term $e^{-\imath \frac{\pi}{r_0 \lambda}(x^2+y^2)}$ incorporates the curvature of the wavefronts into superposition from the

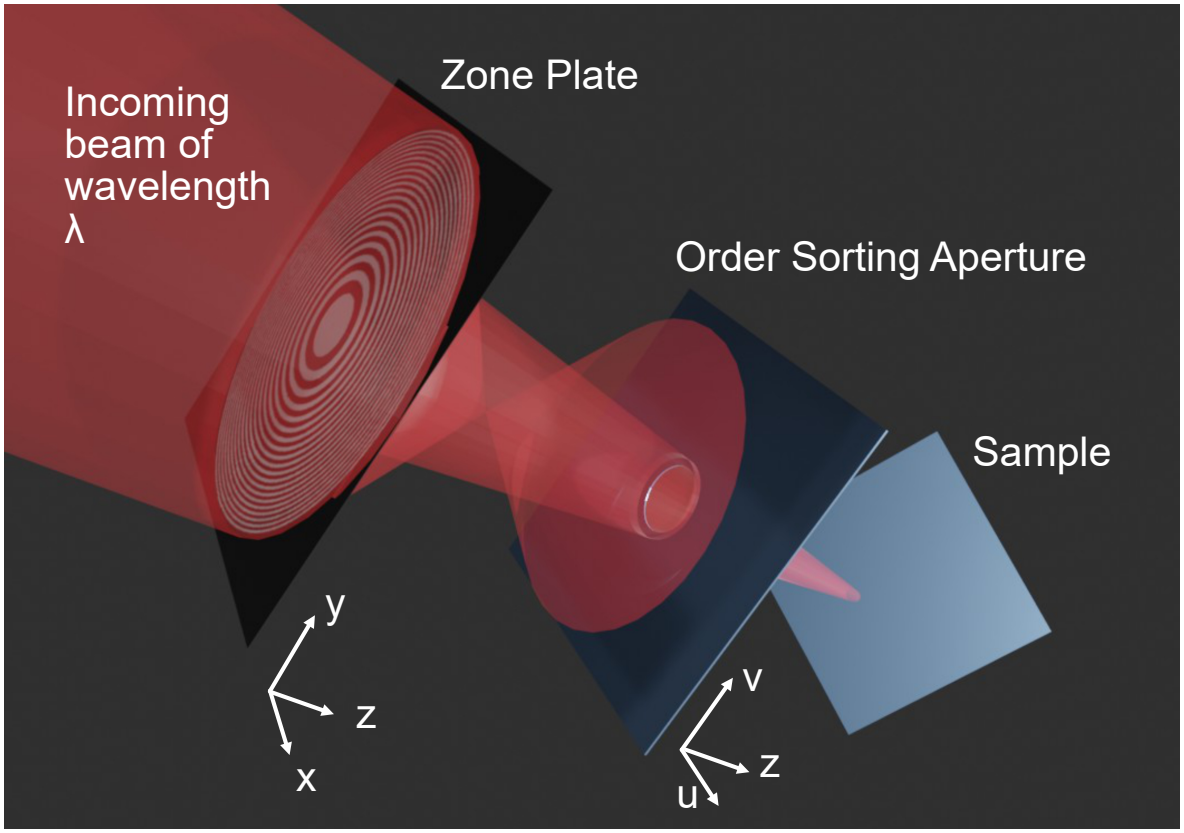

Figure 5.3: Zone plate in experimental set up. One crucial instrument in zone plate-based coherent scattering is using order sorting aperture(OSA) which can be seen here between the zone plate and the sample. The order sorting aperture acts as a filter masking all other beam propagation-related different orders of focus but one. We see in the schematic drawing that the oSA blocks the beams corresponding to a higher order focus formed in between the zone plat and the OSA but a lower order focus passes through

propagated waves. In the far field limit, where $(x^2+y^2)/r_0 \ll \lambda$ that term approaches 1 and the far field distribution resembles a Fourier transform. The term $f(x,y)$ encodes the aperture function which will be developed as the zone plates. Thus using the Rayleigh-Sommerfield equation one can evaluate the propagated wavefront from the zone plates at any distance away from the zone plate surface.

Now we will set up the machinery to numerically forward propagate spherical wavefronts in transmission from the zone plate. For a given wavelength of plane wave illumination, we show below a zone-plate construction of 20 zones with $\Delta r_N \sim 200$ nm and an outer radius of 20 μm. We solve the equation 5.3 numerically to evaluate the beam propagation from an aperture function to an observation plane, which is our sample surface. To do this we will consider the impulse response of the aperture function. The impulse response is found with replacing the aperture function with a delta function in the origin. We denote impulse response as $h(u,v) = \frac{\imath}{\lambda}\frac{e^{\imath kr}}{r}$. Hence the equation for the super position of sources at sample plane

$$F(u,v) = \frac{\imath}{\lambda}\int_Z P f_{ZP}(x,y)\frac{e^{\imath k\sqrt{r_0^2+(u-x)^2+(v-y)^2}}}{r}\,dx\,dy$$

can be rewritten as a convolution integral

$$F(u,v) = \int_Z P f_{ZP}(x,y)h(u-x,v-y)\,dx\,dy \tag{5.4}$$

where ZP stands for doing the integration over the zone plate. Now if we take a Fourier transform on both sides and apply the convolution theorem of the Fourier transform we get

$$\mathcal{F}(F(u,v)) = \mathcal{F}(f_{ZP}(u,v))\,\mathcal{F}(h(u,v)) \tag{5.5}$$

Since convolution in real space is just multiplication in Fourier space equation 5.5 tells us that to evaluate the beam propagation all we have to do is to take the Fourier transform of the

impulse response in the Fresnel limit, multiply that with the Fourier transform of the zone plate aperture function, and finally take an inverse Fourier transform to get F(u,v) at the sample plane. The impulse response now contains the information about the curvature of the wavefronts which are summed over the superposition integral. Thus, we arrive at the equation which we use to find the beam propagation numerically

$$F(u,v) = \mathcal{F}^{-1}(\mathcal{F}(f_{ZP}(u,v))\mathcal{F}(h(u,v))) \tag{5.6}$$

In the simulation we illuminate the zone plate with soft X-rays with energy 852 eV. We designed the zone plate on a 512×512 pixel frame with binary pixels. Each pixel has a dimension of 80nm which is well above the fabrication limit of lithography nowadays. The focal length for the first-order focus is found at 6.4 mm. Also, we can see another higher-order focus around 2 mm. Furthermore, we show the intensity distribution at the focal plane where a clean single beam spot is visible. In nano-diffraction, transmission microscopy, and ptychography experiments such beam spot is utilized.

5.2.2 Modified Fresnel zone plates:

Design - A: To deviate from the regular design and to create multiple beam spots, we argue on symmetry grounds. Since the symmetry of the function f(x,y) in general is also a symmetry of the function F(u,v). If we lower the symmetry of f(x,y) from C_∞ to C_2 the symmetry of F(u, v) will also be lowered. Based on this principle, we first show the design of a zone plate that can create two beam spots. The symmetry of the zone plate is lowered to create the two beam spots. One interesting outcome of this design is that the depth of focus is quite high. However, the efficiency is very low. Such a design may be useful for extremely bright coherent light sources such as 4^{th} generation Synchrotron sources. However, we demonstrate proof of the principle on which we based our argument.

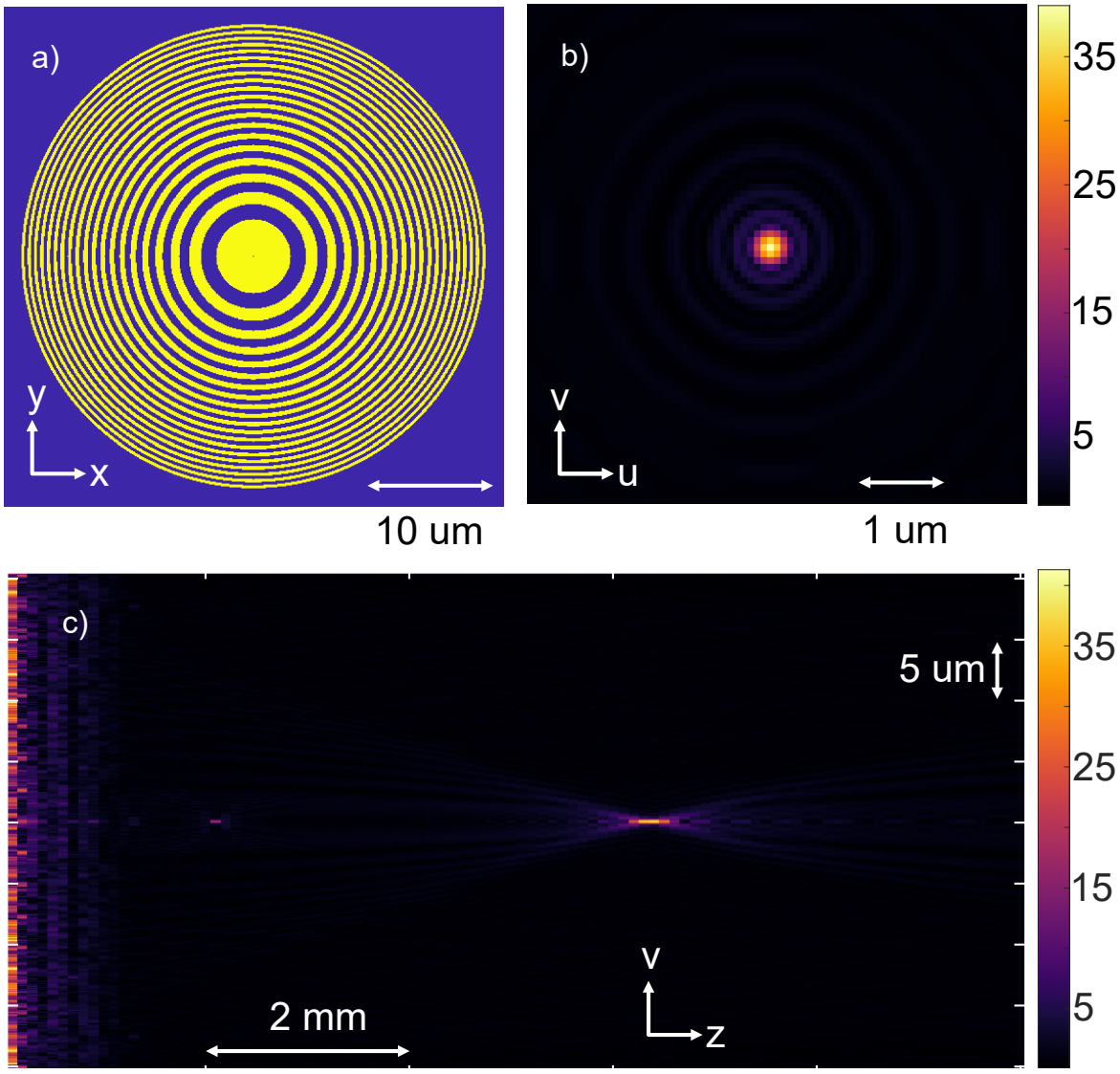

Figure 5.4: Intensity propagation and profile at the focus for a typical Fresnel zone plate (a) The real space design of the zone plate the bright regions are of pixel value 1 and the dark regions are of pixel value 0. The bright regions allow the incoming beam to pass while the dark region blocks them. We use this setup to create all aperture function zone plates here and discussed beyond. Each pixel of the 512 x 512 array represents linear dimension of 80nm(b) Intensity profile at the focal plane. The focal spot is approximately 300 nm while the outer ring radius was 200 nm. For conventional zone plates design the outer ring radius determines the focal spot size (c) Intensity propagation along the wave vector of the beam propagation. The simulation shows the converging and diverging beams towards and away from two focal points: one, at 6.4 mm downstream, and the other higher order focus at around 2mm downstream of the zone plate. Each pixel roughly represents 100 μm. along z direction and 100nm in v-direction.

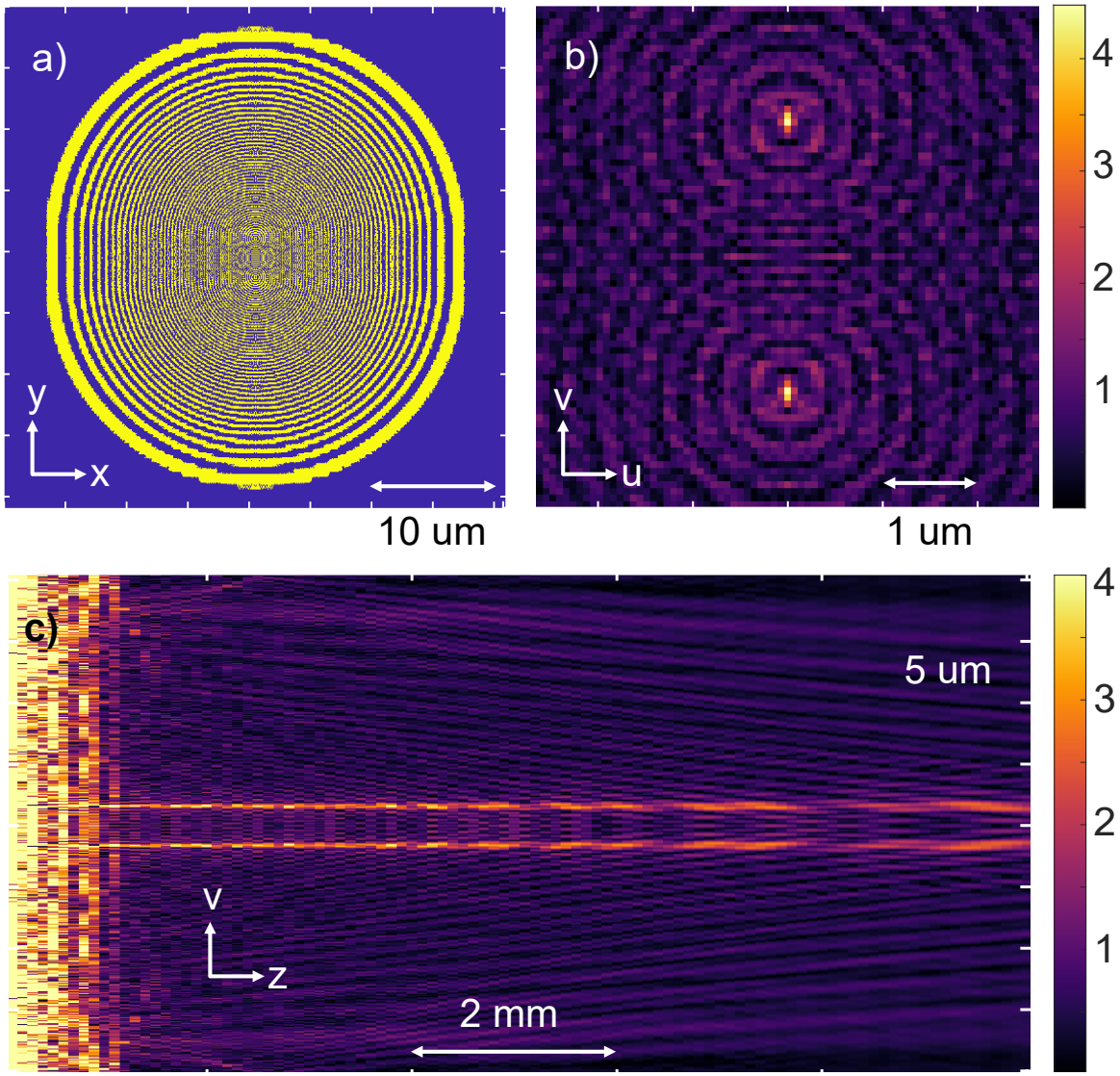

Figure 5.5: Two Spot Creation: Design A (a) Design of the zone plate on a 512 x 512-pixel array with each pixel representing 80nm (b) Intensity profile observed 2 mm downstream of the zone plate where we can see two beam spots of 100 nm in size and are separated from each other by $\sim 3\mu$m (c) Beam profile along the wave vector of beam propagation showing a laser beam like beam creation

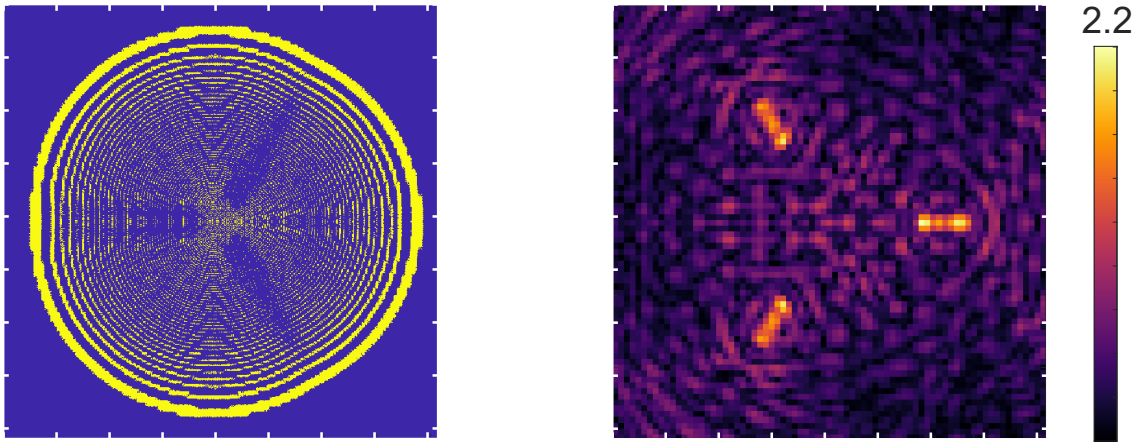

Figure 5.6: Three Spot Creation: Design A (left) The design of the zone plate with each pixel representing 80nm (right) beam profile on 3.7 mm downstream of the zone plate. Each spot is approximately 100 nm in size and comes in pairs. They are positioned on the vertices of an equilateral triangle of side length $\sim 2\mu$m. The OSA can be designed accordingly to select only one of them

Increasing the number of beam spots is rather straightforward. To create three beam spots we lower the symmetry to C_3. We have shown below the construction of a three-beam spot focus from a modified zone plate design. The wavelength has always been 852 eV. Smallest pixel size is set to be 80 nm considering the lithography techniques used to fabricate the zone plates [reference]. However, advancement of the lithography techniques has helped to create high resolution and low defect zone plates. One of the experiments at Advanced Light Source achieved a resolution of 12 nm The algorithm to create the zone plate designs starts from N holes symmetrically arranged around the focal point. Also, the arrangement of holes obeys the new symmetry we want it to obey. We then take the Fresnel transform and digitize the intensity distribution of the transform. This gives us the desired zone plate design. Taking a Fresnel transform of the aperture function gives us two beam spots in the soft X-ray regime. We note

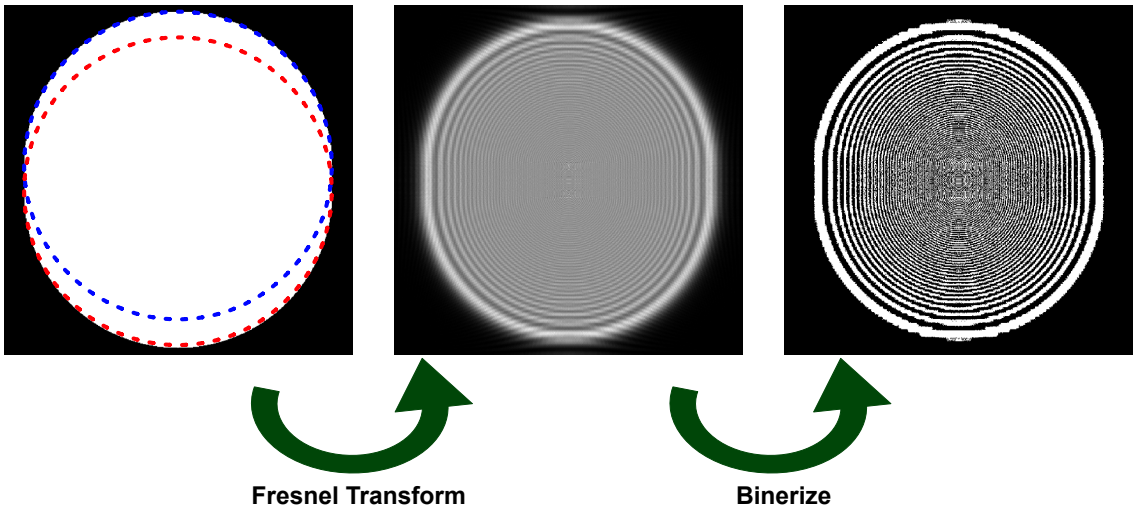

Figure 5.7: Algorithm to create zone plates using design A

that this design is scalable easily to a higher number of beam spots. The figure illustrates the algorithm to create the design responsible for creating multiple beam spots as per design A. On the leftmost panel, we have shown two overlapped circular holes slightly off-centered from each other to break the axial symmetry. The boundaries of the circles are marked by red and blue dashed lines for illustration. First, we take a Fresnel transform of this aperture function to create the middle panel. the wavelength used for the transform is the same wavelength which we intend to use the zone plate with. The middle panel is what essentially gives us the desired aperture function which is responsible for the zone plate design. However, during the fabrication process using lithography, it is useful to have two well-defined limits of transparency. We achieve that here by binarizing the middle panel above a threshold value of 0.58. The final design is shown on the rightmost panel which is again used in the demonstration figure 5.5.

Design B: Here we discuss another design to create multiple beam spots. This design is also scalable to larger number of beam spots. Unlike previous argument, here we exploit the fact that if f(x,y) hosts a topological defect that is propagated in the wave field pass through the

zone plate. Similar to our discussion in Ch 3 where we observed the topological defect of a spin texture leaves a fingerprint on the scattered beam, if we create a defect of winding number N, we observe $2 \times N$ lobes in the scattered beam. Angular symmetry of the defect on the zone plate design selects the correct Bessel mode which translates the essence of the topological defect. Using this methodology we can create $2N$ beam spots where $N \in \mathbb{Z}$. In the following illustrations, we show two such examples where we have created 2, 4, and 6 beam spots. All of the designs discussed require a sorting aperture to limit higher-order contaminations. We denote that the efficiency of the zone plate decreased with number of beam spots increased.

To create the zone plate with a topological defect we multiply the regular zone plate design with gradient masks as shown in the figure. The gradient masks can be defined by a function $\Theta(x-x_0, y-y_0)$ where (x_0, y_0) is the defect location. For our calculation, we have set

$$\Theta(x-x_0, y-y_0) = tanh(tan^{-1}\frac{y-y_0}{x-x_0})$$

. Since $tanh(x)$ ranges between $(-1, 1)$, before multiplying with the zone plate design we rescaled them from $(0, 1)$. Then multiplying the zone plate with this function simply creates an envelope following the tanh function which has a singularity. This singularity is seen as the sharp contrast between the white and the black region in the middle panels. Since the gradient multiplied Zone plate blocks 50% of the beam we compensate that section with an inverted design of the same zone plate. Following the Babinet principle, we know that the diffraction pattern from the two inverted designs will be identical and will just add up. Each design contains the same defect thus the effect of the defect also survives. Finally, adding up we get the design we have used to demonstrate the beam propagation along the axis in Fig 5.8. The reason for creating a topological defect to split the beam can be understood from the point of view of Jacobi -Anger expansion. The angular symmetry of the zone plate selects the fundamental Bessel function to be propagated. The two-dimensional intensity distribution of Bessel functions of the first kind also obeys the

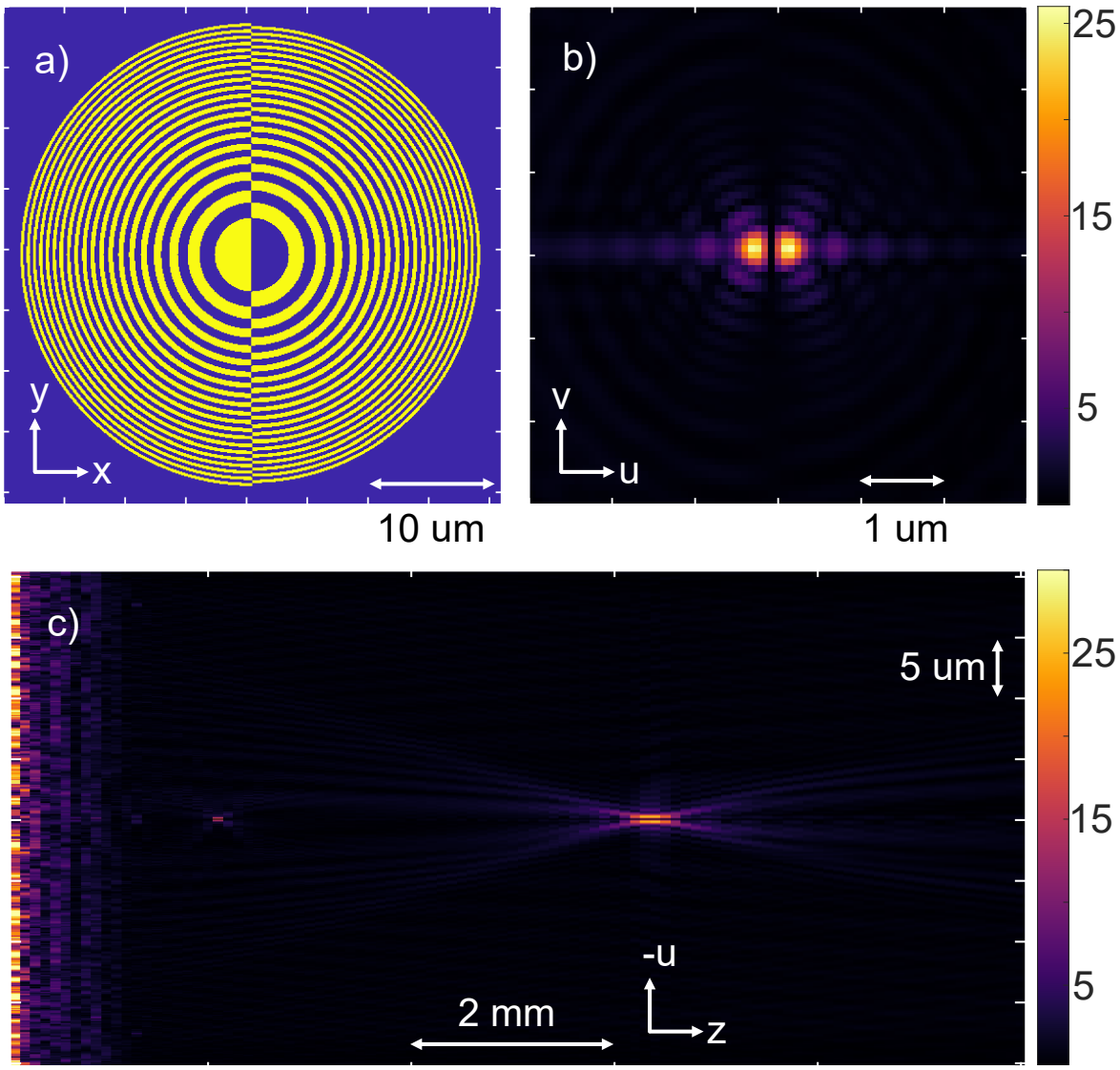

Figure 5.8: Two Spot Creation: Design B (a) Design of the zone plate on a 512 x 512 pixel array with each pixel representing 80nm linear dimension (b)

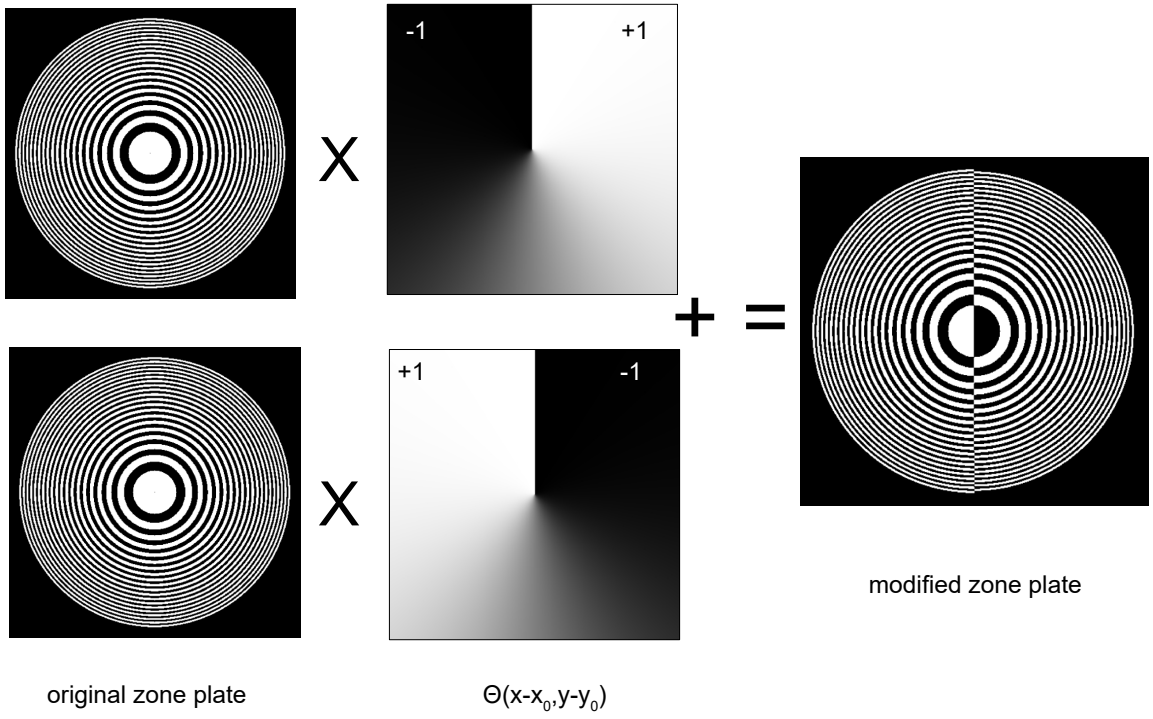

Figure 5.9: Algorithm to create the zone plate using design B

same angular symmetry cast by the zone plate design. Any Bessel function other than the J_0 lacks intensity at the center and hence splits the intensity distribution. Thus from an isotropic intensity distribution at the focal plane, we get a beam spot with two split beam spot

Thus, we have shown that coherent beam spots can be created with modified zone plate constructions. To design these modified zone plates we argued based on the symmetry and topology of the aperture function and its influence on the propagated beam. There are simpler ways one can create two beamspots too. For example, just by blocking off the beam using two slits or two pinholes one can in-principle create multiple spots. Although if the slits are tightly spaced higher order diffraction effects will show up on top of the fundamental aperture function. Since we already utilize diffaction effect in designing the zone plates, the designs are free from such aberrations.

5.3 Discussion: Using Multiple Coherent beam spots

5.3.1 Enhancement of existing experiments:

Now that we have created two beam spots we move on to discuss the benefit of utilizing multiple beam spots in our experiments. The fundamental advantage of using two beam spots over a single beam spot comes from the simplicity of the scattered speckle pattern. As we saw previously, speckle pattern arising from such dilute domain distribution helps us to extract the distribution of domains without a phase reconstruction algorithm. Thus, we expect that a dilute distribution of coherent beam footprint will simplify the existing experiments we carry out on our samples. To illustrate this point we show here two experiments where we take advantage of the two beam-spot coherent scattering.

Domain Orientation: It is often found that the mesoscopic domain structures have a preferential direction for growth after nucleation [2, 4]. For example, as shown in the case for $NdNiO_3$ thin film measured with X-PEEM. The step terraces of the substrate provided the motif

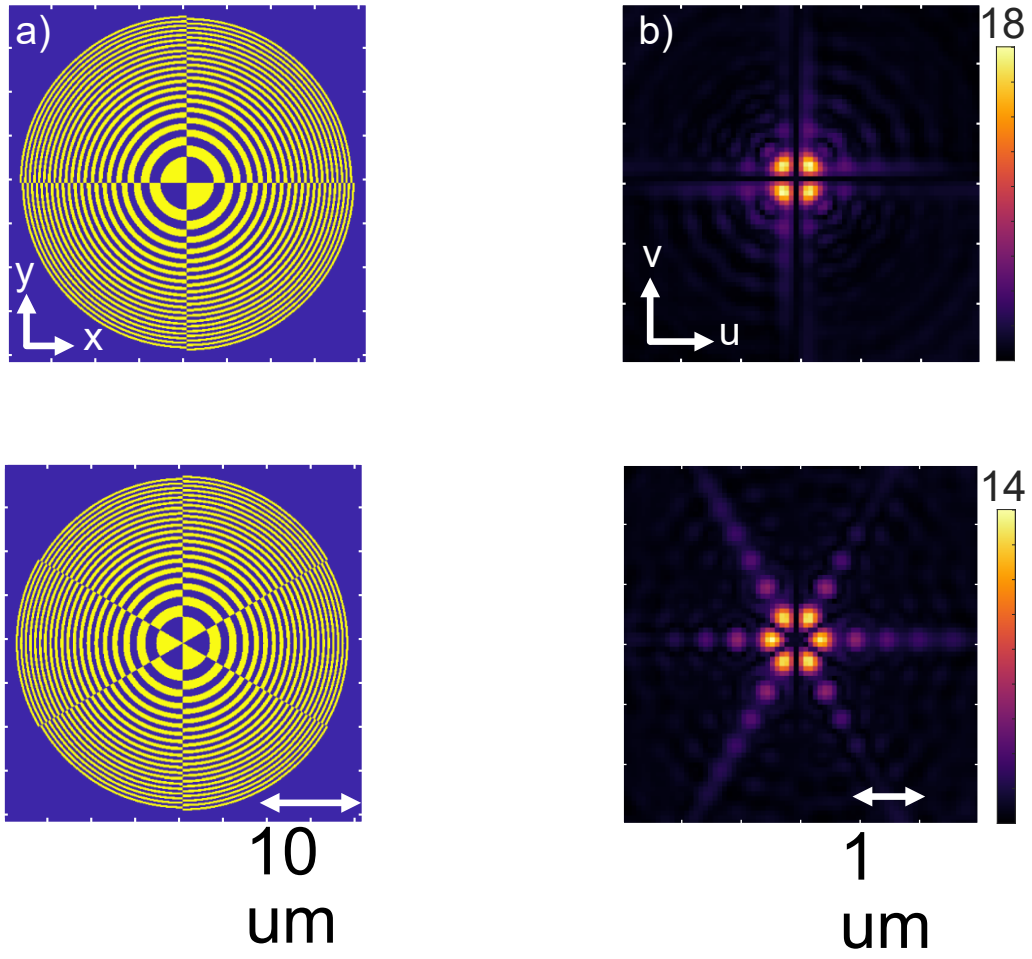

Figure 5.10: Four and Six Spots Creation: Design B (left) the zone plate design scaled to produce 4 and 6 beam spots at the vertices of a symmetrical polygon(b)

in this case and thus 200nm thick but long structures of thin films were deposited. The individual strips eventually coalesce together but provides a growth barrier for the nucleating insulating domains below the metal-insulator transition as shown here in the figure. Now X-PEEM is a microscopy technique so we could see the preferential domain orientation readily. However, if we were to do a coherent resonant X-ray scattering we will tune to the coupled antiferromagnetic order emerging in the insulating states and let us assume that they would follow the same mesoscopic distribution as the insulating domains. Then deciphering the domain orientation will not be easy from the scattered data.

In the figure above we simulate the single spot scattering experiment. With many domains participating in the scattering process, we see a complex speckle pattern. We observe two major high intensities in the speckle pattern and they are arranged with two different symmetries. To understand the relative role of the correlations we need to characterize further possibly with a four-point correlation resolved in angle space. However, we show below that with two beam spot experiments, this observation becomes readily interpretable from the scattered intensity. In the figure below we discuss scattering from the two beam spots as we rotate the sample. With the preferential domain growth direction aligned perpendicular to the separation vector of the beam spots, we can clearly see the high intensity as the dominant super-modulation on the peak. On the other hand, if the beam spots are arranged parallel to the domain anisotropy it hides the information under the complex correlation.

Thus, we have shown here that we can use the two beam spots instead of one as a spatial filtering mechanism to simplify the experiment at hand. Even though we argued for a two-fold (C_2) symmetry of domain orientation we can easily scale the experiment for a different C_n symmetry of domain orientation.

Single shot imaging: To study the mesoscopic organization and evolution single shot imaging is essential. We have established that over and over throughout the development of this thesis. However, depending on the contrast we saw that the single shot speckle pattern can

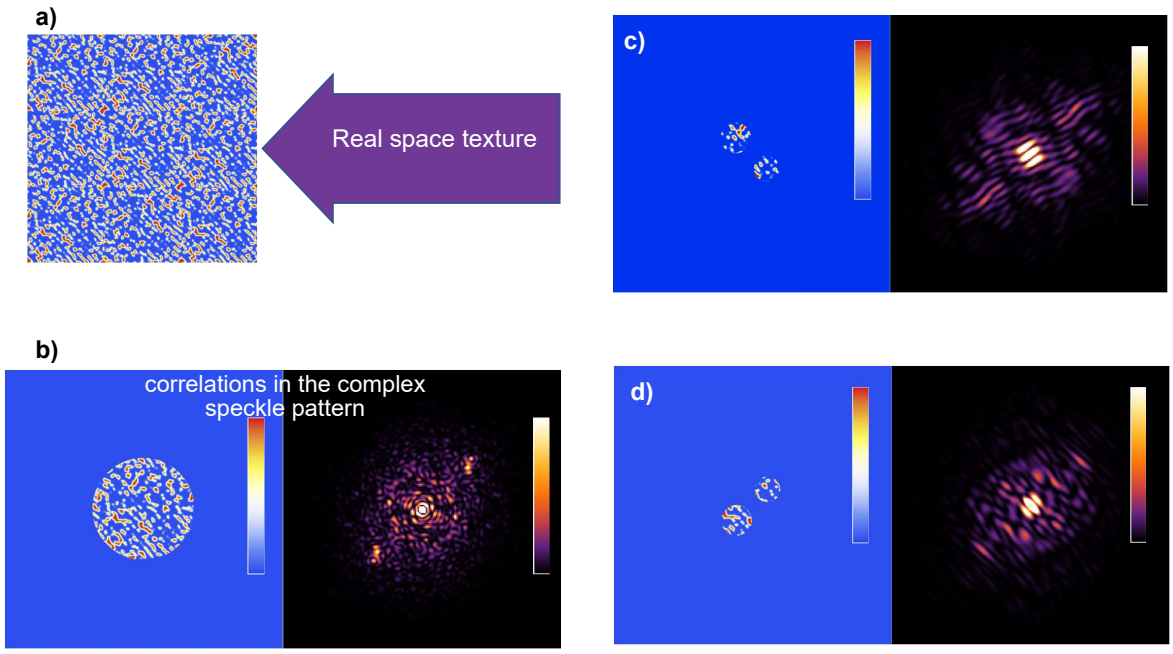

Figure 5.11: Demonstration through Simulation I: a) a real space domain texture created from using experimental phase heterogeneity observed by Mattoni et al during an X-PEEM experiment[2]. The preferential orientation of the domains are along the diagonal of the panel b) Simulation of coherent scattering outcome if we do single beam-spot coherent scattering from this texture. The result is a complex scattering pattern c-d) Two beam spot scattering from the domain patterns with two different orientations of the beam spots relative to domain orientations. When the separation vector between the beam spots is parallel to the modulation direction we see clear supermodulation peaks in the speckle pattern as seen in d).

be either studied with a phase reconstruction algorithm - that suffers from multiple possible solutions or, resort to a higher order correlation of the speckle pattern. However, holography gets around the problem of phase information lost by the use of a reference beam. With the two beam spots we show here that we can simulate a similar scenario. The advantage is of course the simplicity in finding the real space image. In holography, one usually drills a fine enough hole through the sample to have a reference beam interfere with the transmitted beam scattered from the heterogeneous sample. One simply takes a Fourier transform of the speckle pattern observed on the detector to get the real space image.

We have shown such a scenario with two beam spots where one beam spot illuminates a region with a complex domain arrangement while the other illuminates only a single domain. Such an experiment can be designed first by knowing the correlation length of the domains at the temperature of the experiment from incoherent scattering data, and then following it up with the construction of an asymmetrical two-beam spot experiment. For the case of devices where one is certain of the interested region, the problem of creating a single domain under one of the beam spots can be solved by utilizing focused ion beam damage as well. We can see from our simulated illustration that the image of the domain arrangement could be easily found from the inverse Fourier transform. Since the scattered signal is convoluted with the reference domain we estimate a resolution on the order of the reference domain size.

Such an experiment is possible with single-spot experiments but we are often bound to image the location close to the reference spot which has suffered from fabrication techniques such as focused ion beam milling. For strongly correlated electronic systems such perturbations may change significantly the electronic character of the area under investigation. With two beam-spot constructions, we can separate the beam spots far enough that the fabricated area does not interfere with the area imaged.

Lateral structure of Emission: In 4^{th} generation Synchrotron sources the coherence is significantly high. It has been recently shown that such an incoming beam with a long longitudinal

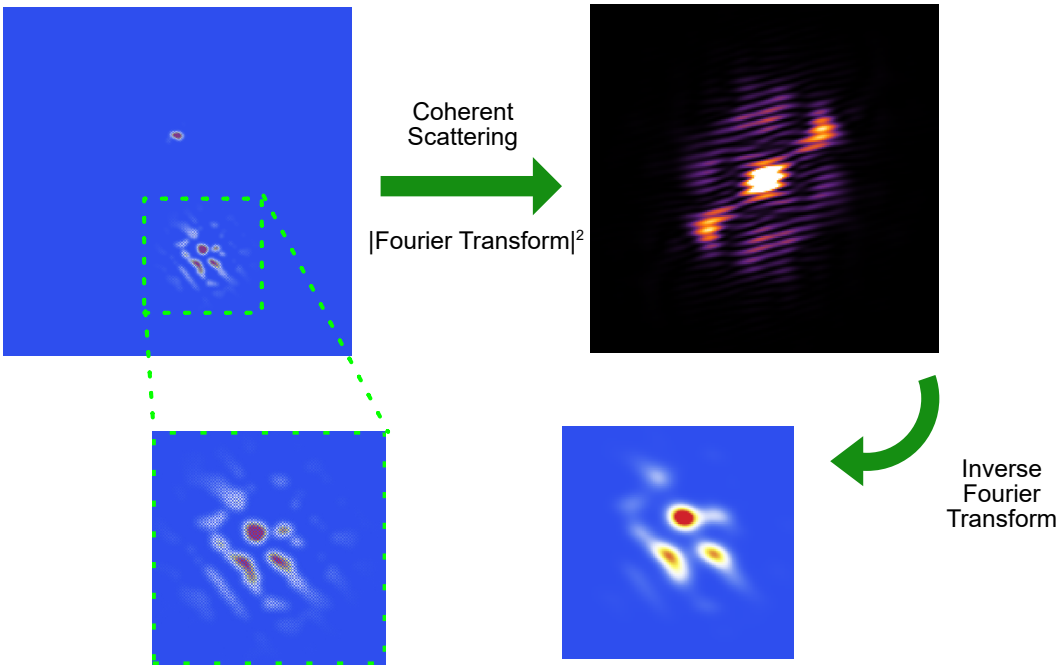

Figure 5.12: Single shot imaging using two beam spot coherent scattering: (a) We show the real space texture contributing to the speckle pattern after two beam spots illuminate the domain distribution in the sample. If under one beamspot there is only one domain then the experiment essentially becomes a holography experiment convoluted with single-domain scattering instead of a reference beam. Thus the image of the scattering complex domain distribution can be found simply by taking the inverse Fourier transform on the observed speckle pattern(b), evaluated here by an amplitude Fourier transform. The resolution of the imaging experiment will be limited by the single domain size under the top beam-spot (c) zoom in on the real space complex domain arrangement (d) inverse Fourier transform of the speckle pattern. The similarity between (c-d) proves the imaging aspect of this experiment. The texture is adapted from [2]

coherence length (3μm) can image the fluorescence centers [5, 6, 7]. To show this the authors created two beam spots on a Cu foil of 20 μm thickness. The two beam spots were created using compound refractive lenses along with phase grating to split the beam. The incoming pulses of 10 fs duration and photon energy of 9 keV pass in transmission through the Cu foil before it is recorded in an area detector. We have reprinted their experimental details in Fig 5.13 to facilitate the discussion. The photon energy was chosen to be just slightly above the Cu Kα_1 and Kα_2 to facilitate fluorescence emission. They found that the intensity-intensity correlation, $g^2(q)$ obtained from each one of the 58 million recorded frames showed the fringe pattern expected from two fluorescing centers, just like double-slit interference.

The lifetime of the core-hole excitation associated with the fluorescence emission is 0.6 fs. They were generated over the time of 67 fs which is required for the incoming pulse to travel the thickness of the Cu foil. However, this was only possible because of the high brilliance compensating for the low signal-to-noise ratio. Another way to compensate is probably creating multiple beam spots in an array instead of two beam spots, which we would like to discuss here.

That beam spot engineering in coherent sources can extract information previously unseen, has been comprehensively demonstrated by the experiment discussed [5]. If the spectral line width is small on the order of a few meV one can potentially get a coherence time on the order of 1ns, which brings us to the realm of the fastest area detector available for 3rd generation Synchrotron sources. Utilizing these detectors in third-generation Synchrotron sources, we propose to create an array of beam spots with well-defined separation on the sample. This is ideally a grating on the sample surface able to resolve energies. Now, we set an incoming beam to one of the resonance edges of the sample. This not only increases the photon count on the output but also creates a core hole near the valence shell of the electron which relaxes back following all possible electronic excitation pathways available in the system. Let us suppose for the sake of discussion that we have a strongly correlated electronic system with a transition metal ion of Ni. If we create a $2p \rightarrow 3d$ transition using Ni-L3 edge, it will emit at the energy of Ni-L3 along with Ni-L3+1 eV

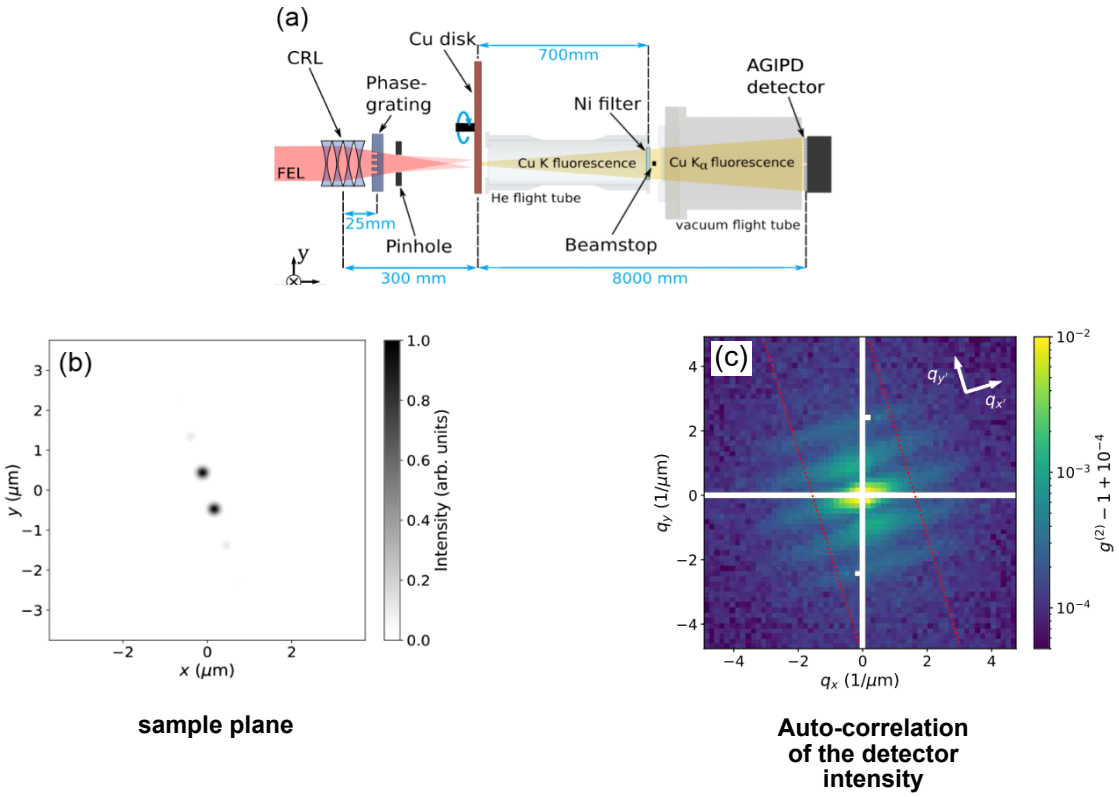

Figure 5.13: Imaging via correlation of X-ray fluorescence[5]: (a) The experimental set-up splits the coherent beam using CRL and phase grating. The expected beam spot profile is shown in panel (b) where we see two beam spots separated by about a micron. The FEL pulses pass through the 30 μm Cu-foil and the foil fluoresce at Cu K α edge shown in (a). The detector collected 58 million frames of intensity patterns with very low contrast. However, taking auto-correlation on the pattern the authors could find fringe patterns related to the fluorescence centers. Thus from the auto-correlation patterns, they could reconstruct the image of the two spots.

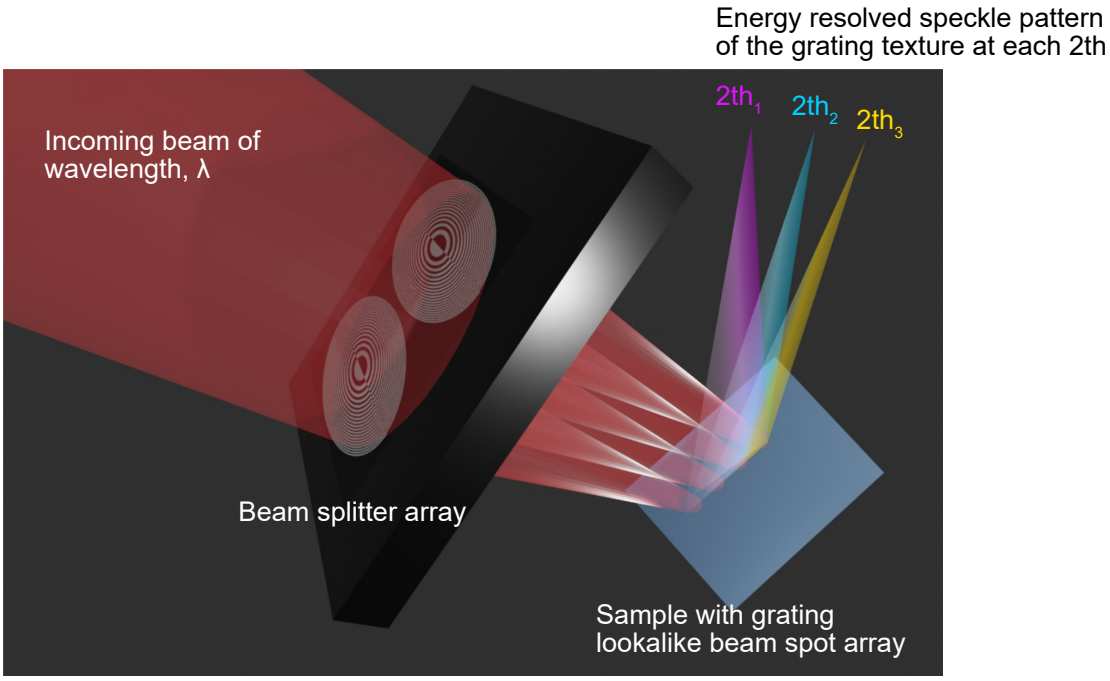

Figure 5.14: Combining Resonance Inelastic scattering with coherence:

for the *dd* excitation, and all other possible emission lines. Those lines that have a very sharp bandwidth on the order of 1-10meV can be studied. Under the grating, the emission lines will create their diffraction peaks at different angular positions in space. Thus, to select a specific energy we need to park our detector at the respective 2θ angle.

The first-order or second-order correlation in the intensity pattern recorded will be able to tell us the real space distribution of the emission scattering centers. Furthermore, we can correlate this real space information with the elastic line which will be resolved similarly. The elastic contribution will tell us information similar to energy-integrated coherent scattering. Thus, in this way, we propose to resolve the speckle pattern in energy space.

5.3.2 New mode of coherent experiments for driven systems:

Here we explore the possibility of utilizing two-spot experiments as a possible probe for studying systems under dynamic equilibrium. Even though we had been studying the static phase organization of the samples, in practice condensed matter systems are often used for voltage and current response from the material. Thus understanding physical systems under the gradient of potential is of considerable importance. In the context of temperature one can think of a situation where the base temperature of the sample is set at T while the left edge is connected to a source with T+ΔT and the right edge is connected to a sink of T-ΔT. Such a system will be coupled to a thermal current. We can subsequently design experiments to probe the evolution of the domain organization to study the coupling. With the directionality in-built in the two beam-spot we can easily employ such tools to study these problems.

Examples of directionally driven systems: The design of magnetic racetrack memory is built around this idea of a directionally driven system[8]. The authors showed that short pulses of spin-polarized current can be used to drive the domain walls in a permalloy nano-wire. The domain arrangement of alternate magnetic moments can be used to load non-volatile memory into the nano-wire. Then the domain arrangement can be driven from one end while the data is read out at a different suitable position along the 1-dimensional distribution of domain arrangement. This is precisely the kind of system we wish to study. Another similar work has been shown in the context of topological defects, such as skyrmions in a 1-dimensional channel of metallic ferromagnets [9]. Here the current pulses coupled to the skyrmions and moved them at speeds exceeding 100 ms^{-1}. Both of these experiments will show more complexity in higher dimensional version where other degrees of freedom will be important and will influence the kinetics significantly. If we consider that only energetics drive the equation of motion for the domain walls and skyrmions then not only observing their kinetics will tell us about the fabrication quality of the next-generation magnetic storage system but will provide us with a direct experimental methodology to study the driven system in a dynamic equilibrium. On top of the energy landscape driving most of these kinetics,

all motion will suffer from fluctuations and dissipation which will make the kinetics richer in phenomenology.

To understand the kinetics we need to devise an experiment that can be done in a single shot. Then the time evolution can be recorded with subsequent shots. Coherent scattering is such an experiment that collects data about the phase organization in a single shot. However, since the data is collected over a large region it suffers from complexity as discussed above. Thus, we propose to simplify the result using multiple beam spots where the beam spots are arranged according to the science question one is looking for.

Illustration of the new mode schematically: A demonstration of a hypothetical experiment is shown below using two-beam spot coherent scattering where we can see the scattering output change due to the domain motion as shown by an arrow in the second plot. Here we consider the motion of the domains towards a direction noted by the arrows. Left and right columns correspond to a former and later instant of time, respectively. For each instant of time, we show the real space domain distribution and the Fourier transform depicting the coherent scattering outcome. We vary the beam spot shape between the top and bottom rows.

On the top row of the panels, we show the speckle pattern that will be observed had we experimented with a coherent beam spot similar to the circle drawn on each real space panel. The left and right panels are two instants of real space tecture and corresponding coherent scattering outcome. The two reciprocal space speckle patterns can be considered two shots of the experiment. We note that the speckle pattern remains relatively similar. However, the distinct scattering outcome can be observed from the bottom panels where two smaller beam spots were used to filter out all other information. The fringe pattern for the bottom-right panel in the reciprocal space tells us about the separation of the domains. By tracking the fringe pattern on the detector thus we can record the kinetics of the domain motion.

A single large beam-spot coherent scattering gets all possible interference patterns that can be generated from individual domains. Thus the coherent scattering results on the top row

are complex and hardly reveal any information from the single-shot mode about the motion the domains underwent. The power of diluting the beam spot comes from spatially filtering the scattering field to simplify the scattered speckle pattern. Designing two nano-beam spots helps us create a well-separated and well-directed scattering filter from the sample. Simplification makes it possible to directly observe the evolution from single shot coherent scattering outcome.

5.4 Conclusion

In this chapter we have shown that if we create multiple beam spots of coherent beam we can expand our experimental methodology to study domain dynamics at mesoscale. Furthermore, these multiple beam spot creation help us simplify existing experiments for a direct single shot observation of the experimental question at hand. Thus can be easily expanded to a time domain characterization.

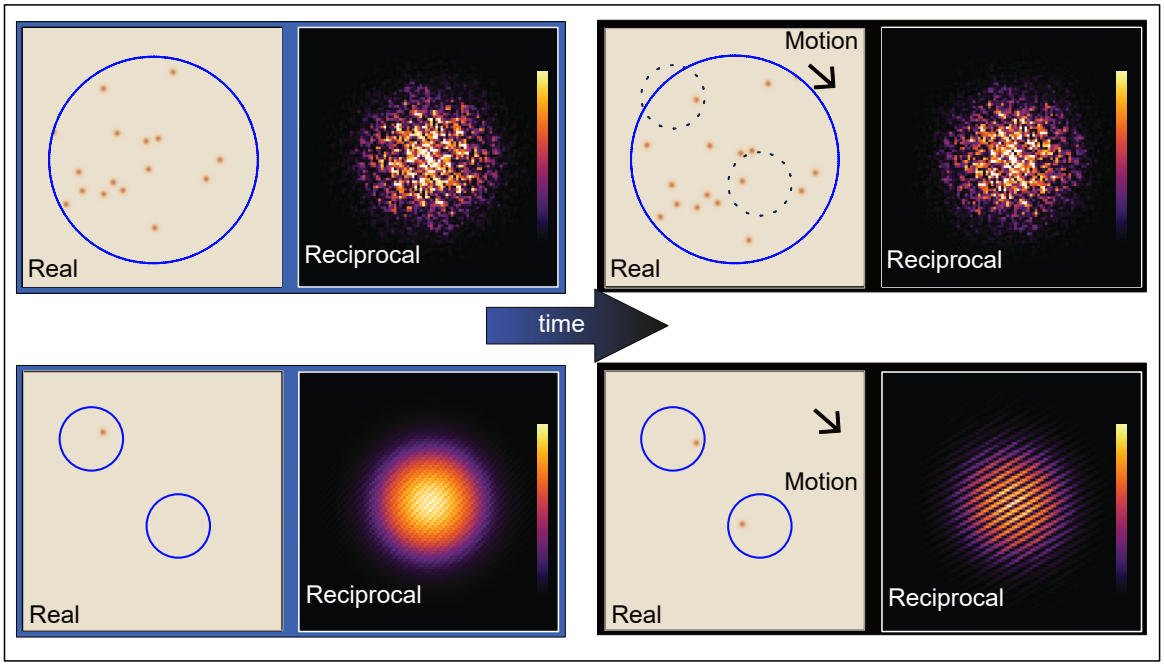

Figure 5.15: New mode of coherent scattering experiment where we can study the kinetics of real space textures. The top row shows two instances of the regular coherent scattering experiment using a single beam spot possibly created with a pinhole. The real space domain distribution moves along the directed motion arrow however the complexity of the speckle pattern fails to capture it. The same domain motion is now studied using two-beam spot scattering. The single-shot coherent scattering outcome considerably changes indicating a phase texture change. The real space figure in the top right panels shows the relative comparison between the beam spot structures where the two-beam spot is shown with dashed lines

Bibliography

[1] Martin Bluschke, Rourav Basak, Andi Barbour, Ashley N. Warner, Katrin Fürsich, Stuart Wilkins, Sujoy Roy, James Lee, Georg Christiani, Gennady Logvenov, Matteo Minola, Bernhard Keimer, Claudio Mazzoli, Eva Benckiser, and Alex Frano. Imaging mesoscopic antiferromagnetic spin textures in the dilute limit from single-geometry resonant coherent x-ray diffraction. *Science Advances*, 8(29):eabn6882, July 2022. Publisher: American Association for the Advancement of Science.

[2] G. Mattoni, P. Zubko, F. Maccherozzi, A. J. H. van der Torren, D. B. Boltje, M. Hadjimichael, N. Manca, S. Catalano, M. Gibert, Y. Liu, J. Aarts, J.-M. Triscone, S. S. Dhesi, and A. D. Caviglia. Striped nanoscale phase separation at the metal–insulator transition of heteroepitaxial nickelates. *Nature Communications*, 7(1):13141, November 2016. Publisher: Nature Publishing Group.

[3] Chris Jacobsen, Malcolm Howells, and Tony Warwick. Zone-Plate X-Ray Microscopy. In Peter W. Hawkes and John C. H. Spence, editors, *Springer Handbook of Microscopy*, pages 1145–1204. Springer International Publishing, Cham, 2019.

[4] Longlong Wu, Yao Shen, Andi M. Barbour, Wei Wang, Dharmalingam Prabhakaran, Andrew T. Boothroyd, Claudio Mazzoli, John M. Tranquada, Mark P. M. Dean, and Ian K. Robinson. Real space imaging of spin stripe domain fluctuations in a complex oxide. *Phys. Rev. Lett.*, 127:275301, Dec 2021.

[5] Fabian Trost, Kartik Ayyer, Mauro Prasciolu, Holger Fleckenstein, Miriam Barthelmess, Oleksandr Yefanov, J. Lukas Dresselhaus, Chufeng Li, Sa ša Bajt, Jerome Carnis, Tamme Wollweber, Abhishek Mall, Zhou Shen, Yulong Zhuang, Stefan Richter, Sebastian Karl, Sebastian Cardoch, Kajwal Kumar Patra, Johannes Möller, Alexey Zozulya, Roman Shayduk, Wei Lu, Felix Braußе, Bertram Friedrich, Ulrike Boesenberg, Ilia Petrov, Sergey Tomin, Marc Guetg, Anders Madsen, Nicusor Timneanu, Carl Caleman, Ralf Röhlsberger, Joachim von Zanthier, and Henry N. Chapman. Imaging via correlation of x-ray fluorescence photons. *Phys. Rev. Lett.*, 130:173201, Apr 2023.

[6] Fabian Trost, Kartik Ayyer, and Henry N. Chapman. Photon statistics and signal to noise ratio for incoherent diffraction imaging. *New Journal of Physics*, 22(8):083070, August 2020. Publisher: IOP Publishing.

[7] Fabian Trost, Kartik Ayyer, Dominik Oberthuer, Oleksandr Yefanov, Saša Bajt, Carl Caleman, Agnes Weimer, Artur Feld, Horst Weller, Sébastien Boutet, Jason Koglin, Nicusor Timneanu, Joachim von Zanthier, Ralf Röhlsberger, and Henry N. Chapman. Speckle contrast of interfering fluorescence X-rays. *Journal of Synchrotron Radiation*, 30(1):11–23, Jan 2023.

[8] Stuart S. P. Parkin, Masamitsu Hayashi, and Luc Thomas. Magnetic domain-wall racetrack memory. *Science*, 320(5873):190–194, 2008.

[9] Seonghoon Woo, Kai Litzius, Benjamin Krüger, Mi-Young Im, Lucas Caretta, Kornel Richter, Maxwell Mann, Andrea Krone, Robert M Reeve, Markus Weigand, et al. Observation of room-temperature magnetic skyrmions and their current-driven dynamics in ultrathin metallic ferromagnets. *Nature materials*, 15(5):501–506, 2016.